Università degli Studi di Torino
Scuola di Dottorato

Development of a compact neutron spectrometer for BNCT based on multi-element activation analysis

Ettore Marcello Mafucci

Università degli Studi di Torino
Scuola di Dottorato

Dottorato in Fisica

Development of a compact neutron spectrometer for BNCT based on multi-element activation analysis

Candidate: Ettore Marcello Mafucci

Tutor: Prof. Marco Costa

Reviewers: Dr. Peter Schillebeeckx[1]**, Prof. Carles Domingo Miralles**[2]

[1] EC JRC Geel, Belgium.
[2] Universitat Autònoma de Barcelona, Spain.

"*...timeo Danaos et dona ferentes.*"

Virgilio, *Eneide II*

Abstract

In recent years, the introduction of accelerator-based Boron Neutron Capture Therapy (BNCT) facilities has led to a significant increase in interest from the medical and scientific communities. Monitoring and characterization of neutron beams and intercomparison of different facilities are becoming mandatory [1]. This stimulates the development of dedicated dosimetry and spectrometry techniques.
This work aims to present a novel compact spectrometer with an isotropic response called Neutron Capture Therapy-Activation Compact Spectrometer (NCT-ACS). The spectrometer is highly sensitive, covering the energy interval from thermal up to 100 keV, and designed for a single irradiation exposure. The detector geometry is composed of a spherical moderator shell containing different material foils exhibiting neutron radiative capture resonances covering the wide energy domain for BNCT. The manuscript will first focus on the extensive simulation work done to optimize, in terms of response and efficiency, the detector geometry and its material composition. Irradiation and activation measurements on a first prototype have been performed at the electron LINAC facility installed at the University of Turin, where a well-known epithermal neutron field is available. The materials activation was measured using a HPGe gamma detector opportunely calibrated for accounting all the effects due to the spectrometer geometry. A careful analysis of the activation gamma spectra has been performed to correctly estimate the statistic and systematic uncertainties.
The Turin epithermal neutron spectrum was then extracted using the unfolding code FRUIT [2] and compared with the standard measurement performed with the Bonner Sphere Spectrometer technique. The agreement between the two measurements is within few %. This provides a proof of concept of our novel neutron spectrometer NCT-ACS.
Finally, a particular effort has been focused in transferring the entire procedure implementing the use of a LaBr(Ce) detector, slightly less performant, but significantly smaller than the HPGe detector. This guarantees the portability of the entire measurement system, making it suitable for in-situ measurements.

Contents

1

Neutron Physics

The aim of this first chapter is to provide some theoretical notions regarding neutron production, detection and application. While not aiming to be exhaustive, it is intended to deal with the main aspects on neutron physics and to introduce the topics useful for the upcoming chapters.

1.1 Neutron classification

Neutrons interact with matter differently from charged particles such as protons or α, but also differently from γ rays. The reason is that they do not interact through electromagnetic force, but only through strong and weak forces. The cross sections for atomic processes are immensely larger respect to the nuclear processes, therefore neutrons can easily penetrate matter without losing a significant amount of energy.

The neutrons kinetic energy is strongly determined by the production mechanism. Once generated, a neutron can not be accelerated using electric field because of its neutral charge. It can be slowed down via elastic or inelastic collisions with atoms of disparate elements or materials. Such a process is called *neutron moderation* (section 1.5). It should be noted that the same material or element moderates differently neutrons with low or high kinetic energy. Moreover, if the moderator is cooled, it can further lower the kinetic energy compared to a non-cooled moderator.

Neutron beams can be produced from a large variety of nuclear reactions and characterized by energy distributions that can vary over ten orders of magnitude. Since the interactions of neutron in matter depends on its energy, a dedicated nomenclature for different energy has been defined (table 1.1).

Nomenclature	Energy Range	λ (Å)	Application
COLD	< 0.012 eV	> 2.61	Immaging, Scattering, Magnetic Field Analysis
THERMAL	0.012 eV - 0.4 eV	0.45 - 2.61	BNCT, Diffraction, Imaging, Scattering, NAA, Nuclear Reactor
EPITHERMAL	0.4 eV - 0.1 MeV	0.09 - 0.45	Imaging, Scattering, BNCT, NAA
FAST	> 0.1 MeV	< 0.09	Scattering, Fast Reactor, Neutron Probe

Tab. 1.1.: Neutron energy subdivision and main applications. **NAA** is the **N**eutron **A**ctivation **A**nalysis and **BNCT** is the **B**oron **N**eutron **C**apture **T**herapy.

It should be interesting to note that the upper limit for the thermal range is arbitrary fixed. In this work a value of 0.4 eV has been chosen to separate thermal from epithermal neutrons. This value represents the so-called "cadmium cut-off" [3]. In this work the thermal and epithermal ranges were mainly considered.
In particular, the neutron energy domain interested by this work is from thermal up to 100 keV.

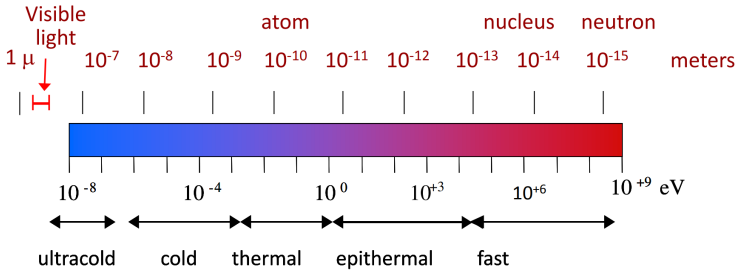

Fig. 1.1.: Subdivision of the neutron energy spectrum. At the top is shown the classification in wavelength, at the bottom in energy.

As can be seen from table 1.1, applications are often spread over multiple energy ranges. Depending on the energy interval used, different information can be extracted from the same application.
For instance, considering the neutron imaging application, the use of cold neutrons allows to study the object on a scale larger than 2.61 Å (molecular distances). While using the epithermal component allows studying the sample on a (0.09 - 0.045) Å scale (atomic distances).
For example, BNCT involves a rather wide range of energies. Depending on the type of cancer and its location, it is important to select an appropriate energy component to maximize the therapy effectiveness.

1.1.1 Neutron sources

The existing neutrons sources are classified by the physical process that determine the kinetic energy of neutrons. Some examples of typical spectra of the mainly used sources are shown in fig. 1.2-1.5:

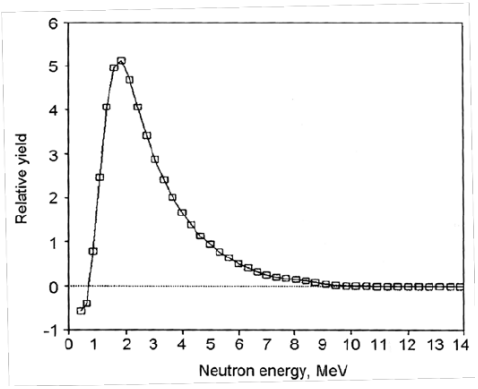

Fig. 1.2.: Neutron ^{252}Cf fission energy spectrum [4]

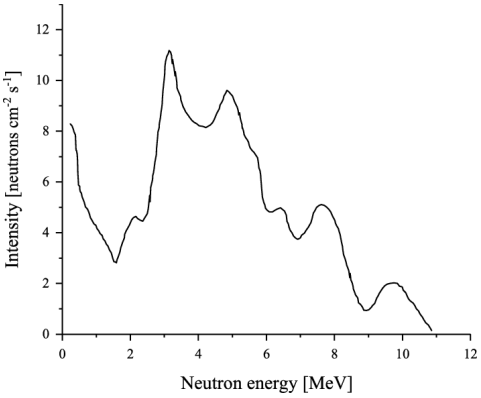

Fig. 1.3.: Am-Be (α,n) conversion energy spectrum [5].

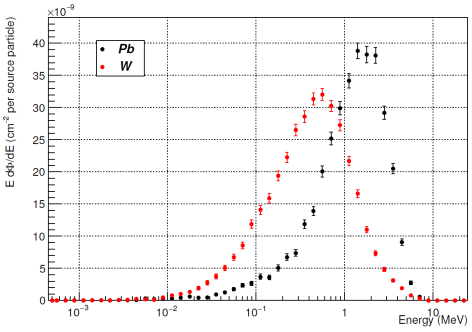

Fig. 1.4.: Photo-production using two different 5 cm thick targets [6].

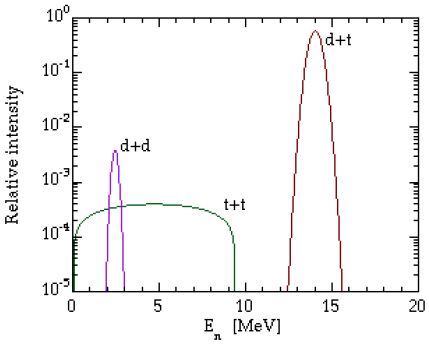

Fig. 1.5.: Neutron energy spectrum for some fusion reactions [7].

- **Nuclear fission source**

  In nuclear fission, a heavy atomic nucleus, such as ^{235}U or ^{239}Pu, absorbs a thermal or fast neutron, depending on the used material. This absorption makes the nucleus highly unstable. As a result, the nucleus splits into two or more smaller nuclei, along with several neutrons and a significant release of energy. The process is highly exothermic, and the energy released is in the form of kinetic energy of the fission products and of the emitted neutrons. These neutrons can further initiate fission reactions in nearby fissile nuclei, creating a self-sustaining chain reaction. The fission can be also spontaneous (only when A>230), as in the case of ^{252}Cf (figure 1.2).

- **(α, n) Conversion source**

  Alpha-n (α-n) neutron sources, such as Am-Be or Am-B, operate on the principle of utilizing radioactive decay to produce neutrons. In these sources, a radioactive element, typically ^{241}Am, decays emitting α particles. These particles possess relatively high energies (>5 MeV). The key to neutron production lies in the interaction of these alpha particles with a specific target material, which is often Be or B. When the emitted alpha particles collide with the target material, nuclear reactions are triggered. One of the significant reactions that take place is the (α, n) resulting in the emission of neutrons.

  To ensure safety, α-n neutron sources are encapsulated and appropriately shielded to prevent accidental exposure to radiation. These sources are valued for their portability and are used in multiple applications. A typical energy spectrum for an Am-Be source is shown in figure 1.3.

- **Nuclear fusion source**

  In a fusion source, two light atomic nuclei, often isotopes of hydrogen like deuterium and tritium, combine to form a heavier nucleus. Fusion reactions release a significant amount of energy in the form of kinetic energy and high-energy neutrons. To achieve fusion, the fuel (D and T) is heated to extremely high temperatures, typically in the millions of Celsius degrees. Magnetic confinement (as in a Tokamak) or inertial confinement (as in laser fusion) are needed to confine fusion fuel in the form of a plasma. When the fuel reaches these extreme temperatures and pressures, the atomic nuclei overcome their electrostatic repulsion and collide, undergoing fusion reactions. The fusion reactions releases high-energy neutrons, characterized by energy spectra that present a distribution highly peaked around the mean value (figure 1.5).

- **Spallation source**

  In a spallation neutron source, a primary beam (most commonly protons) impinges on a target composed by a high mass number. The primary particle reacts with nucleons. This can create an intranuclear cascade where some energetic hadrons escape as secondary particles. Then, evaporation takes place when the excited nucleus relaxes by emitting low-energy (less than 20 MeV) neutrons, protons, alpha particles, etc., with the majority of the particles being neutrons.

  Secondary high-energy particles produced during the intranuclear cascade move roughly in the same direction as that of the incident proton and can

collide with other nuclei in the target. The reactions that follow are a series of secondary spallation reactions that generate more secondary particles and low-energy neutrons.

- **(γ, n) Photoproduction source**

  In these processes a high energy photon interacts with the nuclear field, for elements with A>200 the neutron production cross-section dominates for energy above 13-15 MeV; proton production is, in fact, suppressed by the coulombian barrier of the nucleus.
  For this work, data were collected at the e_LiBANS (University of Turin) and GELINA (EC-JRC-IRMM, Geel) facilities. Both of them produce neutrons via the (γ, n) reaction. Section 1.4 is dedicated to a more in-depth and detailed description of these type of sources.

1.2 Physical relevant quantities

The aim of this section relies on the description of the physical quantities that are used throughout this work. Some of these are useful almost only in the neutrons area of interest and therefore require a specific definition.

First, a physical quantity that will be used repeatedly is the *Fluence* Φ. According to ICRU Report 85 [8] it is defined as the quotient of dN/da, where dN is the number of particles incident on a sphere of cross-sectional area da, thus:

$$\Phi = \frac{dN}{da} \tag{1.1}$$

The use of a sphere of cross-sectional area da expresses in the most simply manner the fact that one considers an area da perpendicular to the direction of each particle. In transport calculation (as those employed in the Monte Carlo software, like MCNP) the fluence in a cell of volume ΔV is frequently expressed in terms of the lengths of the particle trajectories l_i within the i-th cell. In can be demonstrated that the fluence is given by [9]:

$$\Phi = \frac{\sum_{i=1}^{n} l_i}{\Delta V} \tag{1.2}$$

In a stationary field composed of particles with velocity v, the Fluence can be calculated from the particle density n (particles per unit volume) as:

$$\Phi = nvt \tag{1.3}$$

The definition 1.1 implies that an isotropic response is needed to accurately measure the quantity. Devices with prominent directional response,should be used only in mono-directional fields. Otherwise, the variation of their response with the angle of incidence and the directional distribution of the field should be known in advance.

Another quantity of interest is the neutron flux.In particular, the flux is the increment of particle number divided by the interval time [8]:

$$\dot{N} = \frac{dN}{dt} \tag{1.4}$$

The flux unit measure is the s^{-1}, while the unit measure for the fluence (equation 1.1) is cm^{-2}.

Another quantity that is often used is the fluence rate, defined as the ratio between the variation on the fluence and the variation on time:

$$\dot{\Phi} = \frac{d\Phi}{dt} \tag{1.5}$$

For a stationary field characterized by particles of velocity v the fluence rate can be rewritten using the 1.3:

$$\dot{\Phi} = \frac{d\Phi}{dt} = \frac{d(nvt)}{dt} = nv\frac{dt}{dt} = nv \tag{1.6}$$

It is often useful to report the fluence energy spectrum in the equilethargic representation:

$$\frac{d\Phi}{du} = E\frac{d\Phi}{dE} \tag{1.7}$$

where E is the neutron energy and u is the lethargy, which depends on the number of elastic collisions needed to reduce the neutron energy from the initial value E to the final value E'. It is defined by the equation:

$$u = \ln\frac{E}{E'} \tag{1.8}$$

The energy in equi-lethargic representation preserves the integral of the curve also in logarithmic scale, making possible comparison between different spectra [10].

1.3 Neutron cross sections

The following section an overview over all the most relevant neutron interaction processes is presented. This summary is not intended to be exhaustive. For detailed reviews the reader may consult any of the articles or books on the subject [11], [12],[13],[14],[15],[16],[17],[18],[19], [20].

1.3.1 Scattering cross sections

The coherent neutron scattering lengths represents a fundamental nuclear parameter that establish a crucial connection between measured cross-section data on one side and the wave functions and nuclear potentials on the other. Hence, these scattering lengths hold the potential to validate the theoretical frameworks concerning neutron-nucleus interactions.
From the applied point of view, scattering lengths are used as "tools" in various studies of crystals lattice and solids.
Supposing an incident neutron on a target, the incident wave function can be modeled like:

$$\psi(z) = e^{ikz} \tag{1.9}$$

At large distances r form the scattering center (target), the total wave function describing both the incident and scatter neutron is in the form:

$$\psi(r) = e^{ikz} + f_l(\theta)\frac{e^{ikr}}{r} \tag{1.10}$$

$f(\theta)$ describes the amplitude of the scattered component in the direction θ. For s-wave (l=0) neutrons, this factor can be obtained as:

$$f_0(\theta) = \frac{1}{2ik}(e^{2i\delta_0} - 1) = -\frac{e^{2i\delta_0}}{k} sin\delta_0 \tag{1.11}$$

Where k is the wave number and δ_0 is the s-wave phase shift which is related to the scattering length a by the definition:

$$a \equiv -\lim_{k \to 0}\left(\frac{sin\delta_0}{k}\right) \tag{1.12}$$

In the approximation $k \to 0$ (slow neutrons), the scattered component of 1.10 has the form:

$$\frac{a}{r}e^{ikr} \tag{1.13}$$

And, consequently, the scattering cross section for slow s-wave neutrons can be calculated as:

$$\sigma_s = \frac{4\pi}{k^2} sin^2\delta_0 = 4\pi a^2 \tag{1.14}$$

It can also be shown [21] that the spin-dependent scattering lengths a_+ and a_- associated with spins states I = +1/2 and I = -1/2 (where I is the spin of a target nucleus) can be written in terms of the Breit-Wigner formalism. Moreover, considering the coherent scattering length for each spin state, the scattering length can be separated into real and imaginary parts:

$$a_{coh} = R' + \sum_j \frac{2\lambda\Gamma_{nj}(E - E_j)}{4(E - E_j)^2 + \Gamma_j^2} + i\sum_j \frac{\lambda\Gamma_{nj}\Gamma_j}{4(E - E_j)^2 + \Gamma_j^2} \tag{1.15}$$

Where R' is a constant term that can be explained considering the optical model and λ is the De Broglie wavelength:

$$\lambda = \frac{\hbar}{\sqrt{2mE}} \tag{1.16}$$

The imaginary part of the 1.15 can be related to the absorption cross section σ_a [11]:

$$\sigma_a \propto \frac{a_i}{k} \tag{1.17}$$

Being k the wave number. For a massive particle, the wave number depends by the energy of the particle like $k \propto \sqrt{E}$. Replacing the 1.15 into the 1.17 one can be note that the absorption cross section is almost energy independent if it goes like 1/v. However, when neutron resonance is located near thermal energies, the neutron cross section no longer present a 1/v trend and a_i become Energy dependent. More details on how to correct this aspect will be provided in section 1.3.5.

For an element with several isotopes, characterized by different scattering length, the total coherent scattering length is given by:

$$a = \sum_j f_j a_j \tag{1.18}$$

While the quantity f_j is the fractional abundance of the isotope j.

1.3.2 Capture cross sections

Generally a description of the neutron capture cross sections refers to the Breit-Wigner formalism. However, is interesting to mention that in some cases the capture cross sections can be adequately accounted in terms of a non-resonance contribution, i.e. direct capture mechanism. This capture mechanism plays a dominant role in nuclei characterized by an high binding energy, like the light ones or nuclei with

nucleons numbers close to the magic numbers (2, 8, 20, 28, 50, 82, and 126).

For an isolated, neutron resonance, the Breit-Wigner formula for capture reaction can be written in the form:

$$\sigma_{tot} \propto \frac{g\Gamma}{(E - E_r)^2 + \left(\frac{\Gamma}{2}\right)^2} \tag{1.19}$$

Where g is the spin factor and Γ is the total interaction width that is defined by the product of all the possible interaction widths Γ_i, being i a specific decay or interaction channel. The definition of g is:

$$g = \frac{2J + 1}{(2S + 1)(2I + 1)} \tag{1.20}$$

Since the spin S for neutrons is 1/2 the 1.20 can be rewritten:

$$g = \frac{2J + 1}{2(2I + 1)} \tag{1.21}$$

Being J the spin of the resonance and I the spin of the target nucleus.
It should be noted that, for most nuclei, the resonance energy E_r is far from the thermal region (as already mentioned in 1.3.1) and that the resonance energy is much higher compared to the total width Γ. As a result, the contribution from known resonances to the capture cross section at a neutron energy of 0.0253 eV (corresponding to a maxwellian peak at 293.6 K) can be approximated by the incoherent sum:

$$\sigma_\gamma^0 = A\Big(\frac{A}{A+1}\Big)^2 \sum_j^N \frac{g\Gamma_{nj}^0 \Gamma_{cj}}{E_{0j}^2} \tag{1.22}$$

Being A an empirical factor. Similar expressions can be written to evaluate the contribute of the resonances in the thermal region for a specific interaction channel Γ_i simply substituting the Γ_c term with the desired term.
Typical widths Γ of measured resonances are in the order of electron-volts. According to Heisenberg's uncertainty principle, the corresponding life time of the compound nucleus is in the order of $\tau = \hbar/\Gamma \simeq 10^{-15}$ s, several orders of magnitude larger than the typical time needed by a neutron to cross a nucleus without interaction. In direct reactions, as the opposite reaction mechanism to compound nucleus reactions, the incident neutron interacts directly with one or a few nucleons without forming a compound nucleus. The time scale of direct reactions is in the order of 10^{-22} s, much shorter than compound-nucleus resonance reactions. Direct reactions become important for the heavier nuclei at neutron energies higher than about 10 MeV where the De Broglie wavelength of the neutron becomes comparable to the size of nucleons. But also at lower neutron energies, mainly for light or closed shell nuclei, direct reactions may contribute significantly to the total reaction cross section.

Nevertheless, in general for neutrons with energies below 1 MeV the compound nucleus reactions prevail.

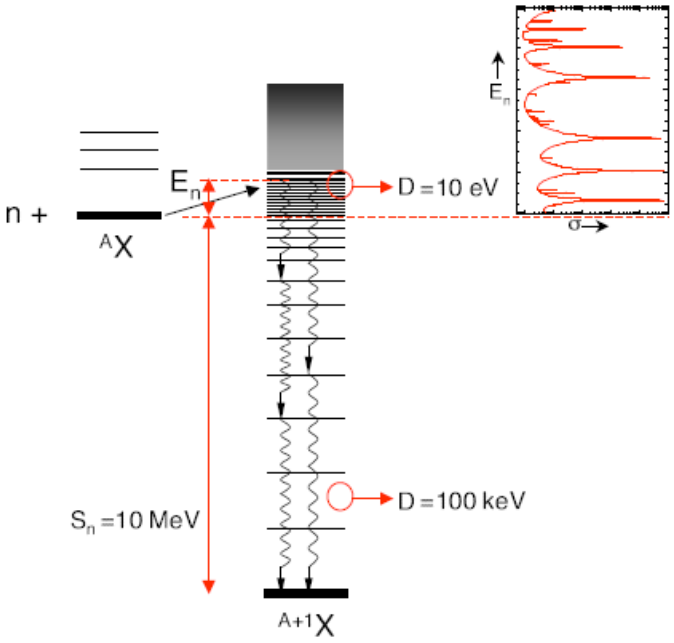

Fig. 1.6.: Schematic view of the formation and decay of a compound nucleus with typical values of level spacing and neutron separation energy. The resonances observed in the reaction cross section correspond to the excitation of nuclear levels.

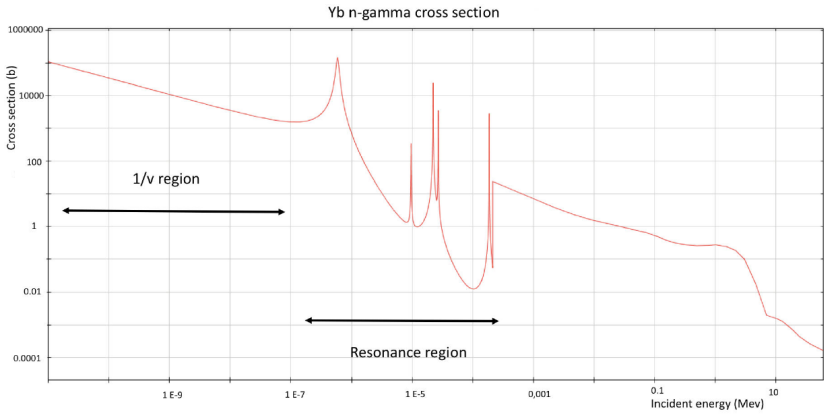

Fig. 1.7.: Yb radiative neutron capture cross section as a function of neutron incident energy [22]

To summarize, studying the overall capture cross section, four region can be distinguished (fig- 1.7):

- For low energy neutrons, before the first capture resonance, σ_c is approximately 1/v where v is the velocity of the neutron.

- At higher energy, isolated resonances can be found and the radiative cross section assume the shape of the typical Breit-Wigner resonance. This region of

isolated resonances begins in the keV region in medium weighted nuclei, in the MeV region in light nuclei and in the eV region for very heavy non-magnetic nuclei. This region is called Resolved Resonance Region (RRR).

- At even higher energy, resonances start to overlap and are not longer distinguishable. The Breit Wigner formalism can not be applied and the formal treatment is based on integral quantities.

- Finally at higher energies ($\approx$ MeV), other reactions begin to intervene in competition with the radiative capture cross section. The result of this trend is a decrease of σ_c to very low values at high energies.

It should be noted that the energy point of separation between the RRR and the URR depends element by element, but ultimately it is determined by the experimental energy resolution. Hypothetically, with a perfect system with close to zero energy resolution ($\Delta E/E \simeq 0$) all the resonances can be resolved and so the RRR would be extended over all the URR.

After the capture reaction, prompt gamma are emitted to de-excite the compound nucleus. After the emission of prompt rays the isotope is, in most of cases, still unstable; it means that it can decays via α or β emission. This delayed emission is completely random in time for the stochastic nature of the process.
Figure 1.8 is strictly related to figure 1.6 and shows how the new nucleus can decay via β decay after the prompt gamma emission process.

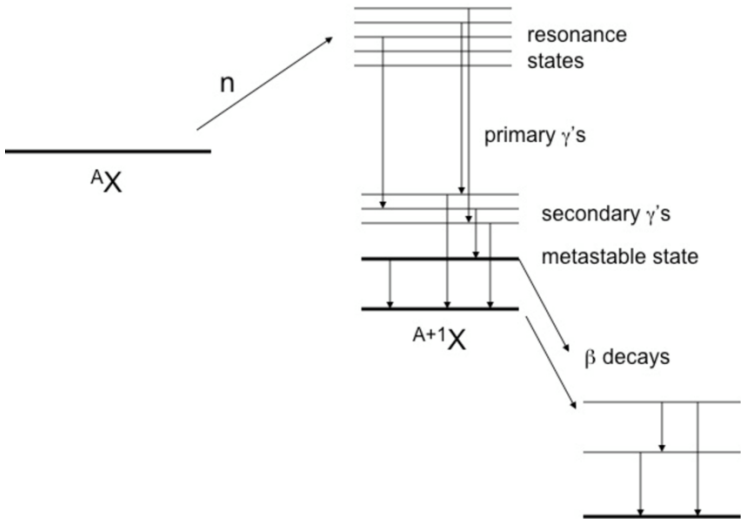

Fig. 1.8.: Neutron capture scheme for the reaction ${}^{A}_{Z}X + {}^{1}_{0}n \rightarrow \left({}^{A+1}_{Z}X\right)^{*} \rightarrow {}^{A+1}_{Z}X + \gamma$. Refer to [23].

A useful feature in studying neutron capture comes from the prompt γ rays which are almost completely unselective in populating the lower excited states, because there are no strong selection rules based on nuclear structure. For instance, if the capture state has spin S = 4, a dipole radiation to populate all 3, 4, 5 spin states can be expected. This is in contrast to α and β decay, where the emission process is mainly driven by selection rules which may forbid decays in certain states. Neutron capture can therefore serve as a complete means of spectroscopy of excited states.

Another interesting application of the (n, γ) reaction occurs when the ground state of the final nucleus is itself unstable (see the scheme in 1.8). In this case, an activity A is induced within the sample exposed to the neutron beam.
A deep treatment of this application will be analyzed within this work.

It should be useful to remember that, for a specific element, the cross section of the process does not depend in any way on the type of decay to which the formed nucleus will undergo. This can be explained using the principle of independence formulated by Ghoshal in 1950 [24]. The only difference between the case in analysis and other capture phenomena relies on the particle emitted during the de-excitation.

1.3.3 Kernel formalism

An useful formalism for the treatment of the capture cross section has been proposed by the Brookhaven laboratory [25].
For simplicity, the model threats the case of a single-level Breit-Wigner (SLBW), introducing a quantity strictly related to the strength of the resonance called kernel:

$$A_\gamma = \int_{-\infty}^{+\infty} \sigma_\gamma(E) dE \tag{1.23}$$

In fact, this quantity is the area of the resonance, calculated integrating over all the energy phase space. From [26] p.89, the expression can be compared with:

$$A_\gamma = 2\pi^2 \lambda\!\!\!^{-2} g \frac{\Gamma_n \Gamma_g}{\Gamma} \tag{1.24}$$

Considering an isolated resonance of the energy E_0 and calling ΔE the energy between E_2 and E_1 range in which the resonance can be considered isolated, the mean capture cross section value can be defined as:

$$\bar{\sigma_\gamma} = \frac{1}{\Delta E} \int_{E_2}^{E_1} \sigma(E) dE \approx \frac{1}{\Delta E} \int_{-\infty}^{+\infty} \sigma_\gamma(E) dE = a \frac{g \Gamma_n \Gamma_\gamma}{\Gamma} \tag{1.25}$$

Where, for brevity, the a term contains all the quantities out of the integral. The equation 1.25 reveals that there is a strong dependence of the average radiative cross section on the area of the resonance itself and also on the reaction widths. The value of a can be obtained with some calculations and its dependence on the energy is $\propto 1/E_0$. This dependence can be largely omitted as long as single resonances case is discussed, but it will play an important role once many resonances must be considered in a single energy group ΔE.
It should be noted that during the resonance parameters evaluation in the RRR, the effect of the resonances outside this energy range should be taken into account. In computing average cross sections these resonances would be accounted by processing codes, but not by kernel equations. Therefore, one should be aware of that and be careful when comparing different data. The most commonly used resonances are:

- Bound resonances. These are introduced primarily to fix thermal region. However, their elastic scattering tail might extend to much higher energies depending on their neutron width. It should be noted that in some cases they are really large. Consequently, they can interfere with the real cross section in the thermal domain. They are characterized by a negative E_0 resonance energy.

- High energy resonances. These are introduced primarily to take care of contribution from missing resonances and to compensate the lack of knowledge in the Unresolved Resonance Region (URR). Again, if their width is too large, the tails would extend to much lower energies.

It should be noted that all these considerations have been proposed within the SLBW approximation. The Multi Level Briet Wigner (MLBW) approximation is, in general, more adequate than the single level one. The collision matrix in this model is:

$$U_{cc'} = e^{-i(\phi_c+\phi_{c'})}\Big(\delta_{cc'} + i\sum_{\lambda}\frac{\Gamma_{\lambda_c}^{1/2}\Gamma_{\lambda_{c'}}^{1/2}}{E_\lambda + \Delta_\lambda - E - i\Gamma_{\lambda/2}}\Big) \tag{1.26}$$

Where c and c' are the initial and final state and Δ_λ is the level shift. Without giving too many details of this complex modeling, from the 1.26 it should be noted that the MLBW collision matrix is not unitary, therefore, the value of σ_c is not the sum of the partial cross sections. Only elastic scattering is actually calculated in MLBW approximation. All other partial cross sections are calculated in SLBW approximation, and the total cross section as the sum over all partials. This avoids negative cross sections yet prevents neither nonphysical peak cross sections nor badly described interference minima for strongly overlapping levels.
It should be highlighted that the calculation of MLBW partial cross sections considering the σ_c equation involves a double sums over levels. This can be time-consuming

if hundreds of levels are to be included, as is not unusual with modern evaluated data. Thus, the partial cross section calculation is most commonly extracted directly from the collision matrix which involves only a single sum over levels.

1.3.4 Doppler broadening and Free Gas model

An important phenomenon that affect the resonance shape is the Doppler broadening. Thermal motion of the target nuclei causes Doppler broadening of the resonance peaks observed in the laboratory system: as the target temperature increases, the peaks become broader while their areas remain practically constant. This changes the average scattering, capture and fission rates. For these reasons it plays an important role in the cross section evaluations.

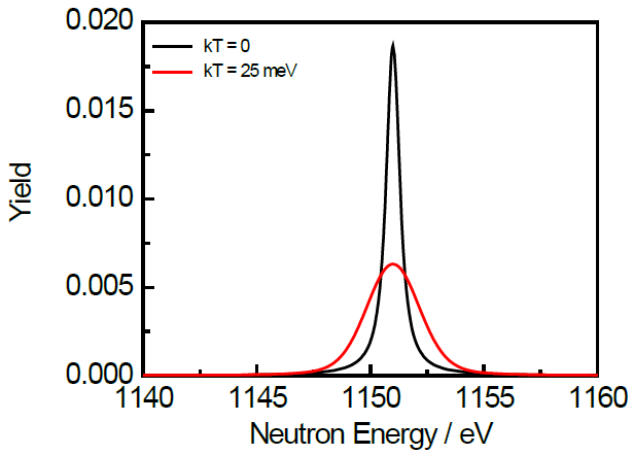

Fig. 1.9.: Doppler broadening for the ^{65}Fe resonance at 1.15 keV. In black is shown the theoretical shape of the resonance at a temperature of 0 K, while in red is shown the real shape at a temperature of 293.6 K (kT=25 meV)

In practical applications (e.g. reactor facilities) resonance cross sections are mostly needed in Doppler broadened form. It is sometimes claimed that for light nuclei Doppler broadening can be neglected. This, in first approximation, can be true for the broad s-wave levels but fails for the narrow p, d or even higher momentum wave levels.
The Free Gas formalism introduce a model to describe the change on the cross section and, in particular, on the width of the resonances. Other models have been conceived and found applications in many fields [27].

Consider a parallel beam of mono-energetic particles with laboratory velocity **v**, colliding with target nuclei whose velocities **u** are distributed in such a way that $p(\mathbf{u})d^3u$ is the fraction with velocities in a small three-dimensional region d^3u around **u** in velocity space. If ρ_1 and ρ_2 are the densities of beam and target particles, re-

spectively, the number of reactions occurring per unit time and unit volume is given by:

$$\rho_1\rho_2 \int p(\mathbf{u})|\mathbf{v}-\mathbf{u}|\sigma(|\mathbf{v}-\mathbf{u}|)du = \rho_1\rho_2 v\bar{\sigma}(v) \tag{1.27}$$

Where $|\sigma(|\mathbf{v}-\mathbf{u})|$ is the unbroadened cross section for a relative speed $|\mathbf{v}-\mathbf{u}|$ between the collision partners, and $\bar{\sigma}(v)$ the effective or Doppler-broadened cross section for incident particles with speed **v**. It can be noted that, from 1.27, a 1/v cross section is not affected by Doppler broadening.
Let now assume that the target nuclei have the same velocity distribution as the atoms of an ideal gas, following a Maxwell-Boltzmann distribution in the form:

$$p(\mathbf{u}) = \sqrt{\frac{1}{\pi^3}} e^{-\frac{u^2}{u_T^2}} \frac{d^3u}{u_t^3} \tag{1.28}$$

Integrating over all possible relative velocities **v**-**u** in polar coordinates and then changing the variable from the velocity to the energy one can be found that the Doppler broadening affect in a symmetric way the resonance shape (Gaussian broadening) and it is expressed by the formula:

$$\bar{\sigma}(E) = \frac{1}{\Delta\sqrt{\pi}} \int_0^{+\infty} \left[e^{-\left(\frac{E-\sqrt{EE'}}{\Delta/2}\right)^2} - e^{-\left(\frac{E+\sqrt{EE'}}{\Delta/2}\right)^2} \right] \sqrt{\frac{E'}{E}} \sigma(E')dE' \tag{1.29}$$

Where

$$\Delta = \sqrt{\frac{4EkT}{M/m}} \tag{1.30}$$

is called the Doppler width. For $E \gg \Delta$, which is usually satisfied above a few eV, one can simplify by retaining only the first two terms of the expansion $\sqrt{EE'} = E + (E'-E)/2 + ...$ in the exponent. Shifting the lower limit of the integral to $-\infty$ thanks to the symmetry of the integral the 1.29 becomes:

$$\sqrt{E}\bar{\sigma}(E) = \frac{1}{\Delta\sqrt{\pi}} \int_{-\infty}^{+\infty} e^{-\left(\frac{E'-E}{\Delta}\right)^2} \sqrt{E'}\sigma(E')dE' \tag{1.31}$$

which means Gaussian broadening of the reaction rate on the energy scale with a width Δ that depends by the temperature (eq. 1.30).

1.3.5 Westcott convention

Thermal neutron fluences are often quoted using the Westcott convention [8]. The use of such approach is due to the fact that the capture cross-section at a certain energy depends by the temperature during the experiment itself. The convention is to consider as reference value the room temperature energy equivalent, that means a value in energy of E_0=0.0253 eV (T_0=293.6 K).

As most of the experiment are carried in nuclear reactor facilities, the temperatures can be slightly different from the reference value T_0. Westcott [28] elaborated a method for converting the value of a cross section σ measured at a temperature T into the corespondent value of σ_0. The model he developed describes the neutron spectrum as a combination of a Maxwellian distribution for the neutron velocity characterized by a temperature T and a component of epithermal neutrons with an energy distribution proportional to $1/E$. For a nuclide whose neutron capture cross section does not follow the $1/v$ trend the cross section can be written:

$$\sigma = \sigma_0(g_w + rs) \tag{1.32}$$

Where g_w is the Westcott factor (see equation 1.34). r is the epithermal index and represents the fraction of the total neutron density in the epithermal energy range. s is a temperature-dependent quantity strictly related to the reduced resonance integral I':

$$s = \sqrt{\frac{4T}{\pi T_0}}\frac{I'}{\sigma^0} \tag{1.33}$$

If the epithermal component is negligible ($r = 0$) the g_w-factor is simply the ratio of the Maxwellian averaged cross-section σ_t to the reference value σ_0:

$$g_w = \frac{\sigma_t}{\sigma_0} = \frac{1}{v_0\sigma_0}\int \frac{4}{\sqrt{\pi}}\left(\frac{v}{v_t}\right)^3 \sigma(v)e^{(-v/v_t)^2}dv \tag{1.34}$$

It should be noted that the Westcott factor is dependent on the temperature T, since the value v_t is given by:

$$E_n = kT = \frac{1}{2}mv_T^2 \tag{1.35}$$

If $\sigma(v) \propto 1/v$ the cross section is equivalent to σ_0 and the g_w factor is equal to 1. Many nuclides present resonances in the absorption cross section at different energy values. For nuclides which have resonances near the thermal range the Westcott g_w-factor is different from unity. For example, ^{155}Gd has g=0.8390 [29], looking at the cross section, it reveals a resonance at 26.8 meV [26], exatcly in the thermal region. Regardless, most of nuclides have the first resonance quite far form the thermal domain and the g-factor is close to 1.

The Westcott convention is also used to calculate the fluence values. this provides a measure of the fluence with small uncertainties, therefore it is ideal for comparing thermal cross sections in activation measurements. The total Westcott fluence rate is defined as

$$\dot{\Phi}_W = n \cdot v_0 \tag{1.36}$$

where n is the total neutron density and v_0 is a velocity which by convention is equal to 2200 m/s, corresponding to the velocity at the peak of a Maxwellian thermal

fluence distribution for a moderator with T=293.6 K. It does not matter which is the actual moderator temperature or the actual shape of the spectrum. On the contrary, these are taken into account if the mean velocity of the neutron field $\overline{v}$ is known and the *true* total fluence rate is calculated by:

$$\dot{\Phi}_{true} = n \cdot \overline{v} \tag{1.37}$$

When activation foils are used for a fluence measurement, the quantity obtained from the activation rate is the neutron density n hitting the target. To translate this value into a *true* fluence rate, the shape of the spectrum should be known. Instead, the Westcott fluence rate is immediately evaluable.

Various different Westcott fluence rates can be defined. The total Westcott fluence rate $\dot{\Phi}_W = n \cdot v_0$, where n includes all the neutron density, the Maxwellian Westcott fluence rate, $\dot{\Phi}_{M,W} = n_M \cdot v_0$, where n_M is limited to the Maxwellian range and does not include the 1/E Westcott fluence rate, $\dot{\Phi}_{(1/E),W} = n_{(1/E)} \cdot v_0$, which concerns the neutron density in the 1/E distribution.

In this work, the NPL formalism is adopted as reported in Thomas and Kolkowski, [8], and the *sub-Cadmium* Westcott fluence rate is taken as reference. This quantity is defined as

$$\dot{\Phi}_{W,th} = n_{th} \cdot v_0 \tag{1.38}$$

where n_{th} is the neutron density measured with the cadmium exposition technique corresponding, in first approximation, to the density of neutrons below the Cd cut-off energy (0.5 eV).

Since v_0 is always lower than $\overline{v}$, the Westcott fluence rate is always an underestimation of the *true* fluence rate. Even for a perfect moderator, which would give a pure Maxwellian with of 293.6 K, the ratio $\overline{v}/v_0$ is equal to 1.128, while for non ideal moderators the ratio is higher.

1.4 Photo nuclear neutron reaction

Photodisintegration, alternatively known as phototransmutation or photonuclear reaction, denotes a nuclear phenomenon wherein an atomic nucleus absorbs a gamma ray of substantial energy, leading to its excitation, followed by a prompt decay through the emission of subatomic particles. This high-energy gamma ray impinging upon the nucleus effectively dislodges one or more neutrons, protons, or an alpha particle. These reactions are denoted as (γ, n), (γ, p), and (γ, α).
During this work the (γ, n) played an important role, since some neutron sources used for the measurements are based on this particular reaction. In this section a brief explanation on the physics of these reaction will be provided.

1.4.1 Giant Dipole Resonance (GDR)

The giant dipole resonance (GDR) absorption mechanism can be conceptualized as the electromagnetic wave, the photon, interacting with the dipole moment of the nucleus as a whole. This results in a collective excitation of the nucleus. It is the most likely process (that is, the process with largest cross section) by which photons interact with the nucleus. Peak cross sections of 6-10 mb can be seen for the light isotopes and 600-800 mb are not uncommon for the heavy elements. Thus, photonuclear collisions may account for a theoretical maximum of 5-6% of the photon collisions. Figure 1.10 shows as an example the photo-atomic ad photo-nuclear cross section in lead. According to Levinger and Bethe [30] the area under

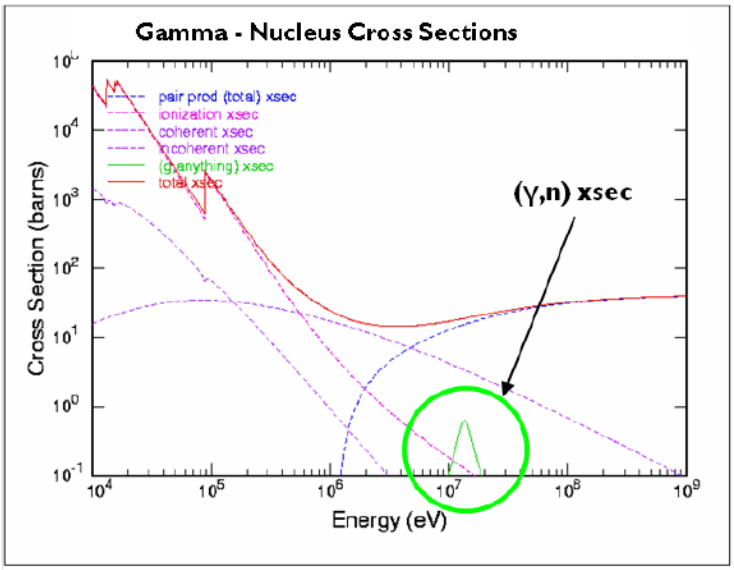

Fig. 1.10.: The logarithmic scale in the y-axes allows observing the contribution of the photonuclear reactions which is indicated with the green curve.

the resonance peak in the photon absorption cross section as a function of the photon energy E, is approximately given by the dipole sum-rule:

$$\int_0^{+\infty} \sigma(E)dE = \frac{\pi e^2 h}{2Mc}\frac{NZ}{A} = 0.06\frac{NZ}{A} \tag{1.39}$$

The large body of experimental photonuclear data showed that the Lorentz shape gives a reasonably good approximation to the GDR:

$$\sigma(E) = \frac{\sigma_G E^2 \Gamma_G^2}{(E^2 - E_G^2) + E^2\Gamma_G^2} \tag{1.40}$$

Where σ_G, Γ_G and E_G are respectively the peak cross section, full width at half maximum and peak position of the giant dipole resonance. Deformed nuclei are represented by two such Lorentzian shapes corresponding to oscillations along the major and minor axes.
An empiric formula for estimating the resonance energy in the case of heavy elements is:

$$E_G \simeq 80A^{\frac{1}{3}} \tag{1.41}$$

The GDR occurs with highest probability when the wavelength of the photon is comparable to the size of the nucleus. This typically occurs for photon energies in the range of 5-20 MeV leading to a resonance width of a few MeV. Outside of this resonance region, the cross section for a GDR reaction becomes negligible.

Axel [31] proposed the idea that the reaction mechanism responsible for generating the Giant Dipole Resonance (GDR) is also accountable for the (n,γ) process in proximity to the neutron separation energy. This proposal equates the gamma absorption cross section to the characteristics of the GDR. Utilizing the principle of detailed balance and calling the Brink [32] hypothesis, which suggests that each excited state includes a GDR with the same shape as the ground state but displaced, Axel derived a relation for the Giant Dipole Resonance width Γ_G.
A proof of this formula can be found in the experimental results on many different target nuclei [33].
In figure 1.11is shown the cross-section for photo-production of neutrons on various Isotopes of the Neodymium (Z=60) depending on the energy of the photon:

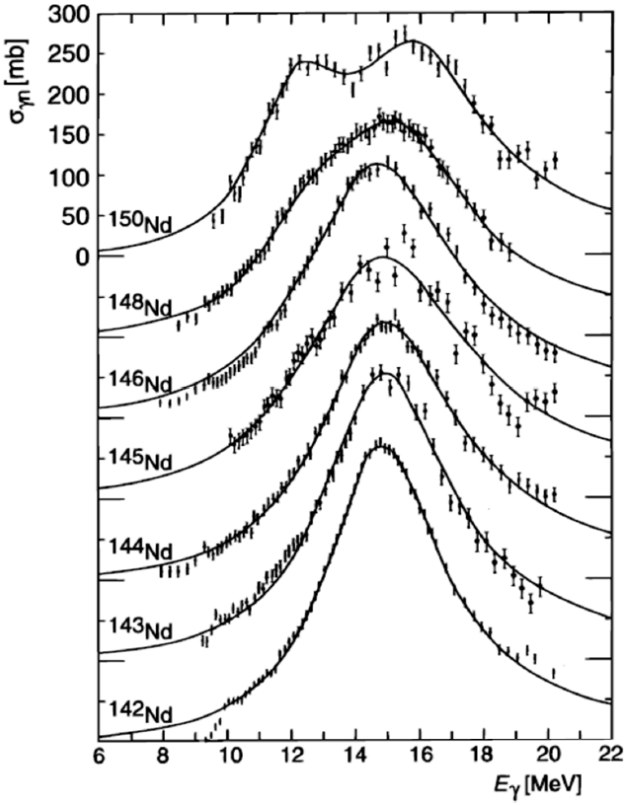

Fig. 1.11.: Giant Dipole Resonance cross section for Nd (Z=60). The mass number dependence on the cross section is clearly visible.

1.4.2 Fermi Liquid model

According to the Fermi Liquid Model (FLM)[166] for a nucleus which is characterized by strongly interacting particle, the damping width of the GDR is energy and temperature-dependent, and is given by:

$$\Gamma_G(E_\gamma, T) = \frac{\Gamma_G^0}{E_G^2}(E_\gamma^2 + 4\pi^2 T^2) \tag{1.42}$$

Where $\Gamma_G^0 = \Gamma_G$ for ($E_\gamma = E_g$,$T = 0$) is the damping width of the GDR at its peak energy, and T is the nuclear temperature of the final state. As can be seen in 1.42, the spreading width is composed of two components: one which is due to the decay of particle-hole states to more complicated configurations, the other is produced by thermal effects arising from the collisions of particles in the nuclear volume.
This model can be generalized to describe adequately the gamma-ray strength functions and width for both spherical and deformed nuclei. For deformed nuclei, the sum of two incoherent terms, with the appropriate Lorentzian GDR parameters, are required. A detailed discussion can be found in [26].

1.4.3 Quasi-Deuteron model

The quasi-deuteron (QD) absorption mechanism, described by Levinger in [34] and [35], can be conceptualized as the electromagnetic wave interacting with the dipole moment of a correlated neutron-proton pair. In this case, the neutron-proton pair can be thought as a QD having a dipole moment with which the photon can interact. This mechanism is not as intense as the GDR but it provides a significant background cross section for all incident photon energies above the relevant particle separation threshold. However it becomes the most relevant photoabsorption process in the energy region above the GDR peak, i.e. above 30 MeV [36].

1.4.4 Particle emission

Once the photon has been absorbed by the nucleus, one or more secondary particle emissions can occur. For the energy range under discussion (below 50 MeV) these reactions may produce a combination of gamma-rays, neutrons, protons, deuterons, tritons, helium-3 ions and alpha particles. The threshold for the production of a given secondary particle is governed by the separation energy of that particle, typically from few MeV to few tens of MeV as a maximum. It should be noticed that for heavy elements, neutrons are emitted preferentially since they are not subject to the high coulomb barrier. In light nuclides, on the other side, the barrier is lower and compensates for the difference in the separation energy for neutrons and protons. Light nuclei show indeed a neutron separation energy higher than proton due to the paucity of states available for the decay by neutron emission.
The (γ,n) reaction is not the only photoabsorption process giving the emission of a neutron in the final state. Other reactions, such as (γ,pn), (γ,αn), (γ,2n), (γ,p2n)..., contribute to the photoneutron production, and the cross section σ(γ,sn), which indicates the contribution of photonuclear processes to the photoabsorption cross section, can be written as:

$$\sigma(\gamma, sn) = \sigma(\gamma, n) + \sigma(\gamma, 2n) + \sigma(\gamma, pn) + ... \tag{1.43}$$

For heavy nuclei, the neutron producing cross section is a good approximation of the total gamma absorption cross section and, in the energy range where the GDR mechanism is dominant (below 35 MeV), the (γ,n) reaction makes usually the major contribution.
Table 1.2 shows the threshold energies for different photoneutron producing reactions in some light and some heavy elements as reported in the NCRP Report n°79 [37].
Most of these particles are emitted via pre-equilibrium and equilibrium mechanisms although it is possible, but rare, to have a direct emission.

Pre-equilibrium emission can be conceptualized as a particle within the nucleus that receives a large amount of energy from the absorption mechanism and escapes the binding force of the nucleus after at least one, but very few, interactions with other nuclei. This is in contrast to a direct emission where the emission particle escapes the nucleus without any interactions. Typically this occurs from QD absorption of the photon where the incident energy is initially split between the neutron-proton pair. Particles emitted by this process tend to be characterized by higher emission energies and forward-peaked angular distributions.
Equilibrium emission can be conceptualized as particle evaporation. This process typically occurs after the available energy has been distributed among the nucleons. In the classical sense, particles boil out of the nucleus as they penetrate the nuclear potential barrier. The barrier may contain contributions from coulomb potential (for charged particles) and effects of angular momentum conservation. Particles emitted by this process tend to be characterized by isotropic angular emission and evaporation energy spectra.
The maximum energy of the emitted neutron, E_n, corresponds to the photon energy, E_γ, minus the separation energy S_n and the centre of mass recoil energy Δ_R:

$$E_n = E_\gamma - S_n - \Delta_R \tag{1.44}$$

but since for all the emission reactions discussed above, the nucleus will most probably be left in an excited state, its excitation energy, $E_{x,A-1}$, must also be subtracted. When the level density of the appropriate states in the daughter nuclide is low, only a few state can participate in the decay process. The spectrum of photoneutrons then consists of only a few discrete lines whose energies in the centre of mass system are given by: $E_n = E_\gamma - S_n - \Delta_R - E_{x,A-1}$. When the density of states in the daughter nuclide is high, i.e. heavy nuclides, the discrete spectrum of decay neutrons becomes continuous. In this case the distribution of levels can be treated by statistical mechanics and different ways can be found in literature to parametrize the deriving neutron energy distribution ([38],[39]).
The excited daughter nucleus will subsequently relax to the ground state by the emission of one or more gamma-rays. The gamma-ray energies follow the well known patterns for relaxation. The only reactions that do not produce gamma-rays are direct reactions where the photon is absorbed and all the available energy is transferred to a single emission particle leaving the nucleus in the ground state.

Element	Photonuclear reaction	Threshold energy (MeV)
^{12}C	(γ, n_0)	18.7
	$(\gamma, n*)$	20.7
	(γ, np)	27.4
	$(\gamma, n\alpha)$	26.0
	$(\gamma, np\alpha)$	38.0
^{16}O	(γ, n_0)	15.7
	$(\gamma, 2n)$	15.7
	$(\gamma, n*)$	21.0
	(γ, np)	23.0
^{14}N	(γ, n_0)	10.5
	$(\gamma, np*)$	14.1
^{23}Na	(γ, n)	12.4
	(γ, np)	19.2
	$(\gamma, 2n)$	23.5
^{56}Fe	(γ, n)	11.2
	(γ, np)	20.4
	$(\gamma, 2n)$	20.5
^{63}Cu	(γ, n)	10.9
	(γ, np)	16.3
	$(\gamma, 2n)$	19.7
^{183}W	(γ, n)	6.2
	(γ, np)	13.8
	$(\gamma, 2n)$	14.3
^{208}Pb	(γ, n)	7.37
	(γ, np)	14.9
	$(\gamma, 2n)$	14.1

Tab. 1.2.: Separation energies for photonuclear reactions in isotopes of light and heavy nuclides. The symbol *, e.g. $(\gamma, n*)$, indicates the excited state of the nucleus after the neutron emission.

1.5 Neutron moderation

In general, when a neutron undergoes an elastic collision, it suffers a loss of energy, this loss can be calculated with the aid of simple mechanics.
The slowing down of neutrons in hydrogenous media is of particular importance. Let consider the general elastic collision between a neutron of mass 1 and a nucleus of mass A, assuming isotropic scattering in the centre of gravity system and supposing A to be initially at rest.

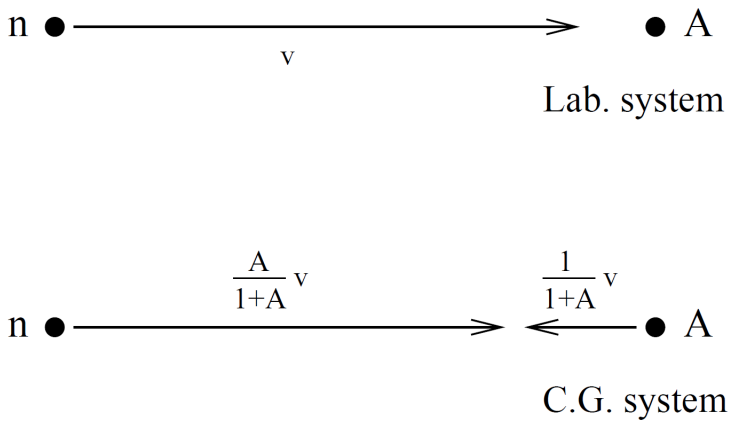

Fig. 1.12.: Elastic neutron-nucleon collision evaluated in laboratory system and in the centre of gravity system (C.G. system).

The initial neutron velocity is v. The first step is to analyze the process into the centre of gravity co-ordinate system (see Fig. 1.12) in which the velocity of the neutron is

$$v_n = \frac{A}{1+A}v \tag{1.45}$$

and the velocity of the nucleus is

$$v_A = \frac{1}{1+A}v \tag{1.46}$$

The effect of the elastic collision results in a change of the velocities directions, without affecting their magnitudes. This is shown in Fig. 1.13, where the neutron velocity makes an angle θ with the original direction.

In order to find the magnitude and direction of the neutron velocity as observed in the laboratory system after the collision, the velocity of the centre of gravity has to be added. The final velocity is v' and can be found that:

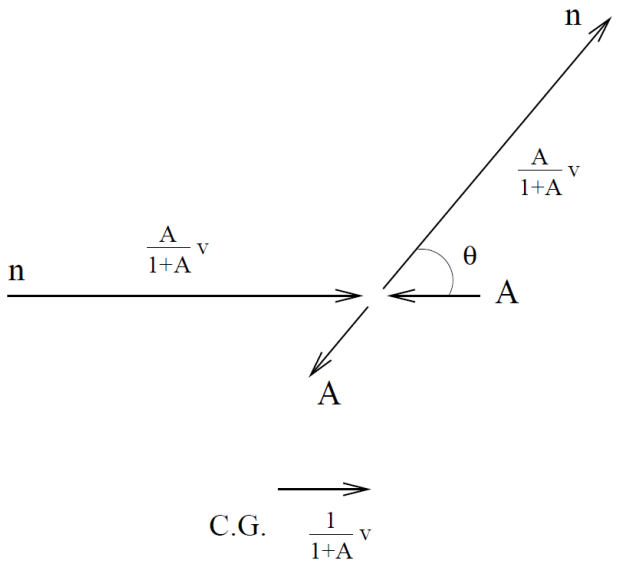

Fig. 1.13.: Kinematic after the interaction.

$$v' = \frac{v}{1+A} \cdot [1 + A^2 + 2A\cos\theta]^{\frac{1}{2}}$$

This result, in terms of kinetic energy can be written

$$E' = E \cdot \frac{1 + 2A\cos\theta + A^2}{(1+A)^2}$$

The maximum value is obtained when θ is equal to zero. The result does not depend by the mass number A:

$$E'_{max} = E \tag{1.47}$$

Th minimum value is obtained when θ is equal to π. The result depends by the mass number A:

$$E'_{min} = E \cdot \left(\frac{A-1}{A+1}\right)^2 \tag{1.48}$$

For a given A, the probability of a certain value of E' is uniform between minimum and maximum value, as long as all $\cos\theta$ are equally probable.

Now the true value for the average energy after a certain number of collisions can be derived. Is useful to introduce the lethargy (1.8):

$$u = \ln \frac{E}{E'}$$

Assuming isotropic scattering:

$$\xi = \int_{E'_{min}}^{E'_{max}} \ln \frac{E}{E'} \cdot dp(E') \tag{1.49}$$

whence

$$\xi = 1 - \frac{1}{2} A \left(1 - \frac{1}{A}\right)^2 \cdot \ln \left(\frac{A+1}{A-1}\right) \tag{1.50}$$

Inserting numerical values, one finds $\xi = 1$ for hydrogen (A = 1), and ξ= 0.158 for graphite (A = 12). Now the mean energy of neutron after n collision can be calculated as:

$$\overline{E'} = E e^{-\xi n} \tag{1.51}$$

For a certain material and a given ξ, is possible to extract the number of collisions needed to reach a wanted value of $\overline{E'}$.
For example, in the case of a neutron with E = 1 MeV that is moderated in hydrogen until an energy of $\overline{E'}$ = 1/40 eV, is found n = 17.5. The corresponding result for graphite is n = 110. For these reasons to moderate neutrons beams generally water or paraffin are used.

The previous calculation has assumed the nucleus from which neutrons scatter to be at rest. This is certainly a good approximation for MeV neutrons, but as thermal energies are approached, thermal motions of the atoms of the moderator begin comparable to the speeds of the neutrons. The scattering in this case is better analyzed using statistical mechanics.
Since thermal equilibrium with the moderator at temperature T is achieved, the neutrons are described by a Maxwellian speed distribution:

$$f(v)\,dv = 4\pi\rho\left(\frac{m}{2\pi kT}\right)^{\frac{3}{2}} v^2 e^{-\frac{mv^2}{2kT}}\,dv \tag{1.52}$$

where $f(v)\,dv$ gives the fraction of neutrons with speeds between v and $v+dv$, m is the neutron mass and ρ is the total number of neutrons per unit volume.
It should be noted that if kT=0.025 eV the most probable velocity v_0 is 2200 m/s.
Rewriting 1.52 in terms of energy gives:

$$f(E)\,dE = 2\pi\rho\,\frac{E^{\frac{1}{2}}}{(\pi kT)^{\frac{3}{2}}} e^{-\frac{E}{kT}}\,dE \tag{1.53}$$

For neutrons at thermal equilibrium in an ideal moderator, the energy spectrum approximates to a Maxwellian distribution. Equation 1.52 and 1.53 represent the spectrum in terms of neutron density (ρ) as a function of the the neutron velocity or the neutron energy. To translate these definitions in terms of fluence rate quantity the following relationship must be applied:

$$\dot{\Phi} = \int_0^\infty \dot{\Phi}(v)dv = \int_0^\infty n(v)\cdot v dv = n\cdot\overline{v} \tag{1.54}$$

where $n(v)$ is the velocity neutron distribution and $\overline{v}$ is the average velocity which is given by the usual formula:

$$\overline{v} = \frac{\int_0^\infty n(v)\cdot v dv}{\int_0^\infty n(v)dv} \tag{1.55}$$

Since the velocity distribution $n(v)$ can be derived by the 1.52, the value of $\overline{v}$ can be calculated by:

$$\overline{v} = \frac{4}{\sqrt{\pi}}\int_0^\infty e^{(-v/v_T)^2}(v/v_T)^3 dv = \frac{2}{\sqrt{\pi}}v_T \tag{1.56}$$

where v_T is the neutron velocity for energy kT, $v_T = \sqrt{\frac{2kT}{m_n}}$.

With these equations, the fluence rate distributions as a function of the velocity v, $\dot{\Phi}(v)$, and of the energy E, $\dot{\Phi}(E)$, can be written as:

$$\frac{\dot{\Phi}(v)dv}{\dot{\Phi}} = 2(v/v_T)^3 e^{(-v/v_T)^2} \frac{dv}{v_T} \tag{1.57}$$

and

$$\frac{\dot{\Phi}(E)dE}{\dot{\Phi}} = \frac{E}{kT} e^{(-E/kT)} \frac{dE}{kT} \tag{1.58}$$

The maximum of fluence rate is located at $E = kT$ and the mean energy for the fluence distribution is $E = 2kT$. The distribution is not symmetric when it is plotted in linear scale.

When a real moderator material is considered some complications must be taken into account:

- The slowing down neutrons will fill the region above the Maxwellian peak, producing a 1/E energy dependence int he epithremal region;
- the temperature parametrising the Maxwellian peak may not be that of the moderator material but it may be an effective temperature above the moderator temperature [8];
- the actual shape of the spectrum could be different from a perfect Maxwellian.

For these reasons, conventions are usually applied to deal with realistic thermal neutron fluences. In this work a formalism coherent with the Westcott convention, as indicated in [8], is adopted.
Cold or ultra-cold neutrons do not have a direct impact on the results of this work. Nevertheless, they are effective in disparate applications because their wavelength is of the order of the inter-atomic and inter-molecular distances. So as to obtain neutrons in this energy range the moderator is cooled or a small fraction of the thermal Maxwellian distribution is selected.

1.6 Neutron detection techniques

A complete description over all the neutron detection techniques is out of the scopes of this manuscript. Nevertheless, a generic overview over the most used conversion reactions and some application is provided. This should be useful for understanding the difficulties in the neutron detection field.

1.6.1 Thermal neutron detectors

A typical neutron detector is composed of a target material designed to convert the primary neutron radiation in secondary charged radiations coupled with a conventional charged particle detector. A nuclear reaction to detect thermal neutrons should have a very high cross section (for a high detector efficiency).
The target element should be enriched respect to natural isotopic abundance and the reaction should be suitable to discriminate gamma-rays (ubiquitous background radiation in neutron measurements). The higher is the Q-value, the greater is the energy transfer to byproducts and the easier is the γ discrimination.
Typical reactions used to convert thermal neutrons into directly detectable particles are:

- **^{10}B(n, α)^{7}Li reaction:**

$$^{10}B + n \rightarrow^{7} Li + \alpha$$

$$Q = 2.792\,\mathrm{MeV}\ (^{7}Li \text{ ground state, B.R. } = 6\%)$$

$$^{10}B + n \rightarrow^{7} Li^{*} + \alpha$$

$$Q = 2.310\,\mathrm{MeV}(^{7}Li \text{ excited state, B.R. } = 94\%)$$

This capture reaction has a very high cross section (σ=3837 b) if compared with other elements. Moreover, natural boron is composed by 19.8% of ^{10}B and this percentage can reach up to 95% in enriched materials. This isotope is normally included in the detectors in gaseous form (BF_3) or in solid compounds applied, for example, to the walls of an ionization chamber.
Since the neutron momentum is several orders of magnitude smaller than the momentum of the byproducts, it is possible to assume that they are directed

back-to-back. In the excited state the α and the ^{7}Li emerge from the nucleus with an energy of 1.47 MeV and 0.84 MeV, respectively.

- **^{6}Li(n, α)^{3}H reaction:**

$$^{6}Li + n \rightarrow ^{3}H + \alpha$$

$$Q = 4.78\,\mathrm{MeV}(^{3}H \text{ ground state, B.R.} \approx 100\%)$$

This process is similar to ^{10}B, but the capture cross section for this isotope is σ=b and, as a consequence, detector would be less efficient. However, the high Q-value of the reaction (Q=4.78 MeV) allows a good discrimination between the signals produced by photons and by neutrons. The efficiency of the detector can be enhanced by ^{6}Li enrichment (up to 90%). As for the ^{10}B, it is possible to create solid conversion substrate made of, for example, ^{6}LiF. Also in this case the reaction products are assumed to be emitted back to back and the energies of the tritium nucleus and of the α particle are 2.73 MeV and 2.05 MeV, respectively.

- **^{3}He(n, p)^{3}H reaction:**

$$^{3}He + n \rightarrow ^{3}H + p$$

$$Q = 0.764\mathrm{MeV}(\text{ground state, B.R.} \approx 100\%)$$

This reaction is the most advantageous in terms of cross section (σ=5400 b) in the thermal range, thus detectors utilizing this isotope usually are more efficient. In the epithermal range the cross section decreases as the neutron velocity increases $\sigma \propto$ 1/v up to energies of 200 keV and then is approximately constant in the interval [200 keV, 2 MeV]. Nonetheless, the cross section remains acceptably high and ^{3}He can be employed with epithermal and low energy fast neutrons too.
Also in this case the reaction products are assumed to be emitted back to back and the energies of the tritium nucleus and of the proton are 0.191 MeV and 0.573 MeV, respectively.

- **Fission reaction:**

  ^{235}U,^{239}Pu or other fissile elements can be used to convert neutrons into charged particle. In this case, the fission process produces heavy nuclear fragments along with numerous gamma rays that can be easily revealed.

- **Radiative Capture (n, γ):**

  Detectors based on radiative capture are used for thermal neutron and take advantage of the prompt photon emitted immediately after the neutron capture. Also Auger electron ejection is possible, instead of the gamma ray. This electron (or the β^- radiation due to the nucleus de-excitation) can be detected and information about the neutrons flux can be extrapolated from this measurement. Some typical elements that can be used for this application are ^{197}Au, ^{155}Gd ^{157}Gd, ^{113}Cd.

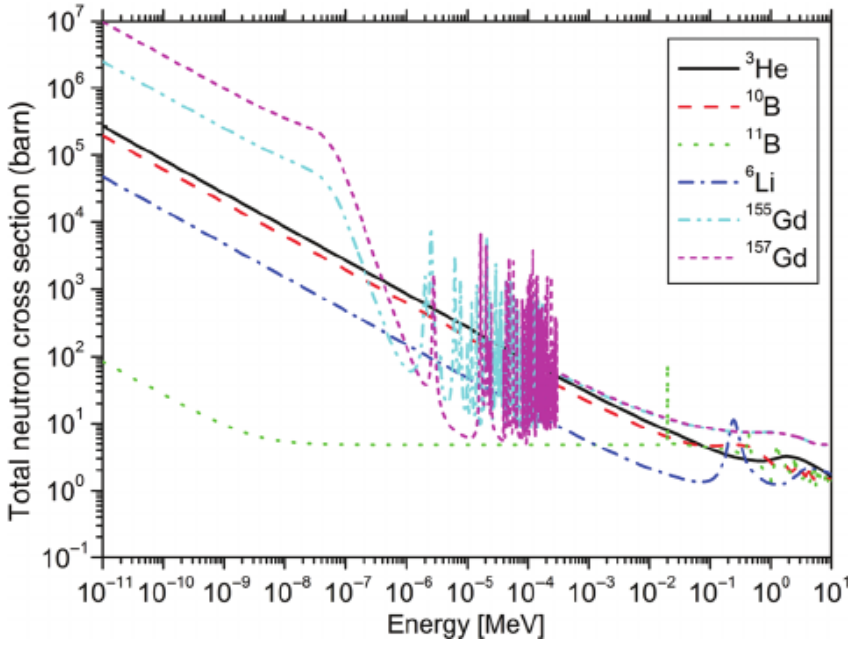

Fig. 1.14.: Cross section versus neutron energy for some reactions of interest in neutron detection [40].

Figure 1.14 shows the cross sections vs neutron energy for the discussed reactions.

In thermal neutron detectors the information on the neutron energy is completely lost in the conversion process of a neutron into charged particles, and so thermal neutron detector, without other devices, can not measure the energy of the neutrons, they only detect the neutron passage in the material.

1.6.2 Fast neutron detectors

Neutron interaction cross sections in the high energy range are much smaller than in the low energy range.
Therefore, fast neutrons are often detected after their moderation to thermal energies. However, during that process the information on the original energy of the neutron, its direction, and the time of emission are lost.

Typical fast neutron detectors are liquid scintillators, ^{4}He based noble gas detectors and plastic detectors. Fast neutron detectors show many differences in term to their capability of neutron/gamma discrimination and sensitivity.
The capability to distinguish between neutrons and gammas is excellent in ^{4}He detectors thanks to their low electron density and excellent pulse shape discrimination property.

Example of a directional fast-neutron detector is described in [41] where multiple proton recoils in separated planes of plastic scintillator material are used. The paths of the recoil nuclei created by neutron collision are recorded; determination of the energy and momentum of two recoil nuclei allow calculation of the direction and energy of the neutron that interacts via elastic scattering with them.

Finally, some fast neutrons detectors exploit the fission reaction on ^{235}U and ^{238}U. These have the advantage of being almost immune to the photonic background, but, in the ^{235}U case, the presence of background due to thermal neutrons may cause problems. As a result, detectors that employs this isotope can be used for fluence measurements in the energy range from 100 keV up to 200 MeV. In cases with relevant thermal neutrons presence the ^{238}U is a valid alternative.

1.6.3 Bonner sphere technique

To perform neutron spectrometry over a wide energy range (ten decades in energy) Bramblett and coworkers [42] proposed a method, today called **Bonner Spheres Spectrometer** (BSS). This is based on a set of high-density polyethylene (HDPE) spheres of different diameter with a thermal neutron detector in their centre. As shown in figure 1.15, a given moderator diameter preferably moderates neutrons in a well-specified energy interval. Thus, the response of given sphere peaks at an energy that is uniquely related to the sphere diameter ([43]). Whilst a 6cm diam. sphere peaks at about 3 eV, a 25 cm sphere peaks at about 6 MeV. With a set of spheres from 5cm (2") to about 30 cm (12") it is possible to cover all energy components form eV to 10 MeV.

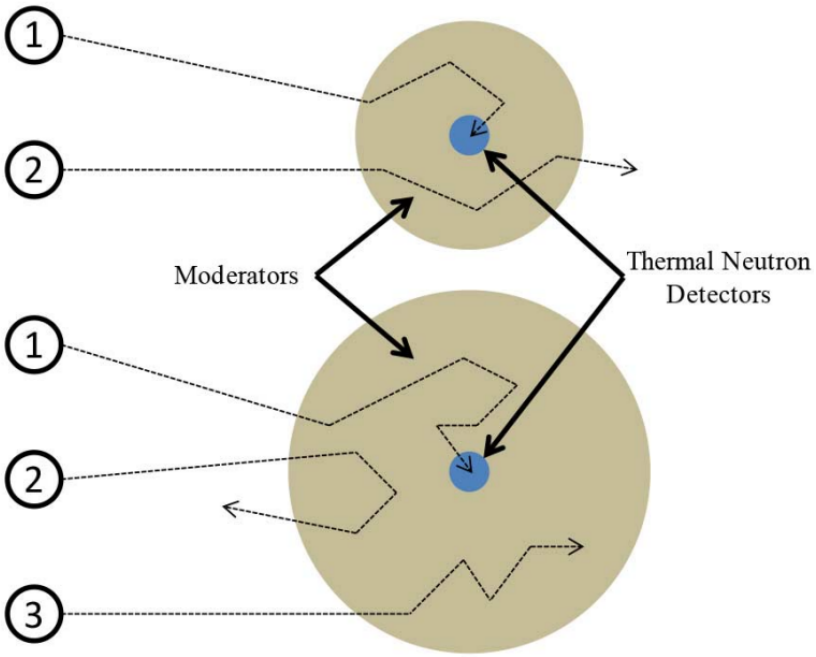

Fig. 1.15.: Sketch of the interactions of neutrons in the Bonner spheres spectrometer. The neutron 1 after some elastic scattering reaches the detector. The 2 neutrons escape the sphere after some interactions and 3 loses all its energy inside the sphere without reaching the detector.

Every sphere responds to all energies, but with a different weight. This concept is at the basis of the definition of the response matrix. The response matrix corresponds to a set of curves, called response f unctions, representing the counts obtained in each sphere, for unit neutron fluence, as a function of the energy. Those curves are evaluated with Monte Carlo codes like MCNP , PHYTS and FLUKA. The one used in this work is MCNP6.

An example of a response matrix is reported in fig. 1.16 obtained with a ^{6}LiI(Eu) as thermal neutron detector. Each curve in figure 1.16 correspond to a different sphere with the diameter reported in the label.

When a sphere is exposed to a neutron fluence $\Phi(E)$ the reading M_i is given by:

$$M_i = \int R_i(E)\Phi(E)dE \tag{1.59}$$

where $R_i(E)$ is the response function of the i-th sphere. The equation can be discretized as:

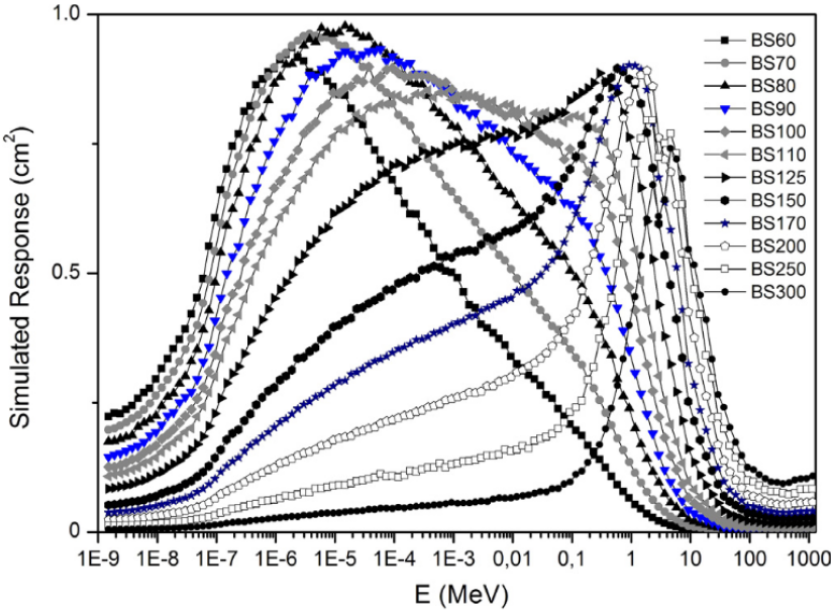

Fig. 1.16.: Example of a simulated response matrix obtained with a 9x3 mm2 ^{6}LiI(Eu) as thermal neutron detector [44]. Each curve correspond to a different sphere with the diameter reported in the label (BS60 = 60 mm diameter).

$$M_i = \sum_{j=0}^{n} R_{ij}\Phi_j \tag{1.60}$$

where R_{ij} is the average of the response function in the bin j and the element Φ_j is the fluence in the energy interval (E_j, E_{j+1}). The approximation becomes more precise as the number of groups, n, increases.
By subsequently exposing m spheres of different diameter a set of m equations like 1.60 is obtained and its solution provides values of Φ_j. However, since usually $m < n$, the system can be solved only either by a trial and error process or by *a-priori* information. This is done in the unfolding procedure [45].

The adequate number of spheres to be used in a measurement to obtain the optimal performance is the largest as possible, provided the shapes of the response functions differ sufficiently. As described by Thomas and Alevra in [46], a pragmatic way to understand how many spheres and which diameters are useful in measuring a neutron spectrum, consists in plotting the measured data as a function of the spheres diameter and interpolate the points with spline curves. The correct number of spheres is at least the one necessary to draw correctly the curve of reading against sphere diameter. All the spectrometric information is contained in these smooth curves. A larger number of spheres with more alike shapes of their response function would not bring any useful information for the unfolding.

2 The Boron Neutron Capture Therapy (BNCT)

The aim of this chapter is to explain the primary aspects of the Boron Neutron Capture Therapy (BNCT). Given its multidisciplinary nature, spanning biology, chemistry, pharmacology, and physics, providing a comprehensive overview within this limited context is challenging. Thus, this section has to be intended like a general overview of the BNCT. A deeper and more comprehensive investigation can be found in many publications and books (e.g. [47] [48] [49] [50] [51] [52])

2.1 Introduction to the BNCT

More in general, the Neutron Capture Therapy, (NCT) is an alternative form of radiotherapy based on neutrons with energy in the keV - tens of keV region (epithermal neutrons). The tumor cells are not directly killed by neutrons impinging the patient but through a "sensitizer" agent in the form of a drug with the following main characteristics:

- designed to reach only malignant cells;
- contains a high percentage of elements with high neutron interaction probability or, more precisely, high neutron capture cross section;
- this neutron absorbing material produces secondary ionizing radiations due to the neutron capture, capable of killing the surrounding malignant cells;
- the secondary particles are preferably charged particles with energy in the order of MeV and range in the order of a few to ten micrometres in tissue. This controlled effect confines the destructive impact to the targeted cells while minimizing harm to surrounding healthy tissue.

Among the elements with highest neutron capture cross section, like ^{3}He,^{157}Gd, ^{10}B, ^{6}Li or ^{235}U, only Gd and B have been evaluated for use in NCT with some results. ^{157}Gd has the highest cross section ($\sigma = 255$ kb), but the secondary particles, electrons and gammas, are weakly ionising if compared to the charged particles

produced by neutron capture in ^{10}B: ^{10}B(n,α)^{7}Li. The ^{10}B cross section is also high and amounts to $\sigma = 3837$ b [26]. Being ^{10}B the best candidate for NCT, this type of therapy is also called BNCT, Boron Neutron Capture Therapy. The characteristics of the ^{10}B(n,α)^{7}Li interaction have been reported in section 1.6.1.

The ^{10}B neutron capture cross section in the slow neutron domain varies with the inverse velocity of the neutron. Thus it is desirable to minimise the neutron energy at the tumor site. Ideally, the neutrons produced by the source should be thermalized within the tumor site. Comparatively, BNCT diverges from radiotherapy involving electrons/gammas and hadrons. BNCT, like hadrontherapy, is generally adequate for tumors that are resistant to electrons and gammas. However, whilst hadron therapy is suited for tumors well defined in space, BNCT operates a cell-by-cell selection as shown in figure 2.1. So it is suitable also for infiltrated tumors.

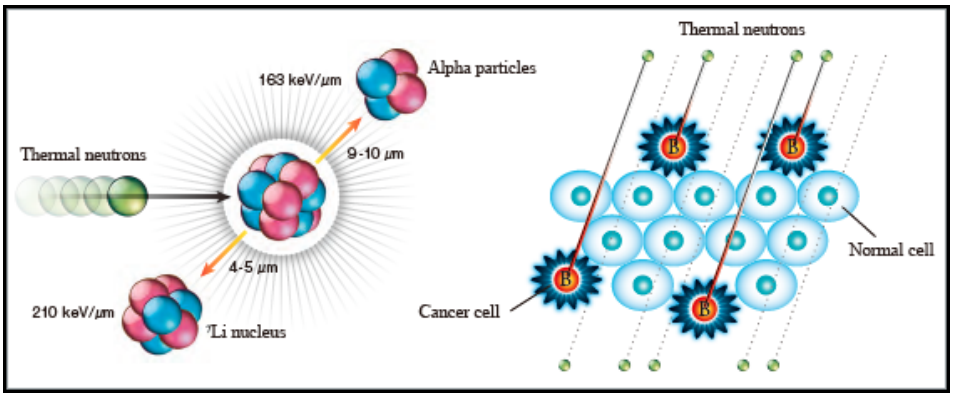

Fig. 2.1.: Sketch of the nuclear and biological process at the basis of the BNCT technique

The first idea of BNCT dates back to 1936 [53], but it became practicable only in the last 30 years. There are two primary scientific challenges currently facing BNCT:

1. the pharmaceutical challenge is designing a drug that maximizes the ratio between the Boron concentration in the tumor and that in the surrounding normal tissues (Boron uptake). Modern drugs achieve a typical uptake of borated drug in the tumor site ranging between 80-90 ppm. The amount deposited in healthy tissue is about 30% of that in the tumor, [54];

2. the challenge for neutron physics is maximizing the thermal neutron fluence rate in the tumor location.

In particular, focusing on the last challenge, the modern techniques to verify the neutron spectrum are still quite limited. These techniques solely measure integrated quantities associated with the energy distribution. New and performing spectrometric techniques would be very desirable. While the BSS technique (sec. 1.6.3) can be used, limitations persist due to the large space required for the measurement.

Therefore, quite often is extremely difficult (or even impossible) to use these spectrometers. The work of this thesis could be a solution for these problems, trying to develop a feasible spectrometric technique for BNCT.

2.2 History of BNCT

After the discovery of neutrons by Sir James Chadwick in 1932 [55] and the examination of the conversion reaction ^{10}B(n,α)^{7}Li by Taylor and Goldhaber in 1935 [56], the fundamental principles of BNCT were theoretically established. In 1936, Locher proposed to introduce small quantities of a strong absorber into the regions where it is desired to release ionization energy.
Subsequently, numerous research groups around the world initiated investigations into the potential use of neutrons for tumor treatment. Following initial explorations, it became evident that the most promising isotope for this purpose was ^{10}B. Other isotopes were also examined but yielded less encouraging results.

The initial experiments, conducted by Kruger in 1940 [57], involved the treatment of in vitro tumor fragments with boric acid, followed by neutron exposure. In the same year, Zahl et al. [58] replicated the experiment in vivo using mice, and both experiments yielded successful outcomes. A decade later, the first clinical applications of BNCT were conducted. As documented in [59], the history of clinical BNCT applications can be divided into four distinct periods, and the most significant literature from those years is compiled in [60]:

1. During the period of early clinical applications in the USA spanning from 1951 to 1961, initial experiments were conducted at the Brookhaven Graphite Research Reactor. Regrettably, these early trials did not yield successful results, since:

    - the available borated compounds did not accumulate selectively in tumors;

    - only thermal neutrons were available, thus producing some effect only in superficial lesions;

    - The adverse impact of residual fast neutrons and photons on healthy tissues resulted in an underestimation of the therapeutic efficacy. This dissatisfaction within the medical community led to the discontinuation of the BNCT program in the USA in 1961. This situation persisted until the 1990s.

2. Pioneering efforts in Japan, led by Hatanaka and his colleagues, from 1968 to the late 1980s marked a significant turning point. In 1968, Hiroshi Hatanaka and his team introduced a groundbreaking boron compound, BSH ($Na_2B_{12}H_{11}SH$), which delivered immediate and exceptional outcomes, rekindling interest in

BNCT. Another boron compound, known as BPA (boronophenylalanine), was introduced in Japan in 1987 and remains in use up to this day.

3. the period of prospective early clinical trials starting mid of the 1990s and still ongoing;

4. The utilization of accelerator-based epithermal neutron facilities is a contemporary development. Presently, there is a growing interest in the concept of generating therapeutic neutrons via an accelerator-based BNCT (AB-BNCT) facility. This design can be feasibly integrated into a hospital setting. Worldwide, numerous projects are currently underway, with the shared objective of advancing accelerator-based BNCT facilities.

Among the numerous global projects dedicated to the implementation of AB-BNCT, this thesis work is conducted within the framework of the ENTER-BNCT project initiated by INFN and completed at the end of 2022.

2.3 Physical hints for BNCT

As already mentioned, BNCT is based on the nuclear capture reaction on ^{10}B, having a massive cross section of $\sigma = 3837$ b.

The product of the reaction are two high Liner Energy Transfer (or LET) fragments: an ^{4}He and a ^{7}Li nucleus (for more details see section 2.3.1). The deposited energy in a generic tissues is in the order of around 160 keV/μm for the former and around 210 keV/μm for the latter. Since the energy of the two fragments is in the order of 1-2 MeV the path lengths in the tissue range from 5 to 9 μm. The normal size of a cell is around 15 μm in diameter, this means that the released fragments can induced lethal damages in the selective area where boron is localized. The minimum concentration required to be successful is about $10^9 - 10^{10}$ boron atoms per cell, corresponding on $\sim$20 μg/g of tissue [61].

The boron reaction entails the interaction with thermal neutrons. Given that the human body primarily consists of water, it effectively moderates neutron velocities and facilitates their capture at thermal energies. Consequently, the utilization of a thermal neutron beam proves advantageous for the treatment of superficial tumors. In contrast, the management of deeper-seated tumors, approximately within the 6-8 cm range, necessitates the use of epithermal neutrons. These neutrons undergo moderation by the surrounding tissues and water, subsequently reaching the tumor site with thermal energy, aligning with therapeutic requirements.
Clinical interest in BNCT primarily centers on the treatment of challenging tumors, notably those situated within the brain, such as high-grade gliomas and cerebral metastases. More recently, BNCT has garnered attention for addressing head, neck, and liver cancers, where conventional treatments, including surgery, chemotherapy, and radiotherapy, have proven ineffective. The effectiveness of BNCT-induced cell death hinges on the radiobiological properties of the radiation employed.

2.3.1 Radio-biological aspects

Radio-biology constitutes a scientific discipline dedicated to the examination of the biological consequences arising from ionizing radiation exposure. These biological repercussions represent the concluding stage within a succession of intricate processes unfolding within the biological material. It is important to acknowledge that all forms of ionizing radiation exert a discernible influence on biological systems. During the conversion of ionizing radiation into chemical energy within the human body, specific sites conducive to radiation-chemical reactions become active. In this context, ionization and excitation events involving atoms and molecules take place

[62].
When an ionizing radiation penetrates a medium, it releases energy in accordance with the Bethe-Block equation. In the context of the ionization process, a parameter, known as Linear Energy Transfer (LET), can be introduced. LET quantifies the energy deposited per unit path length. The International Commission on Radiation Units and Measurements (ICRU) provides the following definition for LET:

$$LET = \frac{dE}{dx} \qquad \left[\frac{\text{keV}}{\mu\text{m}}\right] \tag{2.1}$$

Where dE is the average energy locally transferred to the medium by a charged particle of specific energy while traversing a distance dx.
Ionizing radiation can be categorized into two distinct groups: low-LET (LET $<$ 2), which encompasses X-rays and gamma rays, and high-energy electrons, as well as high-LET (LET $>$ 2), which encompasses alpha particles, protons, neutrons, and ions. Typical values for the most common ionization radiation are given in figure 2.2:

Type of radiation	LET (keV/μm)
cobalt-60 gamma-radiation	0.3
250 kVp X-radiation	2.
10 MeV protons	4.7
150 MeV protons	0.5
recoil protons from fission neutrons	45.
14 MeV neutrons	12.
2.5 MeV alpha particles	166.
2 GeV Fe nuclei	1000.

Fig. 2.2.: LET values for the most used radiation. The values are obtained using track or energy average method. [63]

To ascertain the biological effects induced by radiation, a crucial parameter is the absorbed dose, defined as follows:

$$D = \frac{dE}{dm} \qquad [\text{Gy}] \tag{2.2}$$

Being dE the expected value of the released energy in the units of mass dm. The unity of measurement is defined in 2.2, 1 Gy correspond to an energy deposited of 1 J in 1 kg of mass.
The heightened concentration of ionizations along the trajectories of high-LET particles leads to an enhanced biological effect in comparison to an equivalent

physical dose of low-LET radiation. Introducing a novel parameter known as Relative Biological Effectiveness (RBE) proves valuable:

$$RBE = \frac{D_x}{D_{ref}} \tag{2.3}$$

Being D_x the absorbed dose for the radiation used and D_{ref} is the absorbed dose of a a reference X-rays source, producing the same biological effect. The values of RBE for the most commonly used radiations are shown in figure 2.3:

Radiation	Relative biological efficiency
γ rays from radium x rays of energy 0.1–3 MeV β rays	1
Protons	10
Fast neutrons <20 MeV	10
α rays	20

Fig. 2.3.: RBE of some given radiation defined by comparison with the γ radiation from Ra [64].

The definition of RBE is critically contingent upon a multitude of factors, including the biological state of the irradiated tissue, the specific type of cells involved, and their cell cycle phase. The behavior of RBE in relation to radiation LET is illustrated in figure 2.4:

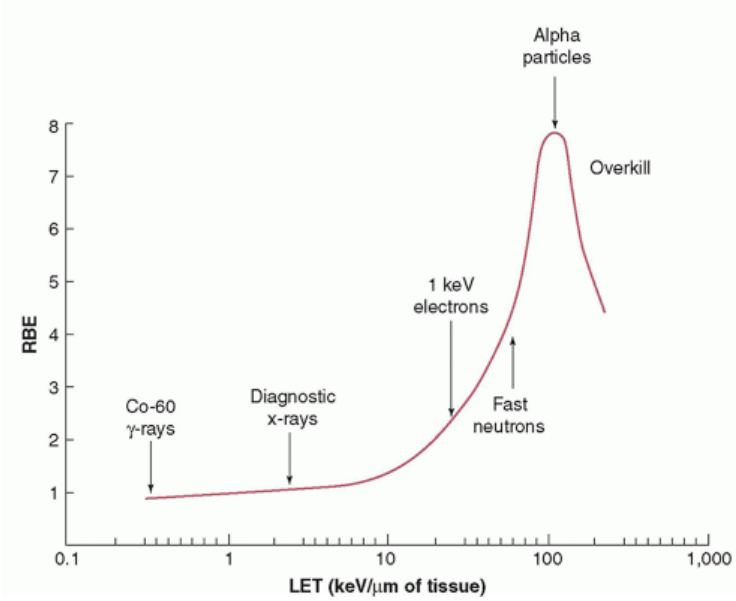

Fig. 2.4.: The RBE of a specific radiation type is a value empirically determined and, generally, under constant conditions, it exhibits an increase with the radiation's Linear Energy Transfer (LET). Nevertheless, once the LET surpasses approximately 100 keV/μm, the radiation becomes less effective due to the concept of overkill, where the maximal potential damage has already been achieved. Any increase in LET beyond this point results in an unnecessary dose.

In the context of a radiation therapy, both the tumor and the surrounding normal tissue coexist, resulting in an inevitable background dose comprising high- and low-LET radiation. Nevertheless, a higher concentration of ^{10}B within the tumor amplifies the total dose delivered to the tumor compared to the surrounding tissues. Considering the reliance of biological effects on the micro-distribution of the isotope, it becomes necessary to employ a more suitable term than RBE, known as the Compound Biological Effectiveness (CBE). CBE encapsulates the biological effectiveness factors assessed for the constituents of the dose emanating from the ^{10}B(n,α)^{7}Li reaction.
The introduction of the Compound Biological Effectiveness (CBE) concept is imperative to elucidate the composite impacts of α-particles and ^{7}Li ions. However, it is essential to recognize that the experimental determination of CBE factors can be significantly influenced by a multitude of variables, encompassing the specific boron delivery agent employed, the distribution of boron within the tumor and normal tissues, the cell type and population under consideration, and even the size of the cellular nucleus.

Notably, the CBE factors exhibit specificity with respect to both the ^{10}B delivery agent utilized and the tissue involved. In clinical trials of Boronophenylalanine (BPA)-based BNCT, various assumptions are employed for the calculation of the reaction component dose in different tissue types, as illustrated in figure 2.5 [65]:

Tissue	Boron concentration	CBE factor
Blood	Measured directly	
Brain	1.0 times blood	1.3
Scalp/skin	1.5 times blood	2.5
Tumor	3.5 times blood	3.8

Fig. 2.5.: CBE factors for a series of tissue and known boron concentration based on current available human and experimental data [66],[67],[68].

2.3.2 Dose in BNCT

The goal of any radiation therapy is to eliminate tumor cells by delivering an amount of energy that can cause lethal damage through multiple pathways.
The doses administered to both the tumor and normal tissues in the context of BNCT result from the energy deposition of three distinct categories of directly ionizing radiation, each characterized by differing Linear Energy Transfer (LET) values:

1. **Low-LET γ-rays**: they are generated predominantly through the boron reaction channel, accounting for 93% of cases. Additionally, gamma rays result from the

thermal neutron capture by hydrogen atoms within normal tissues ^{1}H(n,γ)^{2}H. The absorbed dose from these gamma rays is commonly denoted as D_γ.

2. **High-LET protons**: they originate from the scattering of fast neutrons and from the thermal neutron capture by nitrogen atoms ^{14}N(n,p)^{14}C. The respective absorbed doses are denoted as D_p and D_N.

3. **High-LET α particles and ^{7}Li ions**: they are generated as a result of the fundamental reaction involving ^{10}B, which forms the basis of BNCT. Their role in contributing to the absorbed dose is denoted as D_B

All the absorbed dose contribute to constitute the total photon-equivalent dose D_{eq} [69]:

$$D_{eq} = (D_\gamma \cdot DRF_\gamma) + (D_p \cdot RBE_p) + (D_N \cdot RBE_N) + (D_B \cdot CBE_B) \qquad (2.4)$$

Where D_i represents the different radiation contributions before introduced and they are weighted using a specific radio-biological factor. The Dose Reduction Factor (DRF_γ) is a measure of the radio-biological effectiveness of photons, and its value is contingent upon the dose rate. Conventionally, it is set to 1 for a dose rate of 1 Gy/min. RBE_p represents the radio-biological effectiveness of recoil protons, with values ranging from 2 to 7, dependent on proton energies [70]. RBE_N denotes the radio-biological effectiveness of protons generated through neutrons interaction with nitrogen, and its value spans from 1 to 8 [71]. CBE_B serves as a weighting factor for alpha particles and ^{7}Li ions when combined with ^{10}B, and its magnitude fluctuates between 1 and 4, contingent upon the tissue and distribution, as discussed before.

Ionizing radiation induces distinct types of lesions through two mechanisms, as shown in figure 2.6.

- *Direct Effects* pertain to the excitation of atoms and molecules, along with the disruption of their chemical bonds.

- *Indirect Effects*, conversely, includes the generation of free radicals and ionic fragments via the radiolysis of water. These byproducts can be harmful to the human body, causing damage to essential macromolecules, including nucleic acids, proteins, lipids, and polysaccharides.

In the case of high Linear Energy Transfer (LET) radiation, such as that employed in BNCT, the most significant damages primarily result from direct effects on DNA.

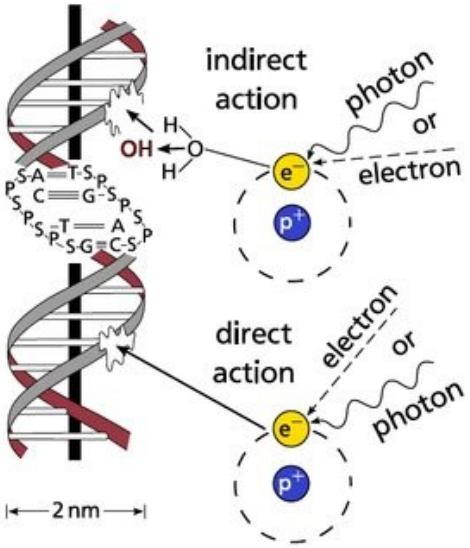

Fig. 2.6.: Direct and indirect radiation damage to the DNA.[72].

These direct effects can give rise to a variety of structural DNA lesions, the incidence of which correlates with the absorbed dose. The principal types of these lesions are explained below and visualized in figure 2.7:

- Single-strand breaks (SSB) refer to the rupture of one strand within the DNA molecule. This type of lesion is readily reparable, owing to the presence of the complementary filament, which serves as a template for repair.

- Double-strand breaks (DSB) involve the rupture of both filaments of the DNA molecule, constituting the most severe form of damage. These lesions include both simple and complex types, with the latter referred to as "clustered DNA damage." Unrepaired DSBs are the primary catalyst for cell death.

- Base damage refers to chemical alterations resulting from the disruption of hydrogen bonds between complementary bases, interruptions in the sugar-phosphate backbone, or disruptions in DNA cross-links.

When DNA damage can be fully and accurately repaired, the cell will proceed with its normal life cycle. However, failure to repair such damage can trigger cell cycle arrest through various mechanisms, including arrest in the G2/M phase, cell death via apoptosis, mitotic catastrophe, or cellular senescence. More details on cellular duplication and death processes can be found on many biology books (e.g. [73],[74],[75],[76]).

In the context of BNCT, in vitro experiments have demonstrated that tumor cells are

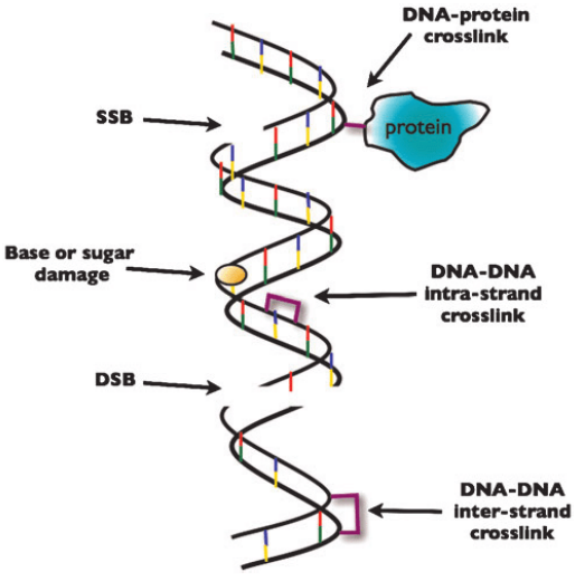

Fig. 2.7.: The primary DNA lesions are as follows, starting from the top: a) Single-strand breaks (SSB), b) Double-strand breaks (DSB), and c) Base damage.

eliminated through cell cycle arrest and apoptosis. Further advancements in BNCT necessitate the establishment of markers for monitoring the induced DNA damage.

2.4 Boron carriers in BNCT

One of the primary goals in BNCT is the development of effective boron carrier agents for successful clinical application. A successful carrier should meet at least the following criteria:

1. Minimal toxicity

2. High tumor concentrations of at least 20 μ g of ^{10}B per gram and minimal uptake in normal tissues, with a high tumor-to-brain (T/Br) or tumor-to-blood (T/B) concentration ratio exceeding 3-4:1.

3. Persistent presence of 10B in the tumor during BNCT, coupled with rapid clearance from blood and healthy tissues.

Actually, the available boron compounds do not simultaneously meet all these criteria, but ongoing efforts are focused on developing new carriers. Several promising carriers have surfaced thanks to advancements in chemical synthesis and a deeper understanding of the biological and biochemical aspects of delivery, as well as the requirements for an effective agent. The most challenging aspect is achieving selective tumor targeting to obtain sufficient boron concentrations for delivering the therapeutic dose while sparing normal tissues. Actually, three distinct groups of boron delivery agents are recognized, each with unique characteristics [77]. The following sections will give some characteristics on these different carriers generations.

2.4.1 First and second generation carrier

The **first generation** of boron carrier consisted of boric acid and some basic derivatives, which were employed as carriers in the initial clinical trials during the 1950s and 1960s. These carriers, while chemically straightforward, lacked in selectivity and exhibited low tumor-to-brain ratios, rendering them unsuitable for therapeutic purposes.

The **second generation** of boron delivery agents emerged in the 1960s and included two low molecular weight boron-containing chemicals. One, known as (L)-4-dihydroxy-borylphenylalanine or BPA, is based on arylboronic acids [78], while the other is sodium mercaptoundecahydro-closo-dodecaborate, often referred to as BSH, based on a recently discovered polyhedral borane anion [79]. In figure 2.8 their chemical structures are shown.

These second-generation compounds exhibited low toxicity, had longer persistence in animal tumors compared to related molecules, and featured T/Br and T/B boron ratios exceeding 1. However, they are not free from limitations. In particular, BSH displayed a high tumor-to-normal (T/N) ratio but had weak accumulation in tumor cells, while BPA accumulated well in tumor cells but had a low T/N ratio [80].

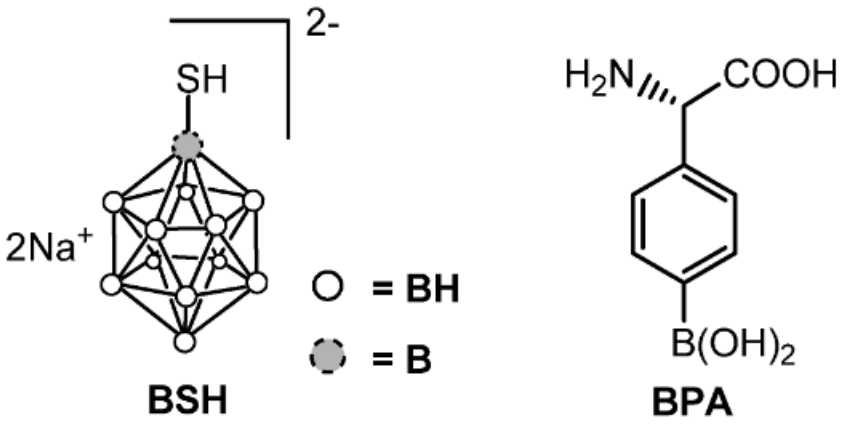

Fig. 2.8.: Structure of the second generation boron carrier [81].

2.4.2 Third generation carrier

Recognizing the limitations of BPA and BSH as boron carriers, extensive efforts have been focused into the development and synthesis of third-generation compounds. These compounds primarily comprise a stable boron group or cluster, connected via a hydrolytically stable linkage to a tumor-targeting component. This targeting part often involves low molecular weight biomolecules or low molecular weight monoclonal antibodies. This third generation includes various derivatives of BPA and other boron-containing amino-acids, including glycine, alanine, aspartic acid, tyrosine, cysteine, and methionine, as well as non-natural amino-acids. These compounds offer the potential to deliver higher concentrations of boron to tumors without an accompanying increase in toxicity. Generally, they exhibit enhanced specificity for tumor cells, the nuclei of tumor cells, and the DNA within tumor cells, potentially reducing the required concentration of boron compounds for effective BNCT. Compounds like GB-10 or N5-2OH have demonstrated low toxicity and are considered promising candidates for clinical evaluation, as shown in figure 2.9
Currently, only BPA and BSH are employed in clinical applications. Consequently, in addition to the quest for new boron carriers, there's a parallel need to enhance the dosing and delivery of BPA and BSH [65].

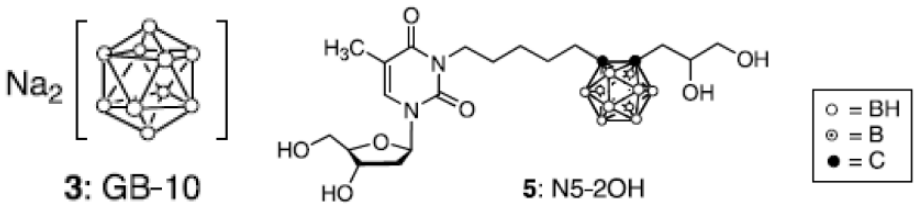

Fig. 2.9.: Third generation boron carriers structure [82].

2.5 Neutron sources for BNCT

The purpose of this section is to provide further details on the type of neutron sources used for BNCT applications. There is a significant effort within the scientific community to expand the range of usable source types while concurrently developing facilities that are more readily accessible and adaptable to clinical requirements.
A general discussion on neutron sources has been provided in the dedicated section 1.1.1.

There are two main manners to generate neutrons for BNCT. Initially, nuclear reactors were used. Thanks to efforts from researchers worldwide, significant progress has been made in developing, making, and testing new low-energy light ion accelerator-based neutron sources (ABNSs).
They come with several benefits when compared to reactor facilities. First, the accelerator can be easily switched off when neutron production is not required. Plus, they don't rely on critical reactions with fissile materials, making licensing and regulation simpler. ABNSs are versatile because they can use various reactions to produce different types of neutrons. A single accelerator can create different types of neutron fields, which can be customized for a patient's tumor. Moreover, building these facilities costs less than establishing a reactor system, and they can be set up in a hospital, often as an addition to an existing radiotherapy room.

2.5.1 Fission reactors

Clinical use of BNCT initially relied on facilities based on fission reactors. Several reactors known for their high-quality neutron beams have been developed and are currently in operation.
The fundamental characteristics of these reactor-based sources have been previously discussed in section 1.1.1. There are two distinct approaches for the conversion of reactors into BNCT facilities. The first approach, commonly referred to as the direct method, involves moderating neutrons to obtain thermal energies within the reactor's cooling medium, typically water and consequently extracting the beam in the thermal column.
Many reactors use this type of approach as the one in Finland called FiR1. A scheme of the clinical application of the Finnish facility is given in figure 2.10 [83].

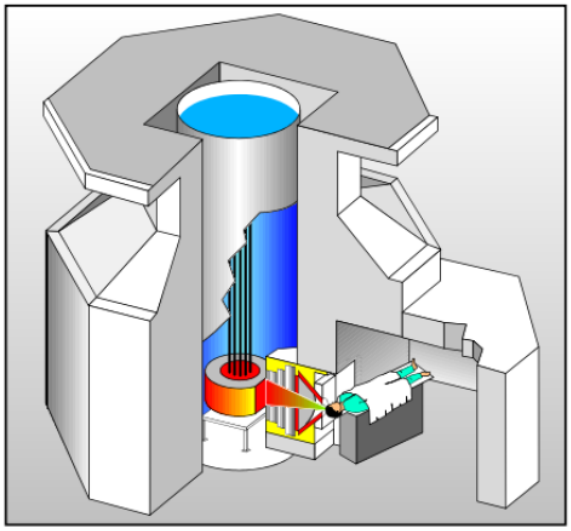

Fig. 2.10.: The BNCT facility at FiR 1 nuclear research reactor. The epithermal (0.5 eV - 10 keV) neutron fluence rate is $1.1{\cdot}10^{9}$ $cm^{-2}s^{-1}$ at the exit plane using a 14 cm diameter collimator at 250 kW power. It started operation in 1962, and it was permanently shut down in 2015.

The second, or indirect, approach involves the utilization of a fission converter plate positioned adjacent to the moderator assembly. In this method, neutrons coming from the reactor core induce fission reactions, thereby generating a neutron beam. The MITR reactor is an exemplar of this approach. Operating at 5 MW, it possesses a higher power output compared to other reactors. Nevertheless, treatment times are relatively brief due to the utilization of the converter. A schematic representation of this system can be found in 2.11 [84].

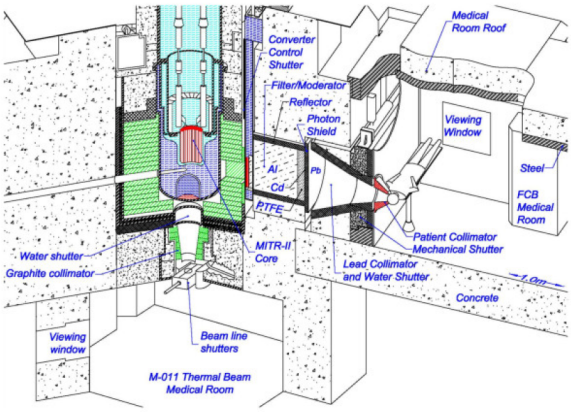

Fig. 2.11.: The schematic diagram of the Massachusetts Institute of Technology Reactor (MITR) displays the fission converter-based epithermal neutron irradiation (FCB) facility, situated within the MITR's experimental hall, and functioning concurrently with other user applications. The in-air epithermal neutron fluence rate registered was $6.2{\cdot}10^{9}$ $cm^{-2}s^{-1}$ at the patient position when employing a 12 cm collimator.

Since the high maintenace costs and the radio-protection rules, most BNCT reactor in the worldwide are being shutting down and more efforts are focused on the development of accelerator-based neutron sources.

2.5.2 Accelerator-based facilities

In recent years, accelerators facilities have been also used to generate neutrons, and a range of Accelerator-Based Neutron Sources (ABNS) is presently under development in various countries. These ABNS systems differ in terms of the accelerator type selected and the target and reaction mechanisms employed for neutron production. A concise overview of the present status of the diverse accelerators designated for Accelerator-Based BNCT (AB-BNCT) facilities worldwide is presented in figure 2.12:

Institute–location	Machine (status)	Target and reaction	Beam energy neutron energy (MeV)	Beam current (mA)
Budker Institute Russia	Vacuum insulated Tandem (ready)	Solid ^{7}Li(p,n)	2.0 <1	2
IPPE-Obninsk Russia	Cascade generator KG-2.5 (ready)	Solid ^{7}Li(p,n)	2.3 <1	3
Birmingham Univ. UK	Dynamitron (ready)	Solid ^{7}Li(p,n)	2.8 <1.1	1
KURRI Japan	Cyclotron (clinical trials started)	^{9}Be(p,n)	30 <28	1
Soreq Israel	RFQ-DTL[a] (ready)	Liquid ^{7}Li(p,n)	4 <2.3	2
INFN Legnaro Italy	RFQ (under construction)	^{9}Be(p,n)	4–5 <2–3	30
Tsukuba Japan	RFQ-DTL (under construction)	^{9}Be(p,n)	8 <6	10
CNEA Buenos Aires Argentina	Single ended ESQ[b] Tandem ESQ (under construction)	^{9}Be(d,n) Solid ^{7}Li(p,n)	1.4 <5.7 2.5 <1	30 30

[a] RFQ-DTL stands for Radio Frequency Quadrupole-Drift Tube Linac.
[b] ESQ means Electrostatic Quadrupole.

Fig. 2.12.: Current status of the AB-BNCT facilities worldwide. Data displayed comprise institute and location, type of machine and its status, proposed target and reaction, beam energy and highest neutron energy, actual or necessary beam intensity and references [85].

Accelerators come in various types, including electrostatic linear accelerators, cyclotrons, and RF electrodynamics machines. They also differ in terms of the materials used to produce neutrons. Designing these target materials requires balancing considerations of neutronics, mechanics, and termodynamic consideration.
Different charged-particle reactions for neutron production in Accelerator-Based BNCT (AB-BNCT) are listed in 2.13.

Reaction	E_{thr} [MeV]	E_{in}[MeV]	total production (n/mA)	$E_n < 1MeV$	Target melting point[°C]
^{7}Li(p,n)^{7}Be	1.880	1.890	6.3×10^{9}	100 %	181
		2.500	9.3×10^{11}	100 %	
^{9}Be(p,n)^{9}B	2.057	2.500	3.9×10^{10}	100 %	1287
		4.000	1.0×10^{12}	50 %	
^{9}Be(d,n)^{9}B	0	1.450	1.6×10^{11}	69 %	1287
		1.500	3.3×10^{11}	50 %	
^{13}C(d,n)^{14}N	0	1.500	1.9×10^{11}	70 %	3550

Fig. 2.13.: Characteristics of four charged-particle reactions considered for AB-BNCT including energy threshold (E_{thr}) and some bombarding energies (E_{in}). The total target neutron production is reported and the associated percentage for which the maximum neutron energy is less than 1 MeV. The target melting points are also listed [86] [87].

One notable endothermic reaction is the ^{7}Li(p,n)^{7}Be reaction, which has a Q-value of -1.644 MeV and a proton threshold energy of 1.880 MeV. At this energy, the resulting neutrons is characterized by about 30 keV kinetic energy, making them suitable for BNCT. Unfortunately, the mechanical and chemical properties of lithium make it less than ideal as a target material. While there have been proposals for Liquid Lithium-based targets for BNCT [88], their high cost has limited their development to research prototypes.

In the context of hospital-based BNCT, alternative neutron-producing reactions are favored. Examples include reactions involving Carbon and Beryllium, table 2.13. These materials exhibit superior thermal and mechanical properties compared to Lithium; however, they result in higher neutron energies. Consequently, moderation-based Beam Shaping Assemblies (BSAs) are essential to reduce neutron energy and shape the beam spatially [89].

A schematic representation of an accelerator-based BNCT system can be observed in figure 2.14. The accelerator-based BNCT system has been successfully implemented in medical institutions. For example, the installation process commenced at the Institute for Integrated Radiation and Nuclear Science at Kyoto University (KURNS) in June 2008 was completed in December 2008. However, it's important to note that these systems have not yet received approval from the Pharmaceuticals and Medical Devices Agency (PMDA), a Japanese regulatory authority, and are currently undergoing clinical trials [90].

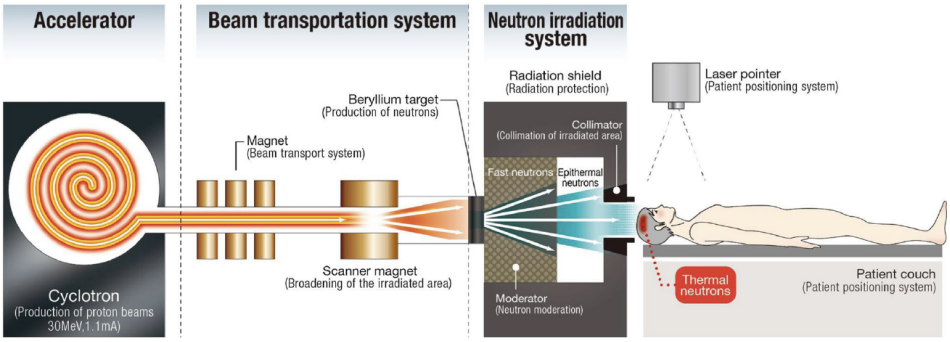

Fig. 2.14.: Schematic view of the accelerator-based BNCT system by courtesy of Sumitomo Heavy Industry Ltd. 2008. It consists of a cyclotron-type accelerator that produces a proton beam of $\simeq$ 2 mA at 30 MeV, beam transport system, beam scanning system on the beryllium target, target cooling system, neutron-beam-shaping assembly, multileaf collimator, and an irradiation position for patients [90].

2.6 The ENTER_BNCT project

As previously mentioned, the effort focused on BNCT involves many countries and Italy is actively engaged in advancing BNCT research. The ENTER_BNCT project, in collaboration with INFN (Istituto Nazionale Fisica Nucleare), was dedicated to the development of BNCT technologies to facilitate the progress of accelerator-based BNCT. ENTER_BNCT involved four INFN units: Pavia, Turin, LNL (National Laboratories of Legnaro), and LNF (National Laboratories of Frascati). The principal goals of this project were:

- Production of a newly designed, efficient beryllium target to produce neutrons through the reaction ^{9}Be(p,n)^{9}B;
- Construction and characterization of the Beam Shaping Assembly (BSA) made up of a new material developed in the previous project BEAT_PRO [91]);
- Development of systems for diagnosis, quality assurance, spectrometric and dosimetric evaluations in beam and in phantom;
- Preparation of the irradiation room, study of the patient positioning systems, radioprotection issues and possible technologies to be used;
- Boron concentration measurements for clinical application (evaluations in the blood to determine irradiation time) and intra-cellular evaluation of boron distribution to calculate dosimetric parameters.

Building upon the group's expertise in neutron spectrometry, this study aims to develop an advanced neutron spectrometer for beam and, eventually, in phantom control in Boron Neutron Capture Therapy (BCNT). The key objectives, as per IAEA guidelines [92], involve achieving portability, high sensitivity in the typical energy range of BNCT neutrons (epithermal), and operational usability.

2.7 The ENTER_BNCT facilities

This section aims to provide a brief description of the facilities made available by the different groups involved in the ENTER_BNCT project. It is not intended to be an exhaustive explanation of the various facilities and their operation but rather an overview to better understand the experimental measurements presented in this manuscript.

For a more in-depth understanding of the different sources, please refer to [93], [94], [95],[96],[97],[6],[98].

2.7.1 The e-LiBaNS facility

The term **e-LiBaNS** denotes the **e**lectron **Li**nac Accelerator **Ba**sed **N**eutron **S**ource. This facility utilizes a reconditioned Elekta Precise 18 MV accelerator, presently located at the Physics Department of the University of Torino.
Originally designed for clinical radiotherapy, this accelerator is capable of delivering beams of both electrons and photons on an energy range from 5 MeV up to 18 MeV. The utilization of a commercial accelerator guarantees operational stability and reproducibility.

Neutron production occurs within a converter target, coupled to the accelerator head, and it intercepts the intense X-ray beam emitted by the LINAC. The neutrons production results from the interaction of high-energy photons with the nuclei of the target material through the (γ, n) reaction.
As already shown in section 1.4.1, this reaction manifests a photon energy threshold, linked to the binding energy of neutrons, typically ranging from 6 to 8 MeV for high atomic number (Z) elements. Certain elements such as Pb and W exhibit a high (γ, n) cross-section value, approximately 600 mb, while photonuclear processes often being negligible in lighter materials. The emitted neutrons are characterized by an energy around 1 MeV, featuring a characteristic evaporative spectrum.

Two different setups have been designed to produce thermal and epithermal neutrons. These setups include a heavy metal conversion target for neutron generation and a moderator volume embedded in large reflector blocks to slow down neutrons to thermal or epithermal energy.
The configurations have been optimized to maximize thermal or epihtermal neutron production while minimizing the presence of fast neutrons and gamma contaminants. The gamma background arises from primary unconverted photons and photons resulting from neutron capture processes in the moderator. Material selection was

a careful process, considering factors like cross-sections, mechanical properties, material availability, and radiation protection. The optimization work involved an extensive Monte Carlo simulation study using MCNP.
A brief description of the two different configurations is presented below:

- **Thermal Mode**
  For this modality, the photoconverter is composed by a lead block serving as a conversion target, which also absorbs unconverted photons from the X-ray beam. The lead block is enveloped by an external graphite structure that works as reflector and moderator. The central core, consisting of heavy water contained in carbon boxes, serves as the primary moderator. Heavy water is particularly advantageous due to its minimal neutron capture probability and high elastic cross-section, facilitating effective neutron slowing down.
  Within the graphite structure, a cavity is formed, providing a thermal neutron field for sample irradiation. To prevent the diffusion of thermal neutrons in the experimental room, the entire structure is enclosed in a 0.8 cm thick borated rubber shield, surrounded by thin polyethylene slabs. The cavity dimensions are $30 \times 30 \times 20$ cm^3, while the overall assembly volume is approximately 1 m^3, weighing around 1 ton.
  Figure 2.15 shows the geometry scheme for this configuration.

- **Epithermal Mode**
  The structural design of the epithermal photoconverter is, in some way, similar to the previous one, with notable distinctions dictated by the necessity to retain neutrons within the epithermal energy spectrum and eliminate the thermal neutron component within the cavity. To achieve this objective, an assembly including aluminum and polytetrafluoroethylene (PTFE) is situated in the central core, accompanied by a Cadmium metallic layer shielding the cavity.
  The resonances in the fast neutron range and a flat minimum in the epithermal region, coupled with a very low absorption probability, characterize the large resonances in the Al and F neutron inelastic scattering cross sections. This property allows fast neutrons generated in the target to undergo scattering processes, transferring part of their momentum without immediate thermalization or capture.
  The strategic alternation of Al and PTFE layers in the appropriate proportions simulates the behavior of a composite material. Given the massive thermal capture cross section for Cadmium, a thin layer (0.5 cm) around the faces of the cavity of proves sufficient to shield against thermal neutrons.
  Figure 2.16 shows the geometry scheme for this configuration.

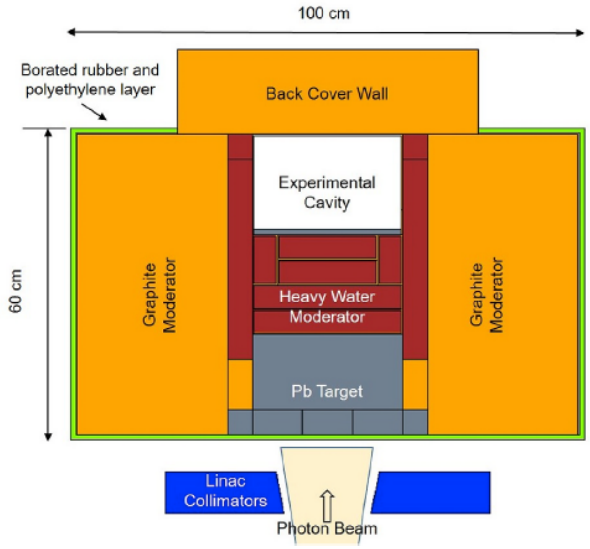

Fig. 2.15.: MCNP6 scheme of the thermal photoconverter geometry (longitudinal view) [95].

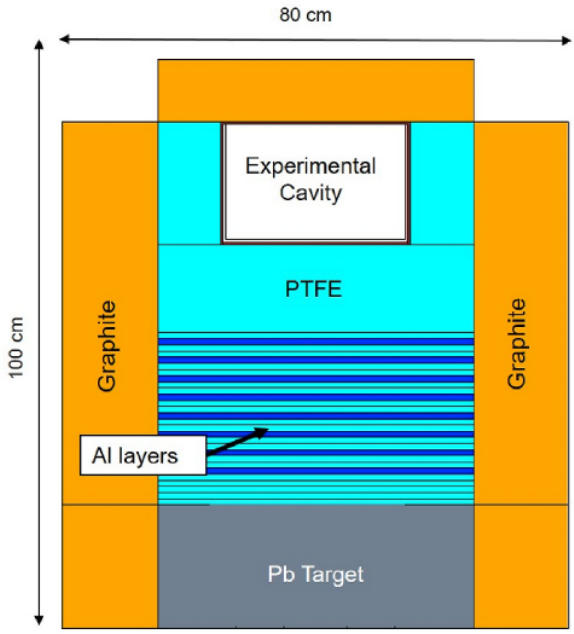

Fig. 2.16.: MCNP6 scheme of the epithermal photoconverter geometry (longitudinal view) [95].

The neutron fields inside the experimental cavity of the thermal and epithermal photoconverter have undergone accurate characterization through various measurement techniques. The neutron energy spectra have been measured using a calibrated Bonner Sphere System (BSS).

The spectrometric system underwent prior calibration, as detailed in [99]. To derive the energy spectra from the detector counts, an unfolding procedure was imple-

mented, relying on the FRUIT unfolding code in Special Gradient Mode [2]. The experimental curve, for the thermal cavity, is shown in figure 2.17 with the simulated curve generated by MCNP6.

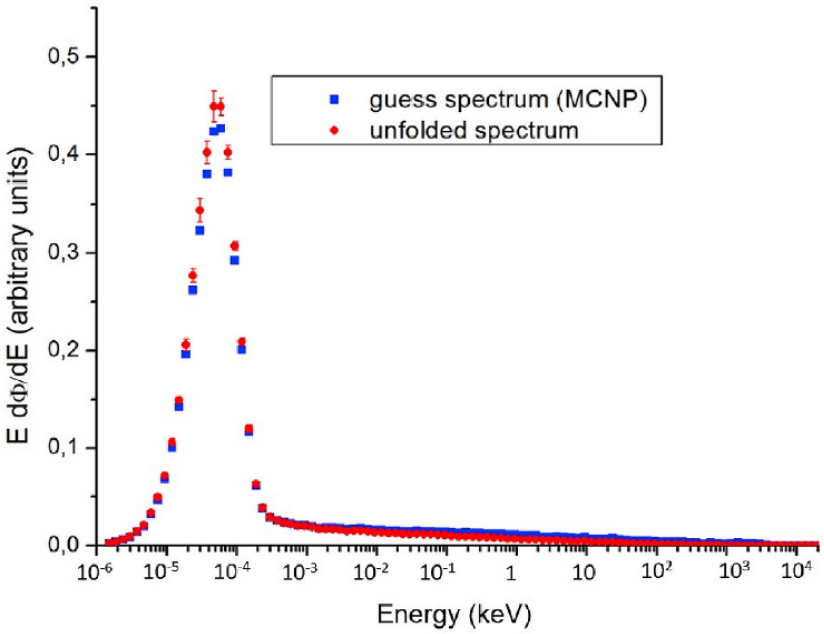

Fig. 2.17.: Neutron energy spectrum measured in the thermal photoconverter cavity. Circle and square points indicate the unfolded data and the MCNP6 prediction, respectively. The spectra are normalized to unit fluence.

The fluence rate within the cavity exhibits a linear dependence on the LINAC current. At the reference work condition of the LINAC (400 MU/min), the benchmark value for the thermal neutron fluence rate at the center of the thermal irradiation cavity has been determined through gold activation foils. It should be noted that 1 MU (Monitor Unit) corresponds to the amount of radiation necessary to deliver 0.01 Gy at the build up in a standard solid water phantom at 100 cm from the LINAC target. The measurements provided a value for thermal fluence rate at the reference working value of:

$$\dot{\Phi}_w(th) = (1.46 \pm 0.10)^1 \cdot 10^6 \,\mathrm{cm}^{-2}\,\mathrm{s}^{-1} \tag{2.5}$$

The experimental curve, for the epithermal cavity, is shown in figure 2.18 with the simulated curve generated by MCNP6.

[1]Unless otherwise specified, $\pm\boldsymbol{u}$ indicates an uncertainty of 1.96 σ, corresponding to a **95% confidence limit**. While **(*u*)** indicates an uncertainty of 1 σ, corresponding to a **67% confidence limit**

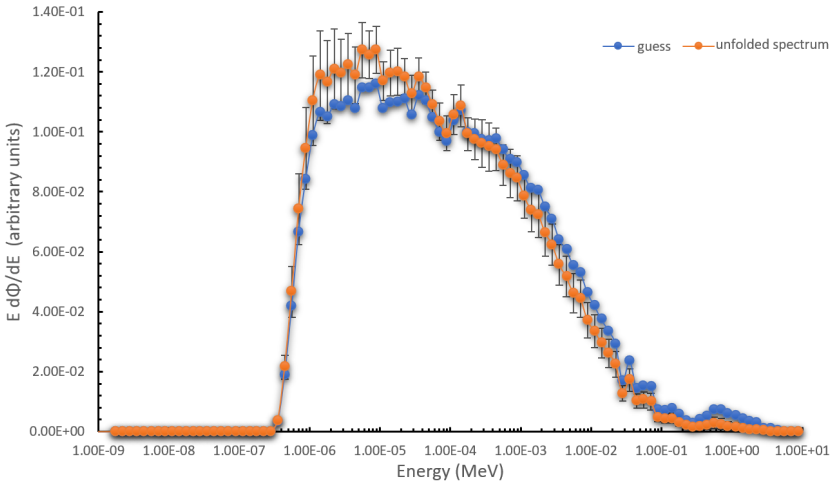

Fig. 2.18.: Neutron energy spectrum measured in the epithermal photoconverter cavity. Blue points represent the MCNP6 prediction, while the orange points indicate the unfolded data. The spectra are normalized to unit fluence.

The measurements provided a value for the epithermal fluence rate at the reference working value of:

$$\dot{\Phi}_w(epi) = (9.32 \pm 0.68) \cdot 10^4 \,\mathrm{cm}^{-2}\,\mathrm{s}^{-1} \tag{2.6}$$

The employed notation, with the subscript "w" refers to the Westcott formalism, as discussed in Section 1.3.5.

Figure 2.19 shows a picture of the LINAC facility with the thermal photonverter.

Fig. 2.19.: External image of the e-LiBaNS facility. The grey structure is the thermal photoconverter.

2.7.2 The HOTNES facility

HOTNES, which stands for **HO**mogeneous **T**hermal **NE**utron **S**ource, is a thermal neutron facility developed through collaboration between INFN-LNF and ENEA-Frascati. The design of HOTNES was optimized utilizing the MCNP Monte Carlo code. A schematic representation of its structure is depicted in figure 2.20. In accordance with figure 2.20, the facility is based on a ^{241}Am-Be neutron source (1.1.1) with a nominal activity of $3.5 \cdot 10^6$ Bq.

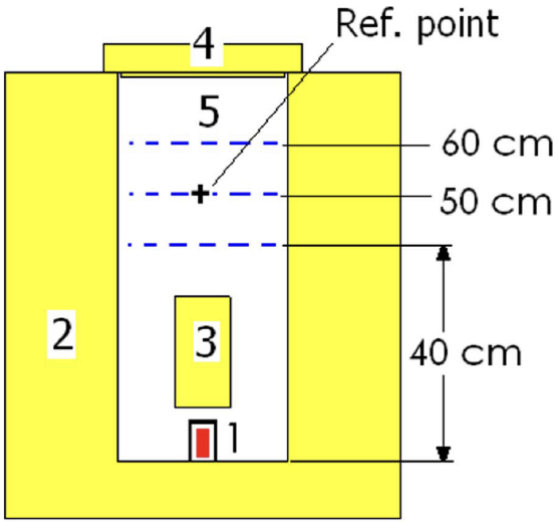

Fig. 2.20.: Lateral section of the HOTNES facility. 1) Am-Be source. 2) High density Polyethylene (HDPE) shielding. 3) HDPE insert. 4) HDPE removable cover. 5) Irradiation volume.

The neutron source is positioned at the base of a cylindrical cavity measuring 30 cm in radius and 70 cm in height, with polyethylene walls, floor, and ceiling defining its boundaries. The source emits isotropically, and neutrons traverse the cavity, undergoing multiple scattering interactions with the polyethylene shields before reaching the designated irradiation volume.
As the distance from the source increases, scattering events lead to a reduction in neutron fluence. A polyethylene shadowing bar separates the irradiation volume from the source, preventing fast neutrons from reaching the irradiation volume and resulting in an enhanced thermal neutron fluence. The combined effects of the shadow bar and lateral walls create a thermal neutron field of approximately 90% purity. The irradiation volume has dimensions of 40 cm in height and 30 cm in diameter, with a 5 cm thick polyethylene cover sealing its top.

The irradiation volume is conceptually divided into an infinite series of disks, forming irradiation planes along the cylindrical axis and parallel to the facility's bottom. These planes can be treated as "iso-fluence surfaces" due to their uniform thermal

fluence values across their entire area. Each plane is identified by its height in centimeters from the cavity bottom. By precisely understanding the vertical fluence gradient, one can choose a specific fluence value by adjusting the vertical position within the cavity. The HOTNES reference point is conventionally designated as the center of the irradiation plane situated at Z = 50 cm, corresponding to the midpoint of the irradiation volume.
In this point the thermal neutron fluence rate is equal to:

$$\dot{\Phi} = (763 \pm 22)\,\mathrm{cm}^{-2}\,\mathrm{s}^{-1} \tag{2.7}$$

This value was obtained using the Au activation foil method.

The neutron energy spectrum at the reference point has been accurately simulated and measured. In figure 2.21 the comparison between MCNP simulation and unfolded measurement is shown. As mentioned before, the spectrum is dominated by the thermal component, with a low epithermal tale and a residual peak in the fast region (1-10 MeV).

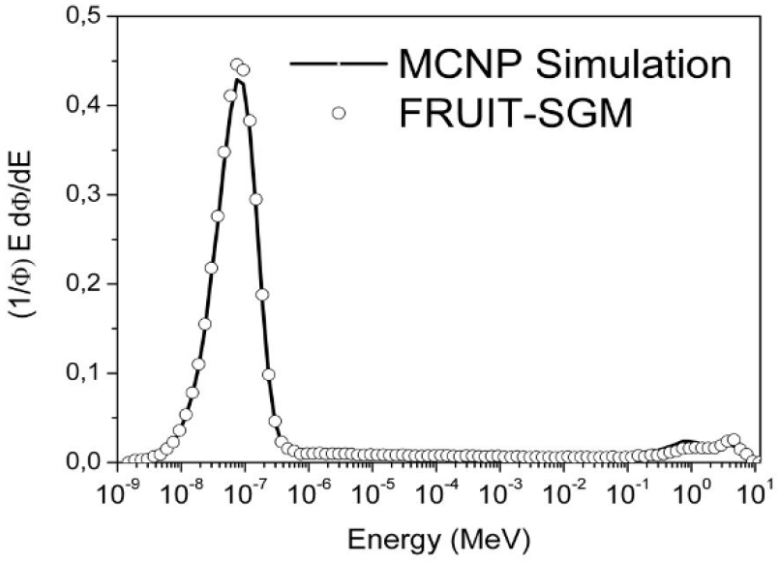

Fig. 2.21.: HOTNES neutron spectrum at reference point at 50 cm from the bottom. Dotted points refer to measurements data.

In figure 2.22 an image of the HOTNES facility is shown. At the top of the image the HDPE can be shown.

Fig. 2.22.: External image of HOTNES facility [93].

2.7.3 The LENA facility

The Laboratory of Applied Nuclear Energy (LENA) in Pavia, Italy, houses a TRIGA Mark II Research Reactor with a steady-state power of 250 kW, designed and manufactured by General Atomics.
This reactor provides in-core and out-of-core neutron irradiation channels with different neutron spectra. Since its initial criticality in 1965 [100], the reactor has been instrumental in conducting various scientific and technical applications. Figure 2.23 shows a picture of the facility.

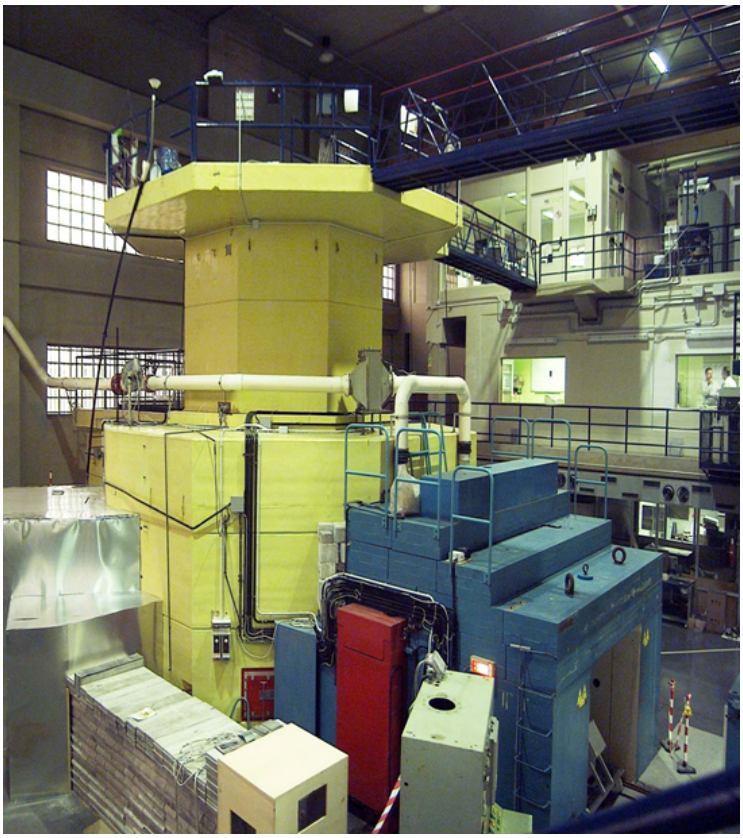

Fig. 2.23.: External image of LENA facility

The LENA reactor features a right-cylindrical core, cooled and partially moderated by light water [101]. The core lattice consists of 90 cylindrical elements arranged in 5 concentric rings around the Central Thimble (CT) channel. These elements serve different purposes: 81 are moderator-fuel elements, 3 rods made of boron carbide and borated graphite control reactor reactivity, one radium–beryllium source triggers the chain reaction during reactor ignition, 3 are vertical irradiation channels penetrating the core for irradiating small samples in the maximum flux region, and the remaining elements are graphite elements.
Fuel elements on the first, second, and third rings have stainless steel cladding, while

those on the fourth and fifth rings have aluminum cladding [102].

The reactor core is surrounded by a 30 cm thick radial graphite reflector. Additionally, the fuel elements themselves act as an axial reflector, thanks to the inclusion of two 10 cm thick graphite cylinders at the ends of the rod. The light water tank in the reactor also contributes as a reflector.
The LENA reactor provides both vertical and horizontal irradiation channels (figure 2.24). Along the vertical axis of the core, the neutron flux is maximized. Four vertical channels are strategically positioned, including the Central Thimble, the Pneumatic Transfer Tube (Rabbit), the Rotary Specimen Rack (Lazy Susan), and the Thermal Channel. These irradiation channels are primarily used for Instrumental Neutron Activation Analysis and isotope production.
The Rabbit channel, located in the outer core ring, can be remotely operated through a pneumatic sample transfer system, facilitating the sending and receiving of samples directly from the dedicated hood in a radio-chemical laboratory.
The Central Thimble is a dry tube capable of accommodating up to 3 samples in cylindrical containers. Its position in the core can be conveniently adjusted to meet irradiation requirements.
The Lazy Susan is an aluminum channel equipped with 40 holes arranged in an annular groove in the upper section of the reactor core. It can load up to 80 samples in cylindrical containers.

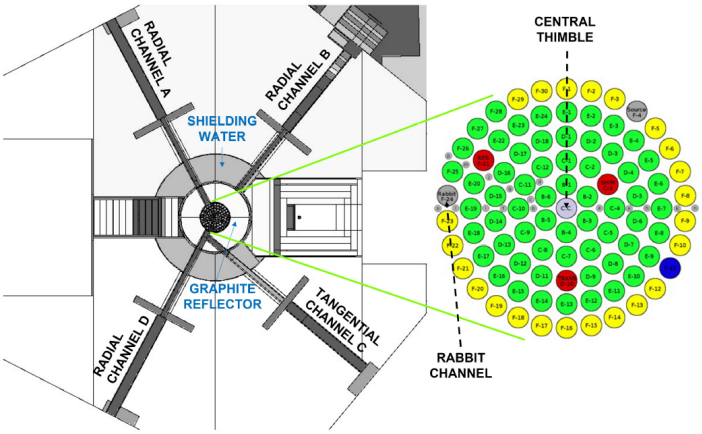

Fig. 2.24.: The diagram shows the horizontal irradiation channels, the water tank, and the graphite reflector encircling the reactor core. On the right side, an enlarged view of the core configuration is presented. Fuel elements are denoted in green, graphite rods in yellow, control rods in red, and the empty slot in blue. The smaller grey circles signify holes on the top core grid. The positions of the two vertical irradiation channels, namely the Central Thimble and Rabbit Channel, are indicated.

The energy spectra in the different channels have been simulated in [102], the results is shown in figure 2.25. Particular attention should be dedicated tot he rabbit

channel, which has been used during this work. In the Rabbit irradiation condition the integrated thermal fluence rate was around $10^{13}\,\mathrm{cm}^{-2}\,\mathrm{s}^{-1}$ (@ 250 kW).

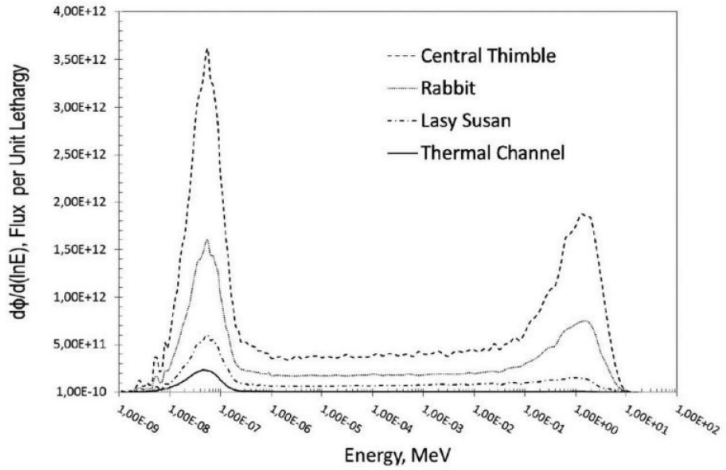

Fig. 2.25.: Fluxes per unit lethargy spectra calculated with Monte Carlo code MCNP in the vertical channels.

3 NCT-ACS development

This chapter aims to describe the process that led to the development of a spectrometer known as **NCT-ACS** (**N**eutron **C**apture **T**herapy **A**ctivation **C**ompact **S**pectrometer). The first idea behind its design will be addressed in section 3.1, while the subsequent sections will study the various aspects that contributed to its final form.
It should be noted that the division into sections and subsections follows a logical order in retrospect, and should not be strictly interpreted as a chronological sequence. The development of NCT-ACS has been a time-consuming process and has undergone numerous transformations. As will become evident to the reader, the final prototype significantly deviates from the initial, and somewhat unachievable, ambitious concept. Nevertheless, the order proposed in this chapter follows a logical thread that starts with the original idea and leads to the completion of the instrument.

All the nuclear data presented below have been obtained from [103] [104] [105] [106] and [107]. Many beta decay data have been taken from the Table of Radioactive Isotopes Database [108], almost all data shown in this database are from the Evaluated Nuclear Structure File (ENSDF). ENSDF is updated and maintained by the National Nuclear Data Center (NNDC) at BNL.
Reference to [26] has been also useful for its substantial and valuable work.

3.1 NCT-ACS concept

NCT-ACS is a compact neutron spectrometer based on the activation phenomenon 1.3.3, characterized by small dimensions in the order of a few centimeters. The primary concept behind NCT-ACS involves using the characteristics of neutron cross-sections within the epithermal range (0.4 eV - 100 keV) to extract spectroscopic information.
Each element, or rather, each isotope, possesses a distinct neutron capture cross-section due to the different nuclear structure. Some elements exhibit a remarkably pronounced resonance in their cross-section which dominates over the other resonances at different energies. Figures 3.1 and 3.2 show two clear examples for this behaviour. By carefully selecting elements with these characteristics, each with the primary resonance positioned at different energies, it becomes possible to sample the spectrum in the epithermal range.

Then, using a commercial gamma detector, the activity of the different elements can be extracted and a relationship between the activity values and the number of capture reaction can be determined. Through appropriate analytical techniques, the activation values can be directly related to the overall neutron energy spectrum, deducing its overall spectrum shape.

An accurate description of the whole procedure can be found in the next sections.

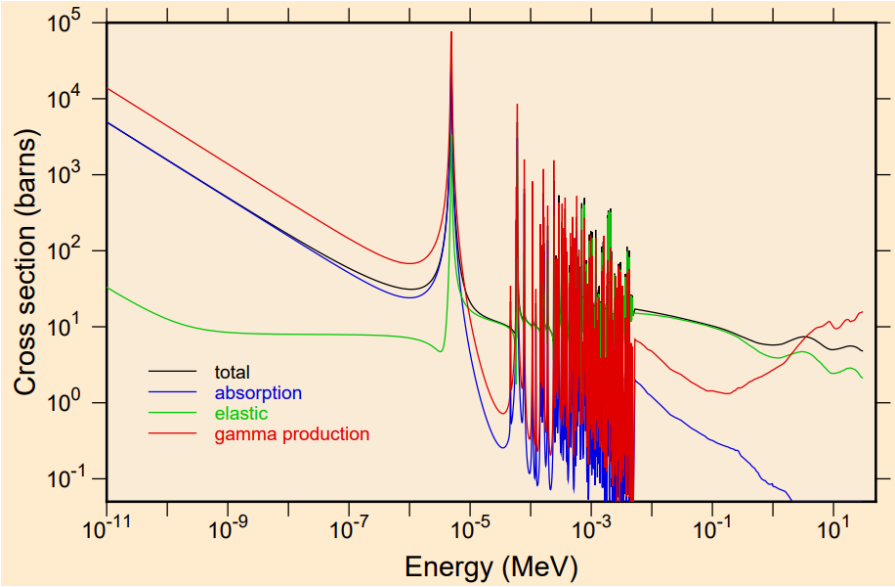

Fig. 3.1.: Neutron cross sections for ^{197}Au (100% isotopic abundance). The strong resonance is well known and it is characterized by a peak energy of 4.890 eV [26] and [109]. The plot is taken from [103].

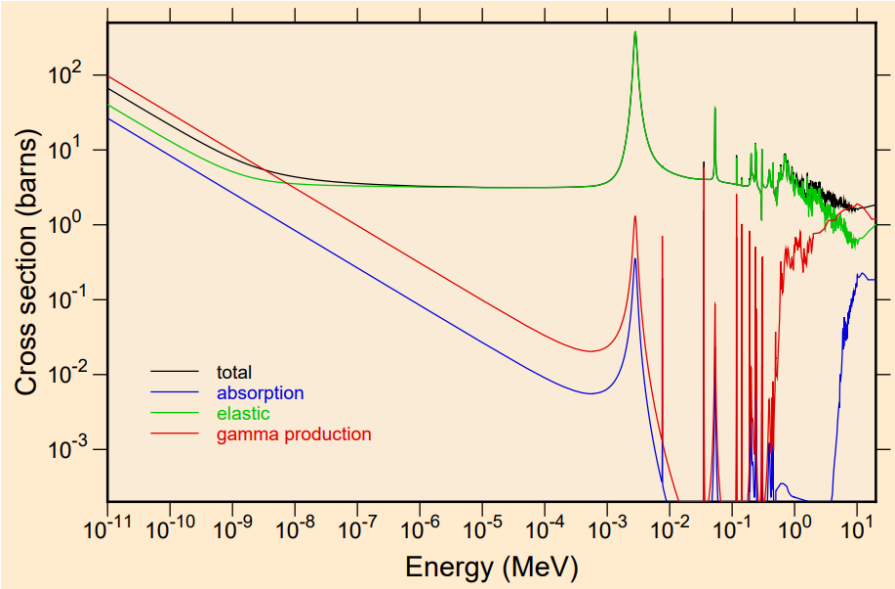

Fig. 3.2.: Neutron cross sections for ^{23}Na (100% isotopic abundance). The strong resonance is well known and it is characterized by a peak energy of 2.787 keV [26]. The plot is taken from [103].

This instrument would be different from standard Bonner Sphere Spectrometers (BSS) in numerous ways. At present, it is evident that the primary distinction lies in the fact that BSS incorporates a thermal neutron detector, while ACS is designed to consist of individual units sensitive to epithermal neutrons. This indicates that there will no longer be a need to thermalize neutrons; instead, populating the energy range between 0.4 eV and 100 keV will suffice.
This approach enables the creation of a compact geometry, facilitating measurements of the energy spectrum under various experimental conditions. As already mentioned in 2.5 the typical collimator dimension BNCT are in the order of 10-15 cm making hard, or even impossible, to use the standard BSS technique to measure the neutron beam just at the exit of the BSA or at the exit of the collimator, where the patient is commonly placed.
Moreover the BSS technique has always revealed some lacks in reconstructing energy spectra in the epithermal energy range because of its response matrix shape [110].

After this introduction, is obvious that one of the main aspects to be analyzed is the elemental composition of NCT-ACS, since from this depends the overall structure.
It could be helpful to keep in mind the main goals considered studying the composition and the geometry of NCT-ACS, here below is listed a short summary to better understand some decision which will be presented later:

1. **Energetic sensitivity**: neutron energies from thermal up to at least 100 keV.

2. **Dimensions**: few cm.

3. **Angular response**: isotropic.

4. **Working conditions**: able to work in a single irradiation phase.

5. **Machinability**: easy to be constructed and used in all the situations.

3.2 The choice of the elements

In section 1.3.2 an exhaustive discussion on the capture reaction have already discussed. It is useful to recall the figure 1.8:

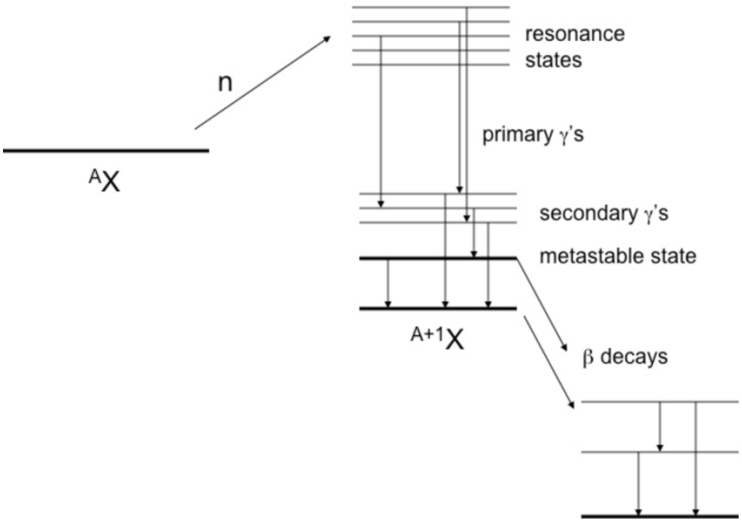

Fig. 3.3.: Neutron reaction capture scheme.

And also the reaction balancing equation:

$$ {}^{A}_{Z}\boldsymbol{X} + {}^{1}_{0}n \rightarrow \left({}^{A+1}_{Z}X\right)^{*} \rightarrow {}^{\boldsymbol{A+1}}_{\boldsymbol{Z}}\boldsymbol{X} + \gamma \rightarrow {}^{\boldsymbol{A+1}}_{\boldsymbol{Z\pm1}}\boldsymbol{X} + e^{\mp} + \gamma \tag{3.1} $$

The most important part, while choosing the elements for NCT-ACS, has been focused not only on the parent nucleus, but also on the activated nucleus and on the final product.
It should be noted that the α decay has not been taken into account since the selected nuclei only decay via β decay.
In order to choose the best elements, many selection criteria have been applied, taking into account physical, practical, economic and also safety aspects.

3.2.1 Applied criteria

In most cases, explicit discrimination values were not applied because the general study was very complex, and a single parameter could have both positive and negative aspects. Therefore, a subsequent selection criterion was chosen, in which at each step, the candidates considered 'worse' were excluded. This approach led to a final list of elements that could adequately satisfy the various criteria:

1. **GENERAL CRITERIA**

- **Natural State**
  Generic applied criterion: No liquid and gaseous state.
  Not all the elements on the period chart are solid in the normal temperature and pressure conditions. Some good candidates were gas (e.g. Cl) or liquid (Hg). In some cases a compound material has been found, in other cases this was not possible due to the characteristics of the compound. Luckily, most of the good candidates were present in metallic or crystal form in nature;

- **Isotopic Abundance**
  Generic applied criterion: High isotopic abundance was preferred.
  This criterion was not one of the most stringent or significant, as isotopic enrichment techniques ensure high-purity compounds, even when the required isotope is present in small quantities. Moreover, isotopic abundance is typically not a concern, unless it is exceptionally low, necessitating a large quantity of material, which can pose geometric and cost-related challenges. Efforts were made to work exclusively with natural, non-enriched elements to manage instrument production costs;

- **Toxicity or Danger**
  Generic applied criterion: No toxic or dangerous elements.
  To ensure the operator's safety during laboratory measurements, efforts were made to minimize the risks associated with element's toxicity or general hazards. Additional risk factors taken into account included element's reactivity with air and water, natural radioactivity, and its tendency to oxidize and disintegrate. This criterion led to the exclusion of some high-risk elements. It should be noted that ^{238}U, although scientifically interesting, requires special permits for possession. Furthermore, its use would entail numerous restrictive safety measures for the operator and transportation, making practical utilization challenging;

2. **NEUTRON CROSS SECTIONS RELATED CRITERIA**

- **Resonance Energy**
  Generic applied criterion: Resonances well distributed in the epithermal range
  This criterion held significant importance in the context of the final selection. Predicting the energy corresponding to the primary resonance using models or empirical formulas is not possible. Therefore, it became mandatory to reference nuclear data repositories for a comprehensive survey of all elements. As discussed earlier in section 1.3, all resonances are confined within the epithermal range, spanning from 0.4 eV to 100

keV. The majority of primary resonances manifest at lower energy levels, with only a select few elements exhibiting such resonances at higher energies, typically within the range of tens of keV. Consequently, the selection among multiple elements was practicable for incident neutron energies up to approximately 1 keV. Beyond this range, one has to rely on the limited elements available. It should be noted that while the primary resonance dominates over the cross-section, it is not the only resonance. The intricate structure of the cross-section introduces an added layer of complexity. This aspect was not incorporated as one of the criteria, so as not to exclude the majority of elements. During the Monte Carlo simulation phase, the complete cross section structure have been considered for correctly modelling the system;

- **Epithermal Resonance Integral**
  Generic applied criterion: High Resonance Integral values were preferred.
  Another crucial criterion in the element selection process consists on the neutron capture cross-section value. Specifically, the parameter of interest under study was the epithermal resonance integral I defined as [111]:

$$I = \int_{0.5\,eV}^{+\infty} \frac{\sigma(E)}{E} dE \tag{3.2}$$

  All the data for this selection have been taken from [105].
  This relationship was fundamental because the activation rate A_r in an epithermal field is given by:

$$A_r = N\dot{\phi}_{epi} I \tag{3.3}$$

  Being $\dot{\phi}_{epi}$ the epithermal fluence rate and N the number of target nuclei. In principle, the higher is the resonance integral value, the higher will be the capture reaction and, consequently, the higher will be the statistical counts for the analysis.
  A more detailed description on how this selection has been applied is reported in section 3.2.3.

3. **BETA AND GAMMA EMISSION RELATED CRITERIA**

- **Half life time of the activated nucleus**
  Generic applied criterion: Half life time ranging from few minutes up to few days.
  This criterion posed one of the most challenging yet crucial aspects of

the selection process. The half-life of the daughter nucleus is intricately connected to its nuclear structure and binding energy. In practical terms, it was crucial to avoid elements with excessively long or short half-lives. The reason behind not opting for elements with excessively long half-lives (greater than few days) was twofold. Firstly, this was done to mitigate the risks of exposure to undesired ionizing radiation days after the measurements, and secondly to enable multiple uses of the same element. This happens because the activation value decrease in time like the well-known formula:

$$A(t) = A_0 e^{-t/\tau} = A_0 2^{-t/t_{1/2}} \tag{3.4}$$

Being τ the mean lifetime, $t_{1/2}$ the half life time and A_0 the initial activity. Having the same activity A_0, the waiting time before considering an activity equal to zero depends by the half life time value. Usually, after 5 mean life times (around 7 half life time) the activity is considered negligible, since it represents less than 1% than the original activity.
Therefore, selecting a candidate with a half-life ranging weeks or even longer risked creating excessively extended intervals between measurements. Adequate corrections, related to the candidate's initial activity at the time of a new measurement, could have been applied, but this would have introduced systematic errors into the measurement, and whenever possible, such a situation was to be avoided. Acquiring a larger quantity of these elements would have resolved the issue but significantly increased the final cost of the detector.

On the other hand, candidates with excessively short half-lives would have been challenging to measure, as the activity would rapidly decrease during the time between irradiation and sample exposure to the gamma detector. Extending irradiation sessions could partially solve this problem, but once saturation conditions were reached, activity would stop to increase, offering no solution to the problem.
The final selection of elements resulted in a range of half life times spanning from 3 minutes to 90 hours.

- **Branching Ratio for the gamma emission**
  Generic applied criterion: High Branching Ratios for gamma emission were preferred.
  In an ideal scenario, all selected elements would exhibit a Branching Ratio (BR) of 100% for gamma emission. Unfortunately, for some elements, the percentage of gamma emission was too low to provide sufficient statistics. Extending the irradiation time would have led to excessive activity in

other elements, compromising the system. Alternatively, a larger quantity of such elements could have been incorporated, significantly increasing the instrument's costs. A specific limit was not set for this criterion, as the elements selected based on other criteria generally had BR values exceeding 5%.

However, some elements were excluded due to extremely low BR values. For instance, ^{30}Si, while displaying certain promising characteristics and a pronounced resonance for high-energy neutrons (4.977 keV [26]), was characterized by a BR for the gamma emission equal to only 0.07%, making its practical use almost impossible.

- **Energy of the gamma emitted**

  Generic applied criterion: Energy of the gamma from few tens keV up to around 2 MeV.

  This criterion has been carefully examined. The main challenge was not related to the absolute value of gamma energy. The gamma energies emitted by the selected elements range from a few keV up to 1-2 MeV.

  The criterion was applied, wherever it was possible, to avoid selecting elements that emitted gamma rays of similar energies. This would have cause issues during the gamma analysis.

  In nearly all cases, it was possible to select elements with sufficiently different gamma emission energies that could be resolved by the detectors used. The only candidate that presented some challenges was ^{186}Re (137 keV) and ^{188}Re (155 keV). Using a HPGe detector, these two peaks are resolved, but considering another detector some difficulties could arise.

  Additionally, it should be noted that low-energy gamma rays (a few keV) may pose challenges in the analysis due to increased background noise within the low-energy γ spectrum caused by x-rays emitted from shielding materials (e.g. Lead, Copper).

- **Number of emitted gammas**

  Generic applied criterion:Low number of gamma emitter were preferred.

  This criterion was initially applied to all considered elements. However, it was later partially abandoned, as it would have excessively restricted the potential element choices.

  Any nucleus in an excited state can de-excite by emitting gamma rays or Auger electrons. The number of gamma rays emitted depends on the nuclear structure of the excited nucleus, following the selection rules [12] and depending by the available nuclear energy levels. For some isotopes, the possible transitions are few, and one transition often dominates over the others. For these reasons, the resulting gamma spectrum will exhibit

a simple structure, facilitating an easier analysis.
In figure 3.4 is shown the decay scheme for ^{198}Au, as can be noted the main transition is over dominating the others, causing a simple gamma spectrum with a basic structure.

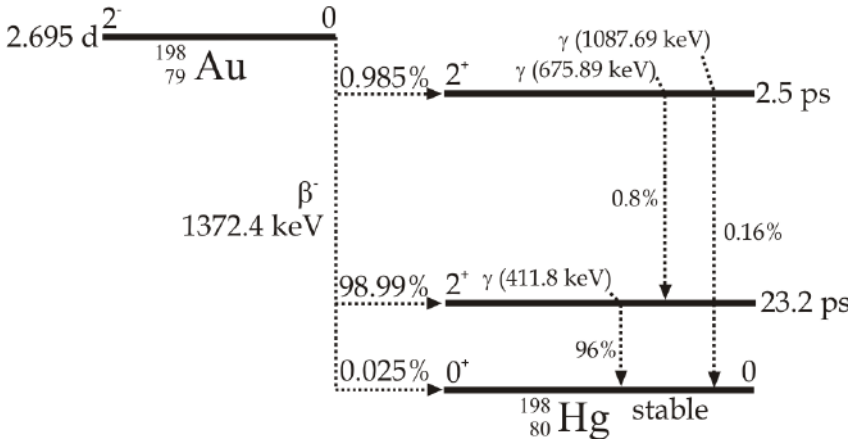

Fig. 3.4.: Decay scheme for ^{198}Au. Three different final state for the β decay are possible, but the main one is heavily dominating over the others. The possible energies for the gamma radiations are: 411.8 keV (96%) corresponding to the transition between the first excited level and ground, 1087.69 keV (0.16%) corresponding to the transition between the second excited level and ground and 675.89 keV (0.80%) corresponding to the transition between the second and the first excited level [112].

Conversely, some elements may de-excite by emitting a large number of gamma rays. In these cases, the gamma spectrum obtained is more complex and challenging to analyze.
An useful example is shown in figure 3.5 where the decay scheme for the ^{116}In* is represented. The metastable nucleus of ^{116}In decays by internal conversion on another metastable level of ^{116}In, then it decays with a β particle emission.

As can be clearly seen, the structure is more complex, also due to the fact that the different transitions have similar probability, so there is not a single transition that dominates like in the Gold case.
Looking into the database more than 45 gamma energies are listed. It should be noted that the transition characterized by a branching ratio higher than 1% are only 8. This is sufficient to produce a quite complex gamma spectrum. During the activation analysis this has been taking into account.

- **Eventual decay chain**
  Generic applied criterion: Decay chain was avoided.
  This criterion proved valuable in excluding certain selected elements that,

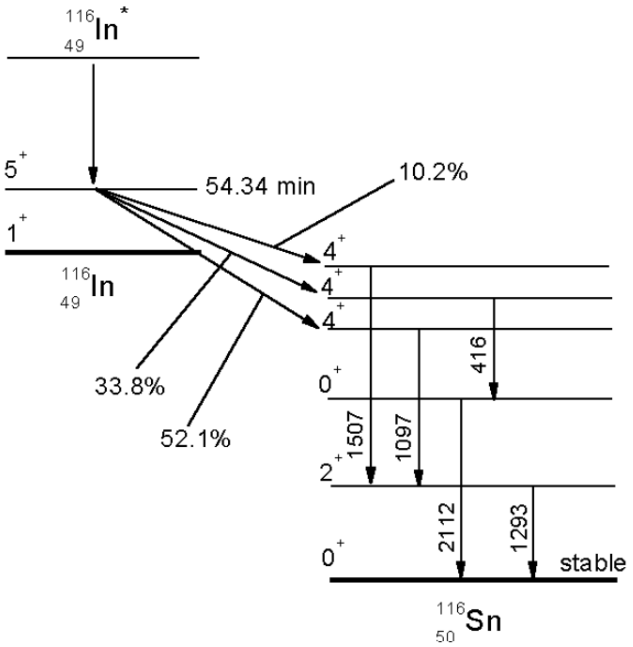

Fig. 3.5.: Partial representation of the decay scheme for the ^{116}In* nucleus. The direct decay from the first excited state to the ground state is improbable due to a small energy difference and a significant spin difference. In the case of the $5^{+} \rightarrow 1^{+}$ transition within ^{116}In, the emitted photon would need to carry an angular momentum of $4\hbar$, corresponding to an electric hexadecapole (E4) transition that is strongly suppressed by the selection rules.

after an initial beta decay, entered a metastable state once more. The reaction depicted in equation 3.1 could thus be prolonged as:

$$ {}^{A+1}_{Z\pm1}X + e^{\mp} + \gamma \rightarrow {}^{A+1}_{Z\pm2}X + e^{\mp'} + \gamma' \quad ... \tag{3.5} $$

In most cases, such a study was unnecessary, as the final products resulting from the initial decay were stable nuclei. However, in cases involving further decay, the same criteria outlined in this list were applied. This was because the subsequent, undesired decay behaved precisely as if it were another element to be selected.
One interesting case studied is related to the ^{185}Re. The final state following neutron capture is ^{186}Re, which, through beta- decay, yields ^{18}Os. This isotope is not precisely stable, as it undergoes alpha decay with a half-life of $2.0{\cdot}10^{15}$ years. As observed, this half-life is extremely long, making it practically equivalent to stability. Furthermore, the alpha particle produced by the decay does not interfere with the measurement, as it cannot penetrate into the sensitive region of the detector.

This criterion would have been pertinent in cases involving heavier ele-

ments that exhibit this characteristic of undergoing numerous subsequent beta decays. For example,^{238}U follows the following decay chain:

$$^{238}_{92}U + n \rightarrow {}^{239}_{92}U \rightarrow {}^{239}_{93}Np \rightarrow {}^{239}_{94}Pu \rightarrow {}^{235}_{92}U \ldots \tag{3.6}$$

In the interest of brevity, the various gamma and beta emissions during the decay processes have been omitted. The final decay shown occurs through the emission of an α particle and produces ^{235}U which is characterized by a long half life time and therefore can be considered stable for our purpose. As already discussed before, ^{238}U, although it is an interesting candidate, can not be used.

4. **PRODUCTION RELATED CRITERIA**

- **Machinability:**
  Generic applied criterion: good machinability was preferred.
  This criterion proved to be among the less stringent ones. Most elements selected based on the *general criteria* were already in conditions favorable to be machined. Only in some isolated cases minor corrections were necessary. For instance, in the case of manganese, the use of pure metal was not viable due to its high fragility. Therefore, a high Mn-content Mn-Cu alloy was preferred, ensuring favorable mechanical and chemical characteristics. It should be noted that the majority of selected elements consisted of metals, and thus were relatively straightforward to be processed;

- **Commercial price:**
  Generic applied criterion: low commercial price was preferred.
  Commercial price was a criterion applied under specific conditions. In situations where two elements exhibited similar characteristics, and it was possible to use either, the more economic option available on the market was selected. This choice aimed to ensure a higher quantity and maintain spare material in case of damage or loss. For instance, Iridium shown some good characteristics concerning energy resonance and epithermal integral, but its cost was extremely high. Therefore, Indium and Gold were preferred.

Once the various criteria to be applied were defined, the elements commonly used in neutron capture measurements were analyzed. This analysis relied on the data available in [107], but, most importantly, it made extensive use of the table in [104], which is presented here in table 3.6.
It should be noted that all the elements shown, were examined and considered:

Isotope	Resonance Energy (eV) [a]	Activated Nucleus [a]	$t_{1/2}$ [a]	E_γ (keV) [a] [b]	I (b) [b]
19F	44700	20F	11.16s	1633.6	0.039
23Na	3380	24Na	14.96h	1368.6 2754	0.303
26Mg	257000	27Mg	9.462min	170.7 843.8 1014.4	0.024
27Al	11800	28Al	2.2414min	1778.9	0.16
30Si	2280	31Si	2.622h	1266.2	0.106
36S		37S	5.05min	3103.4	0.18
37Cl	13700	38Cl	37.24min	1642.7 2167.4	0.29
40Ar	31000	41Ar	1.822h	1293.6	0.41
41K	2960	42K	12.36h	312.7 1524.7	1.41
48Ca	1330000	49Ca	8.718min	3084.4	0.5
45Sc	5130	46Sc	83.83d	889.3 1120.5	11.3
50Ti	63200	51Ti	5.76min	320.1 928.6	0.115
51V	7230	52V	3.75min	1434.1	2.63
50Cr	7530	51Cr	27.70d	320.1	8.1
55Mn	468	56Mn	2.579h	846.8 1810.7 2113.1	13.9
58Fe	637	59Fe	44.50d	142.7 192.3 334.8 1099.3 1291.6	1.28
59Co 64Ni	136 14200	60mCo 65Ni	10.47min 2.517h	58.6 366.3 1115.5 1481.8	39.7 1.13
63Cu	1040	64Cu	12.70h	511 1345.8	4.88
65Cu	766	66Cu	5.120min	1039.2	2.63
64Zn	2560	65Zn	244.3d	1115.5	1.42
68Zn	590	69mZn	13.76h	438.6	0.223
70Zn	17	71Zn	2.45min	121.5 511.6	0.04
71Ga	154	72Ga	14.10h	630 834 894.2 1050.7 2201.7 2491 2491.0 +2507.8 2515 2507.8 2515	30.6
74Ge	3540 3540	75mGe 75Ge	47.7s 82.78min	139.7 198.6 468.8 617.7	0.35

76Ge	583	77mGe	52.9s	159.7	1
	583	77Ge	11.30h	211	2
				215.5	
				264.4	
				367.4	
				416.3	
				558	
				631.8	
				714.4	
				1085.2	
75As	106	76As	26.24h	559.1	52.5
				559.1	
				563.2	
				563.2	
				657.1	
				1212.9	
				1212.9	
				1216.1	
				1216.1	
74Se	29.4	75Se	119.8d	121.1	507
				136	
				264.7	
				279.5	
				400.7	
76Se	577	77mSe	17.36s	162	16
79Br	69.3	80mBr	4.421h		32
	69.3	80Br	17.68min	616.3	132.5
				666.3	
81Br		82mBr	6.13min		34
	152	82Br	35.30h	554.3	50
				619.1	
				698.4	
				776.5	
				827.8	
				1044	
				1317.5	
				1474.9	
85Rb	839	86Rb	18.63d	1077	7.31
87Rb	364	88Rb	17.78min	898	2.4
				1836	
				2677.9	
84Sr	469	85mSr	67.63min	231.9	8.8
	469	85Sr	64.84d	514	9.14
86Sr	795	87mSr	2.803h	388.5	3.2
89Y	4300	90mY	3.19h	202.5	0.006
				479.5	
94Zr	6260	95Zr	64.02d	724.2	0.268
				756.7	
				724.2	
				756.7	
		95mNb	86.6h		
		95Nb	34.97d	765.8	
96Zr	338	97Zr	16.74h	254.2	5.3
				355.4	
				507.6	
				602.4	
				703.8	
				1148	
		97mNb	52.7s	743.4	
		97Nb	72.1min	657.9	
93Nb	574	94mNb	6.26min	871	6.34

98Mo	241	99Mo	65.94h	181.1 366.4 739.5 777.9	7
		99mTc	6.01h	140.5	
100Mo	672	101Mo	14.61min	80.9 191.9 195.9 191.9 195.9 408.7 499.7 505.1 505.9 590.1 590.1 695.6	3.77
96Ru	776	97Ru	2.9d	215.7	6.12
102Ru	181	103Ru	39.35d	497.1 610.3	4.21
104Ru	495	105Ru	4.44h	262.8 469.4 469.4 470.1 676.4 724.3	6.28
		105mRh	45s	129.6	
		105Rh	35.36h	306.1 318.9	
103Rh	1.45 1.45	104mRh 104Rh	4.34min 42.3s	555.8 555.8	82 1275
108Pd	39.7 39.7	109mPd 109Pd	4.69min 13.46h	188.9 311.4 309.1 311.4 647.3	2.26 253
		109mAg	39.6s	88	
110Pd	950	111mPd	5.5h	172.2	0.24
107Ag	38.5	108Ag	2.37min	434.0 618.9 633	96
109Ag	6.08	110mAg	249.8d	446.8 620.4 657.8 677.6 687 706.7 708.1 744.3 763.9 818 884.7 937.5 1384.3 1475.8 1505 1562.3	69
	6.08	110Ag	24.6s	657.5	1112
114Cd	207	115Cd 115mIn	53.46h 4.486h	527.9 336.2	8.7
113In	6.41	114mIn	49.51d	190.3 558.4 725.2	224

115In	1.56	116mIn	54.41min	138.3 416.9 818.7 1097.3 1293.5 1507.4 2112.1	2638
112Sn 116Sn	 107 128	113mSn 113Sn 113mIn 117mSn	21.4min 115.1d 1.658h 13.60d	 255.1 391.7 156 158.6 156 158.6	 26 0.336
122Sn	424	123mSn	40.06min	160.3	0.788
124Sn	74.2 74.2	125mSn 125mSn	9.52min 9.64d	331.9 332.1 822.5 1067.1 1087.7 1089.2	7 0.25
121Sb	13.1 13.1	122msb 122Sb	4.191min 2.724d	 564.2 692.7	1.8 209
123Sb	28.2 28.2	124Sb 124mSb	60.2d 93s	1690.98 498.4 602.7 645.8	118 0.93
123Sb	28.2	124Sb	60.20d	602.7	118
127I	57.6	128I	24.99min	442.9	100
133Cs	9.27 9.27	134mCs 134Cs	2.903h 2.065y	127.5 795.85	32.3 390
130Ba	69.9	131Ba	11.50d	496.26	224
132Ba	143	133mBa	38.9h	356.02	4.6
138Ba	15700	139Ba	83.06min	165.85	0.36
139La	76	140La	1.678d	537.31	11.6
140Ce	7200	141Ce	32.51d	145.44	0.48
142Ce	1540	143Ce	33.10h	293.27	1.17
141Pr	296	142Pr	19.12h	1575.6	16.9
146Nd 148Nd	874 236	147Nd 149Nd	10.98d 1.728h	531.01 96.9 97 114.3 155.1 155.9 198 198.9 208.1 211.3 240.2 267.7 270.2 326.6 347.8 349.2 423.6 425.2 540.5 654.8	2.9 12.1
		149Pm	53.08h	286	

150Nd	173	151Nd	12.44min	255.7	11.2
				1180.9	
		151Pm	28.40h	340.1	
152Sm	8.53	153Sm	46.50h	69.7	3168
				103.2	
154Sm	142	155Sm	22.3min	141.4	33.3
				245.7	
151Eu	0.448	152mEu	9.312h	121.8	2764
				344.2	
				841.6	
				963.3	
	0.448	152Eu	13.54y	121.8	5564
				244.7	
				344.3	
				444	
				444	
				778.9	
				867.4	
				963.4	
				964.1	
				1084	
				1085.9	
				1112.1	
				1408	
153Eu	5.8	154Eu	8.593y	248	1738
				591.8	
				723.3	
				756.9	
				873.2	
				996.4	
				1274.4	
152Gd	16.7	153Gd	240.4d	97.4	3000
				103.2	
158Gd	48.2	159Gd	18.56h	363.5	96
160Gd	480	161Gd	3.66min	102.3	5.78
				165.2	
				283.6	
				314.9	
				360.9	
				480.1	
159Tb	18.1	160Tb	72.3d	86.8	426
				197	
				215.6	
				298.6	
				879.4	
				962.3	
				962.3	
				966.2	
				966.2	
				1178	
				1199.9	
				1271.9	
				1312.1	
164Dy	224	165mDy	1.257min	108.2	425
				515.5	
	224	165Dy	2.334h	94.7	517
				279.8	
				361.7	
165Ho	12.3	166Ho	26.83h	80.6	636
				1379.4	
				1581.9	
				1662.5	

170Er	129	171Er	7.516h	111.6 116.7 124 210.1 210.6 237.1 295.9 308.3	39
169Tm 168Yb	4.8 0.61	170Tm 169Yb	128.6d 32.03d	84.3 63.1 109.8 130.5 177.2 198 307.7	1552 31000
174Yb	602	175Yb	4.185d	113.8 137.7 144.9 282.5 396.3	59
176Yb	412	177Yb	1.911h	122.7 139.3 150.6 898.9 941.8 1028.1 1080.2 1119.7 1149.8 1241.2	7.8
175Lu	16.1	176mLu	3.635h	88.4	581
176Lu	0.158	177Lu	6.73d	112.9 208.4	1160
174Hf	29.6	175Hf	70d	343.4	428
178Hf	7.9	179mHf	18.67s	214.3	1039
179Hf 180Hf	16.2 115	180mHf 181Hf	5.5h 42.39d	93.3 215.4 332.3 443.2 500.7 133 133.0 +136.3 136.9 136.3 136.9 345.9 482.2	6.4 34
181Ta	10.4	182Ta	114.4d	67.8 100.1 152.4 222.1 1121.3 1189.1 1221.4 1231	679
186W	20.5	187W	23.72h	134.2 479.6 551.5 618.3 685.7 772.9	530

185Re	3.4	186Re	3.718d	122.6 137.2	1632
187Re	41.1 41.1	188mRe 188Re	18.6min 17.01h	92.4 106 155 478 633 635 633 635 829.5 931.3	9.4 318
184Os 192Os	114 89.7	185Os 193Os	93.6d 30.11h	646.1 138.9 142.1 138.9 142.1 180 181.8 219 219.1 251.6 280.4 298.8 321.6 361.8 387.5 460.5 556 557.4 559.3 560 556.0 +557.4 559.3 560	1554 7.3
193Ir	2.21	194Ir	19.28h	293.5 328.4 645.1 938.7	1380
198Pt	 106	199mPt 199Pt 199Au 199Au	13.6s 30.80min 3.139d 3.139d	 158.4 208.2 158.4 208.2	 60.9
197Au	5.65	198Au	2.695d	411.8	1550
196Hg 202Hg	93.5 1960	197mHg 203Hg	23.8h 46.61d	134 279.2	413 3.8
204Hg		205Hg	5.2min	203.7	0.8
232Th	54.4	233Th 233Pa	22.3min 26.97d	 300.1 311.9 340.5 375.4 398.5 415.8	83.7
238U	16.9	239U 239Np	23.45min 2.357d	74.7 106.1 209.8 226.4 227.8 228.2	284

Fig. 3.6.: Nuclear data for all the elements studied. For some isotopes, data are missing.
$^{(a)}$ are related to data taken from [104].
$^{(b)}$ are related to data taken from [104] and [107].

The second column shows the effective resonance energy, this value can be calculated by ([113] and [104]):

$$\bar{E}_r^{-\alpha} = \frac{I(\alpha)}{I} \tag{3.7}$$

Where I is the reduced resonance integral for a pure $1/E$ epithermal distribution, while $I(\alpha)$ is the resonance integral for an epithermal distribution like $1/E^{1+\alpha}$.
The quantity α is necessarily introduced for considering deviation from the 1/E shape and it is considered energy-independent.
The effective resonance integral can be also calculated as an α-independent expression:

$$ln\bar{E}_r = \frac{\sum_i w_i \, lnE_{r,i}}{\sum_i w_i} \tag{3.8}$$

Being $E_{r,i}$ the different resonances energy and w_i the weighting factors, given by:

$$w_i = \Big(\frac{g\Gamma_\gamma\Gamma_n}{\Gamma}\Big)_i \; \frac{1}{E_{r,i}^2} \tag{3.9}$$

As already mentioned in 1.3.3 the quantity in the weighting factor expression is the kernel of the resonance, strictly related to the effective area of the resonance itself.
For the calculation of the $\bar{E}_r$ data have been taken from [26]. For all the cases where no data were available, experimental determination of $\bar{E}_r$ was carried out [114].
Due to the large number of elements considered, the previously listed criteria were immediately applied to reduce the candidate pool:

- General criteria were employed to exclude toxic, hazardous, or non-solid candidates. In some cases (e.g. Cl) the possibility to obtain compound material allowed to keep in consideration more elements.

- A cutoff on the half-life time was initially set at a minimum threshold of 10 minutes. This threshold was later reconsidered, and some elements of interest were included despite having a shorter half-life time. With the exception of these isolated cases, this time cutoff proved to be satisfactory.

- A maximum half-life limit was also established, set at 7 days.

- Additional selections were applied based on the resonance integral value and the complexity of the gamma spectrum, determined by the number of gamma rays emitted by the activated nucleus. This selection was contingent on the effective resonance energy value. In cases where two or more elements had a similar resonance energy value, the candidate with a lower number of emitted gamma rays was chosen. An effort was made to have at least two elements per order of magnitude in the effective resonance distribution (0-10 eV, 10-100 eV, 100-1000 eV, 1-10 keV, 10-100 keV).

Applying this first criteria, table in figure 3.6 was reduced and a second list of candidates have been produced. Table 3.7 shows the "survived" elements listed by $\bar{E}_r$, since this was clearly the most important parameter toward the final selection:

Isotope	Resonance Energy (eV) [a]	Activated Nucleus [a]	$t_{1/2}$ [a]	E_γ (keV) [a] [b]	I (b) [b]
115In	1.56	116mIn	54.41min	1293.5	2638
193Ir	2.21	194Ir	19.28h	328.4	1380
185Re	3.4	186Re	3.718d	137.2	1632
197Au	5.65	198Au	2.695d	411.8	1550
152Sm	8.53	153Sm	46.50h	103.2	3168
165Ho	12.3	166Ho	26.83h	80.6	636
121Sb	13.1	122msb	4.191min		1.8
	13.1	122Sb	2.724d	564.2	209
175Lu	16.1	176mLu	3.635h	88.4	581
179Hf	16.2	180mHf	5.5h	332.3	6.4
186W	20.5	187W	23.72h	479.6	530
108Pd	39.7	109mPd	4.69min	188.9	2.26
	39.7	109Pd	13.46h	88	253
187Re	41.1	188mRe	18.6min	106	9.4
	41.1	188Re	17.01h	155	318
158Gd	48.2	159Gd	18.56h	363.5	96
127I	57.6	128I	24.99min	442.9	100
79Br	69.3	80mBr	4.421h		32
	69.3	80Br	17.68min	616.3	132.5
139La	76	140La	1.678d	537.31	11.6
192Os	89.7	193Os	30.11h	138.9	7.3
196Hg	93.5	197mHg	23.8h	134	413
75As	106	76As	26.24h	559.1	52.5
81Br		82mBr	6.13min		34
	152	82Br	35.30h	554.3	50
71Ga	154	72Ga	14.10h	630	30.6
114Cd	207	115Cd	53.46h	527.9	8.7
		115mIn	4.486h	336.2	
164Dy	224	165mDy	1.257min	108.2	425
	224	165Dy	2.334h	279.8	517
98Mo	241	99Mo	65.94h	181.1	7
		99mTc	6.01h	140.5	
141Pr	296	142Pr	19.12h	1575.6	16.9
96Zr	338	97Zr	16.74h	355.4	5.3
		97mNb	52.7s	743.4	
		97Nb	72.1min	657.9	
87Rb	364	88Rb	17.78min	898	2.4
176Yb	412	177Yb	1.911h	150.6	7.8
122Sn	424	123mSn	40.06min	160.3	0.788
55Mn	468	56Mn	2.579h	846.8	13.9
104Ru	495	105Ru	4.44h	262.8	6.28
		105mRh	45s	129.6	
		105Rh	35.36h	306.1	
76Ge	583	77mGe	52.9s	159.7	1
	583	77Ge	11.30h	211	2
68Zn	590	69mZn	13.76h	438.6	0.223
100Mo	672	101Mo	14.61min	191.9	3.77
96Ru	776	97Ru	2.9d	215.7	6.12
86Sr	795	87mSr	2.803h	388.5	3.2
63Cu	1040	64Cu	12.70h	511	4.88
142Ce	1540	143Ce	33.10h	293.27	1.17
30Si	2280	31Si	2.622h	1266.2	0.106
41K	2960	42K	12.36h	1524.7	1.41
23Na	3380	24Na	14.96h	1368.6	0.303
74Ge	3540	75mGe	47.7s	139.7	0.35
	3540	75Ge	82.78min	198.6	
89Y	4300	90mY	3.19h	202.5	0.006
64Ni	14200	65Ni	2.517h	1115	1.13
138Ba	15700	139Ba	83.06min	165.85	0.36

Fig. 3.7.: Elements survived after the selections. The main gamma energy is shown, for the complete list see tables in 3.6

3.2.2 Monte Carlo simulations

One of the main challenges developing NCT-ACS is to make a device sensitive to the epithermal neutron energy range. Therefore, special attention has been given to making this instrument insensitive to thermal neutrons. This consideration is due in part to the fact that, in most cases, the neutron capture cross-section in the thermal range assumes values that are equal to or even higher than resonance integrals. Moreover the thermal fluence rate can be easily measured with a standard sub-Cd subtraction technique [115] with passive detectors (section 5.1), or using a calibrated active detector. Without proper shielding of the instrument from thermal neutrons, it would have been even more complicated to extract the data of interest, as the final activity would have been generated by both thermal and epithermal neutrons simultaneously. To mitigate this problem, a cadmium shield would be placed around the elements. The capture cross-section of cadmium in the thermal range allows us to consider this energy component almost completely suppressed. As previously mentioned in section 1.1, an energy value of 0.4 eV is typically used as the threshold to discriminate between the thermal and epithermal ranges, corresponding to the drop in the neutron absorption cross-section of cadmium. For illustrative purposes, figure 3.8 shows the capture cross-section of ^{113}Cd, which represents 13.47% of the natural isotopic abundance and contributes significantly to the absorption cross-section with a massive value of σ_γ^0=20615(400) b [26]:

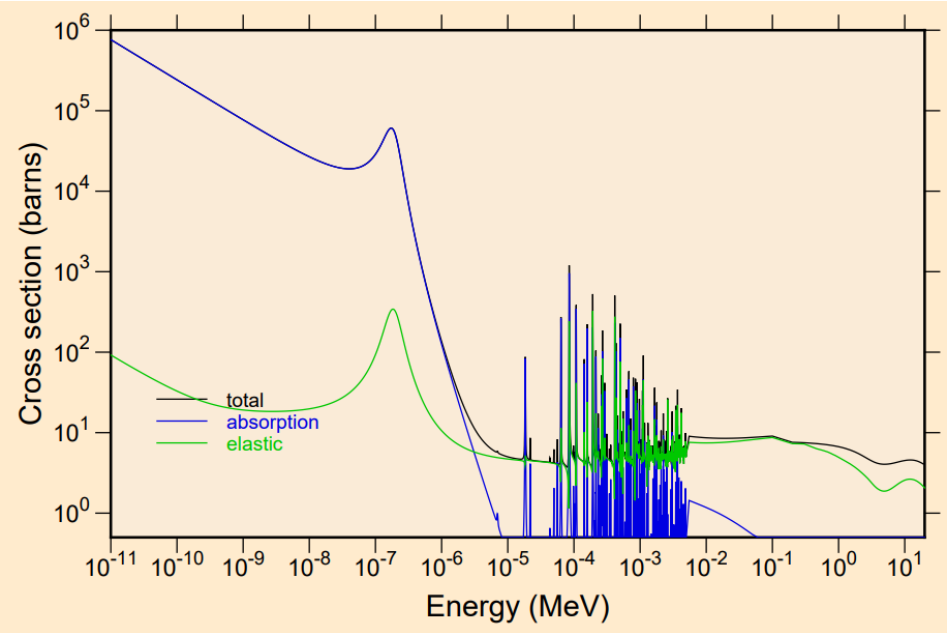

Fig. 3.8.: Neutron cross sections for ^{113}Cd, the drop at around 0.4-0.5 eV is taken as reference to separate thermal from epithermal neutron. The plot is taken from [103].

To evaluate the induced activity in the selected elements, an analytical approach can be considered. In particular, to determine the total activation rate induced by a specific neutron field with fluence rate distribution $\dot{\Phi}(E)$ on a given element characterized by a cross-section $\sigma(E)$, equation 3.3 can be used. This approach is certainly correct, but in order to accurately account for the presence of cadmium shielding, some corrective factors should be calculated through Monte Carlo (MC) simulations. Moreover, considering only the capture phenomenon and neglecting the multiple interactions of neutrons inside the other foils is, in a way, a simplified approach. Under these conditions and with the idea that the final geometry of NCT-ACS would feature multiple elements together, organized in a more complex geometry, a study using Monte Carlo modeling has been chosen.

For this purpose, foils of the elements shown in table 3.7 were simulated using the MCNP6 simulation code [116]. In particular, all simulations were implemented as follows:

- Squared foils of different elements selected in 3.7 with dimensions: 10 mm x 10 mm x 0.1 mm;
- 0.5 mm of ^{nat}Cd shield covering the foils;
- Monochromatic neutron sources ranging from 1.5 meV up to 1.16 MeV;
- The capture (n,γ) reaction rate inside the foils has been studied in function of the produced neutron energy;

The output of these simulations was helpful to determine whether the values of the effective resonance energies were correct or if there were other structures in the cross-section that could potentially pose issues for the ultimate goal. In particular, the aim is to avoid using elements with noticeable continuous structures in the epithermal region to be as sensitive as possible to a narrow energy range for each individual element.

Figures 3.10 and 3.9 show the results for two studied elements. For all the other elements, please refer to appendix A.
The x-axis is in logarithmic scale, since the plots are covering nine order of magnitude in energy. On the y-axes is shown the quantity $R(E)$ that corresponds to the number of capture reaction normalized for source particle. It should be noted that this quantity will be also called as "**response**" in this work. In fact, it represents how the system respond to neutron energy.

The single plot will be also called "**response curve**" and the ensemble of more plots will be called "**response curves**" or "**response matrix**". Such nomenclature is quite often used in neutron physics (e.g. [117]).

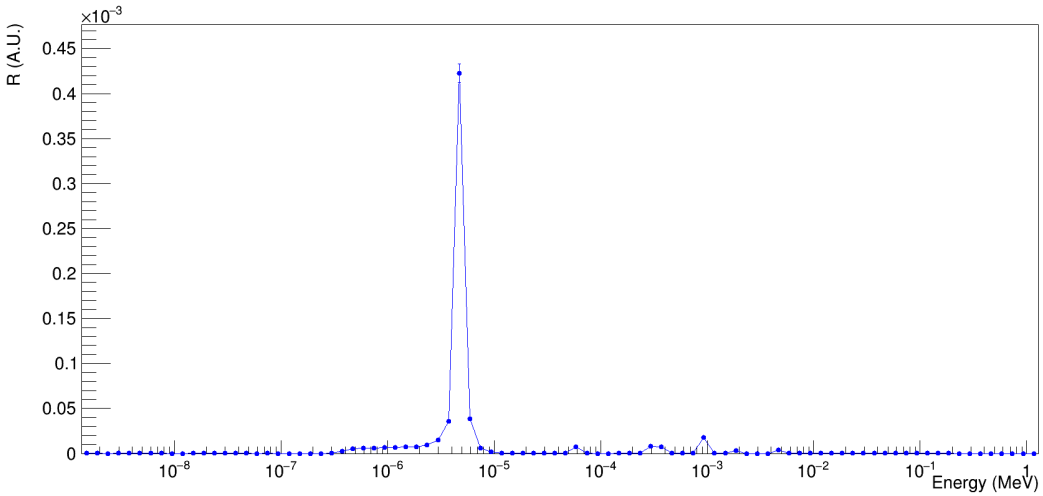

Fig. 3.9.: Response curve for element ^{197}Au calculated with MCNP6.

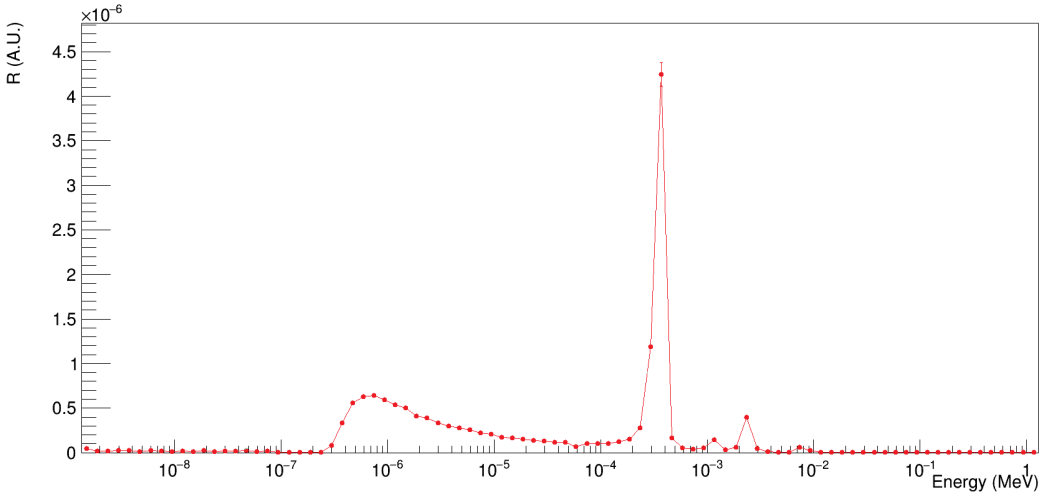

Fig. 3.10.: Response curve for element ^{55}Mn calculated with MCNP6.

As can be clearly seen, the resonance structure is clearly visible as a massive peak in the response curves. On the other hand, the absolute capture rate reaction is very different between Au and Mn (both of them are mono-isotopic still in the natural abundance). The response for the gold foil at its peak is around $0.45 \cdot 10^{-3}$ (A.U.), while for the manganese foil is around $0.45 \cdot 10^{-5}$ (A.U.).
That means that, assuming a flat epithermal neutron spectrum, to obtain the same activity for manganese a thickness 100 times higher is required. In this case a 0.1 mm thick gold foil is more or less equivalent to a 1 cm thick manganese foil.
Figure 3.11 show the response curves for all the selected elements in table 3.7. The

data have been normalized to the integral of the different curves, therefore any curve in this plot has an area equal to 1. This is useful to appreciate the different shape and peaks. Otherwise, plotting the data without any normalization the result would be highly messy, even in a log-log scale.
It should be noted that many curves are characterized by peaked structures that involve a single energy bin. This happens in the case that a resonance is included within a single bin and, therefore, the capture rate for that energy bin dramatically increases.
The choice of binning was calibrated to allow for comparison with previous Monte Carlo simulations and measurements conducted in the facilities used for the experiments.

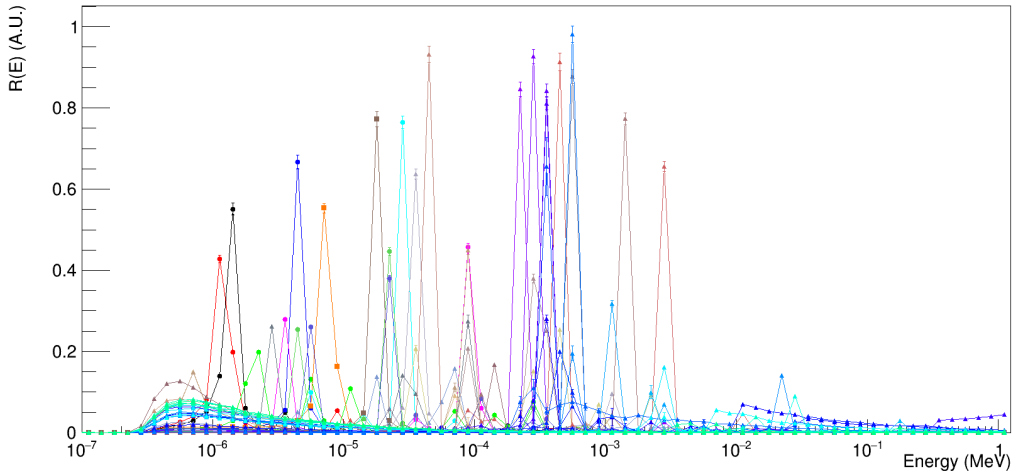

Fig. 3.11.: Response curves for all the elements shown in table 3.7. The legend is not shown since this plot is only for qualitative considerations.

One of the main NCT-ACS goal listed before was to obtain a system able to work in single neutron irradiation to reduce the total time required. A significant difference in the foils thicknesses would not allow to fulfill this requirement while maintaining compact dimensions for the final geometry. Fortunately, it is not necessary to have exactly the same activities among the different elements. However, with the aim of being able to perform a correct and short measurement with the gamma spectrometer, it would be enormously advantageous to have activity values that are similar between each others. In fact, high activity results in an increase in the detector dead time, causing problems during data analysis. Therefore, significantly different activity values would in someway compromise the success of the measurement. Attempting to increase the activity of elements with a lower response would result in excessively high activity in elements with a higher response, creating a hardly manageable disparity.

3.2.3 The final elements selection

In order to perform the last selection, two parameters were mainly taken into account:

- Effective resonance energy.
- Expected activity values after irradiation.

In particular, the second criterion was estimated knowing that after an irradiation time t_{irr} the activity of the foil can be written as:

$$A(t_{irr}) = A_r(1 - e^{-\lambda t_{irr}}) \tag{3.10}$$

Where $\lambda = 1/\tau$is the decay constant of the activated element.
In the condition of a long irradiation ($t_{irr} >> \tau$), the saturation condition is reached, the number of active nuclides produced in the unit of time is equal to the decays number, A=A_r, and the equilibrium is achieved.
As already shown in equation 3.3 the activation rate A_r can be calculated knowing the fluence rate distribution and the cross section in energy.
In this case, instead of the cross section, the response curve, normalized respect the atomic density, was used. The equation can be rewritten as:

$$A_r = N \sum_i \dot{\Phi}(E)_i R_i(E) \Delta E_i \tag{3.11}$$

Where i represents the i-th energy bin and the summation over i is performed from 1.5 meV up to 1.16 MeV, where the response curves are defined.
The fluence rate $\dot{\Phi}(E)$ used for this calculation refers to the e-LiBaNS neutron source [118] in Torino. A more in-detail description of this facility was provided in section 2.7.1.
As the irradiation time may not consistently meet the condition $t_{irr} >> \tau$, the value A_r holds the role of upper limit for numerous elements. The actual activity, as indicated in equation 3.10, necessitates an additional adjustment to account for the time interval elapsed between the conclusion of irradiation and the starting of measurement using the gamma detector (t_{wait}). The modified formula become:

$$A(t_{irr}, t_{wait}) = A_r(1 - e^{-\lambda t_{irr}})e^{-\lambda t_{wait}} \tag{3.12}$$

In order to obtain the final estimate of activity, equations 3.11 and 3.12 were combined. The results of this combination can be seen in table 3.12 under the A_f column. It is essential to note that this table provides an estimate for an irradiation time of $t_{irr} = 1800$ s and a subsequent waiting time of $t_{wait} = 600$ s.

Isotope	Resonance Energy (eV) [a]	Activated Nucleus [a]	$t_{1/2}$ [a]	E_γ (keV) [a] [b]	I (b) [b]	$A_f\,(Bq)$	$\sigma_f\,(Bq)$
115In	1.56	116mIn	54.41min	1293.5	2638	11507	240
193Ir	2.21	194Ir	19.28h	328.4	1380	312	5
185Re	3.4	186Re	3.718d	137.2	1632	51	1
197Au	5.65	198Au	2.695d	411.8	1550	116	3
152Sm	8.53	153Sm	46.50h	103.2	3168	223	4
165Ho	12.3	166Ho	26.83h	80.6	636	225	3
121Sb	13.1	122msb	4.191min		1.8	1821	37
	13.1	122Sb	2.724d	564.2	209		
175Lu	16.1	176mLu	3.635h	88.4	581	1540	22
179Hf	16.2	180mHf	5.5h	332.3	6.4	654	9
186W	20.5	187W	23.72h	479.6	530	104	3
108Pd	39.7	109mPd	4.69min	188.9	2.26	30.7	0.6
	39.7	109Pd	13.46h	88	253		
187Re	41.1	188mRe	18.6min	106	9.4	67.8	0.8
	41.1	188Re	17.01h	155	318		
158Gd	48.2	159Gd	18.56h	363.5	96	35.8	0.8
127I	57.6	128I	24.99min	442.9	100	1079	19
79Br	69.3	80mBr	4.421h		32	208	3
	69.3	80Br	17.68min	616.3	132.5		
139La	76	140La	1.678d	537.31	11.6	1.32	0.04
192Os	89.7	193Os	30.11h	138.9	7.3	1.81	0.04
196Hg	93.5	197mHg	23.8h	134	413	356	6
75As	106	76As	26.24h	559.1	52.5	178	5
81Br		82mBr	6.13min		34	3.00	0.05
	152	82Br	35.30h	554.3	50		
71Ga	154	72Ga	14.10h	630	30.6	19.7	0.3
71Ga	154	72Ga	14.10h	630	30.6	1.34	0.03
164Dy	224	165mDy	1.257min	108.2	425	1741	18
	224	165Dy	2.334h	279.8	517		
98Mo	241	99Mo	65.94h	181.1	7	7.32	0.20
		99mTc	6.01h	140.5			
141Pr	296	142Pr	19.12h	1575.6	16.9	33.2	1
96Zr	338	97Zr	16.74h	355.4	5.3	0.58	0.01
		97mNb	52.7s	743.4			
		97Nb	72.1min	657.9			
87Rb	364	88Rb	17.78min	898	2.4	16.7	0.4
176Yb	412	177Yb	1.911h	150.6	7.8	5.80	0.27
122Sn	424	123mSn	40.06min	160.3	0.788	0.73	0.01
55Mn	468	56Mn	2.579h	846.8	13.9	52.5	0.7
104Ru	495	105Ru	4.44h	262.8	6.28	0.18	0.04
		105mRh	45s	129.6			
		105Rh	35.36h	306.1			
76Ge	583	77mGe	52.9s	159.7	1	0.09	0.02
	583	77Ge	11.30h	211	2		
68Zn	590	69mZn	13.76h	438.6	0.223	0.73	0.03
100Mo	672	101Mo	14.61min	191.9	3.77	12.5	0.9
96Ru	776	97Ru	2.9d	215.7	6.12	0.86	0.04
86Sr	795	87mSr	2.803h	388.5	3.2	172	4
63Cu	1040	64Cu	12.70h	511	4.88	2.72	0.05
142Ce	1540	143Ce	33.10h	293.27	1.17	0.29	0.02
30Si	2280	31Si	2.622h	1266.2	0.106	0.23	0.03
41K	2960	42K	12.36h	1524.7	1.41	0.59	0.06
23Na	3380	24Na	14.96h	1368.6	0.303	0.15	0.02
74Ge	3540	75mGe	47.7s	139.7	0.35	2.25	0.07
	3540	75Ge	82.78min	198.6			
89Y	4300	90mY	3.19h	202.5	0.006	1.93	0.08
64Ni	14200	65Ni	2.517h	115.5	1.13	3.03	0.12
138Ba	15700	139Ba	83.06min	165.85	0.36	1.18	0.09

Fig. 3.12.: Elements survived after the selection with the expected activity value for a 10 mm x 10 mm x 0.1 mm foil. Irradiation parameters: $t_{irr} = 1800$ s, $t_{wait} = 600$ s at the e-LiBaNS facility.

As previously mentioned, the simulated foils were characterized by dimensions of 10 mm x 10 mm x 0.1 mm. The final values achievable using NCT-ACS may vary significantly depending on the foil thicknesses and the specific geometry employed, making these values preliminary estimates.

With a complete list of elements and relevant parameters, it became possible to select the ideal candidates, which were categorized into two groups based on their characteristics. This further classification involved applying cost and machinability criteria, as explained in the preceding section 3.2.

Tables 3.13 ad 3.14 show the final selection of the elements. Two elements, V and

Ca, have been included in the final selections, although they were not considered in the initial stages. This was because candidates with an effective resonance energy beyond 1 keV exhibited less-than-optimal characteristics for the intended application. Therefore, V and Ca were reintroduced into the list, despite their earlier exclusion due to their short half-lives (less than 10 min). In particular, in the case of vanadium, its inclusion was also based on its affordability, isotopic purity, and ready availability.

Isotope	Resonance Energy (eV) [a]	Activated Nucleus [a]	$t_{1/2}$ [a]	E_γ (keV) [a] [b]	I (b) [b]	$A_f\,(Bq)$	$\sigma_f\,(Bq)$
115In	1.56	116mIn	54.41min	1293.5	2638	11507	240
185Re	3.4	186Re	3.718d	137.2	1632	51	1
197Au	5.65	198Au	2.695d	411.8	1550	116	3
186W	20.5	187W	23.72h	479.6	530	104	3
187Re	41.1 41.1	188mRe 188Re	18.6min 17.01h	106 155	9.4 318	67.8	0.8
55Mn	468	56Mn	2.579h	846.8	13.9	52.5	0.7
63Cu	1040	64Cu	12.70h	511	4.88	2.72	0.05
23Na	3380	24Na	14.96h	1368.6	0.303	0.15	0.02
51V	7230	52V	3.75min	1434.1	2.63	42.3	0.8
37Cl	13700	38Cl	37.24min	1642.7	0.29	0.12	0.01

Fig. 3.13.: Final selection of elements for NCT-ACS. Best candidates.

Isotope	Resonance Energy (eV) [a]	Activated Nucleus [a]	$t_{1/2}$ [a]	E_γ (keV) [a] [b]	I (b) [b]	$A_f\,(Bq)$	$\sigma_f\,(Bq)$
193Ir	2.21	194Ir	19.28h	328.4	1380	312	5
175Lu	16.1	176mLu	3.635h	88.4	581	1540	22
127I	57.6	128I	24.99min	442.9	100	1079	19
141Pr	296	142Pr	19.12h	1575.6	16.9	33.2	1
100Mo	672	101Mo	14.61min	191.9	3.77	12.5	0.9
142Ce	1540	143Ce	33.10h	293.27	1.17	0.29	0.02
48Ca	1330000	49Ca	8.7 min	3084.54	0.5	0.17	0.03

Fig. 3.14.: Final selection of elements for NCT-ACS. Good candidates.

It should be noted that many other elements showed interesting characteristics, but for different reasons they were excluded to the benefit of other candidates, with even more interesting characteristics.

Below is shown the list of elements classified as "best", along with an explanation of why they were included in this category, including their main pros and cons:

- ^{115}**In:**

  PROS: high expected activation and consequently good statistic, high isotopic abundance, high gamma B.R. (85%), low cost.

  CONS: many gammas emitted, the massive activation rate force to have very thin foil.

- ^{185,187}**Re:**

  PROS: double elements in a single foil, quite high expected activation and consequently good statistic.

  CONS: high cost, low gamma B.R. (9% and 15%), due to the isotopic fractions thicker foil is required, toxicity is unknown, long half life time for ^{187}Re.

- ^{197}**Au:**
  PROS: high expected activation and consequently good statistic, isotopic purity, very well known cross sections, single gamma emission with high B.R. (100%), good malleability.

  CONS: expensive.

- ^{186}**W:**
  PROS: high expected activation and consequently good statistic, quite high gamma B.R. (23%), low cost.

  CONS: only 28.43% isotopic abundance therefore thicker foil is required , many gammas emitted.

- ^{55}**Mn:**
  PROS: quite high expected activation and consequently good statistic, high isotopic abundance, high gamma B.R. (99%), low cost.

  CONS: poor machinability therefore alloy is required.

- ^{63}**Cu:**
  PROS: low cost, single gamma emission with quite high gamma B.R. (38%).

  CONS: low expected activation.

- ^{23}**Na:**
  PROS: high energy neutron sensitivity, isotopic purity, single gamma emission with high gamma B.R. (100%).

  CONS: low expected activation, water reactive and low toxicity.

- ^{51}**V:**
  PROS: very high energy neutron sensitivity, isotopic purity, single gamma emission with high B.R (100%), low cost

  CONS: short half life time, low expected activity

It should be noted that, in some cases, certain issues have been identified concerning the selected elements. This aspect is due to the fact that finding the perfect candidate is challenging, as each sample has its imperfections.
Gold is without any doubts one of the best candidates, with its capture cross-section

being measured with great precision, as previously reported by Dilg et al. [109].
Rhenium and tungsten were initially placed in the second-choice list 3.14 but were later moved to the list of top candidates to improve the measurement precision with NCT-ACS. For some measurements and Monte Carlo simulations, therefore, they were not included.
Due to its toxicity and hazards, sodium was initially rejected but reconsidered due to the possibility of using it in combination with chlorine (NaCl). This compound is hygroscopic but entirely harmless and very cost-effective, making it a viable alternative. In this way, chlorine (Cl) was also introduced, which was initially excluded because it is highly dangerous in its gaseous form at room temperature.

For illustrative purposes, the reasons for the exclusion of certain elements that were particularly interesting due to specific characteristics are also presented. These elements are not included in either of the two lists shown.

- ^{164}**Dy:**
  This element is characterized by a massive expected activation, due to a high resonance integral value. The half life time is quite long to perform measurements and the cost of the material itself is not very high.
  On the other side, the isotopic abundance of ^{164}Dy is only 28% and the B.R. for the main gamma emission is only 3%. These characteristics involve having to use a large thickness. The combination of ^{55}Mn and ^{187}Re was used to cover the energy region between 40 eV and 400 eV (effective resonance energy parameter).

- ^{75}**As:**
  This element was one of the most interesting due to its characteristics. However, it was initially discarded because of its toxicity but was later reintroduced when combined with gallium (another interesting element) in a compound commonly used in photovoltaic cells: GaAs.
  Nevertheless, this compound presents certain issues, primarily its high fragility, which made it impractical for some measurements. Despite its good features, it was not utilized in this study but remains a promising candidate for potential future developments.

- ^{64}**Ni:**
  Nickel possessed all the qualities to be an excellent candidate. It exhibited a high-energy sensitivity peak (at around 10 keV) and it is a low-cost material with low toxicity. Unfortunately, the required isotope is only present in 0.9% of the total fraction. This would have necessitated a substantial cost to obtain significant enrichment. Even with 100% enrichment, the expected activity

would have been comparable to that of copper-63, which is already considered quite low. For this reason, ^{64}Ni was excluded.

- **^{30}Si:**
  As already mentioned before, ^{30}Si presented good characteristics, being sensitive to high energy neutron (peak in the response at around 2 keV). Due to the low isotopic abundance (only 3.1%) and to the very low B.R. for gamma emission (below 0.1%). The necessary thickness would have been too high to match the required compact dimensions of NCT-ACS. For these reasons this element has been discarded.

A comprehensive discussion of all elements is beyond the scope of this work. It is obvious that other elements could potentially replace some of the chosen ones, but they were considered less interesting than those remaining in the final selection.

For potential future developments, a second selection of elements could be performed with a clear understanding of how the various factors listed in this section may impact the final measurement.

3.3 The choice of the geometry

In this section, the process leading to the development of the final geometry for NCT-ACS is described. The initial concept involved spherical shells of various elements enclosed within a cadmium shell. While this idea was intriguing, it proved to be impractical.
Firstly, not all the selected elements could withstand such processing.
Secondly, this geometry would have been fragile and prohibitively expensive.
Finally, calculating the absolute activity of a foil with such a particular, three-dimensional geometry would have posed an enormous challenge. For these reasons, the initial concept was quickly abandoned, and alternative solutions of more practical feasibility were explored.
Throughout the extensive development process of NCT-ACS, numerous geometries were considered. Some of these are not detailed here, as they either proved unsuccessful or exhibited a level of complexity rendering the use of the instrument impractical.
One of the more exotic geometries explored involved a regular tetrahedral pyramid with a spherical moderator placed at each vertex and the various foils placed inside the different spheres. This geometry took inspiration from the methane molecule and its high degree of symmetry (fig. 3.15), which could have ensured the isotropic instrument response. However, it became evident quite early that this geometry was incompatible with the need to develop a compact and easily manageable instrument.

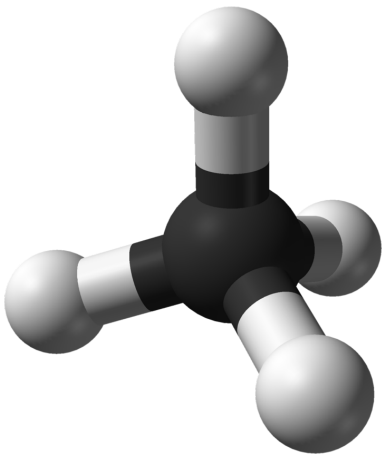

Fig. 3.15.: Scheme of a methane molecule. The spatial organization was taken as inspiration for exploring a specific geometry. This geometry was then discarded due to its complexity and difficulty for matching the small dimension required by NCT-ACS.

3.3.1 First geometry study

The initial and most simple geometry considered was a set of foils (referred to as a "sandwich") placed inside a hollow cadmium cylinder with a thickness of 0.5 mm. The scheme of this geometry is illustrated in figure 3.16

The initial analysis involved recalculating response curves for the scenario in which all the foils were placed together. In this configuration, the real isotopic abundances were incorporated, as none of the selected elements required enrichment for practical use. Moreover, the foils dimensions in the simulations matched those of the foils purchased, as detailed in table 3.1. The indicated thickness values were evaluated and chosen considering not only the foil thickness but also factors related to the real isotopic abundances and the circular shape of the foils used.
The formula for correcting the values shown in table 3.13 is as follows:

$$A(t_{irr}, t_{wait})^* = A(t_{irr}, t_{wait}) \cdot F_{is} \cdot \frac{V^*}{V} \frac{A_r^*}{A_r} \tag{3.13}$$

Where $A(t_{irr}, t_{wait})$ is the activity value extracted from 3.5, F_{is} is the isotopic fraction, V^*/V represents the correction due to the different volume and A_r^*/A_r represents the correction due to the different activation rate (extracted by the Monte Carlo simulations).

Element	Diameter (cm)	thickness (μm)	Mass (g)	Number of foils
In	0.635	127	∼0.1249	1
Au	0.635	51	∼0.123	2
Mn	0.635	51	∼0.037	4
Cu	0.635	127-254	∼0.144-0.288	8-4
Na	0.635	1905	∼0.482	2
V	0.500	500	∼0.249	1-2
Re	0.600	1000	∼2.619	1
W	0.625	1000	∼2.416	1

Tab. 3.1.: Foils dimensions and mass. The number in the last column refers to the total number of foils implemented in the simulations and in the measurements.

The very first study on this simple geometry was dedicated to the angular response of a single sub-Cd sandwich. One of the request for NCT-ACS is the isotropy, therefore, no dependence on the incoming neutron angle should be obtained. Using the

geometry shown in figure 3.16, the incoming neutron beam was modified in order to impinge on the geometry at different angles ranging from -90° up to 90°, with step of 15°. Where the angle of 90° correspond to neutrons perpendicular respect to the foil surfaces, while an angle of 0° correspond to neutrons travelling parallel to the surfaces themselves.

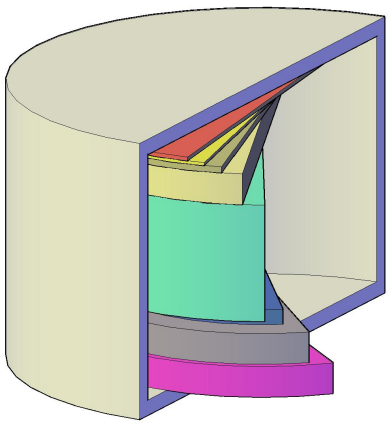

Fig. 3.16.: Scheme of the first geometry. The different foils are form top to bottom: In, Au, Mn, Cu, NaCl, V, Re, W.

In order to evaluate the isotropy of the system, the values of A_r have been extracted by Monte Carlo simulations for all the angles of the incoming neutrons.
From a geometrical point of view, the dependence of A_r by the angle should be described by a sinusoidal function. Otherwise, on the case of a pure isotropic response, the fitting function should be a constant.

A first approach was based on fitting the A_r distribution with a sinusoidal fit in the form of:

$$A_r(\theta) = |A_0 + B \cdot sin(C \cdot \theta + D)| \tag{3.14}$$

Being A_0 the minimum activation rate expected for incoming neutron forming an angle of 0° degrees respect to the the surface.
The parameter C should be, in principle, close to 1 since the geometry should be characterized by symmetry for rotation of π radians respect to the foils axes (neglecting the absorption contributes due to the other foils). In this analysis, it was not fixed. In fact, for isotropic response C should be close to 0 and the function become simply a constant.
It should be noted that the absolute function allows describing simultaneously the positive and negative angle condition. Unfortunately, the assumption of symmetry between negative and positive angles was noted to be completely unsatisfactory.
Thus the two angular regions, respectively positive and negative values, were distinguished and the formula 3.14 has been modified, removing the absolute value.

Nevertheless, during the fitting procedure, some issues have been encountered, since in some cases, the sinusoidal fit was absolutely not adequate to approximate the set of data. In particular for certain foils, the sinusoidal function was able to approximate data for negative angles, but not for positive ones.
A polynomial fitting approach was also explored, but the absence of physical means for using this distribution and the high χ^2 values obtained in some cases, led to abandon this option.
Figures 3.17 - 3.18 and 3.19 - 3.20 show different situations for better understanding the problems encountered during the fit approach.

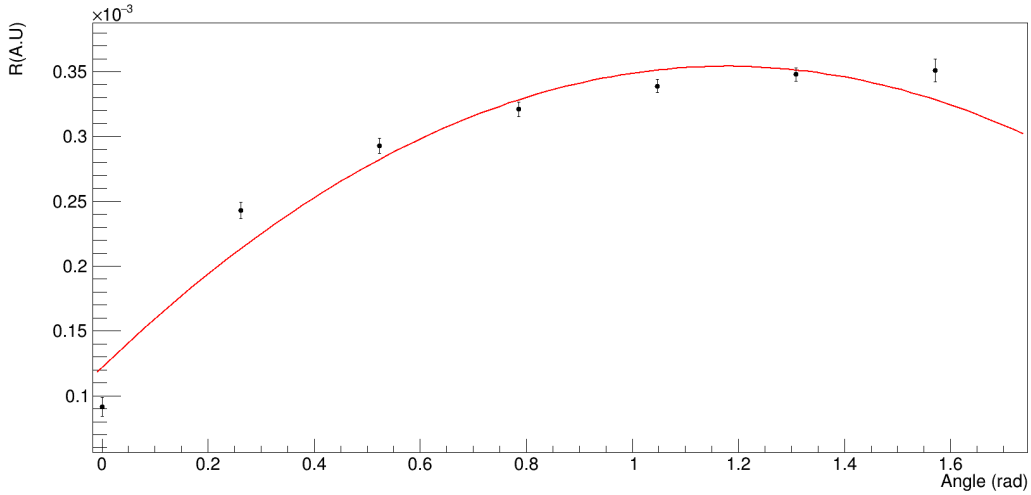

Fig. 3.17.: Angular behaviour on the activation rate for gold foil for positive angles. The sinusoidal fit does not adequately approximate the distribution ($\chi^2 = 20 \gg \chi^2_{crit}$).

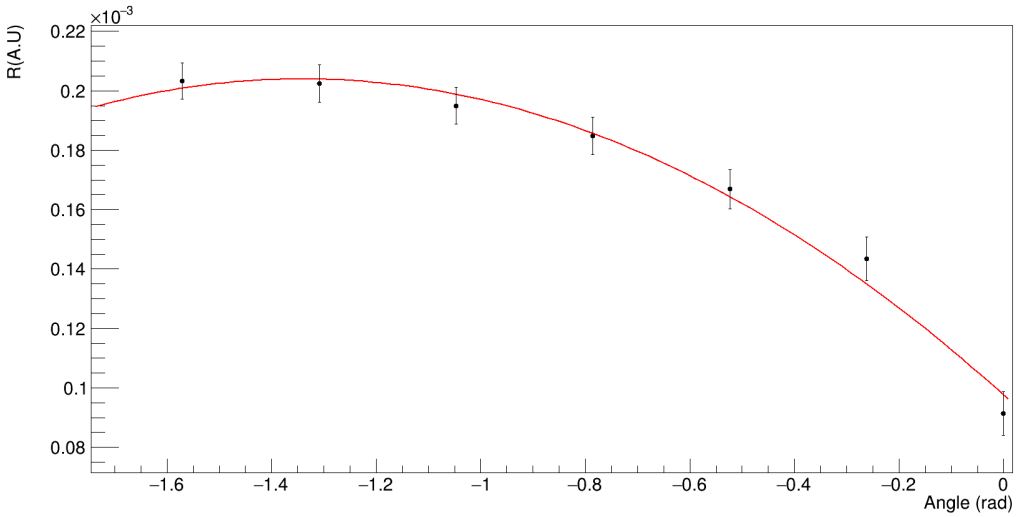

Fig. 3.18.: Angular behaviour on the activation rate for gold foil for negative angles. The sinusoidal fit perfectly approximate the distribution ($\chi^2 = 2.8 < \chi^2_{crit}$).

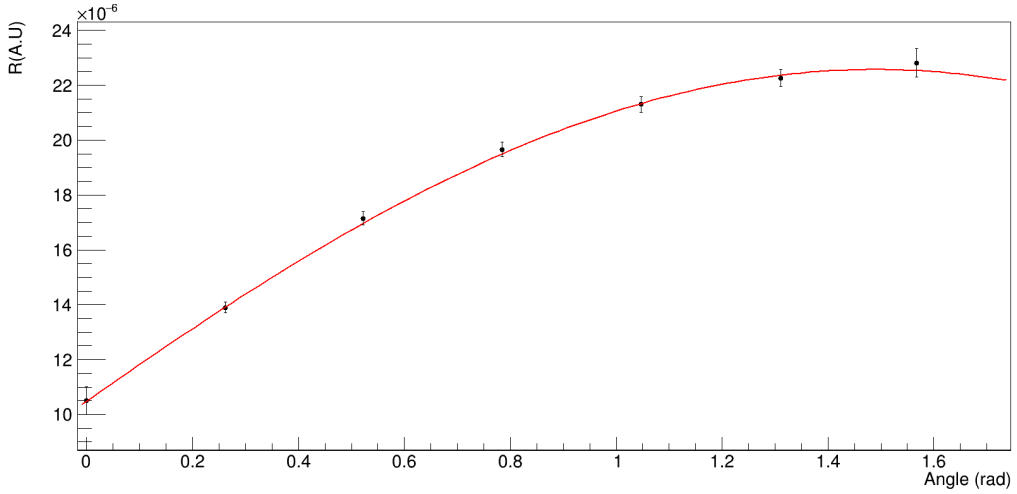

Fig. 3.19.: Angular behaviour on the activation rate for manganese foil for positive angles. The sinusoidal fit perfectly approximate the distribution ($\chi^2 = 0.5 < \chi^2_{crit}$).

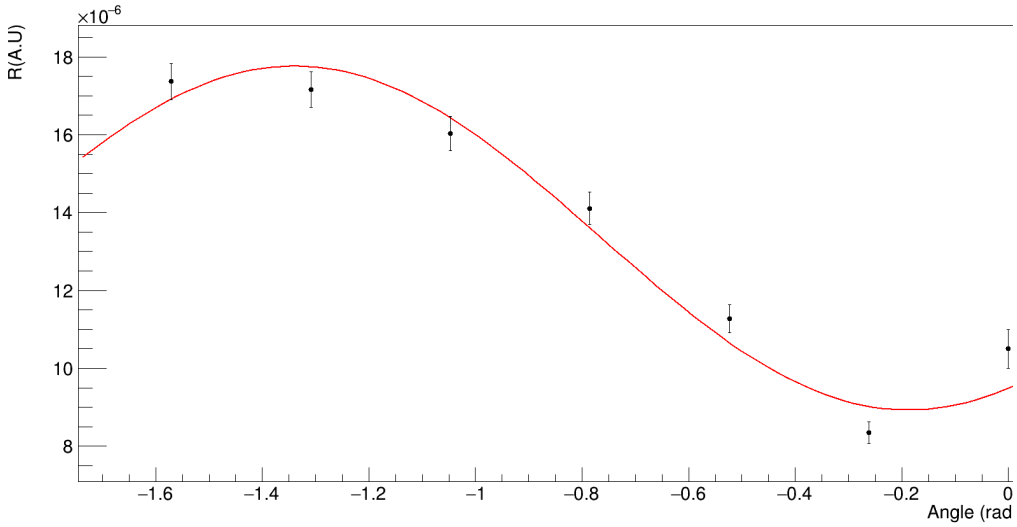

Fig. 3.20.: Angular behaviour on the activation rate for manganese foil for negative angles. The sinusoidal fit does not adequately approximate the distribution ($\chi^2 = 17.9 \gg \chi^2_{crit}$).

The absence of a single model curve to fit the data led to the decision to use the average value as the best estimator for the subsequent analysis. In fact, it can be noted that, starting from the average integral definition:

$$\bar{A}_r = \frac{1}{\Delta\theta} \int_0^{\Delta\theta} A_r(\theta)\, d\theta \tag{3.15}$$

And discretizing the formula:

$$\bar{A}_r = \frac{1}{\Delta\theta_{tot}} \sum_i A_{r\,i} \Delta\theta_i \tag{3.16}$$

The second expression, represents the weighted mean. The knowledge of the $A_r(\theta)$ function is not longer needed and the discrete value can be calculated.
Since the Monte Carlo simulations were performed maintaining a binning of 15°, the value of $\Delta\theta_i$ is constant and can be called $\Delta\theta$. Formula 3.16 can be rewritten as:

$$\bar{A_r} = \frac{\Delta\theta}{\Delta\theta_{tot}} \sum_i A_{r\,i} = \frac{1}{n} \sum_i A_{r\,i} \tag{3.17}$$

Where it can be noted that in the last formula, the definition of mathematics mean is obtained (n is the number of angular bins).
Once the value of $\bar{A_r}$ is obtained, the variable m is defined as:

$$m_i = A_i - \bar{A_r} \tag{3.18}$$

Invoking the central limit theorem, the m variable can be considered to be gaussian, with mean value $\bar{m} = 0$.

When possible ($\chi^2 < \chi^2_{crit}$), a comparison between the mean integral extracted by the fit and the mean value has been performed. In these cases the difference between the two estimations were calculated to be under 2%.
It should be noted that using sinusoidal together with polynomial and other fitting models (e.g. sigmoidal), probably could result in providing the χ^2 compatibility for all the data set. Nevertheless, the impossibility to correctly fit all the set of data with the same model could introduce a bias in the analysis (due to the arbitrariness in using a function instead of another one). This provides an evidence on the best significance using the mean value as the best estimator.
The quantity Ψ has been introduced and defined as:

$$\Psi_i = \frac{A_i - \bar{A_r}}{\bar{A_r}} \tag{3.19}$$

Since the numerator quantity is gaussian and the denominator is simply a normalization factor, variable Ψ is also gaussian and its standard deviation represents how much in percentage the A_i values are widespread over the mean value $\bar{A_r}$.
Thus, the anistropy of the system has been called Λ, with $\Lambda = 1.96 \cdot \sigma_\Psi$. With this definition, a threshold on anisotropy represents the maximum value within which the 95% of the A_r values are included.
The 3% value as been fixed in order to do not make hard assumption on the isotropic response of the system, this value will be considered in the total systematic uncertainty:

$$\Lambda = 1.96\,\sigma_\Psi = 3\% \tag{3.20}$$

The values of Λ are shown in table 3.2:

Element	Anisotopy Λ (%)
In	49.9
Au	32.9
Mn	13.4
Cu	7.68
Na	6.26
Cl	8.94
V	7.87
^{185}Re	5.73
^{187}Re	3.80
W	5.60

Tab. 3.2.: Anistropy parameter values for a single sub-Cd sandwich.

In figures 3.21 and 3.22 the changes due to the different angles can be seen in two different cases: Au and Na. The graphs display the two most distinct cases, namely 0 and 90 degrees. For all other angular values, an intermediate response curve is obtained.
In the In case, a rather significant modification in the curve's shape can be observed, with the maximum peak decreasing noticeably and deforming, broadening.
On the opposite side, in the case of Na, a different behavior is observed, where the main peak is lowered but not significantly deformed. Even the large bell-shaped distribution, peaked at around 1 eV, remains relatively unaffected.

This difference between the two elements can be explained by considering two factors of different nature:

1. The two foils have different thicknesses. The Na one is approximately 30 times greater than that of In. From a geometric point of view, this has a significant impact. In the limit case of a foil where the thickness is comparable to its surface area, anisotropy should be close to 0 (better spherical approximation).

2. The resonance energies of the two elements are significantly different (1.56 eV for In and 3380 eV for Na). This indicates that the scattering and energy loss phenomena of neutrons in other foils or the cadmium shielding have a much greater influence on the angular response of In compared to Na.

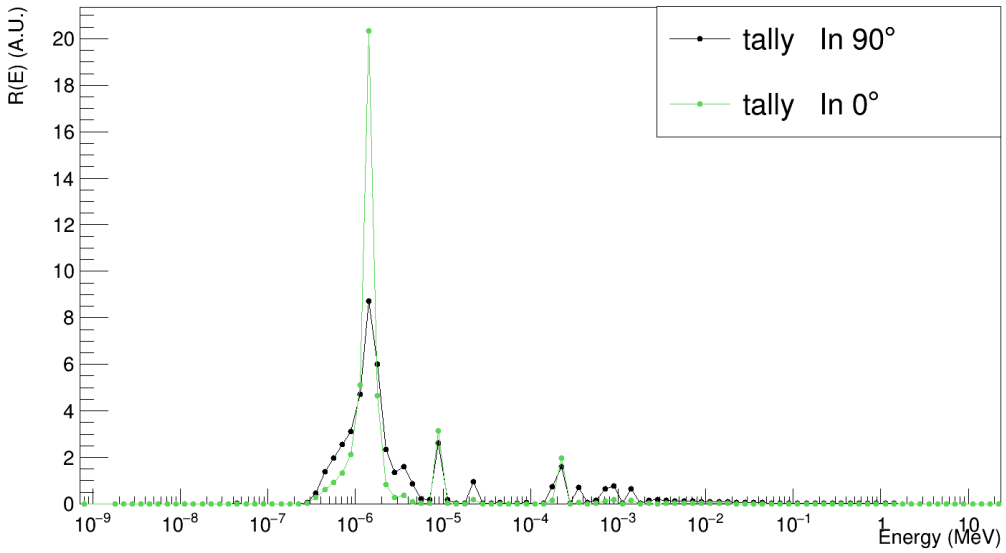

Fig. 3.21.: Angular response curves for the In foil for a neutron incoming angle of 0° and 90°. No normalization have been applied.

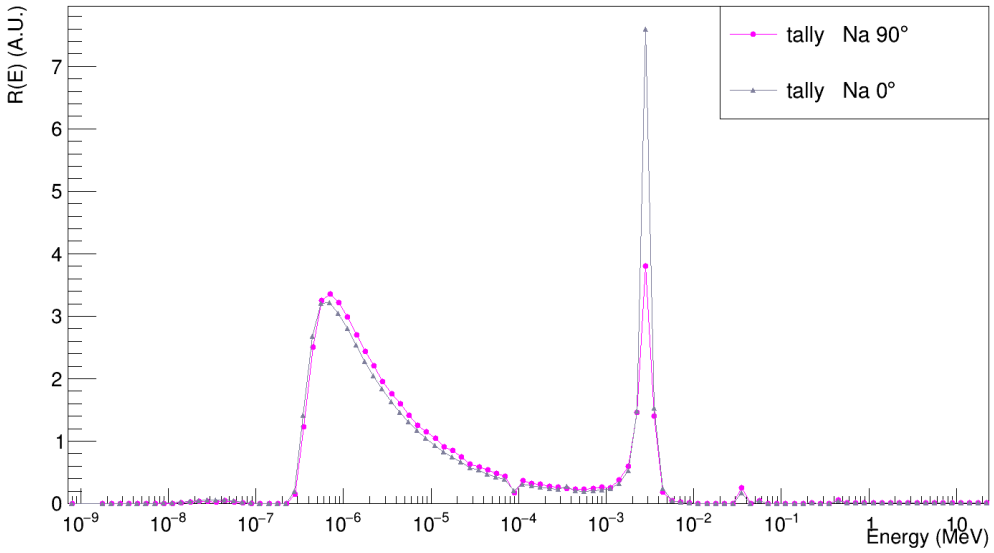

Fig. 3.22.: Angular response curves for the Na foil for a neutron incoming angle of 0° and 90°. No normalization have been applied.

For completely describing the geometry, in figure 3.23, the response curves of the first geometry are shown in the case of a neutron beam incident at an angle of 0° relative to the normal to the surface.
It can be observed that the structure of the response curves is not significantly different from what was previously shown in figures 3.9 and 3.10. This is due to the fact that the analyzed geometry is very simple, and the interference phenomena among the various components of the system are nearly negligible.

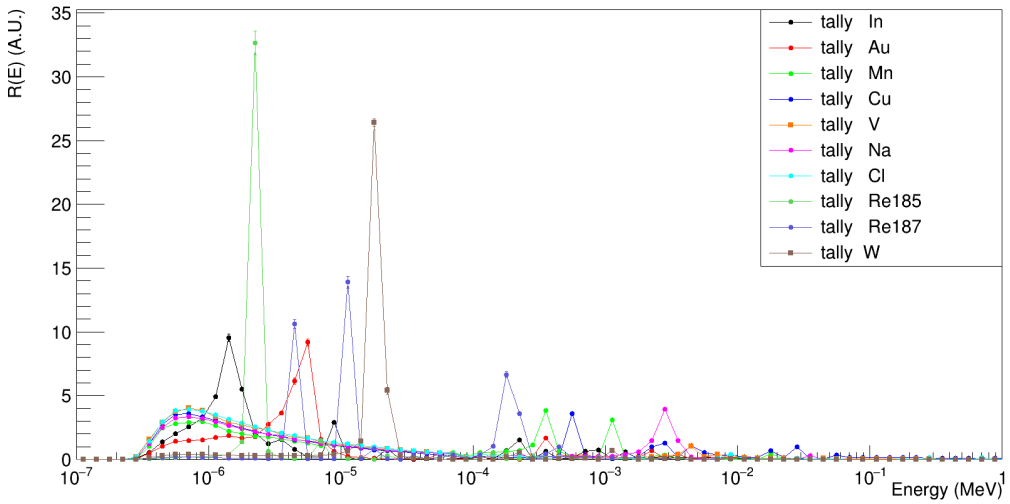

Fig. 3.23.: Angular response matrix for the first geometry. The neutron incident angle is 0° respect to the normal at the foils surface.

As evident from table 3.2, the condition of isotropy for the first geometry was not achieved, which was predictable due to the low degree of symmetry.
Therefore, a decision was made to explore a new geometry.

3.3.2 Final geometry study

With the aim of improving the geometry of NCT-ACS, the decision was made to incorporate an additional layer of moderator, external to the structure of the individual sandwich in the initial geometry. This choice was based on two considerations:

1. The presence of the moderator introduces a significant neutron scattering component. As described in section 1.5, this process occurs stochastically. Neutrons subject to elastic scattering experience random directional changes, modifying the angular distribution of incident neutrons on the moderator. For sufficiently thick moderators, scattering phenomenon become dominant, rendering the angular distribution of incident neutrons largely insignificant. Under these conditions, the new angular distribution can be approximated as isotropic, since neutron come from all the possible directions, without any preferences.

   This is one of the concepts which validate the use of the Bonner Spheres Spectrometer. This system is used in neutron fields with unknown angular distributions because the detector response within the spheres can be considered isotropic due to the presence of the moderator. In line with these considerations, the studied moderator shape was spherical.

2. The addition of the moderator alters the response curves of NCT-ACS (depicted in figure 3.23), making them smoother. This change was considered crucial for the subsequent unfolding procedures. Working with highly peaked response curves and pronounced resonance structures might pose challenges for the algorithm in reconstructing the neutron spectrum.
   A comprehensive treatment about this aspect will be presented in section 3.3.3.

Intensive investigation into various geometries was conducted through Monte Carlo simulations.
In particular, a sphere made of High Density Polyethylene (HDPE) was added to the geometry studied in the initial phase. The radius of this sphere was varied between 10 mm and 40 mm at intervals of 5mm. For each moderator size, the response curves of NCT-ACS were computed. Similar to the previous geometry, the simulated neutron sources was composed by flat and parallel neutron beams incident at various angles between -90° and 90°, with intervals of 15°.
In figure 3.24 the simulation scheme for one of the studied configurations is shown

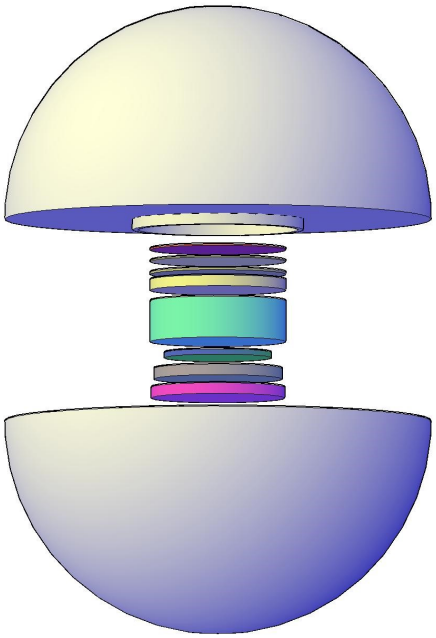

Fig. 3.24.: Geometry scheme for the Monte Carlo simulation with a moderator sphere shell of 20mm. Inside the sphere is placed the activation foil sandwich.

Consequently, for each size of the moderator sphere, 13 different angular conditions were simulated, and for each of these angular conditions, 10 response curves were analyzed (one for each selected element).
In order to evaluate the isotropy of the simulated system, the same analysis performed for the first geometry has been carried out. In particular the same considerations about the fit model and the statistical approach have been formulated and the same quantities have been evaluated.

Therefore, the anisotropy parameter Λ has been calculated for each foil in all the different geometrical configurations. In order to a more complete overview on the phenomenon, an additional configuration has been analyzed using a moderator sphere with a radius of 80 mm.
In figure 3.25 the dependence of the Λ parameter by the HDPE sphere radius is shown

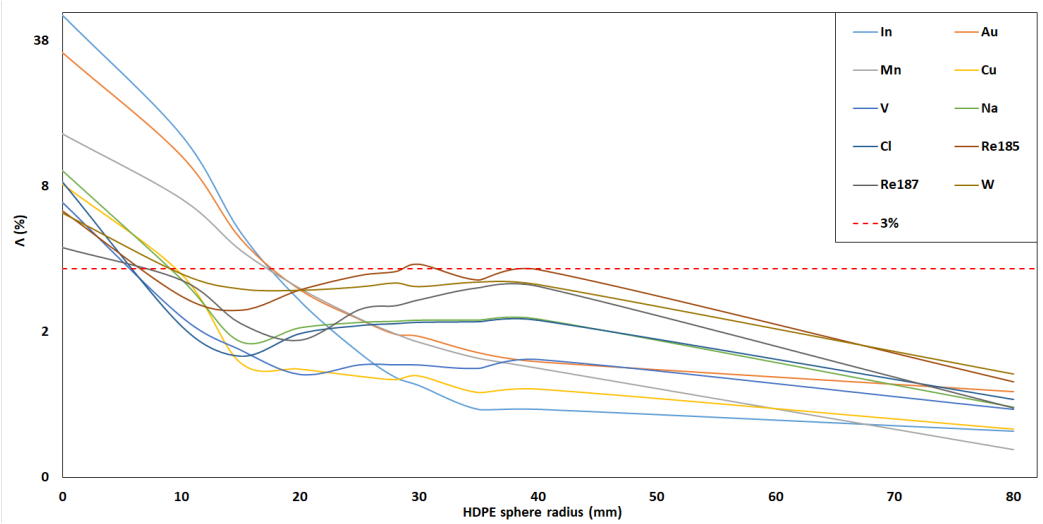

Fig. 3.25.: Λ in function of the sphere radius. The red dotted line represents the 3% threshold chosen as maximum acceptable anisotropy value.

As can be clearly noted, the Λ parameter decrease while increasing the sphere radius. The red dotted line represents the 3% threshold fixed before and considered as maximum acceptable anisotropy (systematic uncertainties).
For radius larger than 20 mm the anisotropy parameter decrease and goes below the threshold, therefore the isotropic assumption can be accepted.
It should be noted that the Λ parameter quickly decrease up to 20 mm in thickness and then it reaches a sort of plateau, oscillating around a value of 2.5%. A slow decreasing is then evident for higher values on the moderator thickness.
The simulation results for the 80 mm revealed that the anisotropy parameter for this specific simulation is very close to zero. In fact, the isotropic response is achieved within a systematic uncertainty of 0.9%.
Since one of the main requirements for the NCT-ACS device was the compact geometry, the 80 mm configuration was not classified as one of the best candidate and the smaller radius geometries were preferred. In fact, the gain in term of isotropy, compared to the size of the geometry was not considered worthy.
Moreover, increasing the moderator thickness leads to a reduced value on the activation rate A_r. This is due to the neutron absorption within the moderator itself. In figure 3.26 the A_r values, in function of the different radius are shown for all the elements.

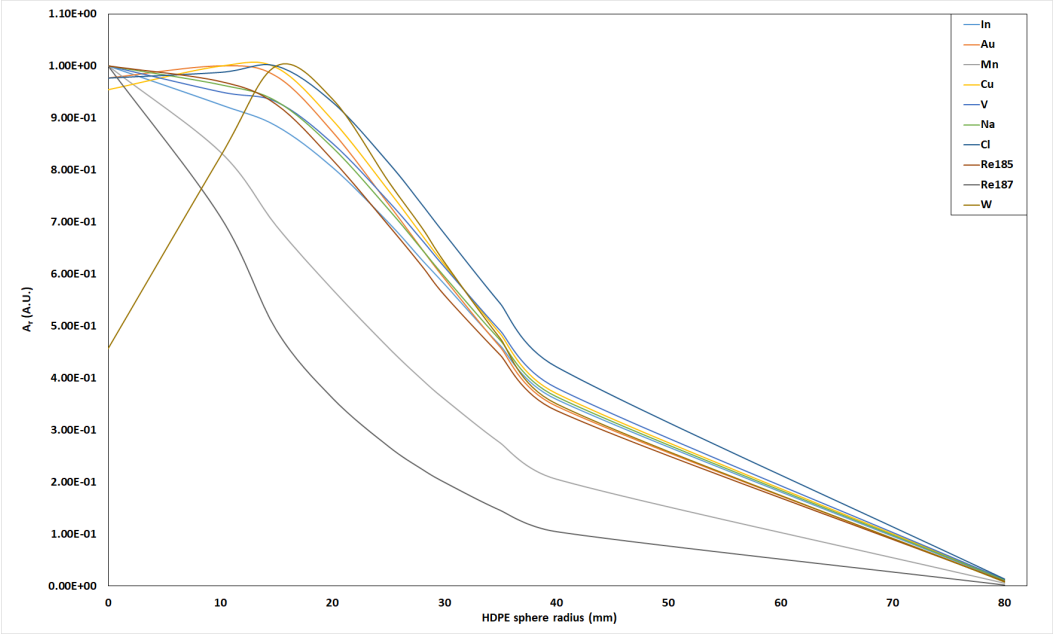

Fig. 3.26.: A_r values varying the HDPE sphere radius. The mean value for the different angular conditions has been considered. The values are plotted normalizing the data to the maximum value. Therefore the highest value for all the distribution is equal to the unity.

It should be noted that the curves are primarily decreasing while the moderator thickness increases, with the sole exception of W, which peaks at a thickness of 15 mm and then follows a trend perfectly comparable to that of the other elements.
It should be also noted that for a moderator thickness of 20 mm, the activation rate A_r is for almost all the elements between 80% and 98% respect to the maximum value. An exception is represented by Mn and Re, which show values around 60% and 40% concerning the maximum, still maintain a decreasing trend while increasing thickness.
Conversely, for a thickness of 40 mm, the A_r values are within 40% - 60% for most of elements and within 10% - 25% for Mn and Re. The sensible variations leads to prefer smaller thickness. In fact, using the same neutron source and experimental setup the 40 mm geometry induces to almost double the irradiation time increasing the time required for the whole procedure.
This argument is even more valid for the 80 mm thickness, where the A_r values are massively reduced due to the presence of the moderator. In fact, almost all the elements show a decreasing on the A_r leading to a value of 0.5-1% respect to the maximum value.

In conclusion, a moderator thickness between 20 mm and 40 mm has been considered to be the best option for the NCT-ACS anisotropy, activation values and dimension requirements.

3.3.3 Response matrix validation

In order to chose the correct dimension on the moderator, the sole isotropy behaviour is reductive. Thus the need to find the best option while considering the response matrix validation.
The unfolding code used in this work is FRUIT [2]. In particular, the numerical iterative configuration has been employed. This approach relies on the GRAVEL algorithm procedure and allows to obtain fast and precise results. A more in detail discussion is provided in appendix B where a general overview on the different unfolding algorithms and their functioning is reported.

Within the scope of this work, it should be useful to summarize the most important quantities that are relevant for performing an unfolding procedure using this specific code:

- **Experimental data**
- **Guess spectrum (or other information)**
- **Response Matrix**

In this section the discussion will be focused on the **Response Matrix** aspect, since it is geometry dependant. The response matrix includes how the system responds to neutrons of different energy, representing a sort of efficiency curve, but with distinct characteristics. As these curves constitute a fundamental part for the accurate operation of the unfolding process, their capability to provide accurate information is imperative.
In particular, two aspects have been considered to be critical for the unfolding procedure: the shape of the different curves and how much energy information the curves themselves can produce.

The shape of the response curves is crucial to ensure the algorithm's optimal performance. A response matrix with extremely sharp curves can produce issues during the code numerical iterative process. This can lead to non-physical structures within the process, resulting in unwanted oscillations in the final result. This phenomenon decreases while the moderator thickness increases, as shown in figure 3.27. Thus, the moderator plays a significant role not only in ensuring the isotropy, but also for shaping the response curves.

From figure 3.27 it can be also noticed that increasing the thickness of the moderator, the response curves is modified until a completely different shape (80 mm situation).

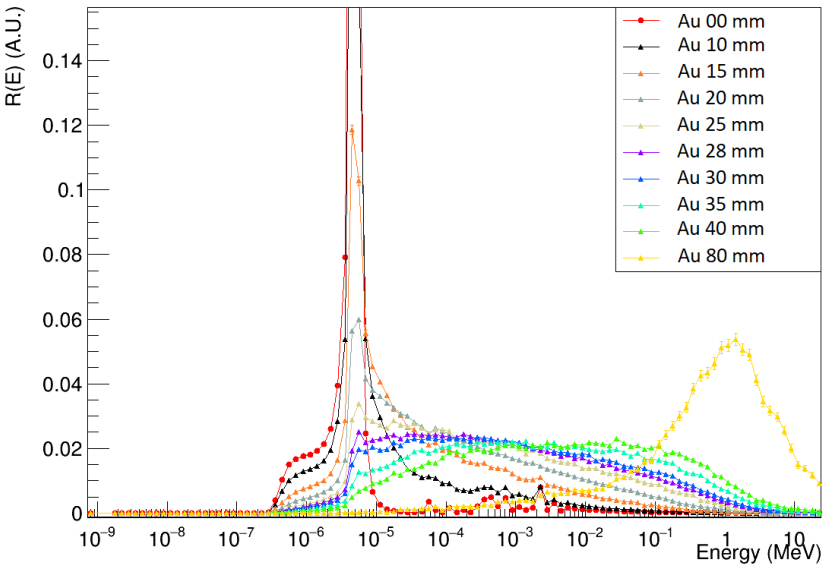

Fig. 3.27.: Response matrix for the Au foil while increasing the size of the moderator. The shape is smoother for higher moderator radius. An incoming neutron angle of 30° has been chosen. The same behaviour is clearly distinguishable for all the other cases (different element and different angles).

This change directly leads to the second critical point.
It should be useful to remind that a response matrix contains information on how the system reacts to neutrons of different energies. Thus it is evident that using a sole response curve, the energy spectrum cannot be reconstructed. Generally, at least 5-6 curves are required for an unfolding procedure. The necessary condition, however, is that the selected curves should not be excessively similar. If the curves are highly analogue, the energy information provided to the unfolding algorithm is reduced, potentially leading to inadequate convergence of the procedure.
This peculiarity explains why the BSS technique traditionally struggles while processing epithermal energy spectra. This occurs because the response curves of the BSS in the epithermal range show similar trends, reducing its reconstruction capacity.

In figures 3.28 and 3.29 the response curves for all the elements in the 00 mm and 80 mm configurations are shown. These two configurations are diametrically opposite since in the 00 mm the response curves for the selected elements are evidently different between each others, while in the 80 mm configuration, they are superimposed. Therefore the 80 mm geometry is absolutely not useful for applying the unfolding procedure since it is equivalent to an hypothetical case in which a single curve is provided to the algorithm. Otherwise, the 00 mm reveal very peaked response curves, therefore, even if the isotropy was achieved, it would not be used for the unfolding procedure since it could have produced instability in the algorithm.

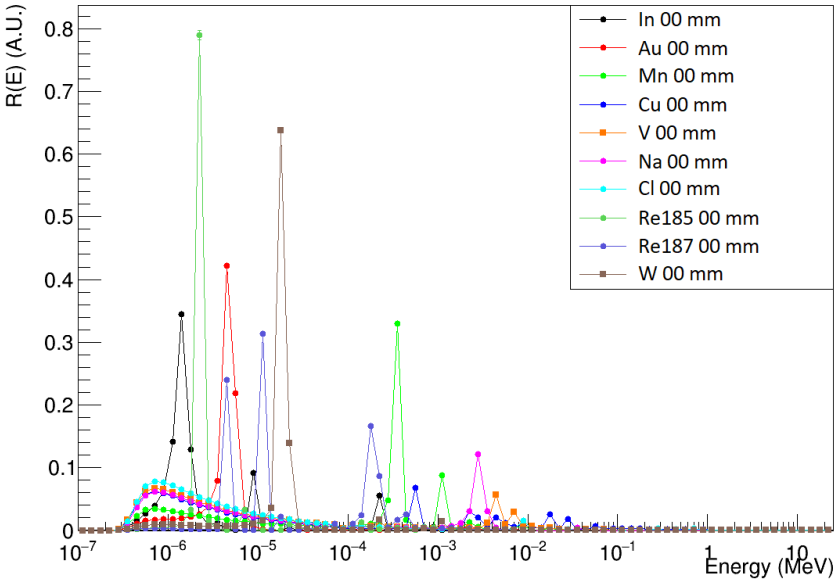

Fig. 3.28.: Response matrix for the 00 mm moderator radius. The response curves are clearly distinguishable and their shape are different.

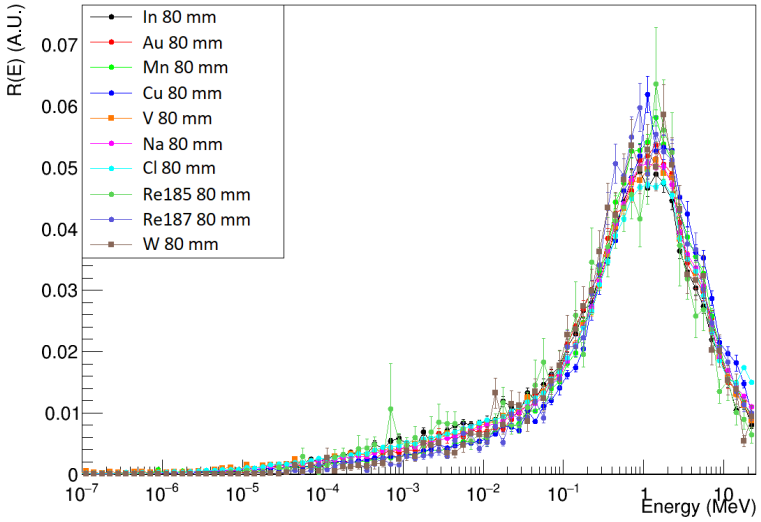

Fig. 3.29.: Response matrix for the 80 mm moderator radius. The response curves are almost superimposed with same shape.

Initially, a statistical approach was considered to evaluate the diversity of response curves (e.g. chi-square test, Kolmogorov-Smirnov test). However, this study was early abandoned as it wasn't possible to define a priori statistical variable without introducing bias into the unfolding procedure. Considering these aspects, and since the only observable physical aspect is the energy spectrum, the strength of a response matrix was evaluated based on its capacity to perform during an unfolding procedure.

In order to evaluate this capacity, an iterative approach was chosen, divided into distinct phases:

1. The response matrix has been extracted for all the different configurations from 15 mm up to 40 mm in radius explored in the previous section. Since the assumption of isotropic response for the detector was correct within a 3% of uncertainty (Λ parameter), the angular distribution of the incoming neutron is not relevant while choosing the curves. Nevertheless, the set of curves for a 30° incoming angle neutron beam has been chosen. Considering all the different angles, the 30° degrees value was noted to be almost constantly the one which produced the closest A_r respect to the average value.
   It should be noted that the 15 mm configuration does not satisfy the isotropy condition, bust still is very close to that, therefore it has been included for having a more complete overview

2. The A_r values produced by folding the response matrix with the e-LiBaNS epithermal neutron spectrum have been calculated. It should be noted that these values were already calculated in the previous considerations.

3. A misleading guess, different by the e-LiBaNS spectrum, has been used as "guess" spectrum for the unfolding procedure. The iterative algorithm implemented on FRUIT and based on the GRAVEL method, is highly sensible to the guess information, therefore a completely different spectrum (e.g. fission spectrum) could lead the algorithm to do not converge properly.
   In figure 3.30 the e-LiBaNS spectrum used for extracting the A_r values and the misleading spectrum are shown.

4. The unfolding procedure using the FRUIT numerical method has been used, trying to reconstruct the correct energetic distribution starting from the misleading guess.

5. In order to evaluate in which condition the procedure was able to reconstruct the correct distribution, a statistical test has been performed.

About the statistical test, the FRUIT code calculates some variable that are useful to control and check the procedure [2].
In particular, the λ parameter can be defined as:

$$\lambda_{i,k} = \frac{1}{u_i}|C_i - C_{i,k}^{calc}| \tag{3.21}$$

Where:

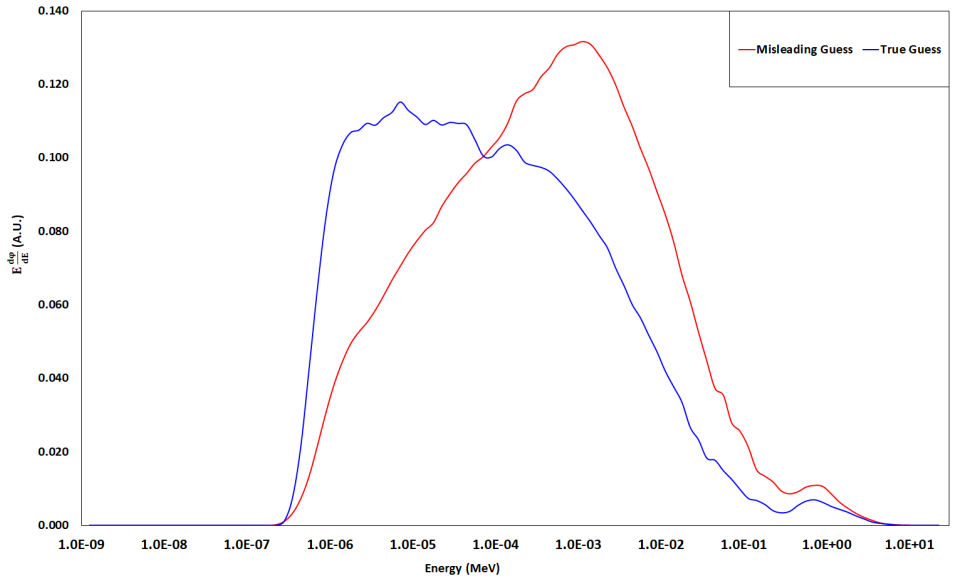

Fig. 3.30.: In blue the true Monte Carlo spectrum for the e-LiBaNS facility working in "epithermal mode" (see section 2.7.1) is shown. In red the misleading guess used to validate the response matrix is also reported.

- C_i is the input value for the foil count, it should be the true value for the counts in the detector i. In this case it is calculated by folding the response curve with the e-LiBaNS epithermal spectrum;

- $C_{i,k}^{calc}$ is the calculated foil count, obtained folding the response curves with the spectrum at the step k. Since the starting spectrum is different from the real one, C_i and $C_{i,k}^{calc}$ are different;

- u_i is the uncertainty on the count C_i.

And, consequently, the mean value of λ is given by:

$$\bar{\lambda_k} = \frac{1}{n}\sum_{i}^{n}\lambda_{i,k} \tag{3.22}$$

In order to validate the unfolding procedure the iterative process has been conducted until the variation on the λ_k parameter was under 2%:

$$\Delta(\bar{\lambda}) = \frac{\bar{\lambda_k} - \bar{\lambda_{k+1}}}{\bar{\lambda_k}} \tag{3.23}$$

It should be noticed that the 2% variation has been chosen arbitrarily, looking at the behavior of the procedure on the different cases. Some tests fixing the threshold at 3% have been conducted, producing similar results.
Fixing a lower limit value for the $\Delta(\lambda)$ value was necessary to avoid the iterative algorithm to produce not physical oscillations. In order to reduce the average de-

viation, after some iterations the algorithm introduces peaked structures that are purely mathematics artefact, without any physical meaning.

Then, to finally validate the obtained spectrum, the $\bar{\lambda}$ value and maximum deviation value λ_{max} have been considered. Since the latter is a gaussian variable, a normal test can be conducted.
It should be noted that this statistical test has to be contextualized. The unfolding procedure can lead to quite different distribution that may fail a statistical normal test, but still are in a very good agreement with the true spectrum. Thus, the statistical test has to be considered more like an indicator on the goodness of the results and not like a accept-reject study.

In figure 3.31 the unfolding results in the different conditions are shown, the real spectrum and the misleading guess are also reported.

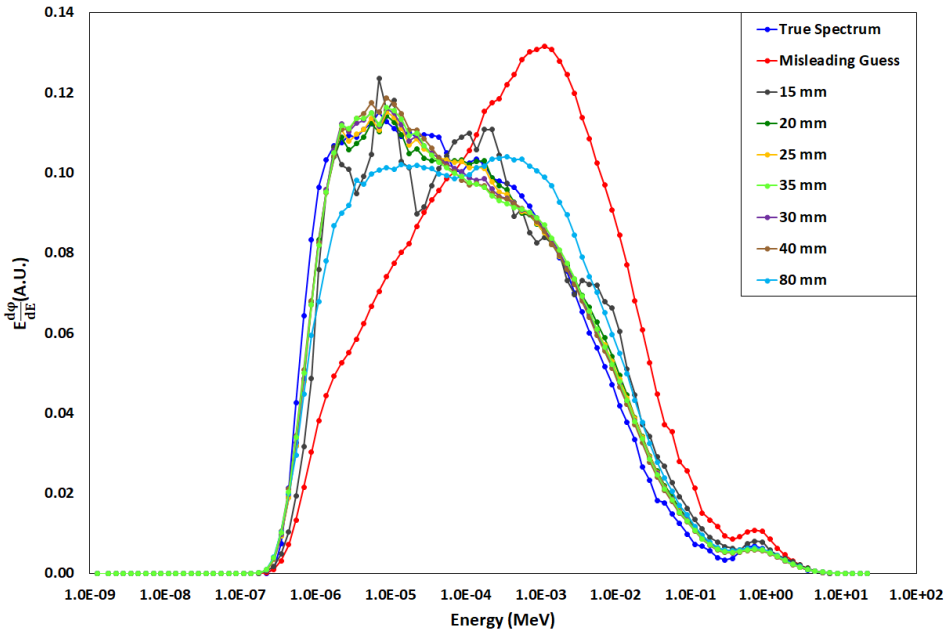

Fig. 3.31.: Unfolded spectra for many different moderator radius. The true spectrum is plotted in blue, while the misleading spectrum is plotted in red.

In order to better understand the results, some considerations can be made:

1. The 15 mm configuration is the most unstable, with many fluctuations and some interference provided by mathematical artefacts. This behaviour implies that for such a small moderator radius the peaked structure of the resonances are still too important and leads to a unsatisfactory result;

2. On the other hand, the 80 mm configuration is very smooth and without any structure, but it is far away from the true results. In this case, the response

curves are good considering their smoothness, but they are completely lacking on the energy information;

3. For all the other configurations, the result are comparable between each other and in a good agreement with the true spectrum. Thus is evident that from 20 mm up to 40 mm the NCT-ACS geometry can be work properly. In table 3.3 the values of λ_{max} and $\bar{\lambda}$ are shown.

Configuration	$\lambda_{\mathbf{max}}$	$\bar{\lambda}$
15 mm	1.49	0.51
20 mm	1.06	0.40
25 mm	0.91	0.32
30 mm	0.85	0.34
35 mm	0.86	0.41
40 mm	1.09	0.48
80 mm	1.85	1.01

Tab. 3.3.: Maximum and average deviation values at the end of the unfolding procedure in the different geometry configurations.

From table 3.3 can be noted that the 15 mm and 80 mm configurations show the worst combination of maximum and average deviation. This aspect reinforces what was previously hypothesized.

The 20 mm and 40 mm configurations are slightly worse respect the 25-30-35 mm. It should be noted that all these combinations are still acceptable and the results shown in figure 3.31 confirm the goodness of these geometry. Nevertheless, the 20 mm and 30 mm configurations have been chosen.
The 20 mm geometry allows to obtain a better count statistic, in the e-LiBaNS irradiation scenario this characteristic has been evaluated as the most relevant. The 30 mm configuration was also considered, since it was evaluated to be the best option. Due to some operational difficulties during the design phase, the final radius of the sphere was fixed at 28 mm instead of 30 mm. The whole simulation study has been then reproduced for this extra geometry, obtaining results very similar to the 30 mm scenario ($\lambda_{max} = 0.86$ and $\bar{\lambda} = 0.33$).

3.4 Summary of the NCT-ACS development

The study and development of the composition and geometry of NCT-ACS has gone through several phases. Here is a summary of the main obtained results.

The elements that composed the NCT-ACS sensible part and the dimensions of the foils are:

Element	Diameter (cm)	thickness (μm)	Mass (g)	Number of foils
In	0.635	127	∼0.1249	1
Au	0.635	51	∼0.123	2
Mn	0.635	51	∼0.037	4
Cu	0.635	127-254	∼0.144-0.288	8-4
Na	0.635	1905	∼0.482	2
V	0.500	500	∼0.249	1-2
Re	0.600	1000	∼2.619	1
W	0.625	1000	∼2.416	1

Tab. 3.4.: Foils dimensions and mass. The number in the last column refers to the total number of foils implemented in the simulations and in the measurements.

All the foils shown in table 3.4 are organized in a sandwich structure and are placed inside a cadmium shield characterized by a hollow cylindrical shape. The thickness of the cadmium shield is 0.5 mm.
The cylinder containing the different foils is placed inside a moderator sphere made of High Density Polyethylene HDPE. After an extensive Monte Carlo simulation work, two different radius have been chosen: 20 mm and 28 mm.
The response matrix in both configurations have been extracted, the results are sown in figure 3.32 and 3.33:

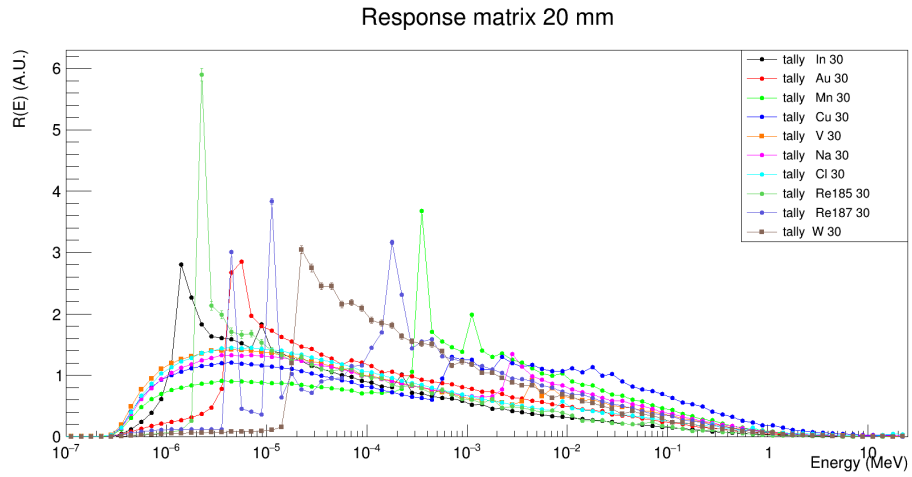

Fig. 3.32.: Response matrix for the 20 mm configuration. An angle of 30° for the incoming neutrons has been considered.

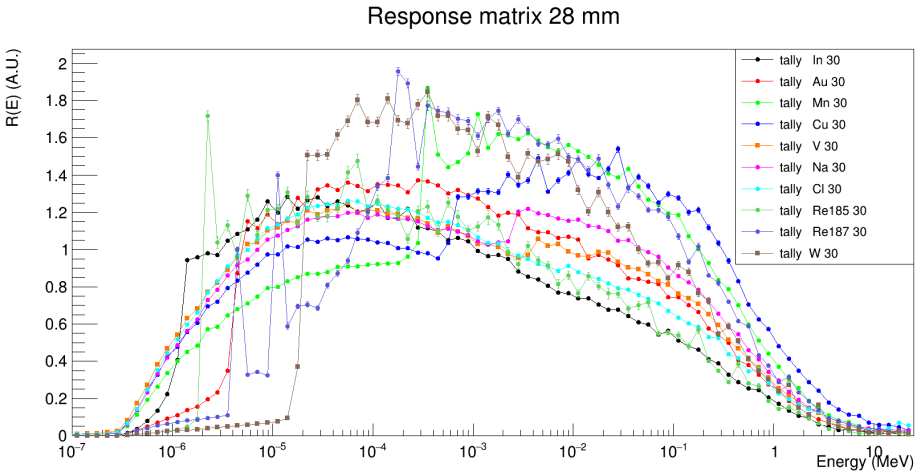

Fig. 3.33.: Response matrix for the 28 mm configuration. An angle of 30° for the incoming neutrons has been considered.

In both configurations the anisotropy has been evaluated to be below 3% and the unfolding procedure can work properly, within the statistical constraints.
In figure 3.34 the unfolding procedure test results are reported.

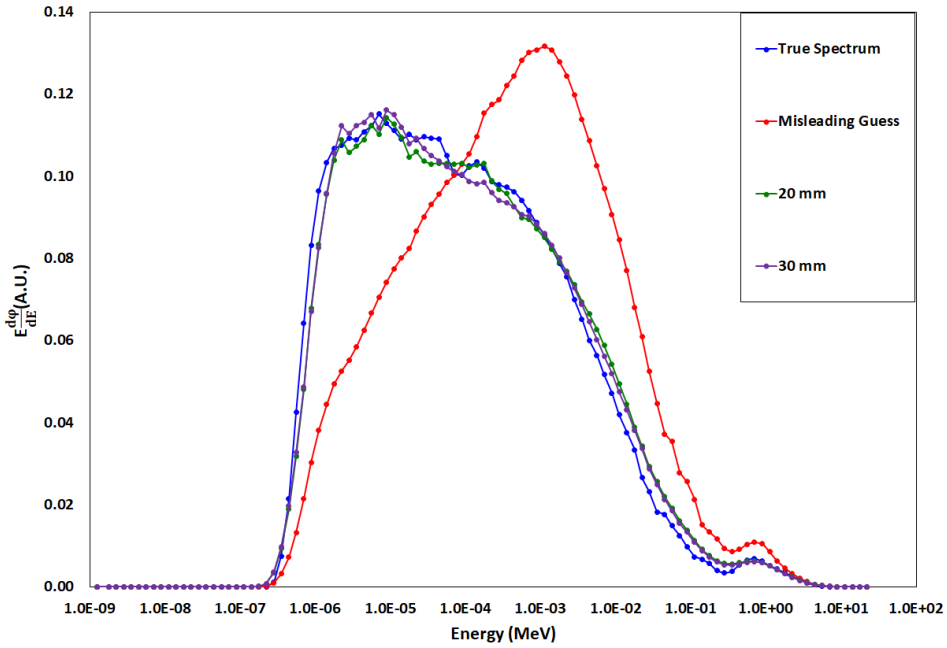

Fig. 3.34.: Unfolded spectra for 20 mm and 30 mm moderator radius. The true spectrum is plotted in blue, while the misleading spectrum is plotted in red.

During this process, a threshold of 3% on the anisotropy for the NCT-ACS geometry has been fixed. This value was obtained in section 3.3.2 and represents a precautionary estimation of the real anisotropy of the system. This choice has been taken in order to do not underestimate the systematic uncertainty related to the angular response of the whole system. Thus, a systematic contribute to the total uncertainty and equal to the maximum anysotropy for the 20 mm (2.3%) and 28 mm (2.4%) must be considered:

$$S_{\text{anisotropy}} = 2.4\% \tag{3.24}$$

4 HPGe gamma detector calibration

The aim of this chapter is to explain the HPGe calibration procedure. The detector was situated in the Physics Department at the University of Turin.
The initial part of the chapter provides an overview over the gamma interactions with matter and over the main features of the HPGe detectors. Subsequently, various considerations will be provided about the different approximations and analysis methods adopted. In the last part the measurements for the detector calibration will be presented.

4.1 Gamma interaction with matter

The interaction characteristics of photons in matter markedly deviate from those of charged particles. Notably, the absence of electric charge in photons precludes the numerous inelastic collisions with atomic electrons that are distinctive of charged particles. Instead, the primary interactions of x-rays and γ-rays in matter comprehend:

1. **Photoelectric Effect**
   The photoelectric effect is characterized by the absorption of a photon by an atomic electron, leading to the subsequent ejection of the electron from the atom. The energy of the ejected electron is given by the equation:

$$E_e = h\nu - B.E. \tag{4.1}$$

   where (B.E.) represents the binding energy of the electron.
   The photoelectric effect is constrained by the inability of a free electron to absorb a photon while conserving momentum. Consequently, this phenomenon exclusively occurs on bound electrons, where the nucleus absorbs the recoil momentum. In figure 4.1, a typical photoelectric cross-section is depicted as a function of incident photon energy. Notably, at energies surpassing the highest electron binding energy of the atom (the K shell), the cross-section is relatively small but experiences a rapid increase as the K-shell energy is approached. Immediately after this point, the cross-section undergoes a drastic decline, marking the absence of K-electrons for the photoelectric effect, and this

reduction is identified as the K absorption edge. Below this energy threshold, the cross-section once again ascends, exhibiting fluctuations at the L, M, and subsequent levels, known as the L-absorption edges, M-absorption edge, etc.

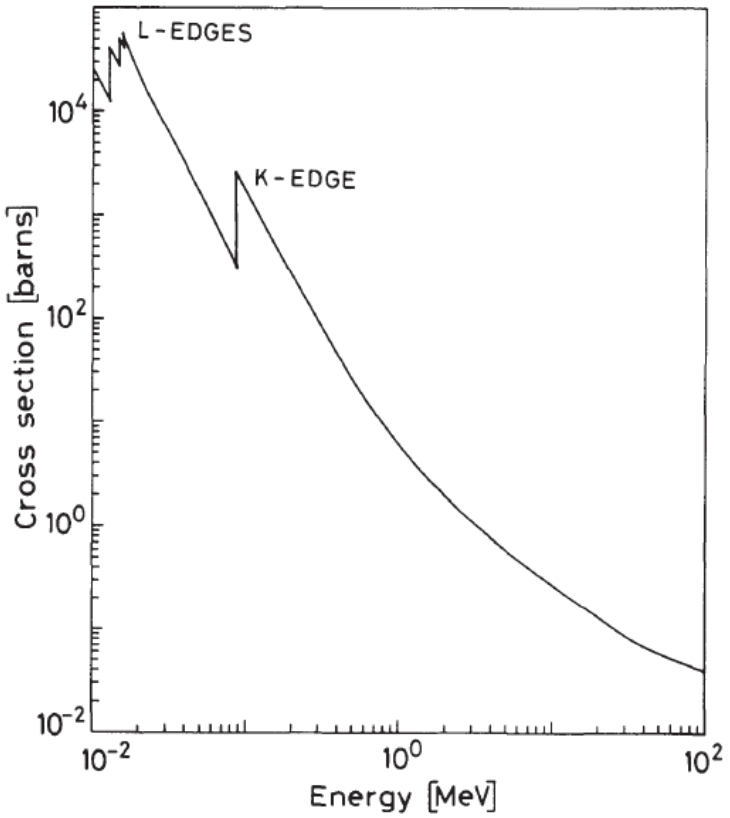

Fig. 4.1.: Calculated photoelectric cross section for lead.

The dependence of the cross-section on the atomic number Z is interesting. Although this dependency exhibits some variability based on the photon's energy, at MeV energies, it scales approximately as Z to the 4th or 5th power. Evidently, materials with higher atomic numbers (Z) are more favorable for photoelectric absorption.

2. **Compton Scattering**
   Compton scattering stands out as one of the most comprehensively understood processes in photon interactions. As a reminder, it involves the scattering of photons on free electrons. In materials, electrons are bound; nevertheless, when the photon energy significantly exceeds the binding energy, the latter can be neglected, and the electrons can be essentially treated as free.
   The full theoretical treatment can be calculated using the quantum electrodynamics formalism and is known as the Klein-Nishina formula.

Figure 4.2 shows the total Compton scattering cross section:

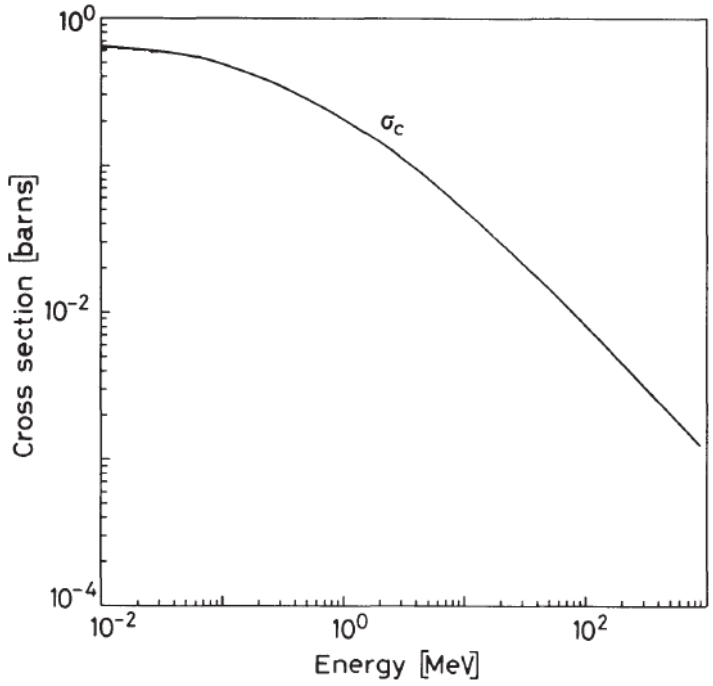

Fig. 4.2.: Total Compton scattering cross sections in lead as a function of the γ energy.

3. **Pair Production**
   Pair production is a process where a photon is transformed into an electron-positron pair. Conservation of momentum dictates that this process can only occur in the presence of a third body, typically a nucleus. Additionally, for the creation of the pair, the photon must possess a minimum energy of 1.022 MeV. Theoretically, pair production is linked to bremsstrahlung through a simple substitution rule, allowing calculations for one process to yield immediate results for the other. Similar to bremsstrahlung, the screening effect of atomic electrons surrounding the nucleus holds significance in pair production.
   A theoretical interesting approach on the phenomenon can be made using the Born approximation calculation. Because of the Born approximation, the results are not very accurate for high Z or low energy. A more complicated formula valid for low energies and no screening has been derived by Bethe and Heitler [119].

Figure 4.3 shows the total pair production cross section.

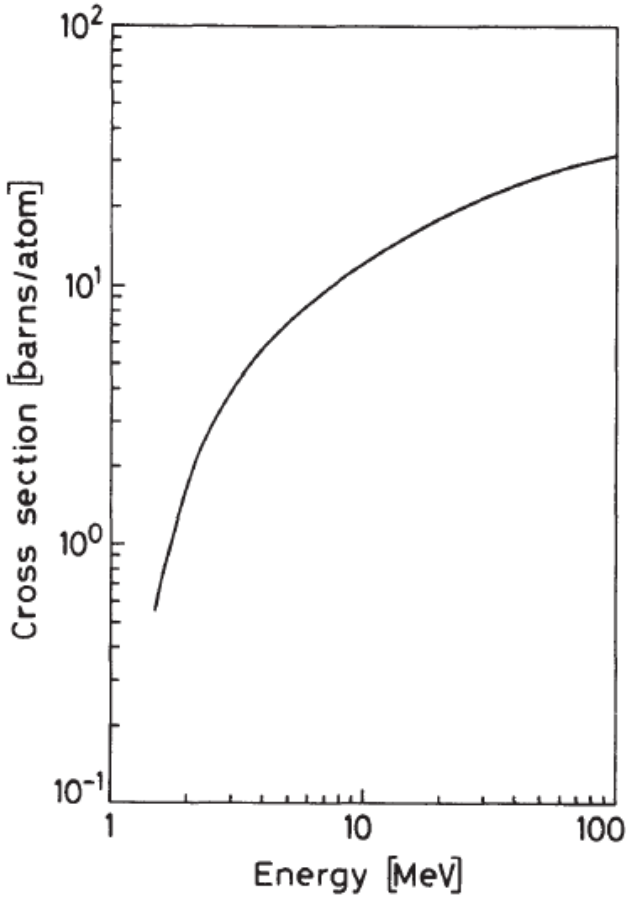

Fig. 4.3.: Pair production cross section in lead.

The total cross section for a γ ray traveling through matter can be calculated simply summing the different components, the results can be seen in figure 4.4. As can be seen, the total cross section behaviour can be divided into three energy regions:

1. **from 0 up to $\sim$ 800 keV:** here the dominant effect is the photoelectric interaction;

2. **from $\sim$ 800 keV up to $\sim$ 3 MeV:** here the dominant effect is the Compton scattering

3. **above $\sim$ 3 MeV:** here the dominant effect becomes the pair production.

The numeric values can vary depending the material under study, these values are related to a lead absorber material.

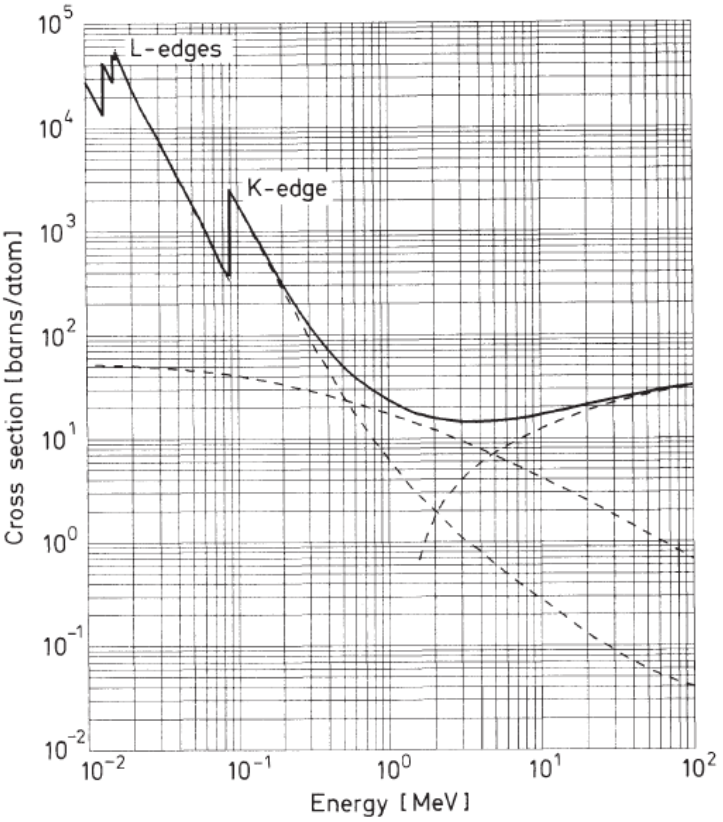

Fig. 4.4.: Total energy photon cross section for lead.

The attenuation observed by a photon beam can be model to be exponential with respect to the thickness:

$$I(x) = I_0 e^{-\mu x} \tag{4.2}$$

Being I_0 the incident beam intensity, x the thikness of absorber and μ the absorption coefficient that depends by the material and its density.

4.2 HPGe detectors

Semiconductor detectors make use of the small energy gap between the valence and conduction bands of semiconductors, exemplified by germanium (Ge) with a 0.67 eV gap, to detect ionization particles. At low temperatures, electrons predominantly occupy the valence band, forming covalent bonds within the semiconductor crystal. Energizing these electrons through interactions with ionizing radiation shifts them into the conduction band, enabling unrestricted movement within the crystal. The liberation of an electron from the covalent bond results in a positively charged ion. Application of an electric potential difference to the semiconductor prompts current flow through the conduction-band electrons and the movement of positive charges, termed holes. A hole can traverse the crystal by accepting a bound electron from an adjacent atom. In practice, semiconductor materials are never completely pure. Acceptor atoms act as impurities, possessing one fewer electron in their valence band. When present within a semiconductor crystal, this absence of an electron in the covalent bond with semiconductor atoms creates a vacancy, attracting an electron to form a hole capable of conducting current. Conversely, donor impurities carry an extra electron, readily released into the conduction band. Consequently, semiconductor materials inherently harbor free charge carriers-electrons (in n-type semiconductors) or holes (in p-type semiconductors). Under typical conditions, the quantity of free charge carriers is primarily determined by the net discrepancy between acceptor and donor impurities. Throughout the semiconductor crystal's growth process, one type of impurity typically prevails.

The combination of their relatively high density and the small energy required to create an electron-hole pair (averaging 2.9 eV in Ge) makes semiconductors valuable for ionizing radiation spectrometry. However, it is imperative to eliminate all free charge carriers from the material; otherwise, fluctuations in the electric currents generated by these carriers could overshadow signals from radiation interactions. The formation of a diode by combining p and n-type semiconductors creates a depletion region devoid of free charges at the junction, known as the depleted region. This occurs because free electrons from the n-type material diffuse into the p-type material, and vice versa.

Negative and positive immobile ions remain at the filled acceptor-sites and vacated donor-sites, resulting in a space charge that suppresses further charge carrier diffusion. A net potential difference accumulates across the p-n junction. The resulting electric field forces any electrons/holes generated in this region to drift towards the positive/negative potential. Consequently, an electric signal is generated at the edges of the junction, where the depleted region serves as a sensitive volume of a detector. The electric field within the depleted region, and thus the region's width, can be significantly increased by applying an external voltage to increase the potential difference across the p-n junction. This external voltage is called reverse

bias, because the potential difference is applied in the direction in which no current can flow across the diode.
However, due to the small gap between the valence and conductive band energy levels, the temperature of the material can cause spontaneous appearance of charge carriers in the conduction band and thus a small leakage current is always present. To sufficiently deplete the p-n junction region it is therefore necessary to cool the material to cryogenic temperatures.

The electrical signal at the detector contacts arises from the motion of charges within the electric field. The Shockley–Ramo theorem [120] describes the charge Q induced at the read-out electrode by a point charge q positioned between the electrodes.

$$Q = -q \cdot W(x) \tag{4.3}$$

Where $W(x)$ is the weighing potential at the position x for the charge q. The dimensionless weighing potential serves as an indicator of the electrostatic coupling between the charge q and the read-out electrode. It quantifies the electric potential at a specific position within the device, assuming the readout electrode has a unitary voltage, the other electrode has zero voltage, and there is no space charge within the detector volume.

With impurity concentrations at levels as low as 10^9 cm^{-3}, which is the best routinely achieved material purity, the semiconducting germanium is an ideal material for γ-ray detectors.
The depleted region thickness can be calculated using the formula [121]:

$$d \simeq \left(\frac{2\epsilon V}{eN}\right)^{1/2} \tag{4.4}$$

where ϵ is the static permittivity of the material, e the elementary charge, V the reverse bias voltage and N the impurity concentration.
Under typical work condition, equation 4.4 predict depletion depth as large as $d \simeq 10$ cm making possible to produce large detector with useful active volume.

For this study, the HPGe detector category was chosen based on its characteristics, specifically for its low noise, big depleted region and, most importantly, its excellent energy resolution. Although the utilized elements for NCT-ACS were known, some of them exhibited photopeaks in close proximity to each other, thus the necessity for a good energy resolution was fundamental.
The energy resolution of a typical germanium detector can be described as:

$$\Delta E_{\text{total}} = \sqrt{(\Delta E_{\text{noise}})^2 + (\Delta E_{\text{ion}})^2 + (\Delta E_{\text{incomplete}})^2} \tag{4.5}$$

where:

$$\Delta E_{\text{ion}} = 2.35\sqrt{\epsilon F \cdot E} \tag{4.6}$$

The parameter ΔE_{total} represents the width at half maximum amplitude (FWHM) of the gamma-ray peak observed at energy E within the spectrum. ΔE_{noise} denotes the portion deriving from detector leakage current and preamplifier-induced noise. Its contribution remains consistent across various gamma-ray energies but varies based on the detector working conditions.
ΔE_{ion} characterizes the fluctuation in the generation of electron-hole pairs due to ionization statistics. It relies on the mean energy necessary to create an electron-hole pair (ϵ = 2.95 eV), the gamma-ray energy (E), and the Fano factor (F). The Fano factor describes the ionization process, situating it between entirely random independent ionization events (F=1) and an entirely deterministic energy-to-electron-hole-pair conversion (F=0). For HPGe, a Fano factor, approximately F $\simeq$ 0.1, suggests a closer alignment to the latter condition than the former.
$\Delta E_{\text{incomplete}}$ accounts for the variability in collecting all generated electron-hole pairs from the ionization process. This primarily encompasses electron-hole pairs that recombine before collection or charge carriers that get trapped during their drift to the respective electrode. Neglecting the incomplete charge collection term during spectral resolution measurements could overstate the implied Fano factor value.

4.2.1 The Torino HPGe detector

The HPGe detector used in this work was a ORTEC gem20p4-70 model (data sheet is available at [122]). The detector is fabricated from P-type germanium with an outer contact of diffused Li and an inner contact of ion-implanted boron.
The main characteristics are shown in table 4.1, for the other information please refer to the data sheet:

Characteristic	**Value**
Crystal dimensions	2"x2"
Density (g/cm^3)	5.35
Response time	8-10 ns
Energy resolution (@122 keV)	0.67%
Energy resolution (@662 keV)	0.3%
Energy resolution (@ 1333 keV)	0.14%
Efficiency	20%$^{(1)}$

Tab. 4.1.: ORTEC gem20p4-70 main characteristics.$^{(1)}$ relative to a 2.5" x 2.5" NaI inorganic scintillator efficiency.

The energy calibration for the HPGe detector will not be described, since it is a well known technique, widely used in all the γ spectrometry applications. The standard procedure has been applied, using many different sources like: ^{137}Cs, ^{60}Co, ^{133}Ba, ^{152}Eu, ^{22}Na.
In figure 4.5 a picture of the used HPGe detector is shown.

Fig. 4.5.: Image of the HPGe used for this work. On the right of the detector, the readout electronic and the connection with the acquisition pc can be shown.

Figure 4.6 shows the scheme of the sensitive part of the HPGe used for this analysis. The Lithium Diffused substrate allows to shield the detector from the α particles coming from the natural background. The low atomic number of Li permits to neglect its contribution during the gamma interactions.

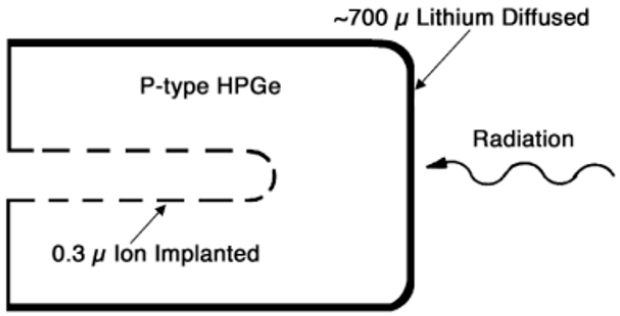

Fig. 4.6.: Scheme of the HPGe detector used for the gamma analysis. Total sizes are 2" in diameter and 2" in height.

4.3 Point source like approximation

In order to better comprehend the subsequent analysis, the dimensions of the selected foils, employed in the construction of NCT-ACS, are shown in table 4.2. The sizing of these foils is determined based on the considerations outlined and discussed in section 3.2.

Element	Diameter (cm)	Total thickness (μm)	Total mass (g)	Number of foils
In	0.635	127	∼0.1249	1
Au	0.635	51	∼0.123	2
Mn	0.635	51	∼0.037	4
Cu	0.635	127-254	∼0.144-0.288	4-8
Na	0.635	1905	∼0.482	2
V	0.500	500	∼0.249	1-2
Re	0.600	1000	∼2.619	1
W	0.625	1000	∼2.416	1

Tab. 4.2.: Foils dimensions and mass. The number in the last column refers to the total number of foils implemented in the simulations and in the measurements.

As should be evident, the foils have a diameter of approximately 0.6 cm, while the detector is a cylindrical device with a diameter of approximately 5 cm. Therefore the foil geometry cannot be considered point-like when those are in contact with the detector. As suggested by [123] (page 10-12), it is possible to overcome this issue by measuring the foils activities at a certain distance from the sensitive zone of the detector. In this position, the assumption is made that the point source approximation is sufficiently accurate to ensure a correct measurement.

In order to evaluate the correct distance, three main factors were considered:

- Longer distance means a reduction in the count rate (by a factor around $1/r^2$);
- The point source like approximation goodness is massively dependant by the sole geometrical aspects;
- The maximum possible distance between the detector and the foils for the experimental set-up was around 17 cm.

It should be noted that the accuracy of the point source approximation is also influenced by the gamma ray's energy. This is because the probability of Compton scattering, which is the dominant interaction mechanism for gamma rays with energy below 3 MeV, decreases as the photon energy increases. This leads to an increased likelihood of high-energy gammas escaping the detector, especially when they impinge the sensitive region with an angle that is not perpendicular.
This aspect is taken into account, since the effect due to the different energy of the gamma rays is considered in the subsequent calibration phase with sources of known activity and energy. Therefore, the only approximation made in this context concerns the simple spatial extension of the source itself.
In figure 4.7 a schematizing of the problem is shown:

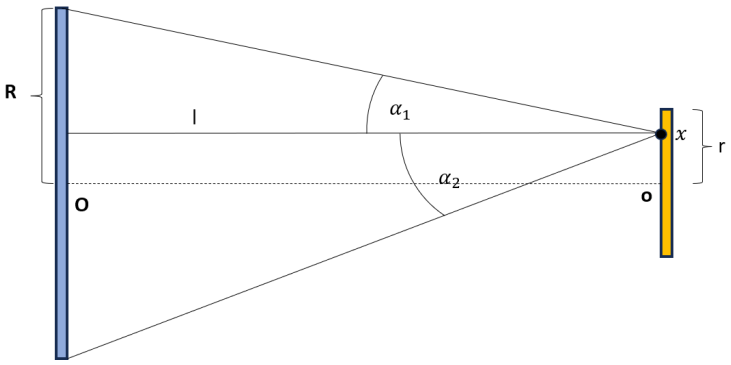

Fig. 4.7.: Geometric scheme of the situation. R is the radius of the HPGe depleted region, r is the radius of the foil, l is the distance between the foil and the detector and α_1, α_2 are the maximum angles for gammas emitted form a generic point (x) on the foil that can impinge on the detector.

The two angles α_1 α_2 can be simply derived by trigonometric considerations:

$$\begin{aligned} \alpha_1 &= arctan\Big(\frac{R-x}{l}\Big) \\ \alpha_2 &= arctan\Big(\frac{R+x}{l}\Big) \end{aligned} \tag{4.7}$$

Where should be noted that x is measured for the centre of the foil o. Thus, the total angle can be calculated simply like:

$$\alpha_{tot} = \alpha_1 + \alpha_2 = arctan\Big(\frac{R-x}{l}\Big) + arctan\Big(\frac{R+x}{l}\Big) \tag{4.8}$$

This set of equations describe the situation in which x>0. When x<0 the angles α_1 and α_2 must be exchanged.
In the ideal point source condition $x = 0$ and therefore the total angle (α^p_{tot}) can be written as:

$$\alpha^p_{tot} = 2 \cdot arctan\Big(\frac{R}{l}\Big) \tag{4.9}$$

For evaluating the discrepancies due to the geometric extension of the foils, the average angle coming from equation 4.8 is calculated:

$$\bar{\alpha_{tot}} = \frac{1}{2r}\Big[\int_0^r (\alpha_1 + \alpha_2)\, dx + \int_0^r (\alpha_2 + \alpha_1)\, dx\Big] \tag{4.10}$$

Where the limits of integration in the second integral have been changed from (-r,0) to (0,r) to avoid negative angle results.
Adopting the opportune variable changes one can obtain:

$$\bar{\alpha_{tot}} = \frac{l}{r}\Big\{\Big[t\cdot arctan(t) - \frac{1}{2}log(1+t^2)\Big]_{R/l}^{(R+r)/l} + \Big[u\cdot arctan(u) - \frac{1}{2}log(1+u^2)\Big]_{(R-r)/l}^{R/l}\Big\} \tag{4.11}$$

While the two new variables t and u are:

$$\begin{aligned} t &= \frac{R-x}{l} \\ u &= \frac{R+x}{l} \end{aligned} \tag{4.12}$$

Merging the two integrals and using the results from 4.9 and 4.11, the ideal case and the realistic one have been compared, varying the value of distance l:

$$D_{\%} = \frac{|\alpha_{tot}^{p} - \bar{\alpha_{tot}}|}{\alpha_{tot}^{p}} \tag{4.13}$$

In figure 4.8 the behavior of this quantity is shown:

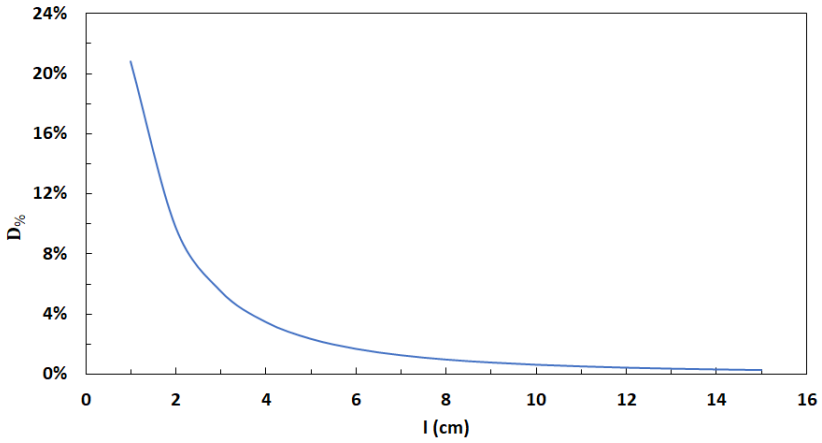

Fig. 4.8.: Percentage deviation form the point source condition plotted in function of the distance l between the detector and the foil.

As can be observed, for values of l greater than 8 cm, the value of D drops below 1%. When l = 10 cm, D=0.65%, and for the limit distance value (l=17 cm), D=0.23%. The advantage, therefore, in placing the foils at a greater distance would be minimal, resulting in a reduction in the count value by a factor of approximately 3. The value l=10 cm was then chosen for all subsequent measurements.

In order to evaluate the possible systematic uncertainties due to wrong foil placement, a parameter "d" has been introduced. This quantity represents the position shift while placing the foils.
The analytic approach is very similar and integral 4.10 should be changed in:

$$\bar{\alpha_{tot}} = \frac{1}{2r}\Big[\int_0^{r+d}(\alpha_1+\alpha_2)\,dx + \int_0^{r-d}(\alpha_2+\alpha_1)\,dx\Big] \tag{4.14}$$

Operating the same variables changing and solving the integrals, the value of $\bar{\alpha_{tot}}$ can be found.
Supposing an error during the displacement of 2-3 mm, the deviation respect the ideal case where the foils are perfectly aligned is 0.52%.

Under these conditions, the total systematic uncertainty S_{geom} due to the point source like approximation and due to the misplacing of the foils and the sources can be calculated:

$$S_{geom} = \sqrt{0.65\%^2 + 0.65\%^2 + 0.52\%^2 + 0.52\%^2} \simeq 1.2\% \tag{4.15}$$

4.4 Gamma spectra analysis algorithm

Throughout this study, it was necessary to analyze gamma spectra of varying complexity. To rigorously proceed with signal analysis, it is mandatory to accurately estimate the measurement background.
When examining a gamma spectrum, it is common to encounter contamination of counts in the photopeak, attributed to various factors. The discussion of background sources in a gamma spectrum is beyond the scope of this work. For further details, one can refer to [124] or any other book on the subject.

The chosen algorithm for the background analysis was based on the SNIP (Sensitive Non-linear Iterative Peak-clip) method. This method has been proposed by C.G. Ryan et al. [125] and was implemented into the ROOT CERN software by Morhac et al. [126]. A detailed analysis of the method will not be discussed in this work, but a general overview is reported.

The SNIP method was essentially based on the subdivision of the spectrum into three equal-width segments, symmetrically positioned around the channel of interest. The high and low-energy segments were assigned a negative sign and unit weight, while the central segment was assigned a positive sign and a weight of two. In regions of the spectrum where it is flat or varies slowly relative to the filter's size, the total area of the filter becomes zero. Mathematically, the filter can be represented as:

$$y'(i) = \sum_{j=i-n}^{i+n} \{2y(j) - y[j-(2n+1)] - y[j+(2n+1)]\} \tag{4.16}$$

Being *y(i)* the data in channel *i*, *y'(i)* the filtered data for channel *i*. The parameter n is selected such that (2n + 1) > FWHM for spectrum peaks. Through the filtered data, it becomes possible to ascertain the lower and upper boundaries of the peak regions.
Once upper and lower boundaries have been obtained, the background value in channel *i* can be extracted:

$$y = A\left\{ \sum_{j=b_1}^{i} [y(j) - y(b_1)] \right\} + y(b_1) \tag{4.17}$$

Where the A factor is given by:

$$A = \frac{y(b_2) - y(b_1)}{\sum_{k=b_1}^{b_2} [y(k) - y(b_1)]} \tag{4.18}$$

Since in many applications the counts *y(i)* can vary over many orders of magnitudes in the same spectrum, a dynamic range compression method has been applied. In particular, the counts *y(i)* have been transformed into a new quantity called *v(i)*:

$$v(i) = log\Big\{log[\sqrt{y(i)+1}+1]+1\Big\} \tag{4.19}$$

Utilizing the logarithmic operator enables operations across multiple orders of magnitude, and the square-root operator selectively amplifies small peaks. Beginning with v(i), the vectors v_1*(i)*, v_2*(i)*, up to v_m*(i)* are iteratively computed, where m is a specified parameter.
After the vector v_m*(i)* is calculated and the inverse LLS operator is applied, the resulting baseline spectrum can be obtained. This compression technique was firstly proposed by Hampton et al. [127] and it is called LLS compression since it applies twice the *ln* operator and once a *square root* operator
Benchmarks of this methods can be easily found in literature: [126], [127], [128], [129], [130].

Within the scope of this work, to assess the performance of the algorithm by setting the parameters in anticipation of subsequent measurements, a test was conducted. To perform this evaluation, two types of measurements were performed:

1. First, a set of measures of a ^{60}Co source has been performed and the counts per second (cps) under the photopeaks were extracted and than the mean values was calculated;

2. Secondly, the same ^{60}Co source was placed together with a source of ^{152}Eu which is characterized by a high number of emitted gammas. The cps under the Co photopeaks were extracted again and the new mean value was calculated again.

The aim of these measurements was to compare the cps obtained into the two different measurements and evaluate the systematic uncertainty due to the SNIP algorithm. Figures 4.9 and 4.10 show an example of the two different spectra obtained in the described configurations.

As already mentioned, the cps under the two ^{60}Co peaks have been extracted using the formula:

$$\text{cps} = \frac{C_{tot}}{t_{live}} \tag{4.20}$$

Where, t_{live} is the live time registered by the acquisition program and C_{tot} are the total count under the peak.

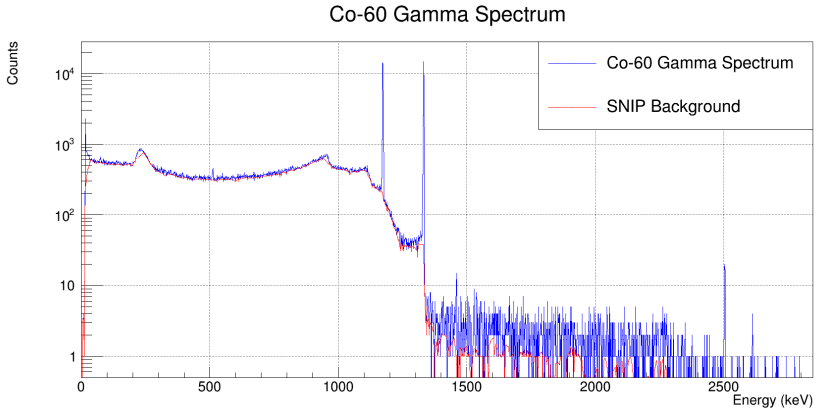

Fig. 4.9.: In blue the ^{60}Co gamma spectrum is shown. The red line is the SNIP prediction for the background.

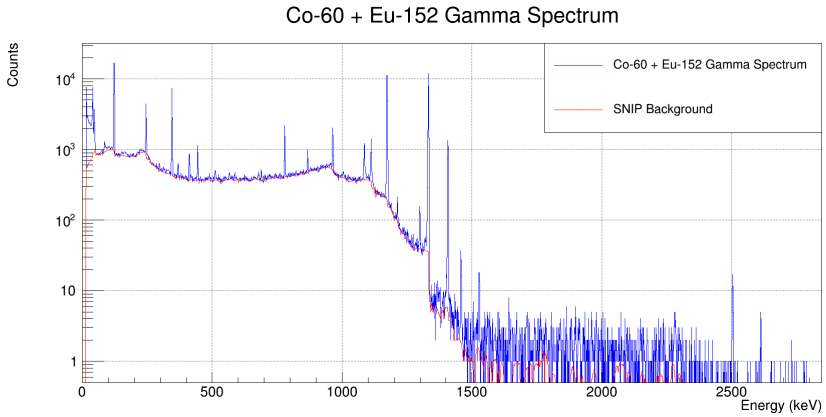

Fig. 4.10.: In blue the ^{60}Co + ^{152}Eu gamma spectrum is shown. The red line is the SNIP prediction for the background.

A total of 15 measurements using only the ^{60}Co source and 15 measurements with the ^{60}Co and ^{152}Eu were performed. The cps values were extracted and the mean value with the related standard deviation were calculated. Table 4.3 shows the results of the two different set of measurements:

Measure	^{60}Co	^{60}Co+^{152}Eu
mean cps 1173 keV peak	12.250 (0.066)	12.347 (0.161)
mean cps 1332 keV peak	10.903 (0.095)	10.902 (0.141)

Tab. 4.3.: Experimental data on the two different configurations.

To evaluate the compatibility between the two results, a normal test has been performed both on the cps from 1173 keV and 1332 keV peaks. The z variable was declared as:

$$z = \frac{|\text{cps}_1 - \text{cps}_2|}{\sqrt{\sigma^2_{cps_1} + \sigma^2_{cps_2}}} \tag{4.21}$$

Where cps_1 and cps_2 are respectively the mean cps calculated for the ^{60}Co and ^{60}Co + ^{152}Eu configuration.
The confidence level was set to $\alpha = 0.05$ and the critic value for the z variable was then $z_{crit} = 1.96$. The hypothesis H_0 is that the two values coming from different measures are not statistically different.
The calculated z values are 0.56 and 0.01. The H_0 hypothesis is therefore accepted and the two pairs of values can be considered coming from the same variable distribution. The confidence level α fixed before represents the probability to commit a first-species error.
To evaluate the systematic uncertainties due to the SNIP algorithm, the relative change in the cps values was used as a good indicator, yielding values of 0.79% and 0.01%.
This was established by the fact that the Eu gamma spectrum is highly complex (providing more than 100 different gammas), therefore this value should be considered as a pejorative estimation for the systematic uncertainty due to the SNIP algorithm.
It should be also noted that the standard deviations from the two different sets of measurements slightly increase in the Co+Eu measures, this is due to the higher order of complexity in the gamma spectrum.
Thus can be concluded that the SNIP algorithm is capable to correctly reconstruct the counts rate, in particular:

- **Precision:** since the standard deviation in the ^{60}Co + ^{162}Eu configuration is slightly higher, the precision of the SNIP algorithm is subject to a partially degradation while the complexity of the spectrum is increasing. Nevertheless, this phenomenon is quite limited and does not produce an alarming broadening in the distributions (from 0.6-0.8% it becomes 1.0-1.3%).

- **Accuracy:** since the cps values in the two configurations are perfectly compatible, the SNIP algorithm is highly accurate.

It should be noted that the statistics in both measurements were controlled to not exceed 30000 counts because of the fact that in the subsequent experimental measurements, the total counts were rarely higher than this value. This way, a better simulation of a typical experimental condition was produced.

The relative change was calculated as the maximum value between the two obtained changes:

$$S_{SNIP} = 0.79\% \tag{4.22}$$

4.5 HPGe efficiency calibration

As previously discussed in section 4.3, at a distance of 10 cm the effects of the foils geometry minimally contribute to the problem, and the point source like approximation can be assumed. It is therefore necessary to determine the efficiency value of the HPGe detector, in function of the gamma energy, for point sources placed at 10 cm. For this purpose, measurements were conducted with sources of known activity emitting gamma rays of different energies. These sources have very small dimensions (few millimeters in diameter), thus validating the point source like approximation at 10 cm. Specifically, the utilized sources are listed in table 4.4:

Source	Activity (kBq)	Reference Date	E_γ (keV)
^{133}Ba	37.0 (1.0)	15/04/2004	276.4 - 302.85 - 356.02 - 383.85
^{137}Cs	37.0 (1.0)	20/12/2018	661.66
^{22}Na	90.4 (0.4)	01/09/2019	1274.54
^{60}Co	19.87 (0.01)	30/01/2018	1173.23 - 1332.51
^{152}Eu	6.34 (0.29)	09/02/2022	121.78 - 244.7 - 344.28 - 411.11 443.97 - 778.9 - 867.37 - 964.0 1112.07 - 1408.0

Tab. 4.4.: List of sources used for the HPGe calibration with respective gamma energies used for the calibration.

It should be noted that placing the sources at 10 cm, also minimize the effect of the gamma coincidence. Regarding the ^{22}Na source, the positron annihilation and the subsequent gamma at 511 keV has not considered into the calibration procedure. This because it's not possible to establish the true position where the two 511 keV gammas are produced, since the positrons travel in the source disk and even outside the source. In order to avoid any systematic error in the calibration procedure, only the gamma at 1274.54 keV has been considered.

In figure 4.11 the scheme of the conducted measurements is shown. The distance value refers to the gap between the detector surface and the top of the source holder.

The activity values at the date of the calibration have been evaluated using the well known formula 4.23.

$$A(t) = A_0 e^{-\Delta t/\tau} \tag{4.23}$$

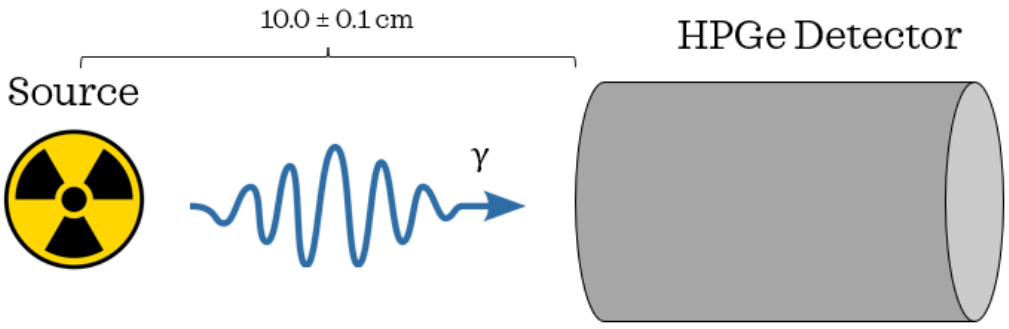

Fig. 4.11.: Scheme of the source calibration measurements set up.

Being A_0 the initial activity at the reference time, Δt the time interval between the calibration date and the reference one and τ the mean life time of the selected nucleus.
For extracting the detector efficiency ϵ values the formula 4.24 has been applied:

$$\epsilon = \frac{\text{cps} \cdot G}{A \cdot B.R.} \tag{4.24}$$

Where B.R. is the branching ratio for the gamma emission (the data have been taken from [108]) and G is a geometric factor due to the thickness of the sources. Placing the disk containing the source at 10 cm, the real distance of the source is slightly higher than 10 cm. Measuring the thickness t of the source disk (expressed in cm), the geometric factor G can be calculated as:

$$G = \frac{(10 + t/2)^2}{10^2} \tag{4.25}$$

Due to the thin source geometry, the highest value for the G factor was G_{MAX} = 1.030 (0.012).
The uncertainty on the ϵ has been calculated propagating the uncertainties on the G factor, on the calculate activity A, on the cps count and on the B.R. values. Thus, the quadratic sum of the relative uncertainties was evaluated:

$$\left(\frac{\sigma_\epsilon}{\epsilon}\right)^2 = \left(\frac{\sigma_A}{A}\right)^2 + \left(\frac{\sigma_{\text{cps}}}{\text{cps}}\right)^2 + \left(\frac{\sigma_{\text{G}}}{\text{G}}\right)^2 + \left(\frac{\sigma_{\text{B.R}}}{\text{B.R.}}\right)^2 \tag{4.26}$$

In order to low the counts uncertainty, the measurements time has been tuned to be sufficiently long to collect at least 10^5 counts under the different photopeaks, corresponding to a pure poissonian uncertainty lower than 0.3%.
Figure 4.12 and 4.13 show two examples of gamma spectra coming from the Eu and Ba measurements:

After calculating all the efficiency values at the different energies, an interpolation fit to extract the functional form that best represented the efficiency as a function of

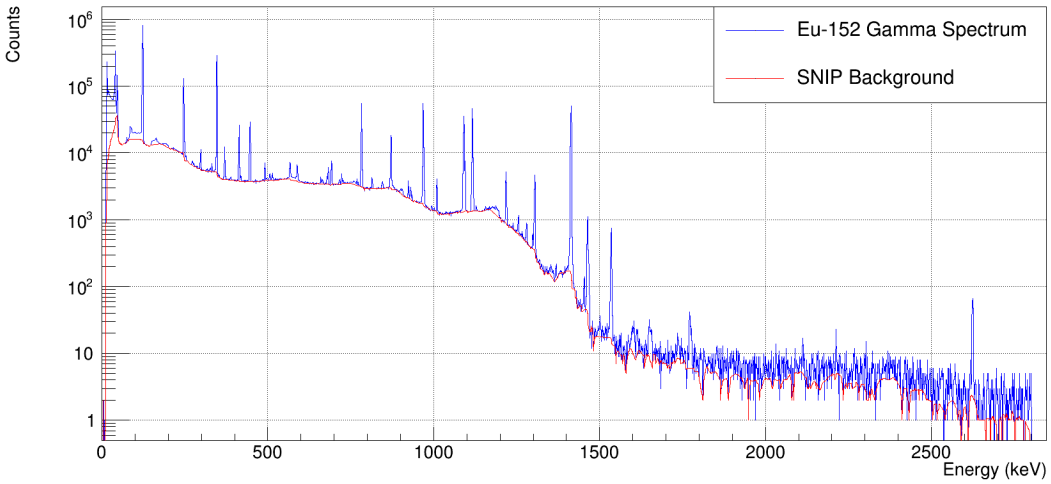

Fig. 4.12.: In blue the overall gamma spectrum for the ^{152}Eu is shown. The red line is the SNIP estimation for the background.

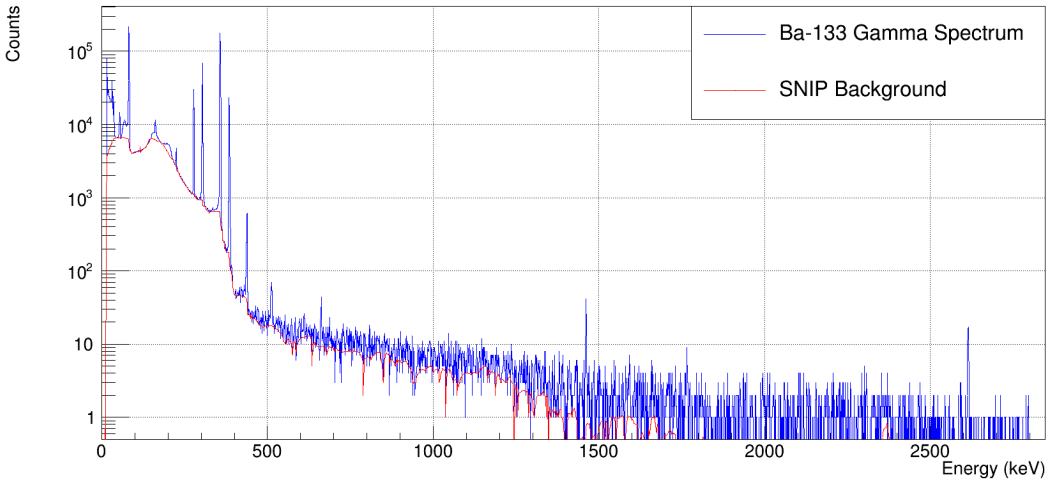

Fig. 4.13.: In blue the overall gamma spectrum for the ^{133}Ba is shown. The red line is the SNIP estimation for the background.

energy was applied. To carry out this procedure, the interpolation formula proposed by Debertin et al. [124] (page 213-222) was employed:

$$log\,\epsilon = \sum_{j=0}^{n} a_j \Big(log\frac{E}{E_0}\Big)^j \qquad E_0 = 1keV \tag{4.27}$$

This relation can be used for energy range from about 60 keV up to 3 MeV. It should be noted that it is a polynomial function in the logϵ-logE space.
Commonly the order of the polynomial is between 2 and 3. The procedure of increasing n to 4 or higher is of limited usefulness. In fact, the number of points must be consistently higher respect to the number of free parameter. Otherwise oscillation can be introduced in the fit, producing unrealistic situations.
In the analyzed case, the number of measured points is 18, so a polynomial grade of 3-4 should be the maximum explorable.

The first attempt has been proposed with a polynomial order of 2, but the relative uncertainties on the fit parameters where too high (50-60%) causing a massive uncertainties on the calculated values for the efficiency. Therefore, a grade 3 polynomial has been used.
The result of the fit is shown in figure 4.14.
The χ^2 value is 5.739. For the significance level α=0.05 and 14 degrees of freedom, the χ^2_{crit} is fixed to 23.68. Therefore, the H_0 hypothesis that the fitting function is correctly approximating the set of data can be accepted.

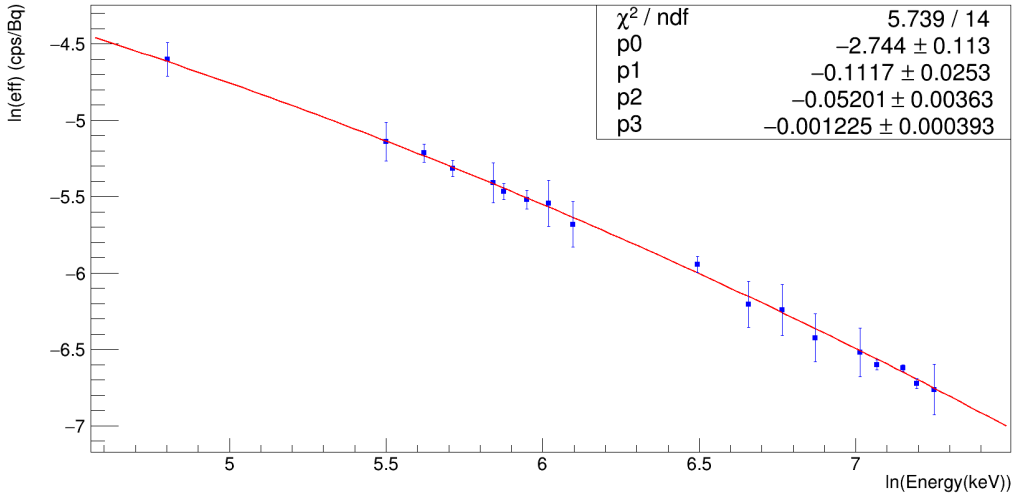

Fig. 4.14.: Fit for the logϵ-logE distribution for the sources placed at 10 cm by the detector.

The used fitting function in 4.14 using the pi parameters as shown is:

$$ln\epsilon = p_0 + p_1 ln\frac{E}{E_0} + p_2\left(ln\frac{E}{E_0}\right)^2 + p_3\left(ln\frac{E}{E_0}\right)^3 \tag{4.28}$$

The goal of the calibration procedure is to obtain the efficiency values for the gamma energies of chosen elements (table 3.13). These energies are (listed not in ascending order): 1293.5 keV, 137.2 keV, 411.8 keV, 479.6 keV, 155 keV, 846.8 keV, 511 keV, 1368.6 keV, 1434.1 keV, 1642.7 keV.
Once extracted the p$_i$ values from the fit, for obtaining the ϵ values the formula 4.28 can be easily used. It should be noted that, to evaluate the uncertainties on the ϵ values, particular attention must be paid to the massive covariance contribute to the final uncertainties.
The standard partial derivative approach was used:

$$\sigma_\epsilon = \sqrt{\sum_i \left(\frac{\partial\epsilon}{\partial p_i}\right)^2 \sigma^2_{p_i} + \sum_{i\neq j} \frac{\partial\epsilon}{\partial p_i}\frac{\partial\epsilon}{\partial p_j}\text{cov}(p_i, p_j)} \tag{4.29}$$

The results of the calculations are shown in table 4.5, for greater clarity, the relative percentage error is also reported.

Element	Gamma Energy (keV)	ϵ (x10^{-3} cps/Bq)	σ_ϵ/ϵ
^{116m}In	1293.5	1.276 (0.020)	1.55%
^{198}Au	411.8	3.822 (0.076)	1.99%
^{56}Mn	846.8	1.958 (0.025)	1.30%
^{64}Cu	511	3.151 (0.054)	1.72%
^{24}Na	1368.6	1.201 (0.020)	1.63%
^{38}Cl	1642.7	0.989 (0.019)	1.96%
^{52}V	1434.1	1.144 (0.019)	1.70%
^{187}W	479.6	3.339 (0.060)	1.80%
^{186}Re	137.2	9.11 (0.31)	3.42%
^{188}Re	155	8.34 (0.27)	3.26%

Tab. 4.5.: Efficiency values for the gamma energies level of the activated nuclei, considering the selected elements used in NCT-ACS.

It should be noted that the relative uncertainties are almost in all cases below 2%. During the first approach the covariance terms were not included in the uncertainties propagation, leading the efficiency values to be affected by uncertainties in the order of 40-50%.

The only values which are affected by uncertainties higher than 2% are related to the Re case and are characterized by low gamma energy. Being on the low energy part, the fluctuations on the fit parameters can more sensibly affect the final value on the uncertainty.

On the opposite way, the efficiency value for Cl has to be carefully considered, because is quite far the range where experimental data have been collected (1643 keV while the maximum experimental value is at 1408). When doing extrapolation, one has always to be cautious. In this specific case, Cl has not produced any troubles since its activation could not be measured due to the low neutron fluence rate. For future application, in higher fluence rate facilities, the value of efficiency for the Cl photopeak energy has to be re-calculated, using higher energy calibration source (e.g. ^{88}Y with E_γ=1836 keV).

4.6 Geometric factor calculation

In order to evaluate the absolute activity of the foils, it is possible to simply conduct measurements at a distance of 10 cm from the detector. In this case, using the efficiency calibration curve allows a direct determination of the activity value. However, this measurement demands either extremely high activity levels or prolonged exposure times.
In particular, long exposures are not feasible for elements characterized by a short half-life time. Therefore, the only alternative is to obtain extremely high activities at the end of the irradiation. However, two difficulties can be encountered:

1. If the induced activities are high, radiation protection measures must be even more stringent, potentially hindering the verification of proper foil placement and the smooth execution of the experiment.

2. The maximum achievable activity is linked to the fluence rate of the neutron facility used. Beyond a certain value, inducing further activity becomes not possible.

To circumvent these issues, several measurements were carried out to acquire gamma spectra by placing the foils directly in contact with the detector. This approach not only facilitates the estimation of the activities of all the foils but also enables the performance of measurements without generating high activity levels, thereby reducing the radiation exposure hazard. Additionally, under these conditions, measurements are significantly faster, permitting a quicker assessment of working conditions.

The conducted measurements followed this procedure:

- The selected foils were irradiated at the e-LiBaNS facility in a "non-standard" condition. In particular, the cadmium shield for the epithermal cavity (section 2.7.1) was removed, and the foils were irradiated bare and outside the HDPE sphere. In this scenario, the spectrum and fluence rate are not precisely known, but it's established that the thermal component ranges between 10^6 and 10^7 $cm^{-2}s^{-1}$. The bare foils, without cadmium shield and polyethylene sphere can be activated even more respect to the standard NCT-ACS configuration, as shown in the previous chapter. These conditions were necessary in order to obtain higher activation values.

- The gamma spectrum produced by the foils was measured under two conditions: at a distance of 10 cm and in direct contact with the detector.

- By applying appropriate corrections, the loss of activity during the measurement is assessed, followed by an evaluation of the count-per-second (cps) ratio in the two configurations.

- The estimated ratio denotes the geometric scaling factor between the induced counts in contact and at distance.

It should be noted that during this procedure, knowing the neutron fluence rate or the spectrum is unnecessary as it's aimed solely at deriving a geometric scaling factor. By establishing a ratio, the dependence on the neutron beam parameters is eliminated.
Figures 4.15 represents a scheme of the described measurements. The distances are measured from the detector surface (Aluminum end cup) to the bottom of the foils.

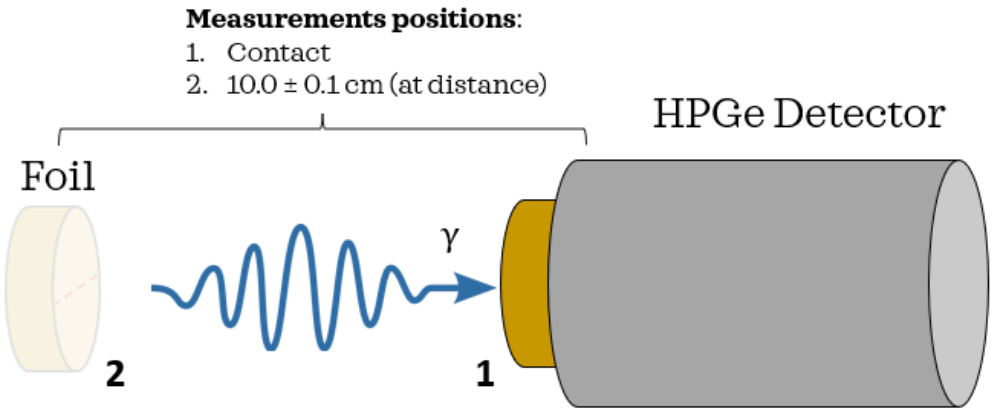

Fig. 4.15.: Measurement setup scheme. The in-transparency cylinder refers to the positions at a distance of 10 cm, while the full color one refers to the contact position. The same holder used for the source calibration was employed.

It is fundamental to recall the formula for the activity after an irradiation and waiting time respectively t_{irr} and t_{wait}:

$$A(t_{irr}, t_{wait}) = A_r(1 - e^{-\lambda t_{irr}})e^{-\lambda t_{wait}} \tag{4.30}$$

During this measures, the irradiation time can be fixed to be infinite and the waiting time for the first measurement can be fixed to zero, with this assumptions, the activity during the first measurement (at contact or at a distance) is considered to be equal to a hypothetical saturation activity.
The cps for the first measurement must be corrected for a decreasing in the activity value during the gamma analysis, this factor (k_c, where c means *counting*) can be

calculated making the ratio between the initial value of activity A_0 and the mean integral value of the well-known function Activity-Time:

$$k_c = \frac{A_0}{\bar{A}} = \frac{A_0}{1/t_c \int_0^{t_c} A(t)dt} = \frac{t_c}{\tau\left(1 - e^{-t_c/\tau}\right)} \tag{4.31}$$

Where t_c is the total measurement time, the so-called real time.
It should be noted that for long half life time elements, the Taylor approximation can be used and the factor can be proved to be close to 1. It becomes relevant for t_c comparable to the mean life of the elements, this condition can be reached by the short mean life time elements, on this case only by V, In and Na (long measuring time is required).

Conversely, the cps for the second measurements must be corrected not only for the factor k_c, but also for a factor due to the time delay by the beginning of the first measurements. In fact, during this time, the activity is decreased by a factor:

$$k_d = e^{-\frac{t_d}{\tau}} \tag{4.32}$$

Being t_d the delay time between the two measurements. It can be noted, that also in this case, for long half life time elements, the corrective factor k_d is close to 1. In any case, these factors were adequately implemented during the analysis to correctly estimate the results.
Identifying the cps of the first and second measurements with cps_1 and cps_2, the so-called **Geometric Factor (F_G)** can be calculated:

$$F_G = \frac{cps_1}{cps_2} \frac{k_{c,1}}{k_{c,2} k_{d,2}} \tag{4.33}$$

For a more clear interpretation of the presented values, the ratio of cps in contact versus at a distance will consistently be provided. It's important to note that the in-contact measurement was not always conducted first. Nonetheless, all necessary corrections were applied in each instance.

Since the e-LiBaNS cavity was used in a not-standard mode, the irradiation parameters hold no direct relevance to the conducted measurements. For illustrative purposes, the main parameters adopted in these measures are listed.

1. **Irradiation time**: around 40 min

2. **Expected thermal fluence rate:** 10^6-10^7 $cm^{-2}s^{-1}$

3. **Waiting time:** around 6-8 min

4. **Gamma measures duration:** variable between 5 min and 1 h for contact conditions and between 10 min and 60 h for distance measures.

Where possible, longer measurements were conducted to accumulate better statistics. In certain cases, additional measurements were performed during subsequent irradiations. These measurements proved helpful in reducing the final uncertainty associated with the geometric factor value.

It should be noted that for short measures only SNIP background corrections were applied, but for longer measurements (t>1 h) a background measurement was acquired and a subtraction was performed, after time normalization.
This correction was completely negligible for almost all the cases, providing a confirm on the SNIP consistency. The only cases where some differences were noted have been the Cu case. Differences in the order of 6% were encountered for the distance measurement conditions. This aspect was easily predictable, since in the natural background spectrum a peak at 511 keV can be found in all the measurements. The Cu gamma energy is on the same value and so the total counts under the peaks are an over estimation of the real counts.
The proposed correction was then applied for all the Cu measurements, also for the shorter ones. For all the other elements, the differences were below the systematic uncertainties, so no more corrections have been introduced.

In table 4.6 the results obtained during the different measures are shown:

Element	**Gamma Energy (keV)**	**F$_G$**	σ_{F_G}/f_G
^{116m}In	1293.5	16.57 (0.22)	1.33%
^{198}Au	411.8	21.37 (0.28)	1.32%
^{56}Mn	846.8	19.31 (0.31)	1.61%
^{64}Cu	511	20.61 (0.26)	1.26%
^{24}Na	1368.6	17.68 (0.43)	2.43%
^{38}Cl	1642.7	-	-
^{52}V	1434.1	19.63 (0.48)	2.45%
^{187}W	479.6	19.18 (0.25)	1.30%
^{186}Re	137.2	21.40 (0.52)	2.43%
^{188}Re	155	18.60 (0.68)	3.66%

Tab. 4.6.: Geometric factor values for the selected elements that will be used in NCT-ACS.

Before proceeding with the study, some considerations should be done:

- All the geometric factor values are in the range between around 17 and 21, meaning that the solid angle aspect is dominating above the effects due to the energy of the emitted gamma and the thickness of the foils. Still some significant variation can be found especially on the case of the In foil;

- Where more measurements have been performed, the mean value has been chosen as the estimator of the final value and the standard deviation was used for the uncertainty value. The weighted mean uncertainty was not used to do not underestimate the total uncertainty. In fact, despite the normal mean and the weighted mean were almost equal, the uncertainties on the different measures were quite low due to the high counts obtained (almost always below 1%). Thus, the dispersion of the points was much higher respect to the estimated uncertainty on the weighted mean. For these reasons the standard deviation was considered to be more indicated as estimator for the final uncertainty;

- The chlorine measurements did not provide enough statistic to evaluate the geometric factor, neither for the contact condition. Therefore the calibration for that element was abandoned;

- The slightly higher uncertainties in the case of Na, V and Re are due to lower number of measurements and also difficulties on achieving a good statistics (Na and V).

To better understand the measurements conditions, the gamma spectra for Au and V are shown in figure 4.16 and 4.17. The two measurements are in someway opposite. The Au measurements have been one of the easiest, since the long half life time, the time delay was not playing an important role and an high statistics was achievable in almost all the conditions. On the other side, the V measurements have been by far the most challenging. The low half life time imposed to be very fast in measuring this element using the HPGe detector, and a compromise between the statistics on a single measurement and the overall uncertainty has been necessary. Enhancing the statistics on the first measurement (generally at contact) would decrease the statistics on the second measure leading to a high final uncertainty on the geometric factor. After many attempts, the best combination was found to be composed by around 1 half life time at contact for the first measurement (250-300 s) and 3 half life times at distance (800-900 s).

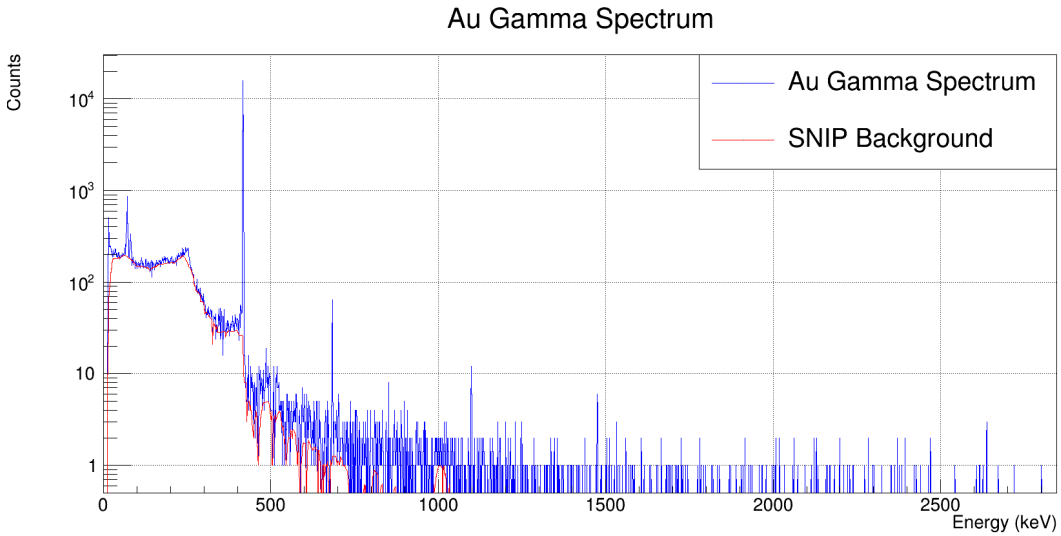

Fig. 4.16.: Au gamma spectrum, the photo peak at 411 keV is clearly visible. For this measurements: t_{real} = 1481 s, counts=19878 (146), DT = 0.08%.

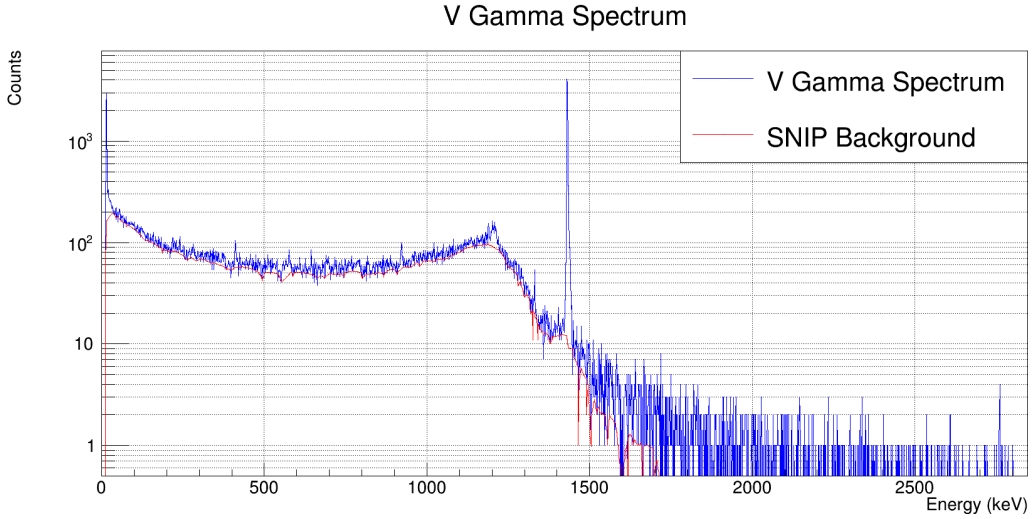

Fig. 4.17.: V gamma spectrum, the photo peak at 1434 keV is clearly visible. For this measurements: t_{real} = 186 s, counts=10126 (113), DT = 0.82%.

4.7 Summary of the calibration results

In this section, a summary of various measurements and the calibration results of the HPGe used in this study are presented.
These operations were fundamental for conducting subsequent measurements under optimal experimental conditions. The calibration scheme is outlined as follows:

1. The HPGe energy calibration ha been performed using calibration sources (^{137}Cs,^{60}Co,^{22}Na,^{152}Eu,^{133}Ba).

2. An efficiency calibration of the detector was carried out by placing the same known-activity sources at a distance of 10 cm. A fit curve of the data was calculated and employed as the calibration curve.

3. The foils, selected for NCT-ACS, were irradiated at the e-LiBaNS facility under non-standard conditions, aiming to induce high activity values.

4. The foils were then analyzed at two different positions relative to the HPGe detector: at 10 cm and in direct contact.

5. The ratio of the estimated cps from the two measurements was derived after necessary corrections, defining the geometric factor. The assumption to a point-like source was estimated to produce a systematic error within approximately 1.2% under the used measurement conditions;

6. With the obtained values, the foils activation can be analyzed by placing them in contact with the detector. This approach allow for reducing neutron irradiation and gamma spectrum acquisition times. Additionally, it allows for increased statistical counts, while maintaining relatively low levels of radioactivity. This process effectively reduces the risk of unwanted radiation exposure during the experimental procedure.

The HPGe detector efficiency values for the different elements used in NCT-ACS are reported in table 4.5, while the geometric factors of the foils are reported in table 4.6.
Combining the values in these tables, the HPGe detector efficiency for the different foils at contact can be determined simply multiplying the two set of values:

$$\epsilon_c = \epsilon_{10} \cdot F_G \tag{4.34}$$

Being ϵ_c the efficiency at contact, ϵ_{10} the efficiency at 10 cm and F_G the geometric factor.

Element	Gamma Energy (keV)	ϵ_c (x10^{-2} cps/Bq)	$\sigma_{\epsilon_c}/\epsilon_c$
^{116m}In	1293.5	2.11 (0.04)	2.0%
^{198}Au	411.8	8.29 (0.20)	2.4%
^{56}Mn	846.8	3.78 (0.08)	2.1%
^{64}Cu	511	6.49 (0.14)	2.2%
^{24}Na	1368.6	2.12 (0.06)	2.8%
^{38}Cl	1642.7	-	-
^{52}V	1434.1	2.25 (0.07)	3.1%
^{187}W	479.6	6.40 (0.14)	2.2%
^{186}Re	137.2	19.5 (0.8)	4.1%
^{188}Re	155	13.8 (0.7)	5.1%

Tab. 4.7.: Efficiency at contact values for the gamma energies of the selected elements used in NCT-ACS.

During the HPGe calibration two sources of systematic uncertainties have been evaluated due to the point source like approximation (section 4.3) and due to the use of the SNIP algorithm during the analysis of the gamma spectra (section 4.4). The overall contribute can be calculated:

$$S_{\text{HPGe}} = 1.4\% \tag{4.35}$$

5 NCT-ACS proof of concept

In this chapter, the results obtained from measurements conducted at the e-LiBaNS facility are presented. The initial part discusses the outcomes of measurements conducted using the *thermal configuration* (section 2.7.1). These measurements served as a validation for the HPGe calibration procedure discussed earlier.

Subsequently, the measurements conducted with the final NCT-ACS geometry, which were performed utilizing the e-LiBans cavity in the *epithermal configuration* (section 2.7.1), are presented.
In conclusion, the final section details the comparison between the experimental results and the simulated ones

5.1 Thermal measurements

The thermal fluence rate for the e-LiBaNS facility operating in thermal mode is well known and has been measured with calibrated detector [118].
In order to validate the HPGe calibration, a set of fluence rate measurements have been performed using some of the selected foils that will be included in the final NCT-ACS geometry.
In particular, couples of the different foils have been exposed simultaneously around the central point of the cavity. In figure 5.1 an example with two couples of Au foils is shown.
For each couple, one of the foils was inserted in a small cadmium cover with a thickness of 0.50 mm and the other was exposed bare. This allows to calculate the pure thermal component of the fluence rate by subtracting the activation due to the non thermal component (corresponding to the residual activation in the cadmium covered foil) to the total activation of the bare foil. The important role of the cadmium shield has been already explained in chapter 3.

It should be noted that this procedure has not been performed for all the selected elements. In fact, the NaCl, Re and W foils were purchased in a second phase and the thermal photoconverter was already dismounted and the epithermal facility was set up. Thus, this measure was conducted with the In, Au, Mn, Cu and V foils.

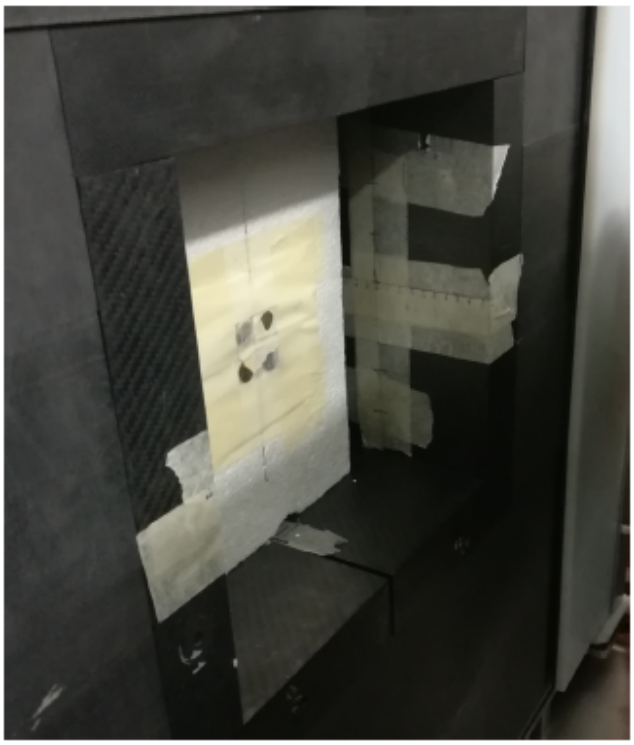

Fig. 5.1.: ^{197}Au foils positioned in the e-LiBaNS thermal cavity during the measurement. Two couple of foils are exposed simultaneously around the centre of the cavity.

5.1.1 Corrective factors evaluation

Equation 3.12 indicates how to calculate the thermal neutron fluence rate once the activity at saturation is known, even if some corrections must be taken into account for better estimation of the flux. A formalism coherent with NPL report DQL RN008 [115] was adopted to determine the conventional thermal fluence rate $\dot{\Phi}_W(th)$ as reported below.

$$\dot{\Phi}_W(th) = \frac{(A_{bare} - \frac{F_b}{F_a} A_{Cd})}{N \cdot \sigma_0 \cdot g} F_c F_d \tag{5.1}$$

where σ_0 is the nominal cross section, N the atom density and g is the Westcott factor correcting for the deviation of the element cross section from the ideal 1/v behaviour. The role of the four factors F is the following:

- F_a corrects for the incomplete thermal neutron attenuation in the Cd cover.
- F_b corrects for the epithermal neutrons attenuation in the Cd cover.
- F_c corrects for the self absorption of the thermal neutrons in the foil. It can be expressed like:

- F_d corrects for the self absorption of the emitted gamma in the foils after the activation.

The influence of each correction depends on the foils and cadmium geometry and on the energy spectrum of the neutron field. For this reason, the values of these three factors for the e-LiBaNS neutron flux have been calculated with appropriate Monte Carlo simulations. Three geometries have been simulated with MCNP6: a bare foil, a foil covered with a cadmium layer (both are called *real*) and an empty cell equal to the foil (called *vacuum*). The neutron spectrum resulting from the complete simulation of the e-LiBaNS photoconverter was used as a source to calculate the number of capture reactions, or integrated capture cross section, in the three conditions.
For every result, the contribution of neutrons with energy below the cadmium cut-off (0.5 eV) is distinguished from the effect due to neutrons above Cd cut-off. The calculated factors for all the used elements are reported in table 5.1.
The factor uncertainties are calculated by propagating the statistical uncertainty associated to the simulation results.

Element	$\mathbf{R}_a$	$\mathbf{R}_b$	$\mathbf{R}_c$	$\mathbf{R}_d$
In	1.0278 σ_a = 0.0079	1.0696 σ_b = 0.0082	1.1834 σ_c = 0.0031	1.0108 σ_d = 0.0010
Au	1.015 σ_a = 0.013	1.036 σ_b = 0.013	1.0694 σ_c = 0.0020	1.0796 σ_d = 0.0012
Mn	1.073 σ_a = 0.027	1.063 σ_b = 0.024	1.0113 σ_c = 0.0045	1.0175 σ_d = 0.0010
Cu	1.085 σ_a = 0.051	1.088 σ_b = 0.054	1.0088 σ_c = 0.0045	1.0617 σ_d = 0.0011
V	1.060 σ_a = 0.014	1.095 σ_b = 0.015	1.0310 σ_c = 0.0046	1.0240 σ_d = 0.0011

Tab. 5.1.: Correction factors obtained by simulation.

The equations to calculate the four factors are:

$$F_a = 1 + \frac{\sigma_{\Phi,ipo}(real,\, Cd)}{\sigma_{\Phi,epi}(real,\, Cd)} \tag{5.2}$$

$$F_b = \frac{\sigma_{\Phi,epi}(real,\, bare)}{\sigma_{\Phi,epi}(real,\, Cd)} \tag{5.3}$$

$$F_c = \frac{\sigma_{\Phi,ipo}(real,\ bare, vacuum)}{\sigma_{\Phi,ipo}(real,\ bare)} \tag{5.4}$$

$$F_d = \frac{N_\gamma(vacuum)}{N_\gamma(real)} \tag{5.5}$$

Where the term $\sigma_{\Phi,ipo}$ refers to reaction rate in the energy range *below* the cadmium cut (0.5 eV), while $\sigma_{\Phi,epi}$ refers to the reaction rate in the energy range *above* the cadmium cut.

5.1.2 Step irradiation factor evaluation

Considering equation 5.1, a correct estimation for the activity of the foils is fundamental for evaluating the thermal fluence rate.
Since the value of activity is determined by the irradiation and wait time (equation 3.12), the different phases must be well known. In particular, the LINAC machine can operate providing a maximum value of 1000 MU for each step. After a single step, a new one should be initialized. This operation takes a variable time depending by many factors and usually is in the order of 30-40 seconds. Therefore the activation formula should be modified to correctly fit the operational conditions. In fact all the time intervals between a step and the following has to be considered as a waiting time interval. Moreover, at the beginning of the next step the foil activity is not equal to zero and the equation should take into account of that.

Thus the value of the irradiation corrective factor $k_{irr} = 1 - e^{-\lambda t_{irr}}$ must be corrected. The model for considering all these aspects rise up from the differential equation:

$$dN = Rdt - \lambda N dt \tag{5.6}$$

Being *N* the number of new activated nuclei and *R* the activation rate. It should be noted that the positive term takes into account of the activation induced by the neutron irradiation, while the negative member considers the disintegration due to the natural decay.
The solution can be calculated as:

$$N(t) = \frac{R}{\lambda}\Big[1 - \Big(1 - \frac{N_0\lambda}{R}\Big)e^{-\lambda t}\Big] \tag{5.7}$$

In the case of the first irradiation step, the initial condition $N_0 = 0$ can be used. Thus, the number of activated nuclei after the first step N_1 is:

$$N_1 = \frac{R}{\lambda}\Big(1 - e^{-\lambda t_1}\Big) \tag{5.8}$$

Introducing a factor $e^{-\lambda t_{w,1}}$ due to the waiting time between the first and second irradiation step and using the result as a new value of N the solution of 5.7 is:

$$N_2 = \frac{R}{\lambda}\Big[1 - \Big(1 - \Big(1 - e^{-\lambda t_1}\Big)e^{-\lambda t_{w,1}}\Big)e^{-\lambda t_2}\Big] \tag{5.9}$$

In order to simplify the notation:

$$C_n(t_n) = \frac{\lambda}{R} N_{n+1} \tag{5.10}$$

Extending the procedure to a generic step number *n* and using the notation introduced in 5.10 one can obtain

$$N_n = \frac{R}{\lambda}\Big[1 - \Big(1 - C_{n-1}(t_{n-1})\Big)e^{-\lambda t_{w,n-1}}\Big)e^{-\lambda t_n}\Big] = \frac{R}{\lambda} \cdot k^*_{irr} \tag{5.11}$$

Where the saturation activity now can be correctly calculated using the new factor k^*_{irr} instead of the previous value k_{irr}.
It should be noted that this correction is more relevant for short half life time elements (mainly V and In), but become less important for the longer half life time nuclides. Nevertheless, to increase the precision of the measurements, such correction has been applied for all the elements.
Taking into consideration the V case and assuming irradiation steps of 180 s with pausing time of 30 s between two steps the activity induced in the foils shows a different behaviour respect to the same activity induced with a continuous irradiation. In figure 5.2 the two different case are shown, the relative activation value respect to the saturation activity was studied:

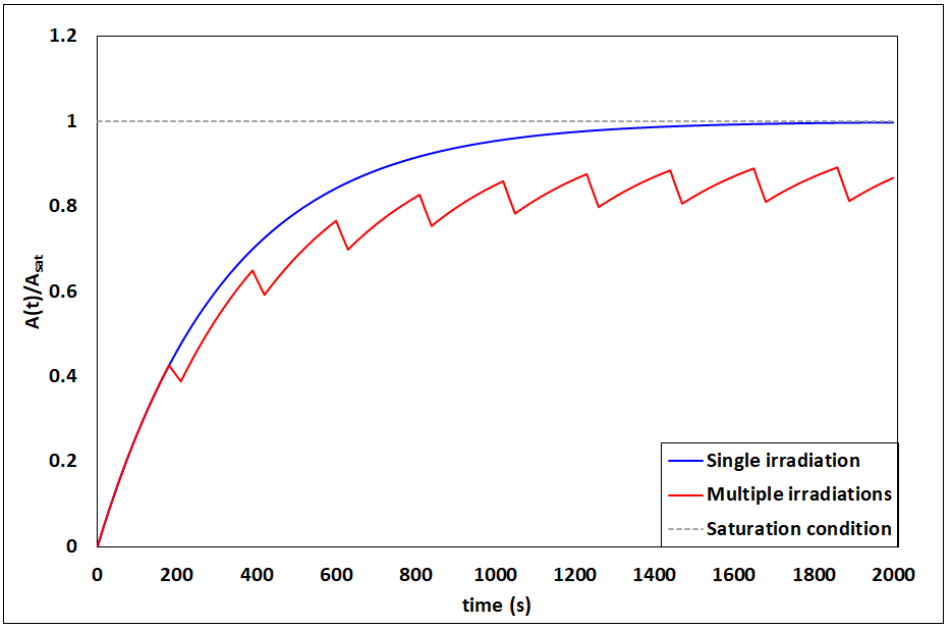

Fig. 5.2.: Activation trend considering two different options: single long irradiation (blue) and multiple short irradiation (red). The saturation condition is also shown as an asymptotic value.

It should be noted that considering a typical work condition of around 2000 s of irradiation; with a single long irradiation the saturation condition would have been almost achieved (99.84%), while in the case of multiple short irradiation (such for the LINAC work conditions), the activation value is only 86.62% respect to the saturation condition.
Thus the necessity to use the model presented in this section.

5.1.3 Experimental conditions and results

As already mentioned, couples of foils have been irradiated in the thermal cavity of the e-LiBaNS source and the sub-Cd subtraction technique has been used in order to extract the thermal fluence rate by the activation of the foils themselves.
To correctly estimate the fluence rate in the cavity, an active detector TNRD (Thermal Neutron Rate Detector) has been placed inside the cavity during the irradiation. Therefore the fluence rate value was on-line monitored. It should be noted that the TNRD calibration was operated in 2015 at the Casaccia reactor [131] [132]. In order to perform a new thermal fluence rate measurement, the detector has been newly calibrated at the HOTNES facility in Frascati (2.7.2). For a more in depth discussion about the calibration measurement and more detail on the TNRD detector please refer to appendix C. The results of the calibration revealed an excellent in-time stability for this detector. In fact the calibration factor changed only by 4% in more than 6 years.

It should be noted that some fluctuations in the absolute value of the thermal fluence rate can be registered, these variations are in the order of few % and can be easily appreciated using the TNRD.
Many measurements were produced with the different foils, below are shown the main parameters maintained during the experimental measurements. It should be mentioned that the individuals measurements can be characterized by slightly different set of parameters. Thus the following list has to be considered as a guideline description of the experimental conditions:

- **Irradiation time:** The total irradiation time was in the order of 2000 s divided into 10 irradiation steps. For each step an uncertainty of 2 s has been considered, providing a total uncertainty of around 0.3%.

- **Waiting time:** The overall waiting time was in the order of 600 s and the uncertainty on this value was considered to be equal to 2 s.

- **Integrated thermal fluence:** The total thermal fluence depends by the fluence rate and by the total time. Generally it was in the order of 10^9 $cm^{-2}s^{-1}$

It can be useful to bring back the activation formula:

$$A(t_{irr}, t_{wait}) = A_{sat}(1 - e^{-\lambda t_{irr}})e^{-\lambda t_{wait}} \tag{5.12}$$

Where the quantity A_{sat} represents the saturation activity as already discussed. Since the information about the thermal fluence rate is contained in this quantity, the cps at the saturation condition has been calculated and then a normalization on the mass value has been applied. Knowing the contact efficiency ϵ_{con} from table 4.7, the Activity value for both bare and suc-Cd foils have been extracted:

$$\frac{A}{m} = \frac{1}{m}\frac{\text{cps}_{sat}}{BR \cdot \epsilon_{con}} \tag{5.13}$$

The activation values were then calculated in both condition: bare and under cadmium shield. Table 5.2 reports all the experimental results with the propagated uncertainties:

Element	**A$_{bare}$ (kBq/g)**	**A$_{Cd}$ (kBq/g)**
In	655 (13)	51.7 (1.3)
Au	288 (5)	39.6 (0.8)
Mn	121 (3)	2.5 (0.3)
Cu	31.0 (2.0)	2.8 (0.5)
V	67.5 (2.7)	0.82 (0.05)

Tab. 5.2.: Experimental activity values normalized respect to the foil mass. Formula 5.13 and efficiency values in table 4.7 were used.

Applying the correction factors in 5.1 and considering the tabulated data for the cross section values [26] and for the Westcott factor [28], the value of the thermal neutron fluence rate in the photoconverter cavity, normalized to 400 MU/min, has been calculated using the different foils. The values are expressed in Westcott convention so that it has not any dependence on the true moderator temperature. The indicated errors represents one standard deviation:

Element	foil $\dot{\Phi}_{th}$ (10^6 cm^{-2} s^{-1})	TNRD $\dot{\Phi}_{th}$ (10^6 cm^{-2} s^{-1})	$t_{student}$
In	1.41 (0.02)	1.39 (0.03)	0.49
Au	1.39 (0.02)	1.39 (0.03)	0
Mn	1.44 (0.03)	1.48 (0.04)	2.43
Cu	1.38 (0.07)	1.44 (0.04)	0.90
V	1.59 (0.07)	1.48 (0.04)	2.05

Tab. 5.3.: e-LiBaNS thermal fluence rate measured with the activation foils technique and with the TNRD detector.

The last column in table 5.3 shows the values for the student variable. This test was preferred to the z test, since the population of measurements was not very large (in some cases 2-3 measures).
The statistical validity of the measurements is proved, since the obtained t values are lower than the critical values.

This measures prove that the whole procedure of analysis is under control and well known. Moreover, these result represent a strong validation of the HPGe efficiency results obtained in chapter 4.

5.2 Epithermal measurements

Since the goodness of the HPGe calibration was confirmed by measuring the thermal neutron filed at the e-LiBaNS facility, NCT-ACS has been studied using the epithermal source configuration. All the details about the working condition of the sources are presented in section 2.7.1.
It should be noted that for these specific measurements it has not been possible to use the TNRD detector, since its response in the epithermal energy range is not well known.

5.2.1 Experimental setup

The experimental setup was composed by:

- The e-LiBaNS LINAC facility, used coupled with the epithermal photoconverter. In figure 5.3 a picture of the source and photoconverter is shown;

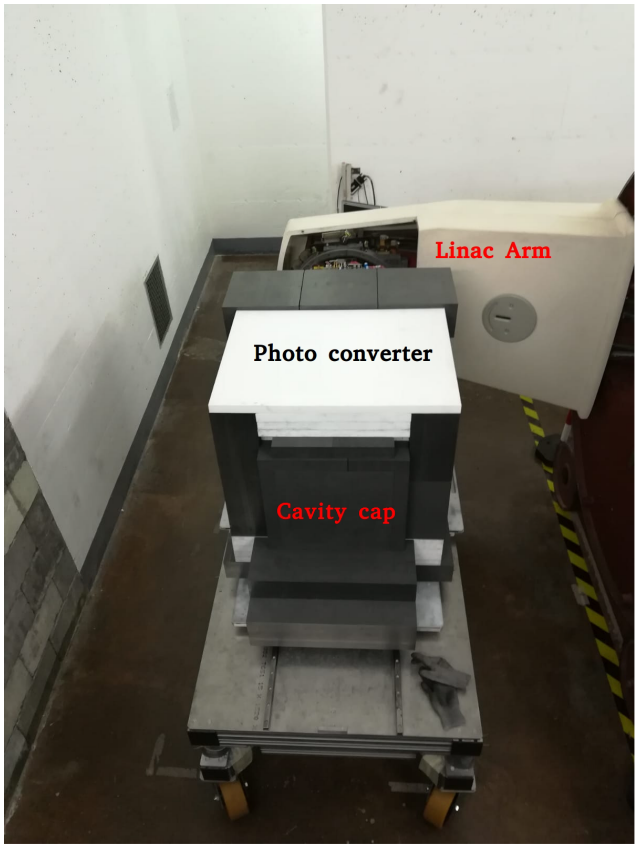

Fig. 5.3.: Picture of the epithermal neutron source facility. The photoconverter is placed on the table, along with its back cover wall (cavity cap). In the foreground the LINAC arm and the LINAC head, hidden behind the photoconverter. On the right, not visible in this picture, resides the LINAC gantry.

- NCT-ACS detector in its final geometry. Both 20 mm and 28 mm configurations have been tested. In figure 5.4 the two geometries are shown;

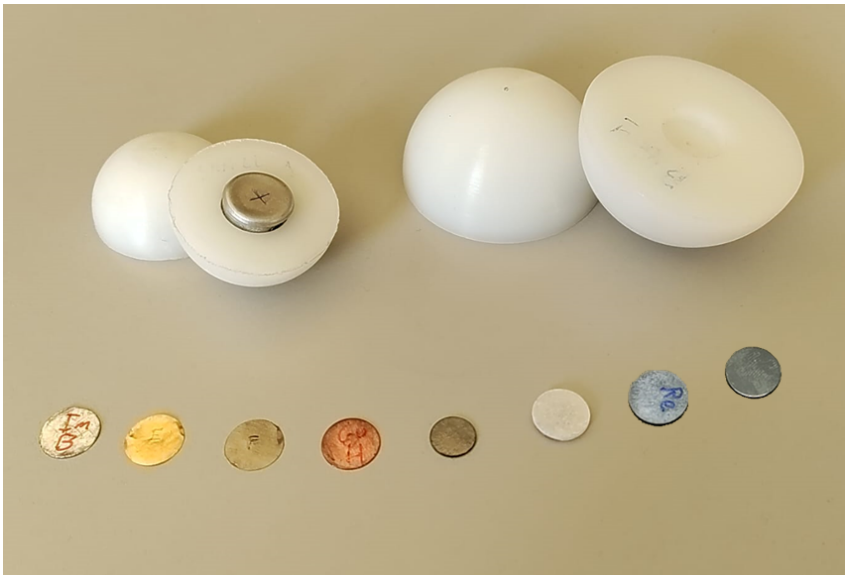

Fig. 5.4.: Picture of the two different NCT-ACS geometries. On the left the 20 mm configuration with the Cd cylinder is reported, while on the right the 28 mm option is shown. On the bottom the activation foils are also displaced, form left to right: In, Au, Mn, Cu, V, NaCl, Re, W.

- A specific holder that was placed in the middle of the e-LiBaNS cavity in order to hold NCT-ACS in the middle of cavity, where the best irradiation condition are achieved. Figure 5.5 shows the complete setup right before the begin of the irradiation

Fig. 5.5.: Picture of NCT-ACS on top of the holder in the irradiation position. The cavity volume is 30 x 30 x 20 cm^3. On the right the cavity cap is visible.

It should be noted that, while placing NCT-ACS on the holder, no particular attention was devolved to maintain the same orientation in the different measures. In particular, the first and second measurement with the 20 mm configuration were made rotating NCT-ACS respect two different axis. Thus an angle of around 90° was formed between those measurement.
A total of 6 different measurements have been performed using the e-LiBaNS epithermal modality: 1 measurements with the 28 mm configuration and 5 with the 20 mm one, divided as follow:

- 4 measurements with the 20 mm geometry and 6 foils: In, Au, Mn, Cu, V, NaCl corresponding to 6 sensitive elements (the Cl activity was too low to be correctly quantified);

- 1 measurements with the 20 mm geometry and 8 foils: In, Au, Mn, Cu, V, NaCl, W, Re corresponding to 9 sensitive elements (the Cl activity was too low to be correctly quantified);

- 1 measurements with the 28 mm geometry and 6 foils: In, Au, Mn, Cu, V, NaCl corresponding to 6 sensitive elements (the Cl activity was too low to be correctly quantified).

The 20 mm configuration was preferred since the epithermal fluence rate achievable at the e-LiBaNS facility was just sufficient to produce a good gamma counting statistics. Using the 28 mm configuration, a lower value on the counts statistic was obtained producing higher uncertainties during the analysis. Moreover the W and Re foils were purchased later and it was possible to use them only in the 20 mm configuration. This was due to a long shut down period of the LINAC machine and due to the long half life time of the ^{187}Re ($\simeq$ 90 h) that forced to be very careful with the radio protection rules.
Nevertheless, as will be shown in this section, an excellent compatibility between measurement in the same configuration (20 mm with 6 elements) has been obtained, proving the reproducibility of the experimental conditions.
For all the other configurations different from the 20 mm 9 elements, a new set of simulations have been performed in order to correctly describe the characteristics of the system, replacing the missing foils volumes with air.

The typical irradiation conditions were very similar to the conditions already shown for the thermal measurements. Contrary to the thermal conditions, the total fluence rate was around a factor 10 lower. Thus the integrated fluence was also reduced by around a factor 10. Longer irradiation times were not possible due to radio protection rules. Furthermore, the induced activation for the V foil (the most challenging

regarding the statistic counts) would not have been enhanced since the saturation condition was almost achieved with the standard irradiation time.
It should be noted that, contrary to what done for the thermal measurements, in this case no correction factors were needed. This because all the information about the self neutron absorption, not perfect cadmium shield etc.. etc.. were already included in the response matrix. The only corrective factor that has been considered is the F_d factor that corrects for the self absorption of the gamma inside the foil. In fact, this phenomenon is not included in the response matrix, since it appears in the gamma spectrum analysis and it's not relevant for the neutron irradiation phase. The R_d values for all the elements are listed in table 5.4 where the values for the Na, W and Re foils are implemented to the already reported values in table 5.1;

Element	$\mathbf{R}_d$
In	1.0108 σ_d = 0.0010
Au	1.0796 σ_d = 0.0012
Mn	1.0175 σ_d = 0.0010
Cu	1.0617 σ_d = 0.0011
V	1.0240 σ_d = 0.0011
Na	1.0360 σ_d = 0.0041
^{185}Re	7.212 σ_d = 0.043
^{187}Re	5.410 σ_d = 0.038
W	1.3562 σ_d = 0.0068

Tab. 5.4.: Complete set of F_d factors obtained by simulation.

It should be noted that for the Re foil the F_d factor is sensibly major than 1. This is due to the fact that the gamma energies for the ^{185}Re and ^{187}Re are respectively 137 keV and 155 keV, moreover the density of the rhenium is around 21 g/cm^3.

Therefore the self gamma absorption is more relevant.

The experimental conditions can slightly vary due to many factor, but they can be summarized as follow:

- **Irradiation time:** The total irradiation time was in the order of 2000 s divided into 10 irradiation steps. For each step an uncertainty of 2 s has been considered, providing a total uncertainty of around 0.3%.

- **Waiting time:** The overall waiting time was in the order of 600 s and the uncertainty on this value was considered to be equal to 2 s.

- **Integrated thermal fluence:** The total thermal fluence depends by the fluence rate and by the total time. Generally it was in the order of 10^8 $cm^{-2}s{-}1$

It should be mentioned that all the activation data that will be shown in the following sections are not normalized to the mass foil in order to directly quantify the activation values of the *real* foils configuration. Nevertheless, they are normalized respect to the operating rate of the LINAC, and the standard conditions of 400 MU/min as been considered as reference.
It should be noted that for the unfolding procedure, the activation data have been then normalized respect to the foils mass, following the work of Bedogni et al. [133].

5.2.2 Results with the NCT-ACS 20 mm configuration embedding 6 elements

As already mentioned, a total of 4 measurements have been performed in such configuration. The activation data was then normalized to the 400 MU/min reference working value. The activation values are calculated at the saturation condition, using the same procedure used for the thermal measurements. In particular, equation 5.12 and 5.13 have been used, in addition to the corrective factors in 5.4.

In table 5.5 the results coming from the different measurements are shown:

Element	Measure 1	Measure 2	Measure 3	Measure 4
In ($\cdot 10^4$ Bq)	1.11 (0.02)	1.12 (0.03)	1.09 (0.02)	1.07 (0.02)
Au ($\cdot 10^3$ Bq)	8.54 (0.20)	8.20 (0.17)	8.56 (0.20)	8.48 (0.19)
Mn ($\cdot 10^2$ Bq)	4.77 (0.13)	4.52 (0.13)	4.92 (0.14)	4.44 (0.12)
Cu ($\cdot 10^2$ Bq)	5.67 (0.17)	5.50 (0.16)	5.56 (0.17)	5.95 (0.18)
Na ($\cdot 10^1$ Bq)	8.93 (0.57)	9.44 (0.60)	8.36 (0.53)	8.65 (0.55)
V ($\cdot 10^2$ Bq)	2.83 (0.14)	2.69 (0.14)	2.65 (0.13)	2.68 (0.14)

Tab. 5.5.: Activation results for the 4 different measurements using the 20 mm configuration with 6 foils, corresponding to 6 sensitive elements.

As can be clearly seen, all the set of data are perfectly compatible between each other. In fact, the maximum z value between the different activation value for the same element has been calculated to be $1.79 < z_c$, therefore all the data can be considered being part of the same statistical population, with a significance level of 5%.
This aspect demonstrates the reproducibility of the measurement and should be considered as an evidence that the entire procedure is robust and under control.

In order to assess whether differences in saturation activity values lead to variations in the extracted spectrum, the unfolding procedure was iterated for each measurement set, and the results were compared to the outcome obtained with the Bonner Spheres Spectrometry (BSS), which is considered a reference value.
The guess spectrum provided to the FRUIT code and used in the unfolding procedure corresponds to the Monte Carlo-extracted spectrum with MCNP6. It should be noted that the spectrum derived from the BSS measurement is slightly different. Nevertheless, the same guessed spectrum used for BSS measurements was chosen to evaluate if NCT-ACS could process the data correctly and be comparable to the reference measurement.
In figure 5.6, the guessed spectrum and the unfolding result using BSS are shown.

All the uncertainties values have been extracted by the FRUIT code that calculates them propagating the experimental uncertainties and any uncertainties on the response curves. Since the resonance parameters have, in some cases, relevant uncertainties, a value of 5% has been used as response matrix uncertainty.

It should be mentioned that, unlike what was shown in section 3.3.3, in this case, it was not possible to establish a unique threshold for the percentage variation on the mean deviation $\bar{\lambda}$. A valid threshold was found to be around 3-4%. Initially, a 2% threshold was set as before, but reaching that value required numerous iterations that introduced non-physical structures. This could be explained as experimental

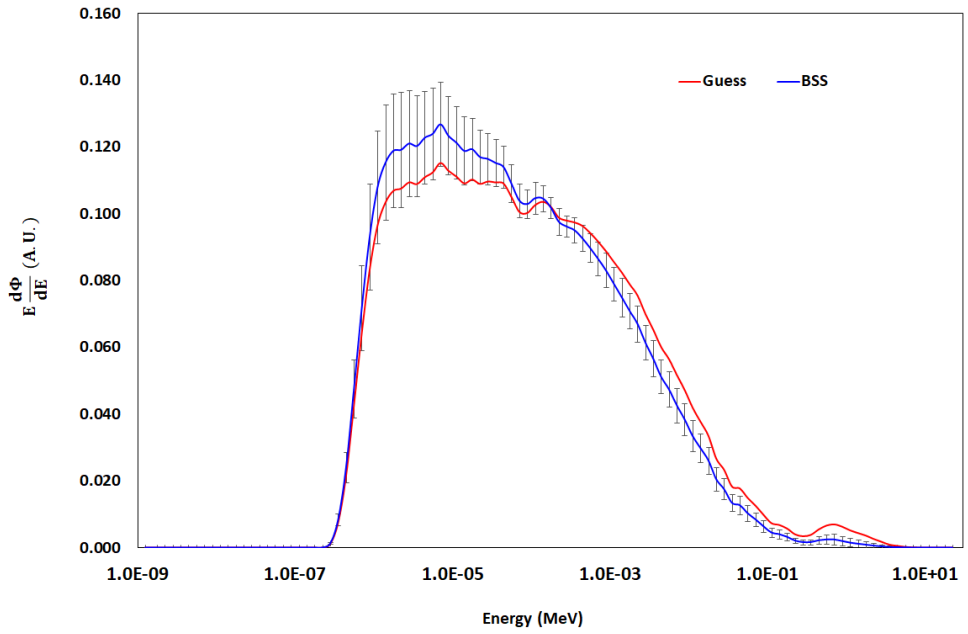

Fig. 5.6.: In red the Guess spectrum coming from the MCNP6 Monte Carlo calculations is shown, while in blue the BSS result is reported. The guess spectrum will be used for all the NCT-ACS elaboration data.

measurements being affected by statistical fluctuations leading to actual values varying around a mean value. In the scenario studied before, the results derived from a mathematical folding operation between response curves and the Monte Carlo spectrum, hence the fluctuations were much smaller since they were only associated with the Monte Carlo uncertainties, which are generally low.
Indeed, it is interesting that, when providing the actual expected spectrum (measured with BSS) to the unfolding algorithm, the procedure still altered the shape to minimize the chi-square, but this minimization only introduce lacked physical meaning.
The results of the unfolding procedure for the 4 cases are shown in figure 5.7:

Some considerations on the results should be done:

- The results obtained with the different data set are in agreement and perfectly comparable. Thus the conclusion that the experimental uncertainties do not sensibly affect the unfolding procedure.

- In the region between 10^{-6} MeV and $3{\cdot}10^{-4}$ MeV the NCT-ACS results show some fluctuations that are not present in the BSS result. This could be to two different factors: the peaked structure of the response matrix and the scarcity of elements. In fact, generally, an unfolding procedure needs at least

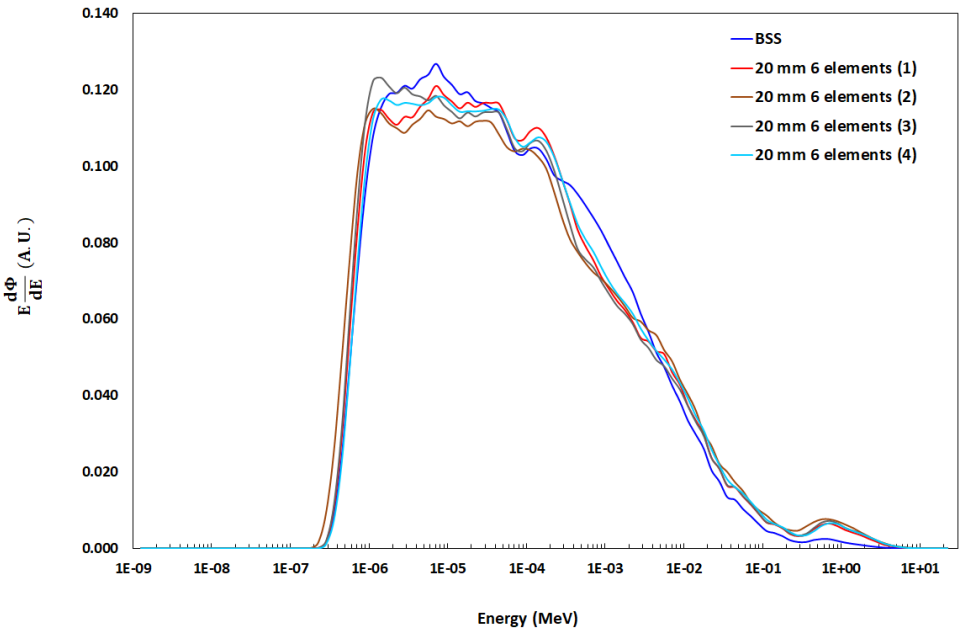

Fig. 5.7.: Unfolding results for the different set of data collected. For better evaluating the graphics the error bar are not shown.

5-6 experimental points, therefore, in this configuration, the system is at the limit in terms of working capability.

- In the region between $3{\cdot}10^{-4}$ MeV and $3{\cdot}10^{-3}$ MeV the NCT-ACS results systematically underestimate the real spectrum value. This is probably due to a lack of information in this energy region and it requires more information (i.e. adding other elements).

- In order to maintain the normalization to the unit area, the region above 10^{-2} MeV is systematically higher respect to the BSS result.

- The fast neutron peak at around 1 MeV is still present in the final results for the NCT-ACS data, while in the BSS results it is much lower. This because the sensitivity of NCT-ACS is low at 1 MeV, therefore the unfolding procedure tends to maintain this peak without distorting the overall spectrum.

Nevertheless, the unfolding results are quite satisfying, because the shape of the spectrum and the decrease in energy is reconstructed. It should be noted that considering the uncertainties on the different bins, the spectra are compatible with the BSS result. The ratio between the NCT-ACS spectra and the BSS result has been performed and the results are shown in figure 5.8

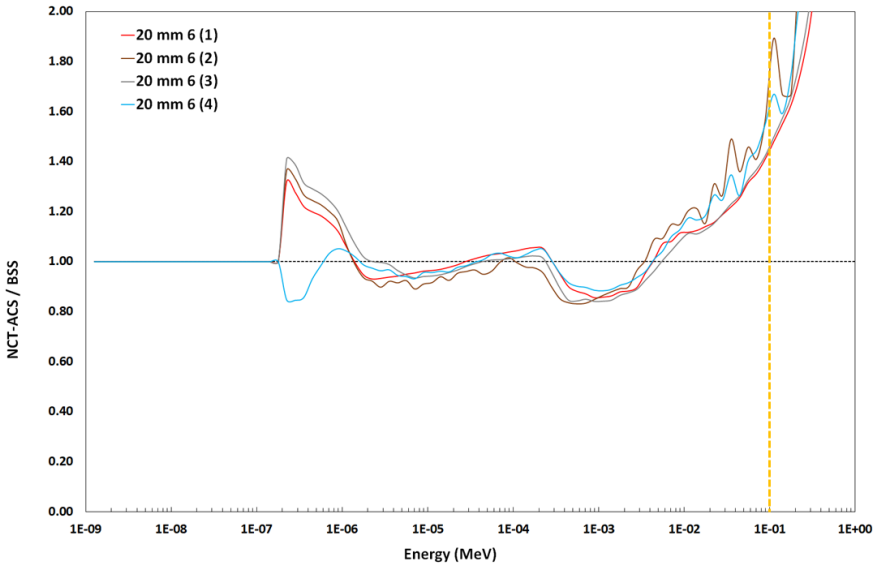

Fig. 5.8.: Ratio between the NCT-ACS spectra and the BSS result in function of the energy. The dotted orange line represents the upper limit of the analyzed energy region.

It should be noted that all the previous considerations are still visible in the ratio distribution. A restricted energy range was used for analyzing the ratio (thermal - 100 keV), in order to correctly consider the NCT-ACS quick sensitivity decrease above 100 keV. In fact, the region at higher energy is completely dominated by the guess information which are quite different from the BSS results, this consequently produced high value in the ratio. Thus, the real sensitivity of NCT-ACS can be determined to be limited up to 100 keV. Since the spectra are compatible with the BSS results within the uncertainties bar, the ratio plot does not show the propagated uncertainties. Nevertheless the average value and the standard deviation for the ratio has been extracted in the energy region between thermal and 100 keV. These quantities can be considered as a proof of the good compatibility between NCT-ACS measures and BSS result. In particular, a value close to 1 for the mean value imply a good accuracy, while a smaller standard deviation imply a better precision. In table 5.6 the results obtained considering the different distribution are shown.

Measure	$\bar{R}$	σ_R
20 mm 6 (1)	1.03	11%
20 mm 6 (2)	1.04	16%
20 mm 6 (3)	1.04	13%
20 mm 6 (4)	1.02	12%

Tab. 5.6.: Mean value and percentage σ for the ratio distributions in the 20 mm with 6 elements configuration.

It should be noted that the mean values are close to 1, meaning that the reconstructed spectra are, in average, very close to the BSS results. Nevertheless, the standard deviations show an high dispersion on the ratio distribution, meaning that on the single bins the differences can be quite high. Indicative values were considered:

$$\bar{R} = 1.03$$

$$\sigma_R = 13\%$$

this implies a 25% dispersion value for an $\alpha = 0.05$ significance level (1.96 σ) in the region between 10^{-9} MeV and 10^{-1} MeV.

In addition, in figure 5.9 a comparison between the BSS result and one of the NCT-ACS result is shown.

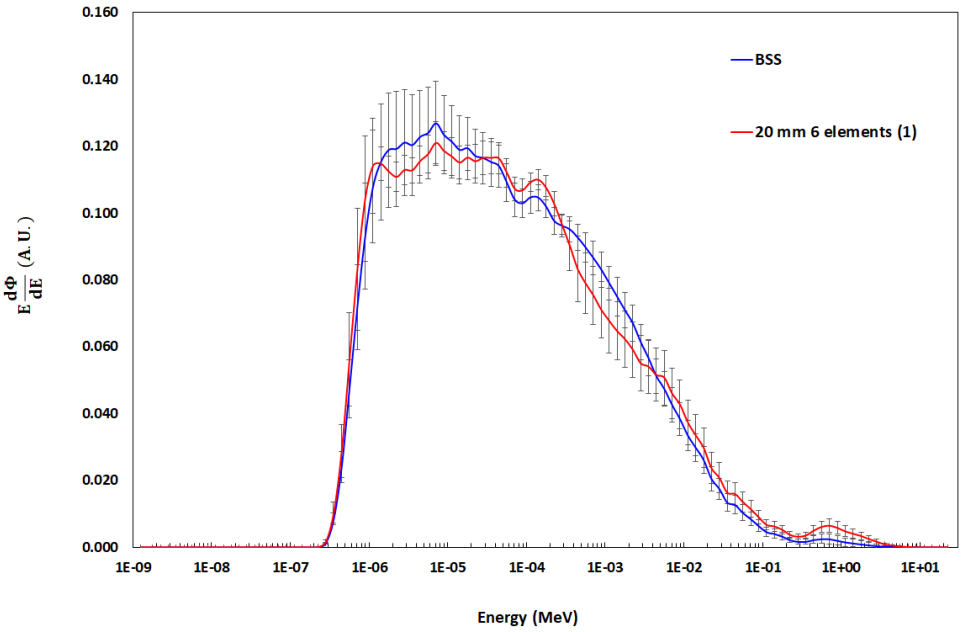

Fig. 5.9.: Comparison between the BSS result and one of the result coming from the different measurements with NCT-ACS. The error bars show that the two spectra can be considered comparable, since the differences are within the uncertainties on the energy bins.

In order to test the robustness of the response matrix when working with the experimental results, a procedure similar to the one proposed in section 3.3.3 was performed. Therefore, a misleading spectrum (figure 3.30) was used as input for the unfolding procedure.
In order to better evaluate the results, the procedure result is shown only for a single data set, the same considerations are also valid for the other measures. In figure 5.10 the results are shown together with the BSS spectrum and the NCT-ACS spectrum obtained with the true guess.

It is immediately clear that the result obtained using the misleading spectrum is not compatible with the BSS results and even with the NCT-ACS result using the true guess. Therefore the robustness of the response matrix in this configuration is not sufficient to correctly elaborate guess spectrum that are not very close to the *real* spectrum.
Moreover, the ratio with the BSS result has been performed, showing a degradation in the σ value, confirming the worse situation:

$$\bar{R}\,(misl) = 0.97$$

$$\sigma_R\,(misl) = 21\%$$

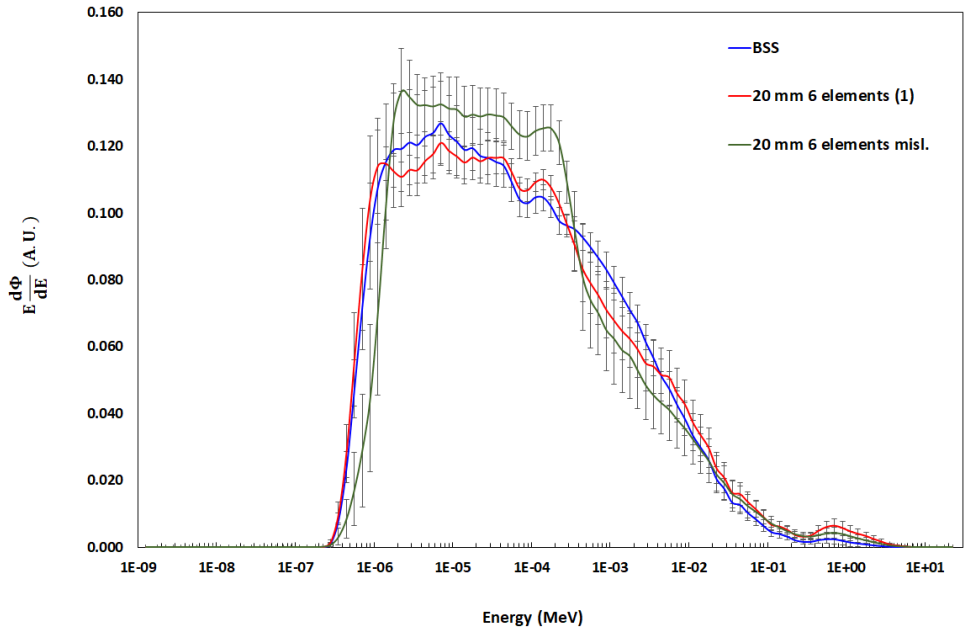

Fig. 5.10.: Comparison between the NCT-ACS results using a misleading guess or using the true guess. The reference BSS result is also shown.

5.2.3 Results with the NCT-ACS 20 mm configuration embedding 9 elements

In order to reinforce the robustness of the response matrix and, eventually, improve the NCT-ACS results, an extended set of foils has been tested using the same experimental conditions. Thus all the preliminary considerations already done could be considered valid. In particular, the W and Re foils have been added, providing three more sensitive elements (W, ^{185}Re, ^{187}Re).
The saturation activity values are reported in table 5.7:

Element	Measure
In ($\cdot 10^4$ Bq)	1.05 (0.02)
Au ($\cdot 10^3$ Bq)	8.46 (0.20)
Mn ($\cdot 10^2$ Bq)	4.31 (0.13)
Cu ($\cdot 10^2$ Bq)	5.61 (0.17)
Na ($\cdot 10^1$ Bq)	8.69 (0.57)
V ($\cdot 10^2$ Bq)	2.63 (0.14)
^{185}Re ($\cdot 10^4$ Bq)	4.37 (0.24)
^{187}Re ($\cdot 10^4$ Bq)	2.26 (0.12)
W ($\cdot 10^3$ Bq)	5.28 (0.16)

Tab. 5.7.: Activation results for the the 20 mm configuration with 8 foils, corresponding to 9 sensitive elements.

The unfolding procedure was then applied and the result is shown in figure 5.11. The BSS result is also reported.

Some considerations on the results should be done:

- In the region between 10^{-6} MeV and $3\cdot10^{-4}$ MeV the NCT-ACS fluctuations are considerably decreased and the spectrum is closer to the BSS one, meaning that in this energy region the unfolding procedure is more robust.

- In the region between $3\cdot10^{-4}$ MeV and $3\cdot10^{-3}$ MeV the NCT-ACS results is perfectly aligned with the BSS result, without showing any underestimation. This means that adding two foils and three sensitive elements provided information in this energy range.

- In the region above 10^{-2} MeV the NCT-ACS spectrum is almost perfectly in agreement with the BSS result.

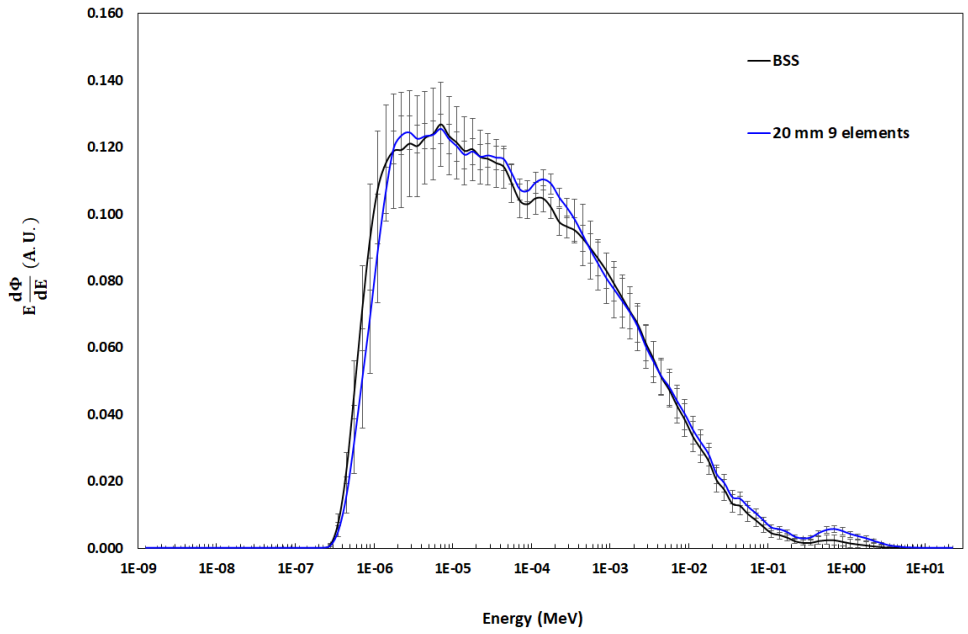

Fig. 5.11.: Comparison between the NCT-ACS result using and BSS result using the same misleading.

- The fast neutron peak at around 1 MeV is still present in the NCT-ACS result. This is due to the fact that adding new element is not extending the sensitivity energy range in this configuration. Nevertheless, the NCT-ACS result is in agreement, within the uncertainties, with the BSS result also in this energy region.

It should be concluded that in this configuration the spectrometric capability of NCT-ACS is dramatically increased, providing results very close to the BSS measure. Moreover, the ratio plot shows in figure 5.12 confirms the improvements in the 20 mm 9 elements configuration.

The same analysis on the ratio R between the NCT-ACS measure and the BSS result was performed and the mean value together with the related standard deviation have been calculated:

$$\bar{R} = 1.01$$

$$\sigma_R = 6\%$$

The 6% σ value implies a 12% dispersion value for an $\alpha = 0.05$ significance level (1.96 σ) in the energy region between 10^{-9} MeV and 10^{1} MeV.

In order to evaluate the robustness of the response matrix using the experimental

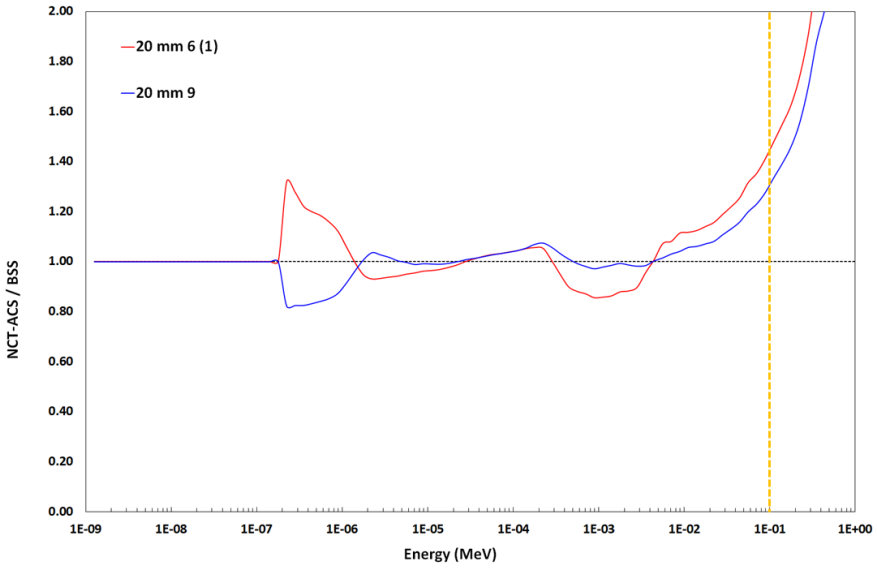

Fig. 5.12.: Ratio between the NCT-ACS spectra and the BSS result in function of the energy. The 20 mm with 9 elements and the 20 mm with 6 elements configurations are shown together. The dotted orange line represents the upper limit of the analyzed energy region.

results, the same procedure as before has been applied, using the same misleading guess. In figure 5.13 the results are shown together with the BSS spectrum and the NCT-ACS spectrum obtained with the true guess.

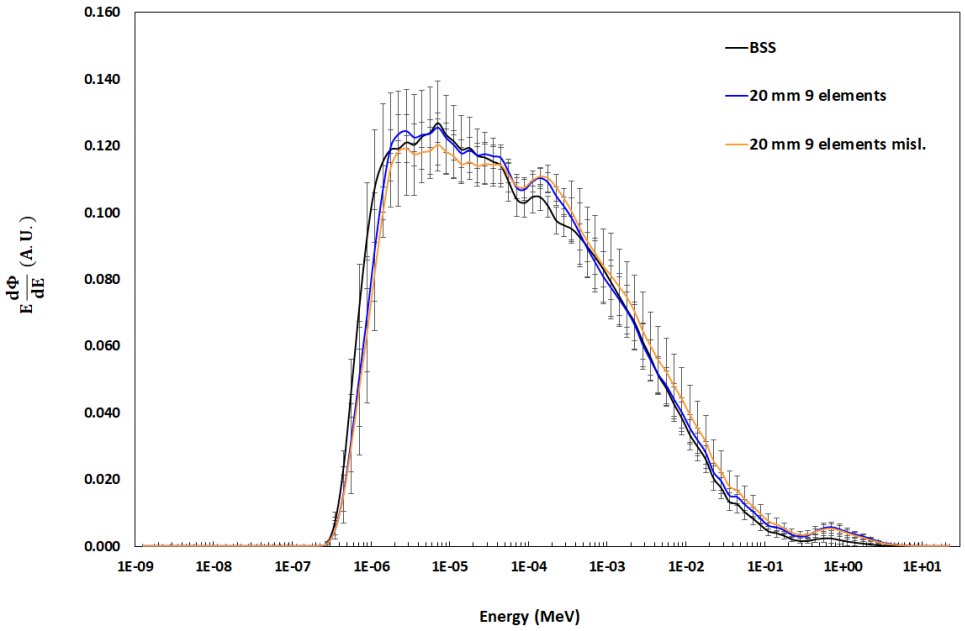

Fig. 5.13.: Comparison between the NCT-ACS results using a misleading guess or using the true guess. The reference BSS result is also shown.

It can be noted that the two unfolded spectra coming from NCT-ACS measures are in perfect agreement between each other and, therefore, with the BSS result. The only region where some differences can be noted are between 10^{-6} MeV and 10^{-4} MeV where the misleading result is slightly below the true result. Anyway, these differences are small compared to the uncertainties on the different bins.
Moreover, the ratio with the BSS result has been performed, showing a degradation in the σ value:

$$\bar{R}\,(misl) = 1.02$$

$$\sigma_R\,(misl) = 11\%$$

It should be noted that, using the misleading guess, the algorithm is forced to work in a worse configuration, nevertheless the 20 mm with 9 elements configuration using the misleading guess is still more accurate and precise respect to the 20 mm with 6 elements configuration using the true guess, reinforcing the conclusion of an improvement in the NCT-ACS capability.
It should be concluded that NCT-ACS in the configuration with 9 sensitive elements is able to correctly reconstruct the neutron energy spectrum both if it is provided a true guess and if it is provided a misleading guess. Showing a good robustness that is sufficient to elaborate input spectra which are not close to the real spectrum.

5.2.4 Results with the NCT-ACS 28 mm configuration embedding 6 elements

In order to further explore the capability of NCT-ACS, the 28 mm geometry was constructed and a measure with 6 different foils was performed. It should be noted that all the preliminary considerations already done could be considered valid.
The saturation activity values are reported in table 5.8:

Element	Measure
In ($\cdot 10^3$ Bq)	8.11 (0.17)
Au ($\cdot 10^3$ Bq)	5.85 (0.13)
Mn ($\cdot 10^2$ Bq)	3.42 (0.09)
Cu ($\cdot 10^2$ Bq)	4.71 (0.14)
Na ($\cdot 10^1$ Bq)	6.76 (0.43)
V ($\cdot 10^2$ Bq)	2.22 (0.11)

Tab. 5.8.: Activation results for the the 28 mm configuration with 6 foils, corresponding to 6 sensitive elements.

The unfolding procedure was then applied and the result is shown in figure 5.14. The BSS result is also reported.

Some considerations on the results should be done:

- In the region between 10^{-6} MeV and $3 \cdot 10^{-4}$ MeV the NCT-ACS result does not show any fluctuations like in the 20 mm configuration case, meaning that in this energy region the unfolding procedure is more robust due to the extra thickness in the moderator shell.

- In the region between $3 \cdot 10^{-3}$ MeV and $3 \cdot 10^{-4}$ MeV the NCT-ACS results is perfectly aligned with the BSS result.

- In the region above 10^{-2} MeV the NCT-ACS spectrum is slightly above the reference one, showing a small systematic difference.

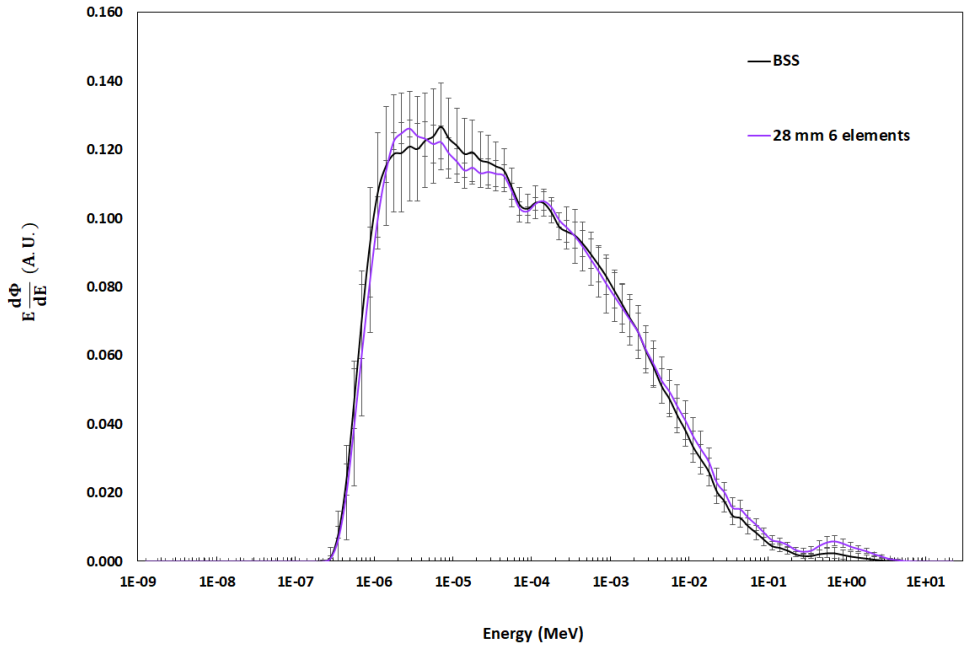

Fig. 5.14.: Comparison between the NCT-ACS result using and BSS result using the same misleading.

- The fast neutron peak at around 1 MeV is still present in the NCT-ACS result. Meaning that the small increasing in the moderator thickness is not sufficient to extend the NCT-ACS sensitivity over this energy region.

It should be concluded that in this configuration the spectrometric capability of NCT-ACS is increased respect to the 20 mm with 6 elements configurations and it is comparable to the 20 mm with 9 elements configuration.
Moreover, the ratio plot shows in figure 5.15 confirms the goodness in the 28 mm 6 elements configuration.

The same analysis on the ratio R between the NCT-ACS measure and the BSS result was performed and the mean value together with the related standard deviation have been calculated:

$$\bar{R} = 1.01$$

$$\sigma_R = 8\%$$

The 8% σ value implies a 16% dispersion value for an $\alpha = 0.05$ significance level (1.96 σ) in the energy region between 10^{-9} MeV and 10^{1} MeV.

In order to evaluate the robustness of the response matrix using the experimental results, the same procedure as before has been applied, using the same misleading

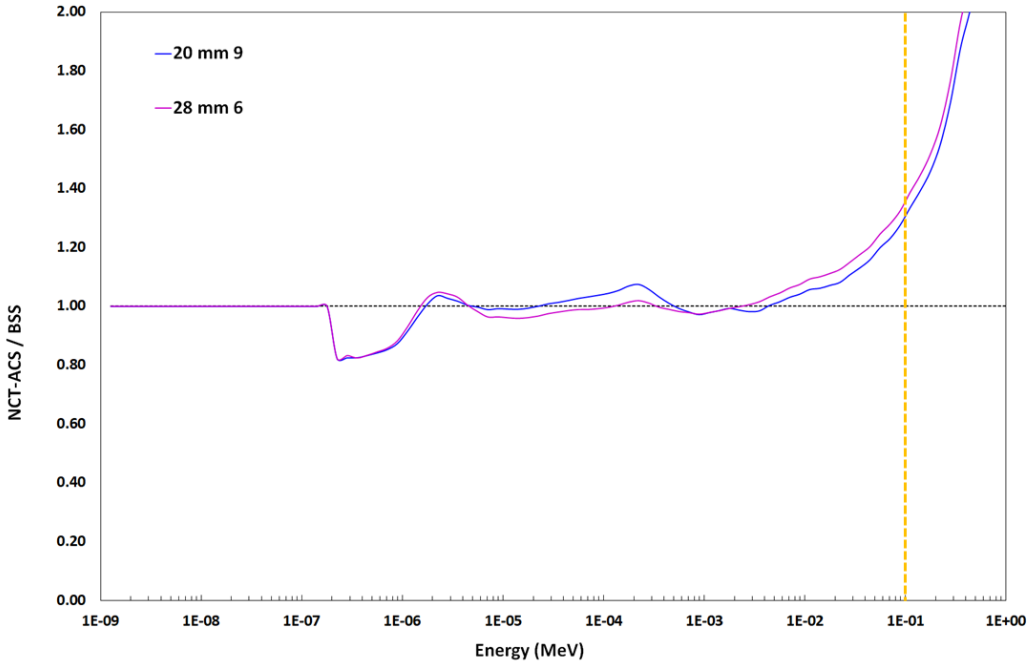

Fig. 5.15.: Ratio between the NCT-ACS spectra and the BSS result in function of the energy. The 28 mm with 6 elements and the 20 mm with 9 elements configurations are shown together. The dotted orange line represents the upper limit of the analyzed energy region.

guess.
In figure 5.16the results are shown together with the BSS spectrum and the NCT-ACS spectrum obtained with the true guess.

It should be noted that the unfolded spectrum using the misleading guess presents some fluctuations in the middle energy region with a massive peak at around 2 eV. This region is dominated by the In resonance which provide massive information and during the iterative unfolding procedure starts rising as soon as the first step is completed. Therefore it not possible to limit this phenomenon, concluding that in this configuration the robustness of the response matrix is not sufficient to correctly reconstruct the real spectrum. Nevertheless the unfolded spectrum is closer to the reference one respect to the 20 mm with 6 elements configurations. Thus, increasing the moderator thickness can enhance the response matrix robustness.
Moreover, the ratio with the BSS result has been performed, showing a degradation in the σ value:

$$\bar{R}\,(misl) = 1.02$$

$$\sigma_R\,(misl) = 19\%$$

The massive broadening in the ratio distribution is described by the σ value around 19% which show again that, using this configuration, the unfolding robustness with a misleading guess is still insufficient.

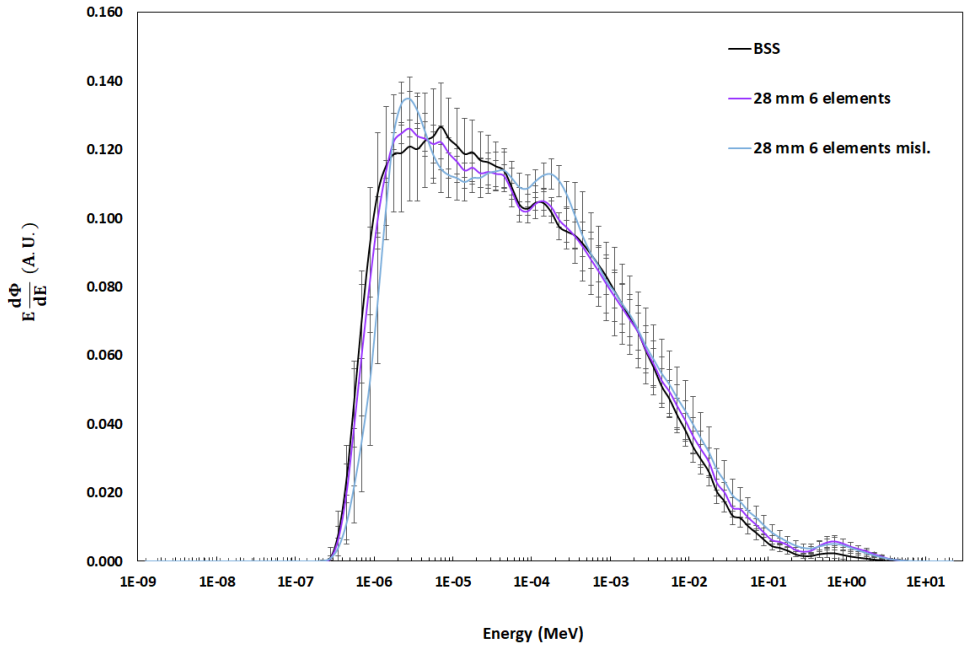

Fig. 5.16.: Comparison between the NCT-ACS results using a misleading guess or using the true guess. The reference BSS result is also shown.

It should interesting to note that adding 3 more elements and increasing 0.8 mm in radius of moderator have both increased the performance of NCT-ACS, but in the first case the robustness goal was achieved, while in the latter the improved results were not sufficient.

5.2.5 Comparison with the simulations results

In order to validate the NCT-ACS simulations, a comparison between the results obtained in chapter 3 and the experimental results has been conducted.
In particular, the validation of the response matrix has been evaluated following the work of Bedogni et al.[133]. Thus the comparison ratio:

$$R^i_{com} = \frac{A^i_{sat}}{A^i_r \dot{\Phi}} \tag{5.14}$$

has been calculated for all the elements, while A^i_r represents the simulated saturation activity of the i-th element normalized for unit fluence. It should be reminded that the fluence rate value is (section 2.7.1), and that the A^i_r value was computed like (section 3.3.3):

$$A^i_r = \sum_j R(E)^{i,j} \phi(E)^{i,j} \Delta E^j$$

In table 5.9 the different values for the ratio R_{com} are shown, together with the z values compared to the unity. In figure 5.17 the obtained R_{com} values are shown.

Element	R_{com}	**z**
In	0.96 (0.02)	-1.67
Au	0.98 (0.02)	-0.72
Mn	0.96 (0.03)	-1.39
Cu	1.04 (0.03)	1.29
V	1.34 (0.09)	3.95
Na	0.99 (0.05)	-0.15
^{185}Re	1.04 (0.07)	0.70
^{187}Re	0.96 (0.06)	-0.77
W	1.07 (0.04)	1.83

Tab. 5.9.: Comparison between Monte Carlo and experimental saturation activities, the comparison was performed following the work of Bedogni et al. [133]. The last column contains the z values.

The results in table 5.9 and figure 5.17 show a very good agreement between Monte Carlo values and experimental ones, with the sole exception of the V foil. In particular, the average value with associated standard deviation has been extracted

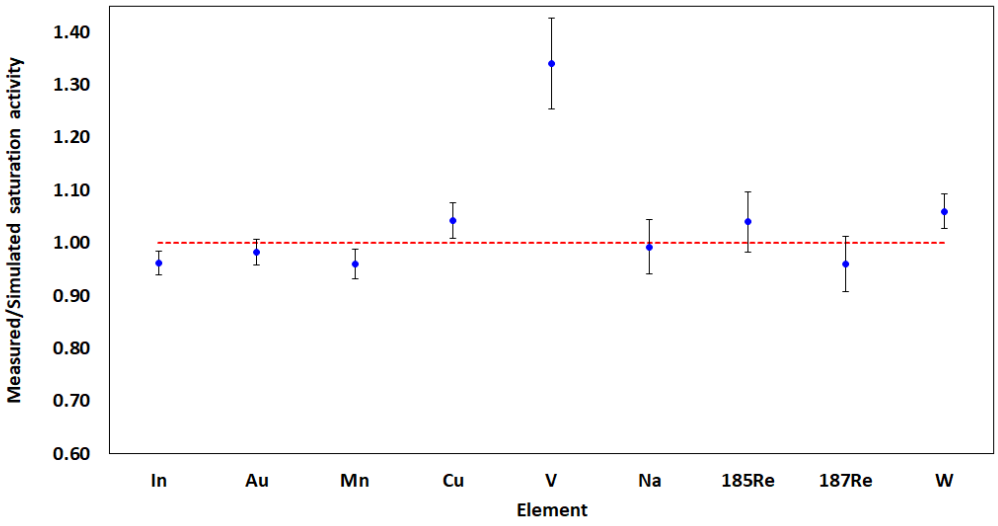

Fig. 5.17.: R_{com} values for the different elements. The dotted red line represent the ideal case for the ratio (=1). The uncertainties bars are mainly driven by the experimental uncertainties, since the Monte Carlo ones are lower than 1%.

in order to provide the better estimator for the R_{com} parameter. It should be noted that since the incompatibility of the V ratio respect to the unity, this value was excluded from this analysis.

$$< R_{com} >= 1.00\,(0.05) \tag{5.15}$$

Therefore, the whole procedure can be considered precise with an accuracy of around 5%. Moreover, it is evident that in the V case, the difference respect tot the unity can not be justified by the simple statistical fluctuation in the measures. The very high z value brings to reject such hypothesis. In particular, the Monte Carlo result for the V case, reveals a strong under estimation respect to the experimental result.

It should be noted that, to correctly evaluate the impact of this discrepancy on the unfolding procedure, the 20 mm with 9 sensitive elements configuration has been analyzed again, excluding the V foil. This created a new configuration, for the 6 sensitive elements configurations the V was fundamental in order to have enough energy information, therefore this exclusion was not possible.
The analysis procedure was the same and in figure 5.18 the unfolding result is shown together with the already analyzed 20 mm with 9 sensitive elements configuration.

It should be noted that the results are very similar. Nevertheless, a small difference in the energy region between 10^{-6} MeV and $3{\cdot}10^{-4}$ keV can be noted, producing a small over estimation for the 8 elements configuration respect to the 9 one. In

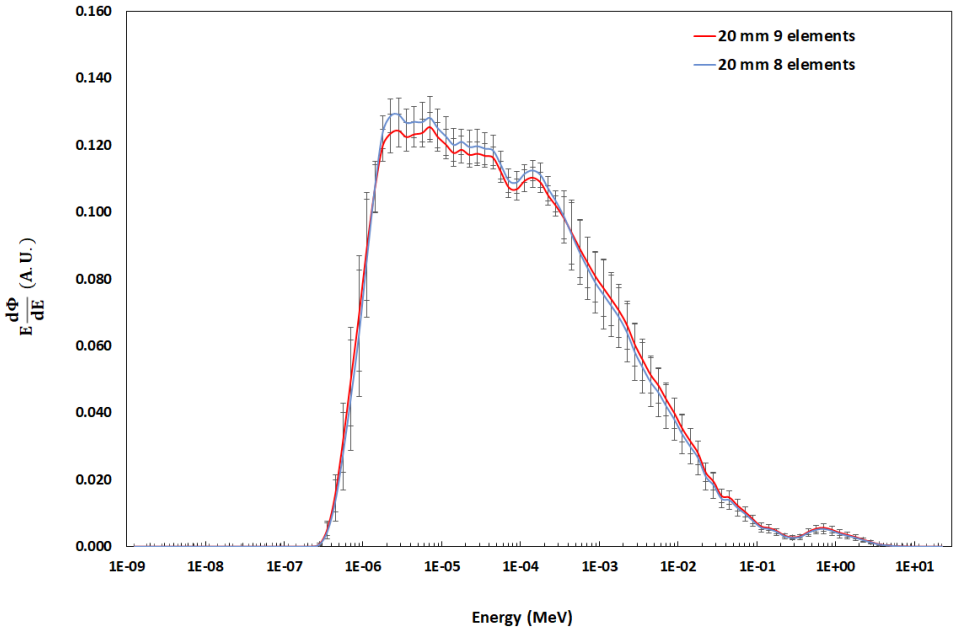

Fig. 5.18.: Comparison between the NCT-ACS results using all the 9 sensitive elements and using only 8 elements (V is excluded). The true guess spectrum was used during the unfolding procedure.

table 5.10 the analysis results are shown in comparison with the 20 mm 9 elements configuration results.

Parameter	9 elements	8 elements (no V)
$\bar{R}$	1.01	0.97
σ_R	6%	9%

Tab. 5.10.: Comparison between 9 sensitive elements and 8 sensitive elements configurations. All the results coming from the unfolding procedure performed using the true guess spectrum.

It should be noted that excluding the V case, the σ_R is slightly higher. Thus, it can be concluded that the gain in excluding an element which present a behaviours different respect to the Monte Carlo results, is not sufficient to cover the degradation in the unfolding power due to the loss of a sensitive element. Nevertheless, the obtained result is still in good agreement with the BSS result, proving the robustness and strength of the unfolding procedure which is not completely driven by the guess information or by the Monte Carlo results.

A possible explanation in the discrepancy for the V foil could rely on a lack in the nuclear data. This provided the possibility to study the neutron cross section on V in a dedicated facility. In particular, some transmission measurements have been performed at the JRC in Geel (Belgium), using the GELINA Time Of Flight (TOF) facility [134]. GELINA is one of the most important laboratory in the nuclear data production field, since it is characterized by an excellent time resolution of 1 ns. This allows to investigate the different resonances in the Resolved Resonance Region (RRR).
Measures using three different V sample configurations have been performed and an intense literature study has been produced. In particular, the literature review revealed a massive lack in the capture data, with few data. Moreover, the data collected are not in good agreement between each other.
The first results on the transmission measures are currently undergoing further analysis aiming to improve the nuclear data libraries. A more in detail treatment with some first results is presented in Appendix D.

Another confirm about the goodness of the Monte Carlo simulations and of the experimental measures, can be evaluated comparing the 20 mm and 28 mm configurations results. In particular, both the ratio between the saturation activity (R_{exp}) and from the activation rate calculated via Monte Carlo simulation (R_{MC}) have been extracted (5.16 and 5.17):

$$R_{exp} = \frac{A_{sat}^{20mm}}{A_{sat}^{28mm}} \tag{5.16}$$

$$R_{MC} = \frac{A_{r}^{20mm}}{A_{r}^{28mm}} \tag{5.17}$$

In particular:

- R_{exp} values have been calculated using the data shown in table 5.5 and table 5.8.

- R_{MC} values have been calculated using the simulation results explained in section 3.3.3 with a particular reference to the plots in figure 3.26 in which the decreasing in the A_r values in function of the moderator thickness is shown.

In table 5.11 the values of the different ratios are shown:

Element	R_{exp}	R_{MC}
In	1.36	1.28
Au	1.46	1.43
Mn	1.39	1.35
Cu	1.21	1.44
Na	1.32	1.33
V	1.27	1.28

Tab. 5.11.: Saturation activity ratio (R_{exp}) and activation rate ratio (R_{MC}) between the 20 mm configuration and 20 mm configuration.

With the sole exception of the Cu foil, all the ratio values are comparable within a 6%. In particular, the average value with standard deviation as uncertainty estimator has been extracted for both set of data:

$$< R_{exp} >= 1.34\,(0.09)$$

$$< R_{MC} >= 1.35\,(0.07)$$

Analyzing the mean values can be easily noted that there is an excellent agreement between the two values, within 1%. Thus the goodness and reliability of the Monte Carlo simulations is reinforced.
It should be noted that, in this discussion, the V case did not present any problematic. This can be explained considering that the ratio between the different quantities allows to eliminate the systematic difference.

5.3 Summary of the NCT-ACS measurements

In this section, a summary of the various measurements performed with NCT-ACS are shown.
Three different types of measure have been performed using different configurations:

1. 20 mm with 6 sensitive elements.

2. 20 mm with 9 sensitive elements.

3. 28 mm with 6 sensitive elements.

For all of these configurations, an unfolding procedure has been applied both with a true guess and with a misleading guess. A comparison with BSS result was also evaluated, considering the BSS measure as reference.
In figure 5.19 the results of the unfolding procedure using the true guess spectrum are shown. While, in figure 5.20 the same results in the case of a misleading guess are reported.

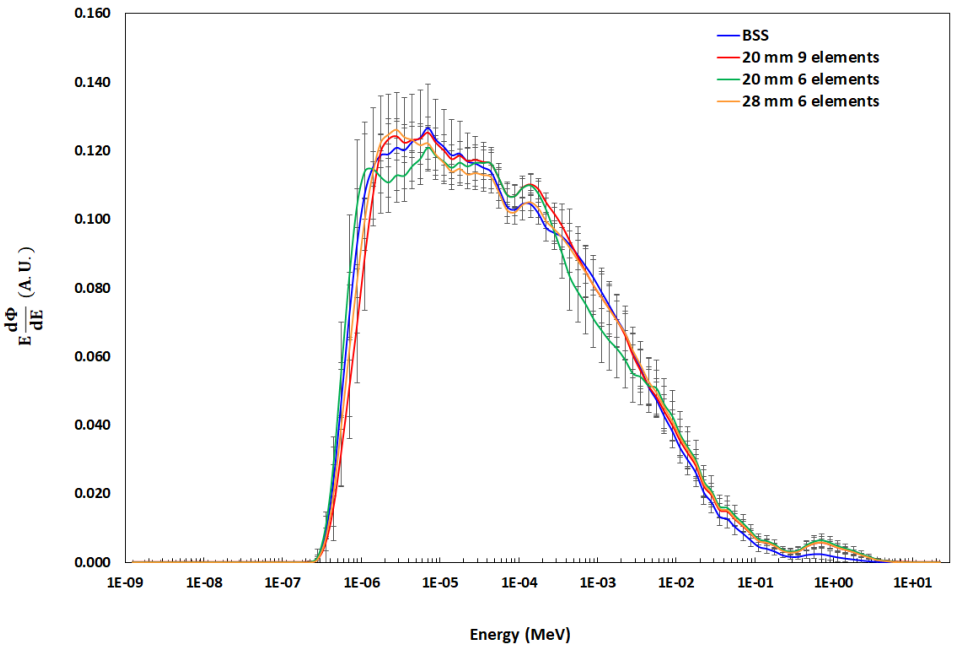

Fig. 5.19.: Unfolded spectra for all the studied configurations providing to the FRUIT code the true guess. The BSS spectrometer is also reported.

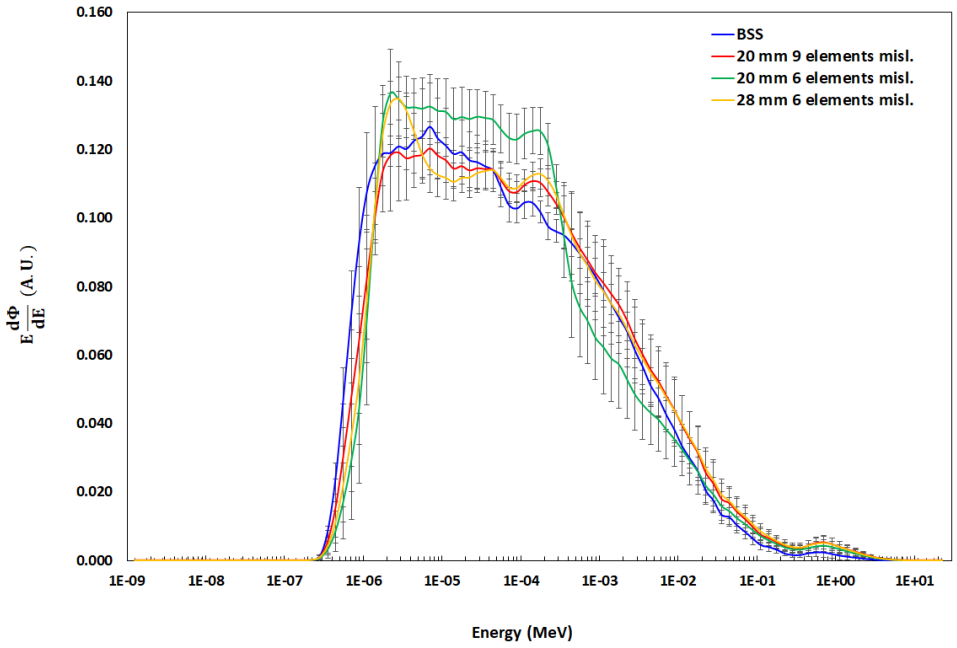

Fig. 5.20.: Unfolded spectra for all the studied configurations providing to the FRUIT code the misleading guess. The BSS spectrometer is also reported.

It should be noted that:

1. Using the true guess spectrum during the unfolding, all the configurations are able to correctly reconstruct the spectrum within the uncertainties and the ratio between the NCT-ACS spectra and the BSS result was calculated:

   - The 20 mm with 6 elements configuration revealed a dispersion value of around 13% (subsection 5.2.2);
   - The 20 mm with 9 elements configuration shown a dispersion value of around 6% (subsection 5.2.3);
   - The 28 mm with 6 elements configuration was characterized by a dispersion value of around 8% (subsection 5.2.4).

   All these values are related to the energy range from thermal up to 0.1 MeV. Above the 0.1 MeV limit, the NCT-ACS sensitivity was found to be too low to correctly reconstruct the spectrum and the guess information became dominant.

2. Using the misleading guess spectrum, only the 20 mm with 9 elements configuration is able to reconstruct the correct spectrum (ratio dispersion of 11%), while the other configurations fail in many aspects (ratio dispersion of 21% and 19 % for the 20 mm and 28 mm respectively).

Thus can be concluded that, actually, the best option is the 20 mm with 9 sensitive elements. This configurations is robust and can also work with a misleading spectrum, being the most stable option.

A comparison with the Monte Carlo values from chapter 3 has been performed, providing a good agreement between Monte Carlo results and experimental data. Thus the response matrix and simulation work have been validated. In particular the average ratio between the two set of values was calculated to be:

$$R_{com} = 1.00\,(0.05)$$

Figure 5.17 shows the results for all the selected elements. During the ratio calculation, the V data was found to be in disagreement with the others, revealing a discrepancy which can not be explained assuming only statistical fluctuations. A possible explanation in the discrepancy for the V foil could rely on a lack in the nuclear data. This provided the possibility to study the neutron cross section on V in a dedicated facility. In particular, some transmission measurements have been performed at the JRC in Geel (Belgium), using the GELINA Time Of Flight (TOF) facility [134]. GELINA is one of the most important laboratory in the nuclear data production field, since it is characterized by an excellent time resolution of 1 ns. This allows to investigate the different resonances in the Resolved Resonance Region (RRR).
Measures using three different V sample configurations have been performed and an intense literature study has been produced. In particular, the literature review revealed a massive lack in the capture data, with few data. Moreover, the data collected are not in good agreement between each other.
The first results on the transmission measures are currently undergoing further analysis aiming to improve the nuclear data libraries. A more in detail treatment with some first results is presented in Appendix D.

Moreover, the robustness of the Monte Carlo simulations has been reinforced by considering the attenuation in the saturation activities between the 20 mm and the 28 mm cases. The reduction in the saturation activities was found to be in perfect agreement with the one predicted by the simulations within a 1% of deviation.

6

Conclusive remarks on the NCT-ACS spectrometer

In recent years, the introduction of accelerator-based BNCT facilities has led to a significant increase in interest from the medical and scientific communities. Monitoring and characterization of neutron beams and intercomparison of different facilities are becoming mandatory [1]. This stimulates the development of dedicated dosimetry and spectrometry techniques.

Within this context, the thesis work conceived and developed a compact epithermal neutron spectrometer capable of operating across an energy range from thermal to 100 keV, known as NCT-ACS (Neutron Capture Therapy - Activation Compact Spectrometer)
The core idea behind this instrument involves using the neutron capture phenomena within specific elements to gather information on the neutron energy spectrum and subsequently reconstruct it using suitable unfolding techniques. Particularly, the identification of strong resonances in the epithermal range within certain elements was pivotal for this project objectives. To appropriately select the elements candidates, an extensive study was conducted, involving the analysis and exploration of numerous potential elements while applying specific selection criteria based on their key characteristics. Following this selection phase, the most promising elements for the operation of NCT-ACS were determined to be: In, Au, Mn, Cu, V, NaCl, Re (both ^{185}Re and ^{187}Re isotopes) and ^{186}W. Circular foils composed of these elements were chosen, and their thicknesses were calibrated appropriately to optimize the spectrometer's performance.

An intensive study employing Monte Carlo simulations was conducted to identify the optimal geometry for NCT-ACS. The purpose of this study was to designing a configuration that enabled NCT-ACS to achieve:

- Isotropic response, mitigating the need for corrections associated with the angular distribution of the source.

- Sensitivity to neutrons spanning from thermal energies up to at least 100 keV.

- Compact dimensions suitable for the confined spaces typical in BNCT applications.

- Feasibility for use with a single irradiation to reduce total acquisition time.

Following this study, the most favorable geometry identified consisted of a small-sized polyethylene sphere housing a cylindrical cavity of 8 mm in depth. Within this cavity a cadmium cylinder, 0.5 mm thick, was placed accommodating various foils of the selected elements. Specifically, two alternative configurations of this geometry were developed, differing solely in the radius of the polyethylene spherical shell: 20 mm and 28 mm.

It's important to highlight how the addition of the moderator allowed achieving isotropic conditions while rendering the instrument response curves suitable for incorporation into an unfolding procedure. Due to the sharp resonance structures, the unfolding algorithm previously introduced non-physical oscillations within the reconstruction of the neutron spectrum.
The anisotropy of this designed geometry was evaluated through Monte Carlo simulations by varying the incident angle of neutrons. The activation rate of the foils was extracted with varying angles of incidence, and the anisotropy was estimated at 1.96 standard deviations from the hypothetical count distribution. A maximum anisotropy value of 3% was chosen, with both selected geometries yielding values below this threshold, considered as a component of systematic uncertainty:

$$S_{\text{anisotropy}} = 2.4\%$$

Before testing NCT-ACS, an extensive study of the HPGe detector available at the University of Turin was conducted. This process enabled the calibration of the instrument to calculate the absolute activity of the foils by placing them directly in contact with the detector. This was achieved by considering both geometric aspects and system analysis. During the calibration phase, the neutron facility known as e-LiBaNS in Turin [135] was utilized.
The calibration scheme is outlined as follows:

1. The HPGe energy calibration ha been performed using calibration sources (^{137}Cs,^{60}Co,^{22}Na,^{152}Eu,^{133}Ba);

2. An efficiency calibration of the detector was carried out by placing the same known-activity sources at a distance of 10 cm. A fit curve of the data was extrapolated and employed as the calibration curve.

3. The activation foils, selected for NCT-ACS, were irradiated at the e-LiBaNS facility under non-standard conditions, aiming to induce high activity values.

4. The foils were then analyzed at two different positions relative to the HPGe detector: at 10 cm and in direct contact.

5. The ratio of the estimated cps from the two measurements was derived after necessary corrections, defining the geometric factor. The assumption to a point-like source was estimated to produce a systematic error within approximately 1% under the measurement conditions used;

6. With the obtained values, the foils activation can be analyzed by placing them in contact with the detector. This approach allow for reducing neutron irradiation and gamma spectrum acquisition times. Additionally, it allows for increased statistical counts, while maintaining relatively low levels of radioactivity. This process effectively reduces the risk of unwanted radiation exposure during the experimental procedure.

The HPGe detector efficiency values for the different elements used in NCT-ACS are reported in table 4.5, while the geometric factors of the foils are reported in table 4.6.
Combining the values in these tables, the HPGe detector efficiency for the different foils at contact can be determined simply multiplying the two set of values:

$$\epsilon_c = \epsilon_{10} \cdot F_G \tag{6.1}$$

Being ϵ_c the efficiency at contact, ϵ_{10} the efficiency at 10 cm and F_G the geometric factor. These values can be find in table 4.7.
During the HPGe calibration two sources of systematic uncertainties have been evaluated due to the point source like approximation and due to the use of the SNIP algorithm during the analysis of the gamma spectra. The overall contribute can be calculated:

$$S_{\text{HPGe}} = 1.4\%$$

The total systematic uncertainty can be then calculated to be:

$$S_{\text{tot}} \simeq 3\%$$

At the conclusion of the calibration procedure, a series of measurements were conducted at the e-LibaNS facility operating in the epithermal mode. Under these conditions, the spectrum and fluence rate of the source are known and measured

using a calibrated Bonner Sphere Spectrometer.
Three different types of measure have been performed using different configurations:

1. 20 mm with 6 sensitive elements.

2. 20 mm with 9 sensitive elements.

3. 28 mm with 6 sensitive elements.

For all of these configurations, an unfolding procedure has been applied both with a true guess and with a misleading guess. A comparison with BSS result was also evaluated, considering the BSS measure as a reference one.
In figure 6.1 the results of the unfolding procedure using the true guess spectrum are shown.

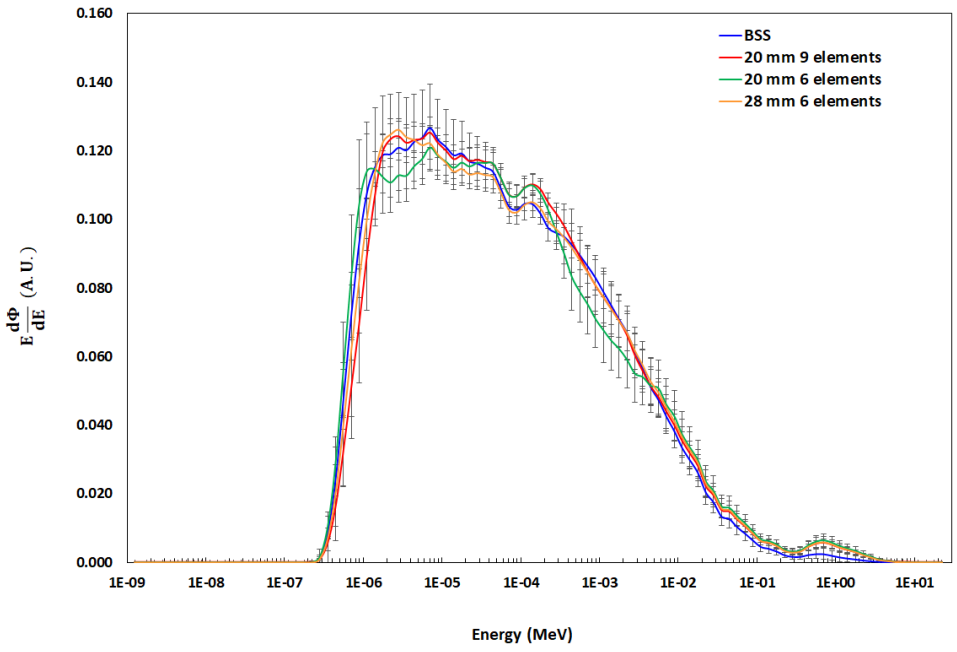

Fig. 6.1.: Unfolded spectra for all the studied configurations providing to the FRUIT code the true guess. The BSS spectrometer is also reported.

It should be noted that:

1. Using the true guess spectrum during the unfolding, all the configurations are able to correctly reconstruct the spectrum within the uncertainties and the ratio between the NCT-ACS spectra and the BSS result was calculated:

- The 20 mm with 6 elements configuration revealed a dispersion value of around 13% (subsection 5.2.2);

- The 20 mm with 9 elements configuration shown a dispersion value of around 6% (subsection 5.2.3);

- The 28 mm with 6 elements configuration was characterized by a dispersion value of around 8% (subsection 5.2.4).

All these values are related to the energy range from thermal up to 0.1 MeV. Above the 0.1 MeV limit, the NCT-ACS sensitivity was found to be too low to correctly reconstruct the spectrum and the guess information became dominant.

2. Using the misleading guess spectrum, only the 20 mm with 9 elements configuration is able to reconstruct the correct spectrum (ratio dispersion of 11%), while the other configurations fail in many aspects (ratio dispersion of 21% and 19 % for the 20 mm and 28 mm respectively).

Thus can be concluded that, actually, the best option is the 20 mm with 9 sensitive elements. This configurations is robust and can also work with a misleading spectrum.

A comparison with the Monte Carlo values from chapter 3 has been performed, providing a good agreement between Monte Carlo results and experimental data. Thus the response matrix and simulation work have been validated. It should be noted that for the V foil, some discrepancies have been founded. A possible explanation in the discrepancy for the V foil could rely on a lack in the nuclear data. This provided the possibility to study the neutron cross section on V in a dedicated facility. In particular, some transmission measurements have been performed at the JRC in Geel (Belgium), using the GELINA Time Of Flight (TOF) facility [134]. GELINA is one of the most important laboratory in the nuclear data production field, since it is characterized by an excellent time resolution of 1 ns. This allows to investigate the different resonances in the Resolved Resonance Region (RRR).
Measures using three different V sample configurations have been performed and an intense literature study has been produced. In particular, the literature review revealed a massive lack in the capture data, with few data. Moreover, the data collected are not in good agreement between each other.
The first results on the transmission measures are currently undergoing further analysis aiming to improve the nuclear data libraries. A more in detail treatment with some first results is presented in Appendix D.

In particular, the average ratio between the two set of values was calculated to be:

$$R_{com} = 1.00\,(0.05)$$

Figure 6.2 shows the results for all the selected elements.

Moreover, the robustness of the Monte Carlo simulations has been reinforced by considering the attenuation in the saturation activities between the 20 mm and the 28 mm cases. The reduction in the saturation activities was found to be in perfect agreement with the one predicted by the simulations within a 1% of deviation.

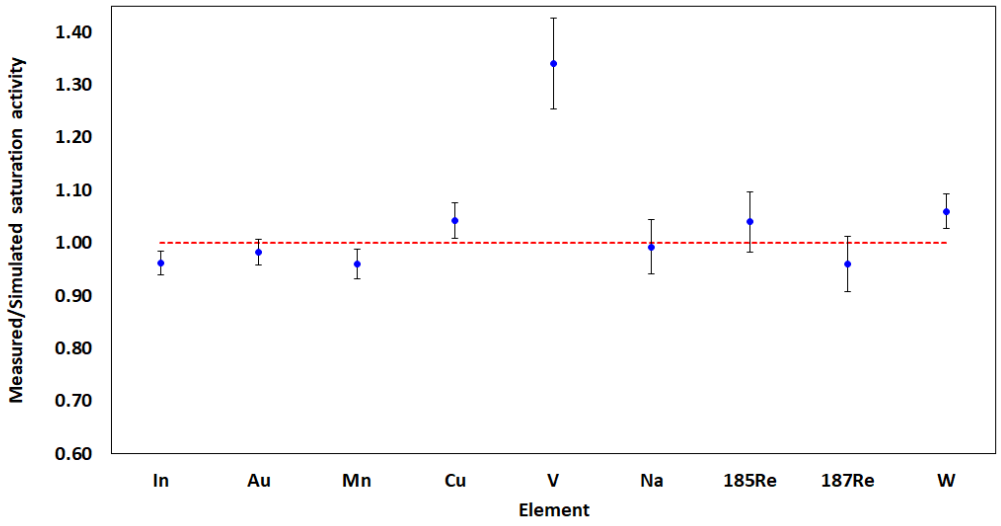

Fig. 6.2.: R_{com} values for the different elements. The dotted red line represent the ideal case for the ratio (=1). The uncertainties bars are mainly driven by the experimental uncertainties, since the Monte Carlo ones are lower than 1%.

It should be noted that the unfolding procedure has been evaluated also excluding the V foil from the analysis. This part was presented in 5.2.5 and reveled that the gain in excluding an element which present a behaviours different respect to the Monte Carlo results is not sufficient to cover the degradation in the unfolding power due to the loss of a sensitive element (table 5.10). This aspect can be considered as another proof of the robustness and strength of the unfolding procedure which is not completely driven by the guess information or by the Monte Carlo results.

In conclusion, the neutron activation spectrometer, known as NCT-ACS, has been developed in two distinct variants, both of which have been thoroughly tested and calibrated. The achieved results show an excellent agreement with the reference measurements, confirming the validity of the instrument and the work performed. This instrument marks an innovation in the field of Boron Neutron Capture Therapy (BNCT), given its capability to measure epithermal spectra in reduced volumes, demonstrating precision and efficiency comparable to the standard technique of

Bonner Sphere Spectrometer.

It should be noted that this first part of the work represented the proof of concept of the NCT-ACS idea validating the analysis procedure. Nevertheless, the use of a HPGe detector represent a limitation for the experimental use, since not all the facilities are equipped with such detector. Moreover the calibration procedure is time consuming and pones some challenges, making the measure hardly manageable. In addition, the HPGe detector is not portable, making impossible to use the calibrated Turin detector for external measurements.
Thus, the aim of the last part of the work was focused on trying to combine NCT-ACS with a LaBr(Ce) crystal scintillator, slightly less performant, but significantly smaller than the HPGe detector. This would provide a complete system suitable for in-situ measurements and making it even more attractive for BNCT applications.

7 LaBr(Ce) gamma detector

This chapter aims to transport the entire analysis procedure to an experimental condition where the HPGe detector is replaced by a compact and portable detector. In fact, with the idea of creating an easily portable system, NCT-ACS must be coupled with a smaller-sized detector. It should be considered that the work conducted with the HPGe detector has validated the proof of concept for NCT-ACS. However, the complex and challenging detector calibration process (chapter 4) makes the technique difficult to be widely diffused, as not all facilities may have an HPGe detector available. Furthermore, even if one is present, the calibration procedures would require a significant amount of time, making the overall measurement less easily usable.

After a brief introduction to the characteristics of LaBr detectors, the calibration and measurement procedure using the new detector will be explained. Finally, a comparison with the results obtained using the HPGe detector will be presented.

7.1 LaBr(Ce) detector

The LaBr(Ce) scintillation detector stands as a robust gamma-ray detection system, featuring a crystalline structure composed of cerium-doped lanthanum bromide. This compound exhibits exceptional scintillation properties, characterized by a high light yield and rapid decay time, rendering it well-suited for gamma-ray spectroscopy. When exposed to gamma radiation, the LaBr(Ce) crystal promptly emits scintillation photons, which are converted into electrical signals for subsequent analysis. This scintillation mechanism forms the foundation of its applicability across diverse scientific domains requiring gamma-ray detection and spectroscopic analysis [136].
LaBr(Ce) detectors excel in providing impressive energy resolution, particularly within the mid to high-energy gamma-ray spectrum. While HPGe detectors traditionally dominate in achieving superior resolution at lower energies, LaBr(Ce) detectors offer competitive resolution in higher energy regions, making them invaluable for studies involving higher energy gamma rays. Additionally, their fast timing properties facilitate accurate time-tagging of gamma-ray interactions. The swift decay time of LaBr(Ce) enables effective pulse shape discrimination and aids investigations involving fast-emitting sources or time-dependent processes.

One of the notable advantages of LaBr(Ce) detectors lies in their heightened detection efficiency for gamma rays compared to HPGe detectors. This increased efficiency is attributed to the denser scintillation material and favorable geometric configuration of LaBr(Ce) detectors. Their robust construction contributes to reduced susceptibility to damage from handling or mechanical stress, a notable contrast to the delicate nature of HPGe detectors. Moreover, the operational viability of LaBr(Ce) at ambient temperatures eliminates the necessity for intricate cryogenic cooling systems, simplifying their deployment and maintenance.
The innate robustness and operational adaptability of LaBr(Ce) detectors render them particularly suitable for applications demanding environmental resistance. Their ability to function effectively across a spectrum of temperature conditions and environmental variations positions them favorably for field measurements, environmental monitoring endeavors, and nuclear safeguards initiatives. This adaptability enhances their utility in scenarios necessitating portable, reliable, and adaptable gamma-ray detection systems.
In conclusion, the LaBr(Ce) gamma detector emerges as a commendable alternative to HPGe detectors, offering distinct advantages in energy resolution, timing properties, detection efficiency, and environmental adaptability.

7.1.1 The Torino LaBr(Ce) detector

The LaBr(Ce) crystal used in this work was a Bril Lan Ce 380 produced by Saint-Gobain Crystals, coupled with a commercial CAEN electronic module. Crystal data sheet with all the characteristics is available at [137].
The main features are shown in table 7.1:

Characteristic	**LaBr(Ce)**	**HPGe**
Crystal dimensions	1.5" x 1.5"	2" x 2"
Density (g/cm^3)	5.08	5.35
Response time	$<$ 1 ns	8-10 ns
Energy resolution (@122 keV)	5.6 %	0.67%
Energy resolution (@662 keV)	2.8 %	0.3%
Energy resolution (@1333 keV)	2.1 %	0.14%
Efficiency	25%$^{(1)}$	20%$^{(1)}$

Tab. 7.1.: LaBr(Ce) and HPGe Turin detectors main characteristics.
$^{(1)}$ relative to a 2.5" x 2.5" NaI inorganic scintillator efficiency.

The energy calibration for the LaBr(Ce) detector will not be described, since it is a standard technique, widely used in all the applications. The standard procedure has been performed, using many different sources like: ^{137}Cs, ^{60}Co, ^{133}Ba, ^{152}Eu, ^{22}Na. In figure 4.5 a picture of the HPGe detector used is shown.

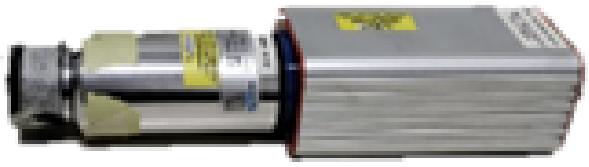

Fig. 7.1.: Image of the LaBr used for this work.

Since the LaBr detector is not shielded against the natural background for all the subsequent measurements an adequate shielding in lead has been placed around the detector in order to reduce the background signal.

7.2 Calibration procedure

The same considerations and operations already shown in chapter 4 have been performed for the LaBr calibration.
In addition to what already discussed for the HPGe work, some considerations should be made:

1. Due to the smaller size of the detector, the efficiency calibration has been performed placing the sources and, then, the activated foils at a distance of 20 cm. Under this condition, the systematic error due to a foil misplacing in addiction to the point source like approximation was:

$$S_{\text{geom}} < 1\%$$

In order to correctly place the calibration sources and the activated foils, a specific double holder has been created using a 3D printer. This particular object could be easily switch between "contact" and "distance" configurations. In figure 7.2 a picture of the LaBr detector with the specific holder is shown.

Fig. 7.2.: Picture of the LaBr detector with the "contact" holder inserted on the aluminum end-cap. On the right the "distance" holder can be seen.

2. The large distance required (20 cm) did not allow to perform the measures using the activated foils using the e-LiBaNS facility since the activation values required were too far from the ones achievable in that facility. Therefore the rabbit channel at the LENA reactor in Pavia has been used (see section 2.7.3). In those conditions a thermal fluence rate of around 10^{13} cm^{-2}s^{-1} was achievable, allowing to induce higher activity values and collect a sufficient statistic for the 20 cm measures.
It should be noted that for the analysis purposes, the facility was not relevant,

therefore all the considerations on the analysis algorithm and procedure could be considered valid also in this discussion.

3. The same considerations about the efficiency calibration with the calibrated sources can be considered. In particular, the same calibration sources have been used. It should be noted that due the lower energy resolution, in this case some peaks on the Eu spectrum were not resolvable, thus the number of points for the calibration was set to be 11 instead of 18.

In figure 7.3 the calibration source plot logϵ-logE is shown.

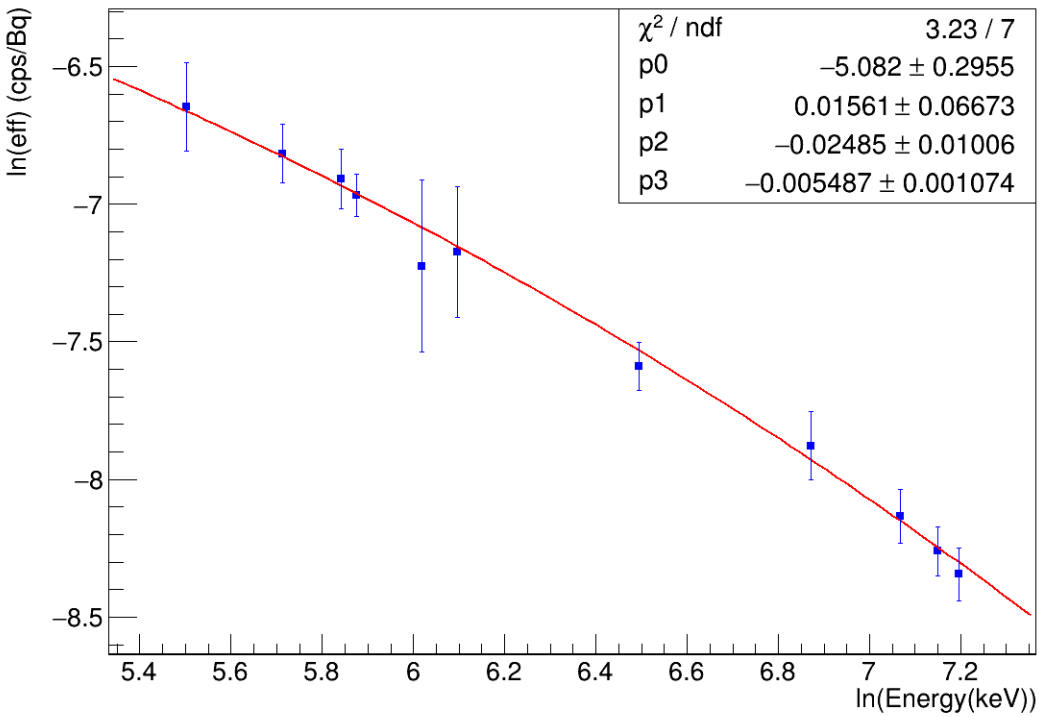

Fig. 7.3.: Fit for the logϵ-logE distribution for the sources placed at 20 cm by the detector.

The χ^2 value is below the critical value, thus the fit can be considered to be adequate in approximate the experimental data. The fitting function is the same used in the HPGe study and it is here reported:

$$ln\epsilon = p_0 + p_1 ln\frac{E}{E_0} + p_2\left(ln\frac{E}{E_0}\right)^2 + p_3\left(ln\frac{E}{E_0}\right)^3 \tag{7.1}$$

The energy efficiencies corresponding to the different gamma energies for the NCT-ACS elements have been calculated interpolating the fitting function and are shown in table 7.2.

Element	Gamma Energy (keV)	ϵ (x10^{-4} cps/Bq)	σ_ϵ/ϵ
^{116m}In	1293.5	2.52 (0.17)	6.8%
^{198}Au	411.8	8.16 (0.45)	5.5%
^{56}Mn	846.8	4.05 (0.19)	4.8%
^{64}Cu	511	6.70 (0.32)	4.8%
^{24}Na	1368.6	2.36 (0.17)	7.2%
^{52}V	1434.1	2.23 (0.17)	7.5%
^{187}W	479.6	7.11 (0.36)	5.0%
^{186}Re	137.2	18.8 (1.9)	10.2%
^{188}Re	155	17.3 (1.7)	9.6%

Tab. 7.2.: Efficiency values for the gamma energies of the selected elements used in NCT-ACS.

It should be noted that respect to the values obtained in the HPGe analysis (table 4.5), these values are around ten times lower, that because the sources were placed at 20 cm and not at 10 cm respect to the sensitive part of the detector itself.
The larger uncertainties are due to the presence of higher background which introduces statistical fluctuations in the peaks analysis.

The geometric factor F_G has been calculated using the same approach already explained previously. All the measures have been performed at the LENA reactor and have been carefully tuned in order to do not have death time higher than 1%.
The result of the geometric factor calculation are shown in table 7.3

Element	Gamma Energy (keV)	F_G	σ_{F_G}/f_G
^{116m}In	1293.5	85.3 (2.6)	3.0%
^{198}Au	411.8	130.2 (2.9)	2.2%
^{56}Mn	846.8	90.0 (1.5)	1.7%
^{64}Cu	511	105.7 (3.4)	3.2%
^{24}Na	1368.6	98.4 (1.1)	1.1%
^{52}V	1434.1	111.6 (1.2)	1.1%
^{187}W	479.6	110.2 (1.6)	1.4%
^{186}Re	137.2	85.0 (4.7)	5.6%
^{188}Re	155	106.8 (3.1)	2.9%

Tab. 7.3.: Geometric factor values for the selected elements that are used in NCT-ACS.

Combining the values in table 7.2 and 7.3, the LaBr detector efficiency for the different foils at contact can be determined simply multiplying the two set of values:

$$\epsilon_c = \epsilon_{10} \cdot F_G \tag{7.2}$$

Being ϵ_c the efficiency at contact, ϵ_{10} the efficiency at 10 cm and F_G the geometric factor.
The values of ϵ_c are shown in table 7.4.

Element	**Gamma Energy (keV)**	ϵ_c **(x10^{-2} cps/Bq)**	$\sigma_{\epsilon_c}/\epsilon_c$
^{116m}In	1293.5	2.15 (0.16	7.5%
^{198}Au	411.8	10.6 (0.10)	5.9%
^{56}Mn	846.8	3.64 (0.19)	5.1%
^{64}Cu	511	7.08 (0.41)	5.8%
^{24}Na	1368.6	2.32 (0.17)	7.3%
^{52}V	1434.1	2.49 (0.19)	7.6%
^{187}W	479.6	7.84 (0.41)	5.2%
^{186}Re	137.2	15.9 (0.19)	11.6%
^{188}Re	155	18.5 (0.19)	10.0%

Tab. 7.4.: Efficiency at contact values for the gamma energies of the selected elements used in NCT-ACS.

During the LaBr calibration two sources of systematic uncertainties have been evaluated due to the point source like approximation (<1%) and due to the use of the SNIP algorithm (1.5%) during the analysis of the gamma spectra. The overall contribute can be calculated to be:

$$S_{\text{LaBr}} = 1.8\%$$

7.3 NCT-ACS measure using the LaBr(Ce)

The same identical approach already described in section 5.2 has been used. For this measure, NCT-ACS with the complete set of 8 foils, corresponding to 9 sensitive elements, has been used.
Unfortunately, the intrinsic peak of ^{138}La at 1436 keV, with the broadening due to the beta signal, massively disturbed the gamma spectrum of V and Na respectively at 1434 keV and 1368 keV. In addition, the activation values for both of those elements was low, therefore the extraction of the activity values was not possible. Therefore only 7 elements were being able to be detected.
The saturation activity values are reported in table 7.5:

Element	Measure	LaBr-HPGe / HPGe
In ($\cdot 10^4$ Bq)	1.12 (0.04)	+6.7%
Au ($\cdot 10^3$ Bq)	8.82 (0.28)	+4.3%
Mn ($\cdot 10^2$ Bq)	4.92 (0.18)	+14%
Cu ($\cdot 10^2$ Bq)	6.08 (0.23)	+8.3%
^{185}Re ($\cdot 10^4$ Bq)	4.85 (0.31)	+11%
^{187}Re ($\cdot 10^4$ Bq)	2.49 (0.22)	+10%
W ($\cdot 10^3$ Bq)	5.53 (0.47)	+4.7%

Tab. 7.5.: Activation results for the the 20 mm configuration with 6 foils, corresponding to 7 sensitive elements. The percentage deviation from the HPGe measures is also reported.

It should be noted that the relative uncertainty on the activation values is higher respect to the previous case with the HPGe detector. This reinforces the hypothesis that the higher background affects the final result, increasing the uncertainty.
A systematic over estimation of the activation values can be quantified in the order of 8%. This aspect was carefully investigated and the explanation could be that the distance between the calibrated source and the LaBr detector was slightly higher respect to the distance between the activated foils and the LaBr itself. In fact, during the measurements, the foils were being placed inside a pocket in contact with the holder, while the calibration sources where placed outside the pocket itself.
This additional thickness could be conduct to an under estimation in the efficiency and then an over estimation on the final activity. Considering a thicknesses of 2 mm, the corrective factor should be $(1.02)^2$=1.04 which can partially correct for this discrepancy.
Nevertheless, the unfolding procedure is not sensitive to any global constant multiplied for all the values since it operates normalizing all the data. For the future

measurements a factor 0.93 will be taken into account to adequately correct the LaBr measurements.

The unfolding procedure was then applied, using the saturation activity values, and the result is shown in figure 7.4. The BSS result is also reported.

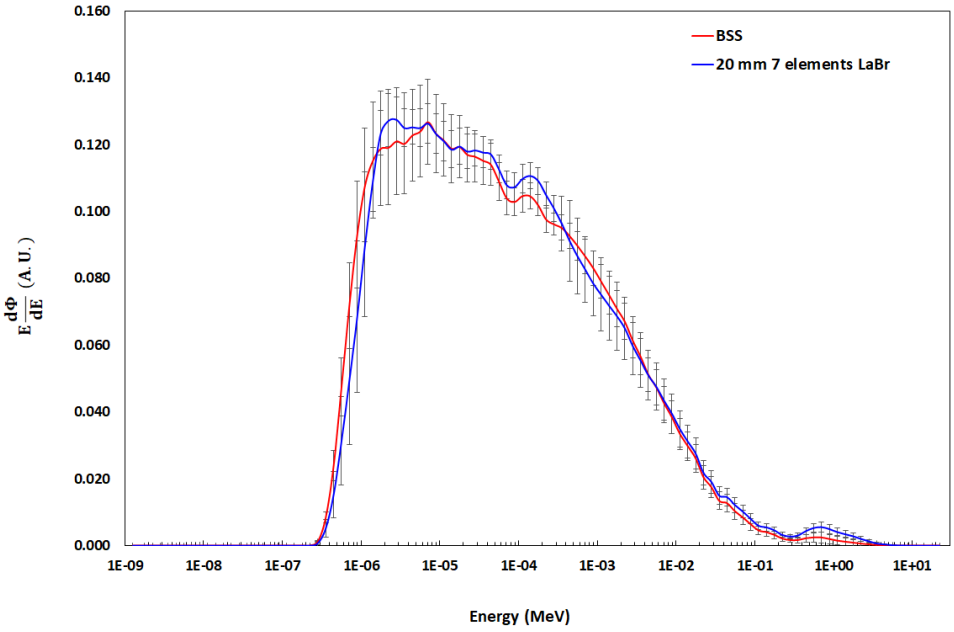

Fig. 7.4.: Comparison between the NCT-ACS result and BSS result using the same guess.

Some considerations on the results should be done:

- In the region between 10^{-6} MeV and $3{\cdot}10^{-4}$ MeV the NCT-ACS result does not show any fluctuations, meaning that in this energy region the unfolding procedure is robust due to the extra elements respect to the configuration studied in 5.2.2.

- In the region between $3{\cdot}10^{-4}$ MeV and $3{\cdot}10^{-3}$ MeV the NCT-ACS results is perfectly aligned with the BSS result.

- In the region above 10^{-2} MeV the NCT-ACS spectrum is slightly above the reference one, showing a small systematic difference.

- The fast neutron peak at around 1 MeV is still present in the NCT-ACS result. Confirming what already noticed in the previous analysis.

- The presence of a peak at around 2 eV, enhancing a behaviour already studied in the HPGe case, is probably due to the small over estimation for the activation

values that in someway affected the final results, that because in this energy region, the In peak is massively dominating, therefore an higher activity value can provide some peaked structure. Nevertheless, it is not dramatically disturbing the remaining part of the spectrum.

It should be concluded that in this configuration the spectrometric capability of NCT-ACS is increased respect to the 20 mm with 6 elements configurations, but it is slightly worse respect to the 20 mm with 9 elements configuration.
Moreover, the ratio plot shows in figure 7.5 confirms the goodness in the 20 mm 7 elements configuration.

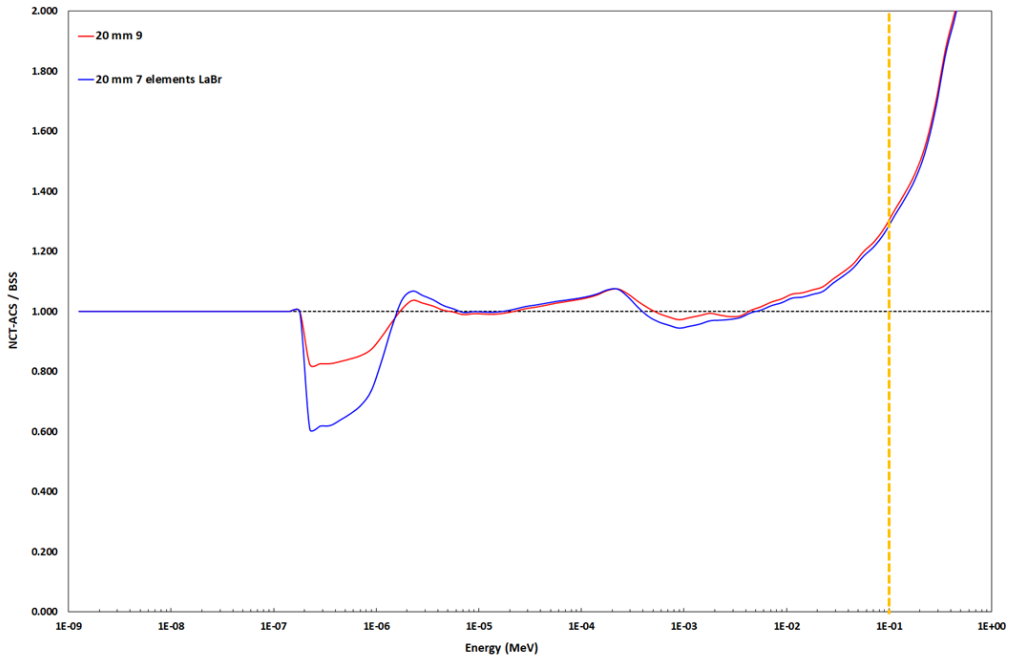

Fig. 7.5.: Ratio between the NCT-ACS spectra and the BSS result in function of the energy. The 20 mm with 7 elements and the 20 mm with 9 elements configurations are shown together. The dotted orange line represents the upper limit of the analyzed energy region.

The same analysis on the ratio R between the NCT-ACS measure and the BSS result was performed and the mean value together with the related standard deviation have been calculated:

$$\bar{R} = 0.99$$

$$\sigma_R = 12\%$$

The 12% σ value implies a 23% dispersion value for an $\alpha = 0.05$ significance level (1.96 σ) in the energy region between 10^{-9} MeV and 10^{1} MeV.
It should be noted that, respect to the 20 mm 9 elements configuration, the only energy region where some notable differences can be shown is from 10^{-7} MeV and

10^{-6} MeV corresponding to the rising part in the spectrum. As already discussed this was due to a small over estimation in the In activity. Neglecting this part, over all the other energy values the two ratio plot are almost identical, proving the goodness of the LaBr measure.

In order to evaluate the robustness of the response matrix using the experimental results, the same procedure as before has been applied, using the same misleading guess.
In figure 7.6 the results are shown together with the BSS spectrum and the NCT-ACS spectrum obtained with the true guess.

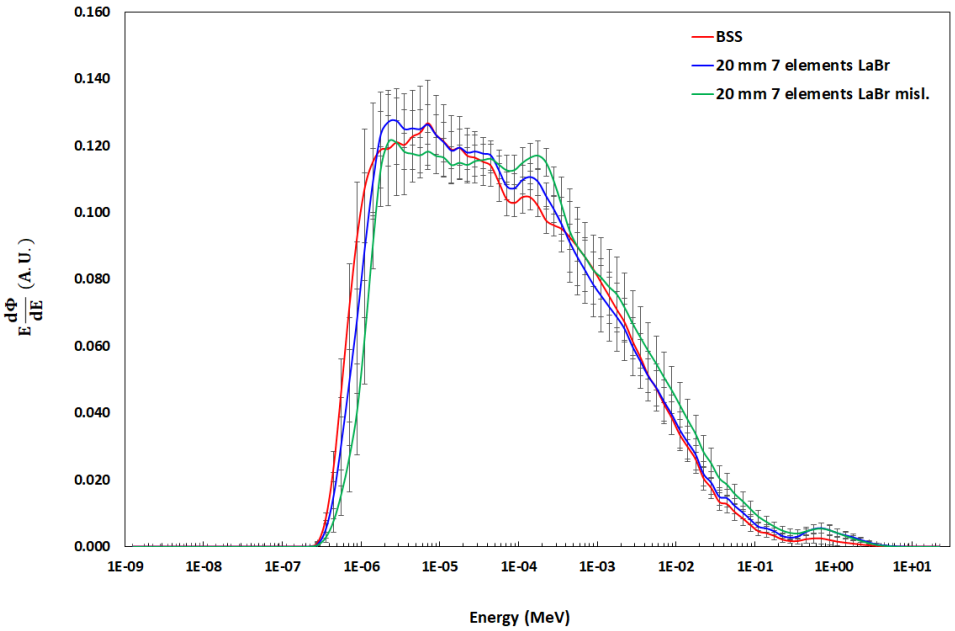

Fig. 7.6.: Comparison between the NCT-ACS results using a misleading guess and using the true guess. The reference BSS result is also shown.

It can be noted that the unfolded spectrum using the misleading guess presents some fluctuations in the middle energy region with a discrete peak at around 100 eV. Moreover an under estimation can be noticed in the low energy range up to 2 eV and then a small over estimation in the final part from 1 keV up to 1 MeV. This sort of mismatching is due to the normalization procedure that induce some region to increase in order to maintain the total area.
Moreover, the ratio with the BSS result has been performed again, showing a degradation in the σ value:

$$\bar{R}\,(misl) = 1.03$$

$$\sigma_R\,(misl) = 25\%$$

The massive broadening in the ratio distribution is described by the σ value around 25% which show that, using this configuration, the unfolding robustness with a misleading guess is still insufficient.

7.3.1 Comparison with the HPGe results

The activation values comparison between HPGe and LaBr has been already discussed in section 7.3.
It should be noted that a direct comparison of the unfolding results obtained int he HPGe and LaBr analysis could provide more information and clarify some aspects.
Therefore, the same approach adopted in the previous comparison analysis has been adopted. Nevertheless, in this case the ratio R^* between the two spectra was evaluated dividing the HPGe and the LaBr unfolding outputs.It should be noted that for the HPGe spectrum, the one obtained using the 20 mm and 9 sensitive elements configuration has been considered.

$$R^* = \frac{\text{HPGe (20 mm, 9 elements)}}{\text{LaBr (20 mm, 7 elements)}}$$

Thus, the result is completely independent by the BSS measure and it provides information only on the compatibility between the different approaches.
In figure 7.7 the ratio result in function of the neutron energy is shown.

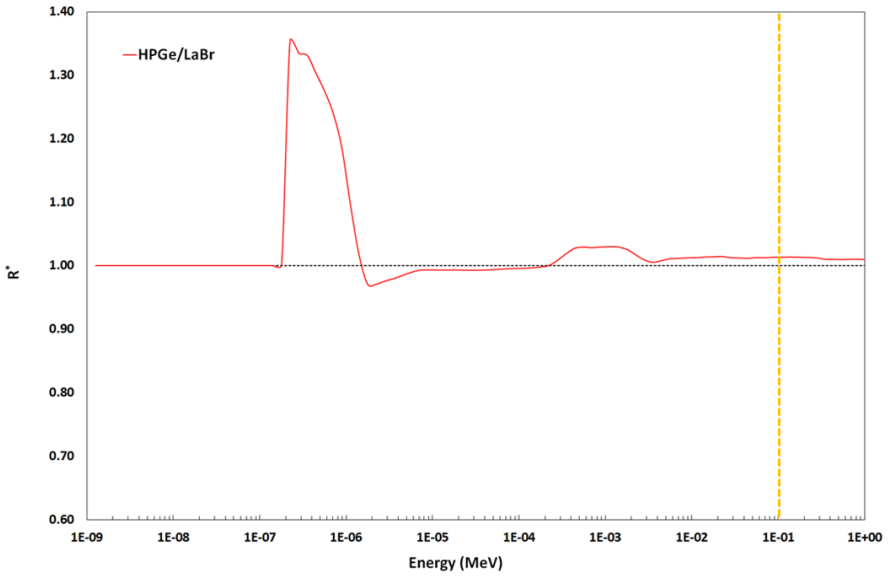

Fig. 7.7.: Ratio between the NCT-ACS spectra obtained with the HPGe and with the LaBr detectors in function of the energy. The dotted orange line represents the upper limit of the analyzed energy region.

As already mentioned in the previous section, the ratio is very close to the unit value, except for the energy region from 10^{-7} MeV up to 10^{-6}. This can be caused by the

lower number of elements. Moreover, this part is the first "signal" region after the Cd cut-off providing some challenges to the response matrix. In fact, a fluctuation in the In activation value could change the sharpness in the rising part.
The mean value and standard deviation of the R^* ratio have been calculated:

$$\bar{R^*} = 1.02$$

$$\sigma_{R^*} = 7\%$$

It should be noted that in this case the two values have been calculated considering the whole energy range and not stopping up to 100 keV. In fact, this analysis aims to evaluate the compatibility between the two measurements (HPGe and LaBr) results and not the direct effectiveness of the technique. The latter has been already discussed in the previous sections.
Considering the results, the compatibility between the two set of data is proved.

7.4 Summary of the LaBr detector study

In this section, a summary of the study involving the LaBr(Ce), option is presented. A calibration procedure similar to the HPGe configuration has been evaluated. Since the reduced crystal dimension of the LaBr(Ce), the point source like approximation can be considered valid (below 1%) for distances between the foils and the detector of 20 cm. The fluence rate at the e-LiBaNS facility, considering both working configurations, is not sufficient to induce activities large enough to perform the calibration. Therefore, the LENA reactor facility has been used. In particular, the Rabbit channel, where a fluence rate in the order of 10^{13} cm^{-2}s^{-1} is achievable, was used. On the contrary, the source calibration, has been performed in the same way as the HPGe case. Thus, the contact efficiency for the different foils was calculated like:

$$\epsilon_{\text{con}} = F_G \cdot \epsilon_{10\text{ cm}}$$

Being ϵ_{con} and $\epsilon_{10\text{ cm}}$ respectively the efficiency at contact and at 10 cm and F_G the geometric factor. In table 7.4 the efficiency values are shown together with the percentage uncertainties.

The same experimental setup as already shown in section 5.2 was adopted and the activities of the different foils have been calculated. The intrinsic background due to the ^{138}La did not allow to correctly estimate the Na and V activities. Therefore, only 7 sensitive elements among the total number of 9 have been used for the unfolding procedure.
In table 7.6 the measured saturation activity values are shown, together with a comparison with the HPGe results.

Element	**Measure**	**LaBr-HPGe / HPGe**
In ($\cdot 10^4$ Bq)	1.12 (0.04)	+6.7%
Au ($\cdot 10^3$ Bq)	8.82 (0.28)	+4.3%
Mn ($\cdot 10^2$ Bq)	4.92 (0.18)	+14%
Cu ($\cdot 10^2$ Bq)	6.08 (0.23)	+8.3%
^{185}Re ($\cdot 10^4$ Bq)	4.85 (0.31)	+11%
^{187}Re ($\cdot 10^4$ Bq)	2.49 (0.22)	+10%
W ($\cdot 10^3$ Bq)	5.53 (0.47)	+4.7%

Tab. 7.6.: Activation results for the the 20 mm configuration with 6 foils, corresponding to 7 sensitive elements. The percentage deviation from the HPGe measures is also reported.

A systematic over estimation of the activation values can be quantified in the order of 8%. This aspect was investigated and a corrective factor of 1.04, due to misplacing during the calibration, can partially correct for this discrepancy.

Nevertheless the unfolding procedure was performed. In figure 7.8 the unfolding result is shown.

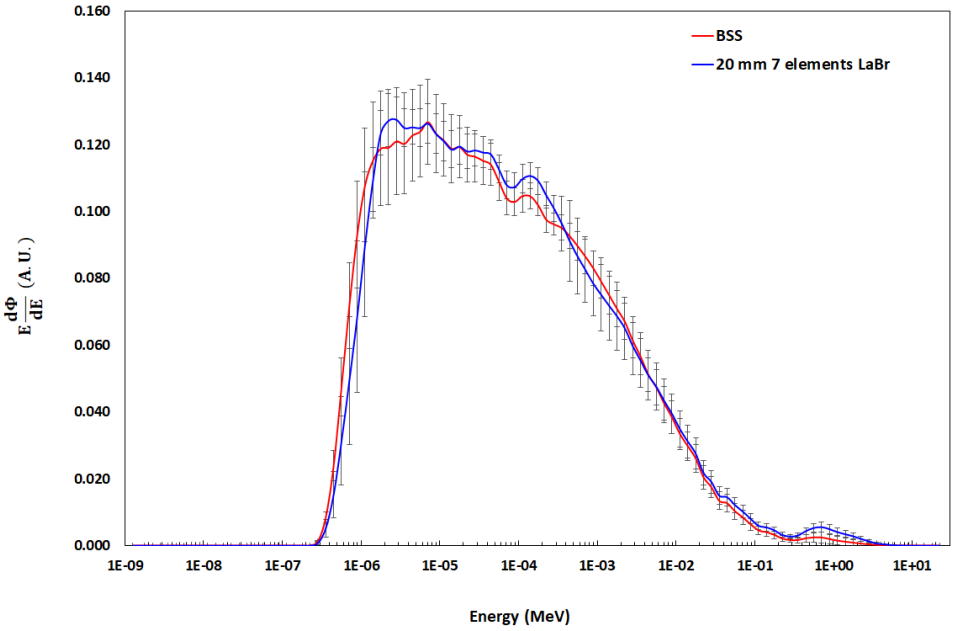

Fig. 7.8.: Comparison between the NCT-ACS result and BSS result using the same guess.

Analyzing the shape of the two spectra it should be concluded that in this configuration the spectrometric capability of NCT-ACS is increased respect to the 20 mm with 6 elements configurations (HPGe), but it is slightly worse respect to the 20 mm with 9 elements configuration (HPGe).
Moreover, the ratio plot which is shown in figure 7.9 confirms the goodness in the 20 mm 7 elements configuration.

The same analysis on the ratio R between the NCT-ACS measure and the BSS result was performed and the mean value together with the related standard deviation have been calculated:

$$\bar{R} = 0.99$$

$$\sigma_R = 12\%$$

In order to evaluate the robustness of the response matrix using the experimental results, the same procedure as before has been applied, using the same mislead-

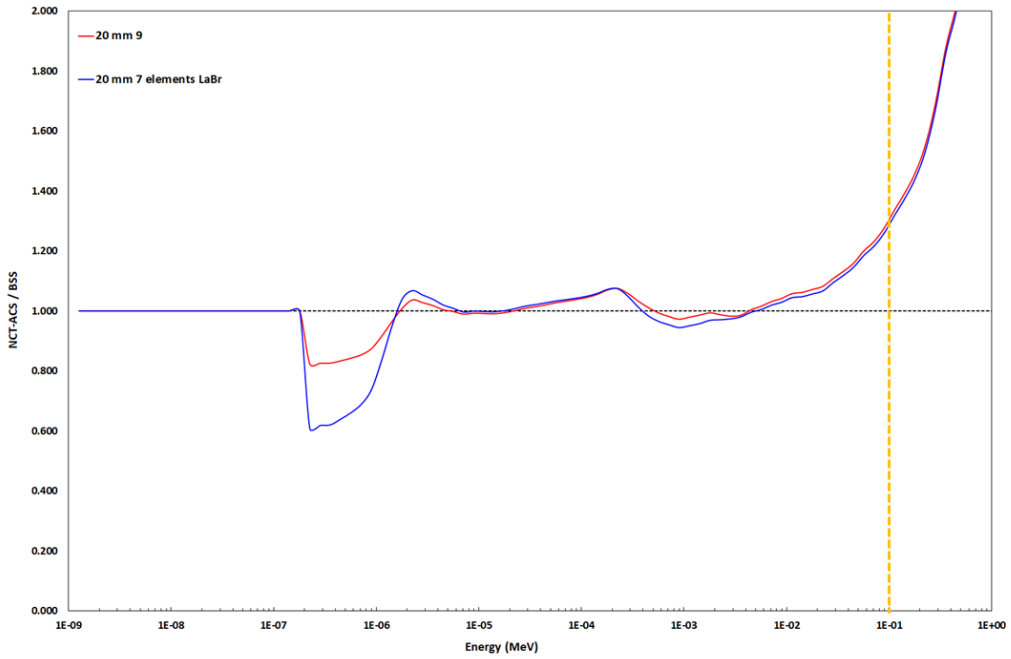

Fig. 7.9.: Ratio between the NCT-ACS spectra and the BSS result in function of the energy. The 20 mm with 7 elements and the 20 mm with 9 elements configurations are shown together. The dotted orange line represents the upper limit of the analyzed energy region.

ing guess. The ratio with the BSS result has been performed again, showing a degradation in the σ value:

$$\bar{R}\,(misl) = 1.03$$

$$\sigma_R\,(misl) = 25\%$$

The massive broadening in the ratio distribution is described by the σ value around 25% which show that, using this configuration, the unfolding robustness with a misleading guess is still insufficient.

A further analysis was then performed concerning the comparison between the LaBr(Ce) and the 20 mm with 9 sensitive elements configuration using the HPGe. The last could be considered as the best working configuration for NCT-ACS. The ratio R^* between the two spectra has been performed and the distribution was then analyzed:

$$\bar{R^*} = 1.02$$

$$\sigma_{R^*} = 7\%$$

It should be noted that in this case the two values have been calculated considering the whole energy range and not stopping up to 100 keV. It can be concluded that the two spectra are compatible within the sensitivity range of NCT-ACS and even on an extended energy range.

It can be concluded that in this configuration the system is less "powerful" respect to the 20 mm and 9 elements configuration analyzed using the HPGe detector. It is also interesting to notice that adding only one element improved the results using a true guess spectrum, while in the case of a misleading one, more elements are required. Nevertheless this configuration represents an excellent alternative to the HPGe measures in order to provide in situ measurements.

8 Conclusions and outlooks

This chapter aims to provide the final conclusion on the NCT-ACS work. It is primarily composed by the "Partial conclusion" section 6 and by the summary on the LaBr(Ce) measure.

In recent years, the introduction of accelerator-based BNCT facilities has led to a significant increase in interest from the medical and scientific communities. Monitoring and characterization of neutron beams and intercomparison of different facilities are becoming mandatory [1]. This stimulates the development of dedicated dosimetry and spectrometry techniques.

Within this context, the thesis work conceived and developed a compact epithermal neutron spectrometer capable of operating across an energy range from thermal to 100 keV, known as NCT-ACS (Neutron Capture Therapy - Activation Compact Spectrometer)
The core idea behind this instrument involves using the neutron capture phenomena within specific elements to gather information on the neutron energy spectrum and subsequently reconstruct it using suitable unfolding techniques. Particularly, the identification of strong resonances in the epithermal range within certain elements was pivotal for this project objectives. To appropriately select the elements candidates, an extensive study was conducted, involving the analysis and exploration of numerous potential elements while applying specific selection criteria based on their key characteristics. Following this selection phase, the most promising elements for the operation of NCT-ACS were determined to be: In, Au, Mn, Cu, V, NaCl, Re (both ^{185}Re and ^{187}Re isotopes) and ^{186}W. Circular foils composed of these elements were chosen, and their thicknesses were calibrated appropriately to optimize the spectrometer's performance.

An intensive study employing Monte Carlo simulations was conducted to identify the optimal geometry for NCT-ACS. The purpose of this study was to designing a configuration that enabled NCT-ACS to achieve:

- Isotropic response, mitigating the need for corrections associated with the angular distribution of the source.

- Sensitivity to neutrons spanning from thermal energies up to at least 100 keV.

- Compact dimensions suitable for the confined spaces typical in BNCT applications.

- Feasibility for use with a single irradiation to reduce total acquisition time.

Following this study, the most favorable geometry identified consisted of a small-sized polyethylene sphere housing a cylindrical cavity of 8 mm in depth. Within this cavity a cadmium cylinder, 0.5 mm thick, was placed accommodating various foils of the selected elements. Specifically, two alternative configurations of this geometry were developed, differing solely in the radius of the polyethylene spherical shell: 20 mm and 28 mm.

It's important to highlight how the addition of the moderator allowed achieving isotropic conditions while rendering the instrument response curves suitable for incorporation into an unfolding procedure. Due to the sharp resonance structures, the unfolding algorithm previously introduced non-physical oscillations within the reconstruction of the neutron spectrum.
The anisotropy of this designed geometry was evaluated through Monte Carlo simulations by varying the incident angle of neutrons. The activation rate of the foils was extracted with varying angles of incidence, and the anisotropy was estimated at 1.96 standard deviations from the hypothetical count distribution. A maximum anisotropy value of 3% was chosen, with both selected geometries yielding values below this threshold, considered as a component of systematic uncertainty:

$$S_{\text{anisotropy}} = 2.4\%$$

Before testing NCT-ACS, an extensive study of the HPGe detector available at the University of Turin was conducted. This process enabled the calibration of the instrument to calculate the absolute activity of the foils by placing them directly in contact with the detector. This was achieved by considering both geometric aspects and system analysis. During the calibration phase, the neutron facility known as e-LiBaNS in Turin [135] was utilized.
The calibration scheme is outlined as follows:

1. The HPGe energy calibration ha been performed using calibration sources (^{137}Cs,^{60}Co,^{22}Na,^{152}Eu,^{133}Ba);

2. An efficiency calibration of the detector was carried out by placing the same known-activity sources at a distance of 10 cm. A fit curve of the data was extrapolated and employed as the calibration curve.

3. The activation foils, selected for NCT-ACS, were irradiated at the e-LiBaNS facility under non-standard conditions, aiming to induce high activity values.

4. The foils were then analyzed at two different positions relative to the HPGe detector: at 10 cm and in direct contact.

5. The ratio of the estimated cps from the two measurements was derived after necessary corrections, defining the geometric factor. The assumption to a point-like source was estimated to produce a systematic error within approximately 1% under the measurement conditions used;

6. With the obtained values, the foils activation can be analyzed by placing them in contact with the detector. This approach allow for reducing neutron irradiation and gamma spectrum acquisition times. Additionally, it allows for increased statistical counts, while maintaining relatively low levels of radioactivity. This process effectively reduces the risk of unwanted radiation exposure during the experimental procedure.

The HPGe detector efficiency values for the different elements used in NCT-ACS are reported in table 4.5, while the geometric factors of the foils are reported in table 4.6.
Combining the values in these tables, the HPGe detector efficiency for the different foils at contact can be determined simply multiplying the two set of values:

$$\epsilon_c = \epsilon_{10} \cdot F_G \tag{8.1}$$

Being ϵ_c the efficiency at contact, ϵ_{10} the efficiency at 10 cm and F_G the geometric factor. These values can be find in table 4.7.
During the HPGe calibration two sources of systematic uncertainties have been evaluated due to the point source like approximation and due to the use of the SNIP algorithm during the analysis of the gamma spectra. The overall contribute can be calculated:

$$S_{\text{HPGe}} = 1.4\%$$

The total systematic uncertainty can be then calculated to be:

$$S_{\text{tot}} \simeq 3\%$$

At the conclusion of the calibration procedure, a series of measurements were conducted at the e-LibaNS facility operating in the epithermal mode. Under these conditions, the spectrum and fluence rate of the source are known and measured

using a calibrated Bonner Sphere Spectrometer.
Three different types of measure have been performed using different configurations:

1. 20 mm with 6 sensitive elements

2. 20 mm with 9 sensitive elements

3. 28 mm with 6 sensitive elements

For all of these configurations, an unfolding procedure has been applied both with a true guess and with a misleading guess. A comparison with BSS result was also evaluated, considering the BSS measure as a reference one.
In figure 8.1 the results of the unfolding procedure using the true guess spectrum are shown.

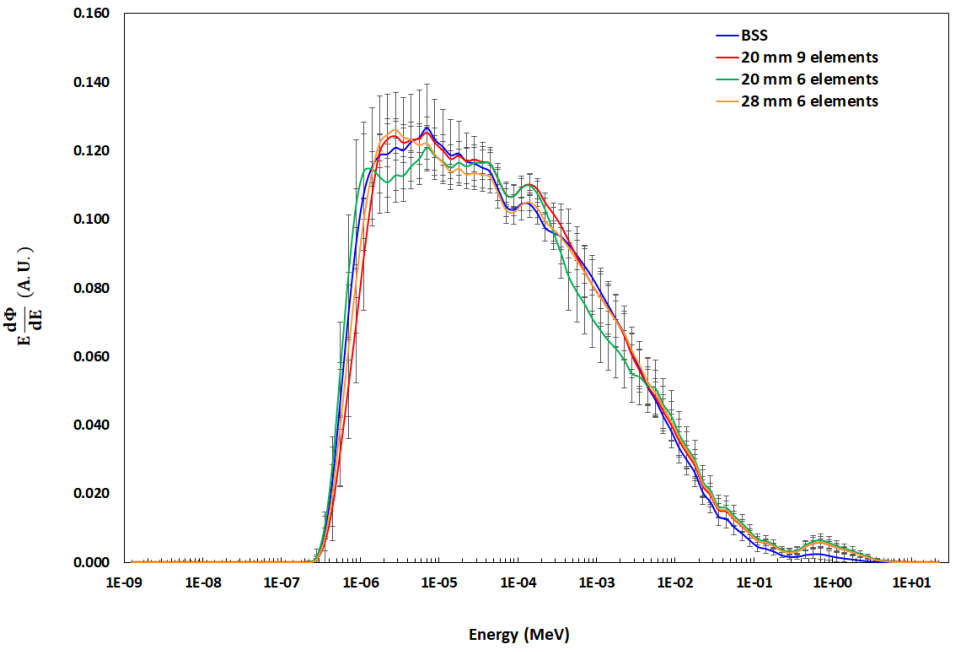

Fig. 8.1.: Unfolded spectra for all the studied configurations providing to the FRUIT code the true guess. The BSS spectrometer is also reported.

It should be noted that:

1. Using the true guess spectrum during the unfolding, all the configurations are able to correctly reconstruct the spectrum within the uncertainties and the ratio between the NCT-ACS spectra and the BSS result was calculated:

- The 20 mm with 6 elements configuration revealed a dispersion value of around 13% (subsection 5.2.2);

- The 20 mm with 9 elements configuration shown a dispersion value of around 6% (subsection 5.2.3);

- The 28 mm with 6 elements configuration was characterized by a dispersion value of around 8% (subsection 5.2.4).

All these values are related to the energy range from thermal up to 0.1 MeV. Above the 0.1 MeV limit, the NCT-ACS sensitivity was found to be too low to correctly reconstruct the spectrum and the guess information became dominant.

2. Using the misleading guess spectrum, only the 20 mm with 9 elements configuration is able to reconstruct the correct spectrum (ratio dispersion of 11%), while the other configurations fail in many aspects (ratio dispersion of 21% and 19 % for the 20 mm and 28 mm respectively).

Thus can be concluded that, actually, the best option is the 20 mm with 9 sensitive elements. This configurations is robust and can also work with a misleading spectrum, being the most stable option.

A comparison with the Monte Carlo values from chapter 3 has been performed, providing a good agreement between Monte Carlo results and experimental data. Thus the response matrix and simulation work have been validated. It should be noted that for the V foil, some discrepancies have been founded. A possible explanation in the discrepancy for the V foil could rely on a lack in the nuclear data. This provided the possibility to study the neutron cross section on V in a dedicated facility. In particular, some transmission measurements have been performed at the JRC in Geel (Belgium), using the GELINA Time Of Flight (TOF) facility [134]. GELINA is one of the most important laboratory in the nuclear data production field, since it is characterized by an excellent time resolution of 1 ns. This allows to investigate the different resonances in the Resolved Resonance Region (RRR).
Measures using three different V sample configurations have been performed and an intense literature study has been produced. In particular, the literature review revealed a massive lack in the capture data, with few data. Moreover, the data collected are not in good agreement between each other.
The first results on the transmission measures are currently undergoing further analysis aiming to improve the nuclear data libraries. A more in detail treatment with some first results is presented in Appendix D.

In particular, the average ratio between the two set of values was calculated to be:

$$R_{com} = 1.00\,(0.05)$$

Figure 8.2 shows the results for all the selected elements.

Moreover, the robustness of the Monte Carlo simulations has been reinforced by considering the attenuation in the saturation activities between the 20 mm and the 28 mm cases. The reduction in the saturation activities was found to be in perfect agreement with the one predicted by the simulations within a 1% of deviation.

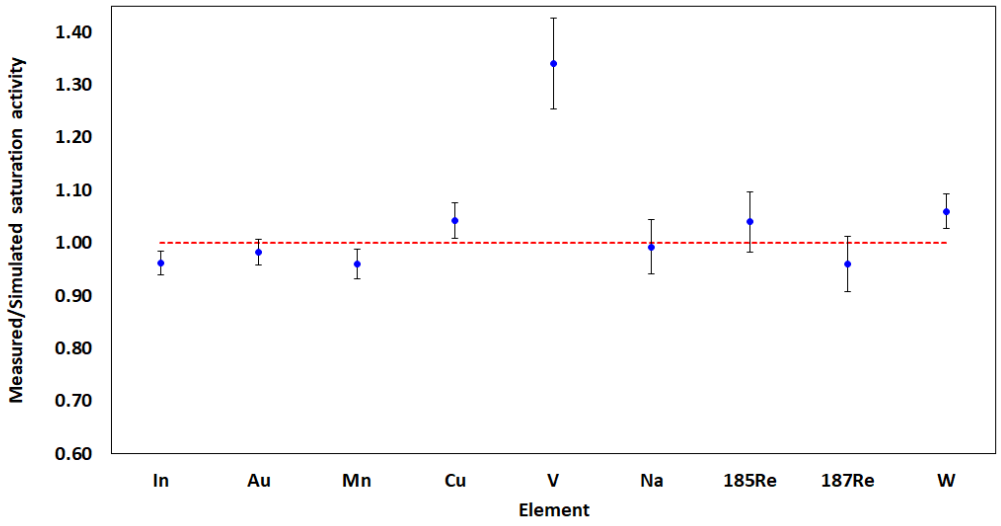

Fig. 8.2.: R_{com} values for the different elements. The dotted red line represent the ideal case for the ratio (=1). The uncertainties bars are mainly driven by the experimental uncertainties, since the Monte Carlo ones are lower than 1%.

Aiming to develop a portable system composed by a gamma detector coupled to NCT-ACS, more efforts was focused on shifting the whole analysis on another gamma detector based on a LaBr(Ce) crystal scintillator. This would represent a further improvements for the NCT-ACS capability, making it even more attractive for BNCT applications.

A calibration procedure similar to what already shown has been performed. To enhance the point like source approximation validity, all the *distance* measurements have been performed at 20 cm from the sensitive region of the detector. The contact efficiency was then extracted using equation 8.1.
The systematic uncertainty due to the gamma detector can be calculated to be:

$$S_{\text{LaBr}} = 1.8\%$$

And the total value is the same as in the HPGe configuration:

$$S_{\text{tot, LaBr}} \simeq 3\%$$

The activation values calculated with the LaBr(Ce) are in good agreement with the values obtained using the HPGe detector. A systematic over estimation of the activation values can be quantified in the order of 8%. A corrective factor of 1.04, due to misplacing during the calibration, can partially correct for this discrepancy. Nevertheless the unfolding procedure was performed. In figure 8.3 the unfolding result is shown.

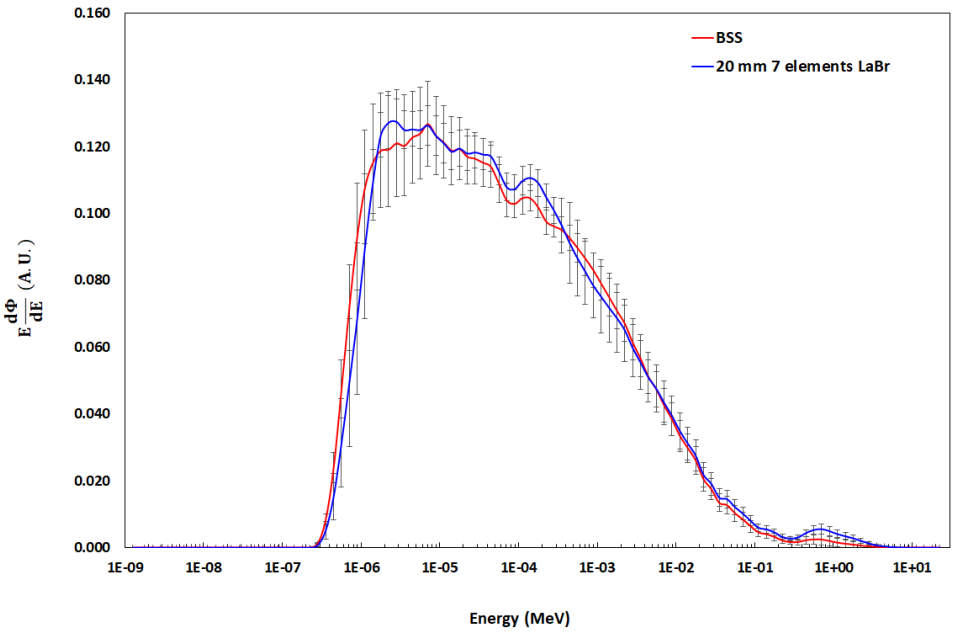

Fig. 8.3.: Comparison between the NCT-ACS result and BSS result using the same guess.

Analyzing the shape of the two spectra it should be concluded that in this configuration the spectrometric capability of NCT-ACS is increased respect to the 20 mm with 6 elements configurations (HPGe), but it is slightly worse respect to the 20 mm with 9 elements configuration (HPGe).
It should be also mentioned that while evaluating the robustness of the response matrix providing a misleading guess, the results were found to be not satisfactory. Thus, using this configuration, particularly care should be focused in providing a well designed guess spectrum.

Moreover, a comparison between the spectrum extracted with the 20 mm with 9 elements configuration (HPGe) and the LABr(Ce) measure revealed an excellent comparison.
It can be concluded that in this configuration the system is less "powerful" respect to

the 20 mm and 9 elements configuration analyzed using the HPGe detector. It is also interesting to notice that adding only one element improved the results using a true guess spectrum, while in the case of a misleading one, more elements are required. Nevertheless this configuration represents an excellent alternative to the HPGe.

In conclusion, the neutron activation spectrometer, known as NCT-ACS, has been developed in two distinct variants, both of which have been thoroughly tested and calibrated using a HPGe detector. The achieved results show an excellent agreement with the reference measurements, confirming the validity of the instrument and the work performed. This instrument marks an innovation, given its capability to measure epithermal spectra in reduced volumes, demonstrating precision and efficiency comparable to the standard technique of Bonner Sphere Spectrometer. Furthermore, an intense analysis was conducted on a compact system consisting of a portable LaBr(Ce) gamma detector coupled with NCT-ACS. The obtained results are highly promising as the unfolding procedure adequately reconstructs the spectrum, providing comparable results to the HPGe option.

Consequently, this study opens the possibility for the development of a well calibrated measurement system, permitting in situ measurements. This achievement stands as a significant milestone in meeting the stringent criteria for the beam quality assurance in Boron Neutron Capture Therapy.

Bibliography

[1] *Advances in Boron Neutron Capture Therapy*. Non-serial Publications. Vienna: INTERNATIONAL ATOMIC ENERGY AGENCY, 2023 (cit. on pp. v, 189, 215).

[2] Roberto Bedogni, Carles Domingo, Adolfo Esposito, and Francisco Fernández. "FRUIT: An operational tool for multisphere neutron spectrometry in workplaces". en. In: *Nucl. Instrum. Methods Phys. Res. A* 580.3 (Oct. 2007), pp. 1301–1309 (cit. on pp. v, 61, 111, 114).

[3] Bob D'Mellow, David J. Thomas, Malcolm J. Joyce, et al. "The replacement of cadmium as a thermal neutron filter". In: *Nuclear Instruments and Methods in Physics Research Section A: Accelerators, Spectrometers, Detectors and Associated Equipment* 577.3 (2007), pp. 690–695 (cit. on p. 2).

[4] Liyuan Zhang, Rihua Mao, and Ren-Yuan Zhu. "Fast Neutron Induced Nuclear Counter Effect in Hamamatsu Silicon PIN Diodes and APDs". In: *IEEE TRANSACTIONS ON NUCLEAR SCIENCE* 1 (Oct. 2011) (cit. on p. 3).

[5] A.D. Vijaya and Arun Kumar. "The neutron spectrum of Am-Be neutron sources". In: *Nuclear Instruments and Methods* 111.3 (1973), pp. 435–440 (cit. on p. 3).

[6] Valeria Monti. "Design and characterization of the Torino Linac based thermal neutron source developed within the e-LiBANS project". PhD thesis. July 2018 (cit. on pp. 3, 58).

[7] Ka-Ngo Leung, Jani Reijonen, Frederic Gicquel, Sami Hahto, and Tak Pui Lou. "Compact neutron generator developement and applications". In: (Sept. 2023) (cit. on p. 3).

[8] D. Thomas. "ICRU report 85: fundamental quantities and units for ionizing radiation". In: *Radiation Protection Dosimetry* 150 (July 2012), pp. 550–552 (cit. on pp. 6, 16, 18, 29).

[9] L Papiez. "Radiance and particle fluence". In: *Physics in medicine and biology* 39 (July 1994), pp. 1053–62 (cit. on p. 6).

[10] Masakuni NARITA and Koichi NARITA. "Average Number of Collisions Necessary for Slowing Down of Neutrons". In: *Journal of Nuclear Science and Technology - J NUCL SCI TECHNOL* 26 (Sept. 1989), pp. 819–825 (cit. on p. 7).

[11] W. Burcham. "Nuclear physics : an introduction / W. E. Burcham". In: *SERBIULA (sistema Librum 2.0)* (Feb. 2020) (cit. on pp. 8, 9).

[12] Robley Evans. “The Atomic Nucleus”. In: *International Series in Pure and Applied Physics* (Jan. 1955) (cit. on pp. 8, 76).

[13] Edoardo Amaldi. *The Production and Slowing Down of Neutrons*. Berlin, Heidelberg: Springer Berlin Heidelberg, 1959, pp. 1–659 (cit. on p. 8).

[14] S. Flügge. *Handbuch der physik*. Handbuch der physik v. 40. Springer, 1957 (cit. on p. 8).

[15] A. M. Lane and R. G. Thomas. “R-Matrix Theory of Nuclear Reactions”. In: *Rev. Mod. Phys.* 30 (2 1958), pp. 257–353 (cit. on p. 8).

[16] R Huby. “The Theory of Neutron Resonance Reactions”. In: *Physics Bulletin* 20.4 (1969), p. 149 (cit. on p. 8).

[17] Institute of Physics (Great Britain), T. von Egidy, and Institut Laue-Langevin. *Fundamental Physics with Reactor Neutrons and Neutrinos: Twenty Six Papers from a Workshop on Fundamental Physics Experiments with Reactor Neutrons and Neutrinos Held at the Institut Laue-Langevin, Grenoble, 10-11 October, 1977*. Conference Series. Institute of Physics, 1978 (cit. on p. 8).

[18] W Gelletly. “Neutron Physics with Contributions by L Koester and A Steyerl (Springer Tracts in Modern Physics Vol 80)”. In: *Physics Bulletin* 28.11 (1977), p. 522 (cit. on p. 8).

[19] R. S. Carter, H. Palevsky, V. W. Myers, and D. J. Hughes. “Thermal Neutron Absorption Cross Sections of Boron and Gold”. In: *Phys. Rev.* 92 (3 1953), pp. 716–721 (cit. on p. 8).

[20] “References”. In: *Reports of the International Commission on Radiation Units and Measurements* os-7.2 (1969), pp. 44–52. eprint: `https://doi.org/10.1093/jicru_os7.2.44` (cit. on p. 8).

[21] G. Breit and E. Wigner. “Capture of Slow Neutrons”. In: *Phys. Rev.* 49 (7 1936), pp. 519–531 (cit. on p. 9).

[22] Nicolas Soppera, Manuel Bossant, O. Cabellos, Emmeric Dupont, and C.J. Díez. “JANIS: NEA JAva-based Nuclear Data Information System”. In: *EPJ Web of Conferences* 146 (Sept. 2017), p. 07006 (cit. on p. 11).

[23] Allison Gicking. “Neutron Capture Cross Sections of Cadmium Isotopes”. In: (Feb. 2020) (cit. on p. 12).

[24] Man Go and Samuel Markowitz. “Test of the Independence Postulate in the Bohr Theory of Compound-Nucleus Decay: 50Cr* System”. In: *Physical Review C - PHYS REV C* 7 (Apr. 1973), pp. 1464–1470 (cit. on p. 13).

[25] P. Oblozinsky, Young-Sik Cho, C. Mattoon, and Said Mughabghab. “Formalism for neutron cross section covariances in the resonance region using kernel approximation”. In: (Jan. 2010) (cit. on p. 13).

[26] Said Mughabghab. *Atlas of neutron resonances: resonance parameters and thermal cross sections Z= 1-100*. Jan. 2006 (cit. on pp. 13, 17, 21, 38, 69, 70, 76, 87, 89, 159, 283–287).

[27] F.H. Frohner. *Evaluation and Analysis of Nuclear Resonance Data*. Jan. 2000 (cit. on p. 15).

[28] Carl H. Westcott. “The specification of neutron flux and nuclear cross-sections in reactor calculations”. In: *Journal of Nuclear Energy (1954)* 2.1 (1955), pp. 59–75 (cit. on pp. 17, 159).

[29] Said Mughabghab. “Thermal neutron capture cross sections resonance integrals and g-factors”. In: (Jan. 2003) (cit. on p. 17).

[30] J. S. Levinger and H. A. Bethe. “Dipole Transitions in the Nuclear Photo-Effect”. In: *Phys. Rev.* 78 (2 Apr. 1950), pp. 115–129 (cit. on p. 19).

[31] Peter Axel. “Electric Dipole Ground-State Transition Width Strength Function and 7-Mev Photon Interactions”. In: *Phys. Rev.* 126 (2 Apr. 1962), pp. 671–683 (cit. on p. 20).

[32] D Brink. “Some aspects of the interaction of light with matter”. PhD thesis. University of Oxford, 1955 (cit. on p. 20).

[33] Carol M. McCullagh, Marion L. Stelts, and Robert E. Chrien. “Dipole radiative strength functions from resonance neutron capture”. In: *Phys. Rev. C* 23 (4 Apr. 1981), pp. 1394–1403 (cit. on p. 20).

[34] Evans Hayward. “Nuclear Photo-Disintegration . J. S. Levinger. Oxford University Press, New York, 1960. 144 pp. $2.” In: *Science* (1960) (cit. on p. 22).

[35] J.S. Levinger. “Modified quasi-deutron model”. In: *Physics Letters B* 82.2 (1979), pp. 181–182 (cit. on p. 22).

[36] Maria Terranova, D. Lima, and J. Filho. “Evaluation of Total Nuclear Photoabsorption Cross-Sections by the Modified Quasi-Deuteron Model”. In: *EPL (Europhysics Letters)* 9 (July 2007), p. 523 (cit. on p. 22).

[37] NationaL Council on Radiation Protection and Measurements. “Neutron Contamination from Medical Electron Accelerators”. In: *NCRP Report n 79* (1984) (cit. on p. 22).

[38] Wolfgang Finkelnburg. *Physics of Atomic Nuclei and Elementary Particles*. Berlin, Heidelberg: Springer Berlin Heidelberg, 1964, pp. 211–343 (cit. on p. 23).

[39] A. Gilbert and A. G. W. Cameron. “A composite nuclear-level density formula with shell corrections”. In: *Can. J. Phys.* 43 (1965), pp. 1446–1496 (cit. on p. 23).

[40] Gabriele Croci, Carlo Cazzaniga, G. Claps, et al. “Characterization of a thermal neutron beam monitor based on gas electron multiplier technology”. In: *Progress of Theoretical and Experimental Physics* 2014 (Aug. 2014), 83H01– (cit. on p. 32).

[41] Peter Vanier, Leon Forman, Istvan Diószegi, Cynthia Salwen, and Vinita Ghosh. “Calibration and testing of a large-area fast-neutron directional detector”. In: Oct. 2007, pp. 179–184 (cit. on p. 33).

[42] Richard L. Bramblett, Ronald I. Ewing, and T.W. Bonner. “A new type of neutron spectrometer”. In: *Nuclear Instruments and Methods* 9.1 (1960), pp. 1–12 (cit. on pp. 33, 267).

[43] Antonino Pietropaolo, M. Angelone, Roberto Bedogni, et al. “Neutron detection techniques from μeV to GeV”. In: *Physics Reports* 875 (July 2020) (cit. on p. 33).

[44] R. Bedogni, A. Pola, M. Costa, V. Monti, and D.J. Thomas. “A Bonner Sphere Spectrometer based on a large 6LiI(Eu) scintillator: Calibration in reference monoenergetic fields”. In: *Nuclear Instruments and Methods in Physics Research Section A: Accelerators, Spectrometers, Detectors and Associated Equipment* 897 (2018), pp. 18–21 (cit. on p. 35).

[45] M Matzke. “Unfolding procedures”. In: *Radiation protection dosimetry* 107 (Feb. 2003), pp. 155–74 (cit. on p. 35).

[46] D.J Thomas and A.V Alevra. “Bonner sphere spectrometers—a critical review”. In: *Nuclear Instruments and Methods in Physics Research Section A: Accelerators, Spectrometers, Detectors and Associated Equipment* 476.1 (2002). Int. Workshop on Neutron Field Spectrometry in Science, Technolog y and Radiation Protection, pp. 12–20 (cit. on p. 35).

[47] Dominika Skwierawka, José López-Valverde, Marcin Balcerzyk, and Antonio Leal. “Clinical Viability of Boron Neutron Capture Therapy for Personalized Radiation Treatment”. In: *Cancers* 14 (June 2022), p. 2865 (cit. on p. 37).

[48] Katsumi Hirose, Mariko Sato, Koji Ichise, and Masahiko Aoki. “Dose Rate Effect on Cell Survival in BNCT”. In: *Current Issues in Molecular Biology* 45 (Aug. 2023), pp. 6986–6994 (cit. on p. 37).

[49] Eric Forton, Frederic Stichelbaut, A Cambriani, et al. “Overview of the IBA accelerator-based BNCT system”. In: *Applied radiation and isotopes : including data, instrumentation and methods for use in agriculture, industry and medicine* 67 (Apr. 2009), S262–5 (cit. on p. 37).

[50] Vidhula Ahire, Niloefar Ahmadi Bidakhvidi, Tom Boterberg, et al. *Radiobiology of Combining Radiotherapy with Other Cancer Treatment Modalities*. Sept. 2023, pp. 311–386 (cit. on p. 37).

[51] Wolfgang Sauerwein and Miha Ulčar. “Overview of Boron Neutron Capture Therapy in 2022”. In: *Cancer Biotherapy and Radiopharmaceuticals* 38 (Dec. 2022) (cit. on p. 37).

[52] Mansoor Ahmed, Diego Alberti, Saverio Altieri, et al. *Overview of Boron Neutron Capture Therapy in 2022*. Sept. 2022, pp. 311–386 (cit. on p. 37).

[53] Lee E. Farr and James S. Robertson. *Neutron capture therapy*. Ed. by H. Vieten and F. Wachsmann. Berlin, Heidelberg: Springer Berlin Heidelberg, 1971, pp. 68–92 (cit. on p. 38).

[54] Hiroaki Kumada, Susumu Tanaka, Fujio Naito, et al. “Neutron beam performance of iBNCT as linac-based neutron source for boron neutron capture therapy”. In: *EPJ Web of Conferences* 231 (Jan. 2020), p. 01003 (cit. on p. 38).

[55] J Chadwick. “The existence of a neutron”. en. In: *Proc. R. Soc. Lond. A Math. Phys. Sci.* 136.830 (June 1932), pp. 692–708 (cit. on p. 40).

[56] H J Taylor and M Goldhaber. “Detection of nuclear disintegration in a photographic emulsion”. en. In: *Nature* 135.3409 (Mar. 1935), pp. 341–341 (cit. on p. 40).

[57] P Gerald Kruger. “Some biological effects of nuclear disintegration products on neoplastic tissue”. en. In: *Proc. Natl. Acad. Sci. U. S. A.* 26.3 (Mar. 1940), pp. 181–192 (cit. on p. 40).

[58] Paul A Zahl, Franklin S Cooper, and John R Dunning. “Some in vivo effects of localized nuclear disintegration products on a transplantable mouse sarcoma”. en. In: *Proc. Natl. Acad. Sci. U. S. A.* 26.10 (Oct. 1940), pp. 589–598 (cit. on p. 40).

[59] Wolfgang Sauerwein, Andrea Wittig, Raymond Moss, and Yoshinobu Nakagawa, eds. *Neutron Capture Therapy*. Berlin, Heidelberg: Springer Berlin Heidelberg, 2012 (cit. on p. 40).

[60] Kavitaa Nedunchezhian. “Boron neutron capture therapy - A literature review”. In: *J. Clin. Diagn. Res.* (2016) (cit. on p. 40).

[61] Rolf F. Barth, Zizhu Zhang, and Tong Liu. “A realistic appraisal of boron neutron capture therapy as a cancer treatment modality”. In: *Cancer Communications* 38.1 (2018), p. 36. eprint: `https://onlinelibrary.wiley.com/doi/pdf/10.1186/s40880-018-0280-5` (cit. on p. 42).

[62] M Donya, M Radford, A ElGuindy, D Firmin, and MH Yacoub. “Radiation in medicine: Origins, risks and aspirations.” In: *Global Cardiology Science and Practice* 2014 (2014), pp. 437–448 (cit. on p. 43).

[63] Wallace Friedberg and Kyle Copeland. “Ionizing Radiation in Earth’s Atmosphere and in Space Near Earth”. In: (May 2011), p. 32 (cit. on p. 43).

[64] François Paquet, M Bailey, R Leggett, et al. *ICRP, 2017. Occupational Intakes of Radionuclides: Part 3. ICRP Publication 137. Ann. ICRP 46(3/4)*. Vol. 46. Dec. 2017 (cit. on p. 44).

[65] Rolf F. Barth, Jeffrey A. Coderre, M. Graça H. Vicente, and Thomas E. Blue. “Boron Neutron Capture Therapy of Cancer: Current Status and Future Prospects”. In: *Clinical Cancer Research* 11.11 (June 2005), pp. 3987–4002. eprint: `https://aacrjournals.org/clincancerres/article-pdf/11/11/3987/1956671/3987-4002.pdf` (cit. on pp. 45, 50).

[66] H. Fukuda, J. Hiratsuka, C. Honda, et al. “Boron Neutron Capture Therapy of Malignant Melanoma Using ^{10}B-Paraboronophenylalanine with Special Reference to Evaluation of Radiation Dose and Damage to the Normal Skin”. In: *Radiation Research* 138.3 (1994), pp. 435–442 (cit. on p. 45).

[67] Jeffrey A Coderre, Eric H Elowitz, Manjeet Chadha, et al. In: *J. Neurooncol.* 33.1/2 (1997), pp. 141–152 (cit. on p. 45).

[68] E H Elowitz, R M Bergland, J A Coderre, et al. “Biodistribution of p-boronophenylalanine in patients with glioblastoma multiforme for use in boron neutron capture therapy”. en. In: *Neurosurgery* 42.3 (Mar. 1998), 463–8, discussion 468–9 (cit. on p. 45).

[69] J W Hopewell, G M Morris, A Schwint, and J A Coderre. “The radiobiological principles of boron neutron capture therapy: a critical review”. en. In: *Appl. Radiat. Isot.* 69.12 (Dec. 2011), pp. 1756–1759 (cit. on p. 46).

[70] E J Hall, J K Novak, A M Kellerer, et al. “RBE as a function of neutron energy. I. Experimental observations”. en. In: *Radiat. Res.* 64.2 (Nov. 1975), pp. 245–255 (cit. on p. 46).

[71] J W Hopewell, G M Morris, A Schwint, and J A Coderre. “The radiobiological principles of boron neutron capture therapy: a critical review”. en. In: *Appl. Radiat. Isot.* 69.12 (Dec. 2011), pp. 1756–1759 (cit. on p. 46).

[72] Dirk Müssig. “Re-scanning in scanned ion beam therapy in the presence of organ motion”. PhD thesis. Dec. 2013 (cit. on p. 47).

[73] Aja M Rieger. “Flow cytometry and cell cycle analysis: An overview”. In: *Cell-Cycle Synchronization*. Methods in molecular biology (Clifton, N.J.) New York, NY: Springer US, 2022, pp. 47–57 (cit. on p. 47).

[74] Lauren Pecorino. “Apoptosis”. In: *Molecular Biology of Cancer*. Oxford University Press, June 2021 (cit. on p. 47).

[75] Zhaoshi Bai, Yiran Zhou, Yaling Peng, Xinyue Ye, and Lingman Ma. “Perspectives and mechanisms for targeting mitotic catastrophe in cancer treatment”. en. In: *Biochim. Biophys. Acta Rev. Cancer* 1878.5 (Sept. 2023), p. 188965 (cit. on p. 47).

[76] Eiichiro Yamamoto, Osamu Yasuda, Keisuke Fukuo, et al. “Crucial role of apoptogenic protein in cellular apoptosis and senescense”. ja. In: *Nihon Ronen Igakkai Zasshi* 48.2 (2011), pp. 138–141 (cit. on p. 47).

[77] Kavitaa Nedunchezhian. “Boron neutron capture therapy - A literature review”. In: *J. Clin. Diagn. Res.* (2016) (cit. on p. 49).

[78] Hiroyuki Nakamura, Masaru Fujiwara, and Yoshinori Yamamoto. “A Concise Synthesis of Enantiomerically Pure L-(4-Boronophenyl)Alanine from L-Tyrosine”. In: *Frontiers in Neutron Capture Therapy: Volume 1*. Ed. by M. Frederick Hawthorne, Kenneth Shelly, and Richard J. Wiersema. Boston, MA: Springer US, 2001, pp. 765–768 (cit. on p. 49).

[79] A H Soloway, H Hatanaka, and M A Davis. “Penetration of brain and brain tumor. VII. Tumor-binding sulfhydryl boron compounds”. en. In: *J. Med. Chem.* 10.4 (July 1967), pp. 714–717 (cit. on p. 49).

[80] Mayya Alexandrovna Dymova, Sergey Yurjevich Taskaev, Vladimir Alexandrovich Richter, and Elena Vladimirovna Kuligina. “Boron neutron capture therapy: Current status and future perspectives”. en. In: *Cancer Commun. (Lond.)* 40.9 (Sept. 2020), pp. 406–421 (cit. on p. 50).

[81] Daniela Imperio and Luigi Panza. “Sweet Boron: Boron-Containing Sugar Derivatives as Potential Agents for Boron Neutron Capture Therapy”. In: *Symmetry* 14.2 (2022) (cit. on p. 50).

[82] Andrea Monti Hughes and Naonori Hu. “Optimizing boron neutron capture therapy (BNCT) to treat cancer: An updated review on the latest developments on boron compounds and strategies”. en. In: *Cancers (Basel)* 15.16 (Aug. 2023) (cit. on p. 51).

[83] I Auterinen and Salmenhaara. *The 250 kW FiR 1 TRIGA research reactor - International role in Boron Neutron Capture Therapy (BNCT) and regional role in isotope production, education and training*. Nov. 2008 (cit. on p. 52).

[84] Rolf F Barth, M Graca H Vicente, Otto K Harling, et al. “Current status of boron neutron capture therapy of high grade gliomas and recurrent head and neck cancer”. en. In: *Radiat. Oncol.* 7.1 (Aug. 2012), p. 146 (cit. on p. 53).

[85] Andres Juan Kreiner, Javier Bergueiro, Daniel Cartelli, et al. “Present status of accelerator-based BNCT”. en. In: 21.2 (Mar. 2016), pp. 95–101 (cit. on p. 54).

[86] C Ceballos and J Esposito. “The BSA modeling for the accelerator-based BNCT facility at INFN LNL for treating shallow skin melanoma”. en. In: *Appl. Radiat. Isot.* 67.7-8 Suppl (July 2009), S274–7 (cit. on p. 55).

[87] Horst Liskien and Arno Paulsen. “Neutron production cross sections and energies for the reactions 7Li(p,n)7Be and”. en. In: *At. Data Nucl. Data Tables* 15.1 (Jan. 1975), pp. 57–84 (cit. on p. 55).

[88] H Horiike, I Murata, T Iida, et al. “Liquid Li based neutron source for BNCT and science application”. en. In: *Appl. Radiat. Isot.* 106 (Dec. 2015), pp. 92–94 (cit. on p. 55).

[89] Thomas E Blue and Jacquelyn C Yanch. “Accelerator-based epithermal neutron sources for boron neutron capture therapy of brain tumors”. en. In: *J. Neurooncol.* 62.1-2 (Mar. 2003), pp. 19–31 (cit. on p. 55).

[90] Minoru Suzuki. “Boron neutron capture therapy (BNCT): a unique role in radiotherapy with a view to entering the accelerator-based BNCT era”. en. In: *Int. J. Clin. Oncol.* 25.1 (Jan. 2020), pp. 43–50 (cit. on pp. 55, 56).

[91] Chiara Magni, Ian Postuma, Michele Ferrarini, et al. “Design of a BNCT irradiation room based on proton accelerator and beryllium target”. en. In: *Appl. Radiat. Isot.* 165.109314 (Nov. 2020), p. 109314 (cit. on p. 57).

[92] *IAEA. Advances in Boron Neutron Capture Therapy*. `https://www.iaea.org/events/evt1905174` (cit. on p. 57).

[93] R Bedogni, A Sperduti, A Pietropaolo, et al. “Experimental characterization of HOTNES: A new thermal neutron facility with large homogeneity area”. In: *Nucl. Instrum. Methods Phys. Res. A* 843 (Jan. 2017), pp. 18–21 (cit. on pp. 58, 65).

[94] R Bedogni, A Pietropaolo, and J M Gomez-Ros. “The thermal neutron facility HOTNES: theoretical design”. In: *Appl. Radiat. Isot.* 127 (Sept. 2017), pp. 68–72 (cit. on p. 58).

[95] V Monti, M Costa, E Durisi, et al. “The E LiBANS project: Thermal and epithermal neutron sources based on a medical Linac”. en. In: *Appl. Radiat. Isot.* 166.109363 (Dec. 2020), p. 109363 (cit. on pp. 58, 60).

[96] V Monti, M Costa, E Durisi, et al. “The e_LiBANS facility: A new compact thermal neutron source based on a medical electron LINAC”. en. In: *Nucl. Instrum. Methods Phys. Res. A* 953.163154 (Feb. 2020), p. 163154 (cit. on p. 58).

[97] M Costa, E Durisi, M Ferrero, et al. “Intense thermal neutron fields from a medical-type linac: The e_libans project”. In: *Radiat. Prot. Dosimetry* 180.1-4 (Aug. 2018), pp. 273–277 (cit. on p. 58).

[98] *LENA reactor website*. `https://lena.unipv.it/il-reattore/` (cit. on p. 58).

[99] R Bedogni, J M Gomez-Ros, M Costa, et al. “An active Bonner sphere spectrometer for intense neutron fields”. en. In: *Nucl. Instrum. Methods Phys. Res. A* 940 (Oct. 2019), pp. 302–306 (cit. on p. 60).

[100] D Alloni, A Borio di Tigliole, A Cammi, et al. “Final characterization of the first critical configuration for the TRIGA Mark II reactor of the University of Pavia using the Monte Carlo code MCNP”. en. In: *Prog. Nuclear Energy* 74 (July 2014), pp. 129–135 (cit. on p. 66).

[101] A Borio di Tigliole, A Cammi, D Chiesa, et al. “TRIGA reactor absolute neutron flux measurement using activated isotopes”. en. In: *Prog. Nuclear Energy* 70 (Jan. 2014), pp. 249–255 (cit. on p. 66).

[102] D Alloni, M Prata, A Salvini, and A Ottolenghi. “Neutron flux characterisation of the Pavia TRIGA Mark II research reactor for radiobiological and microdosimetric applications”. en. In: *Radiat. Prot. Dosimetry* 166.1-4 (Sept. 2015), pp. 261–265 (cit. on p. 67).

[103] *ENDF/B-VII.1 Incident-Neutron Data*. `https://t2.lanl.gov/nis/data/endf/endfvii.1-n.html` (cit. on pp. 69, 70, 89).

[104] A Simonits, L Moens, F Corte, et al. “Ko-measurements and related nuclear data compilation for (n, γ) reactor neutron activation analysis”. en. In: *J. Radioanal. Chem.* 60.2 (Sept. 1980), pp. 461–516 (cit. on pp. 69, 79, 86, 87).

[105] Frans De Corte and András Simonits. “Recommended nuclear data for use in the k0 standardization of neutron activation analysis”. en. In: *At. Data Nucl. Data Tables* 85.1 (Sept. 2003), pp. 47–67 (cit. on pp. 69, 74).

[106] J Kopecky, J Sublet, Simpson C, et al. *Atlas of neutron capture cross sections*. Apr. 1997 (cit. on p. 69).

[107] *Practical Aspects of Operating A Neutron Activation Analysis Laboratory*. TECDOC Series 564. Vienna: INTERNATIONAL ATOMIC ENERGY AGENCY, 1990 (cit. on pp. 69, 79, 86).

[108] *Database WWW Table of Radioactive Isotopes*. `https://nucleardata.nuclear.lu.se/toi/perchart.htm` (cit. on pp. 69, 140).

[109] W Dilg, W Mannhart, E Steichele, and P Arnold. “Precision neutron total cross section measurements on gold and cobalt in the 40 μeV-5 meV range”. en. In: *Eur. Phys. J. A* 264.5 (Oct. 1973), pp. 427–444 (cit. on pp. 70, 97).

[110] D J Thomas and A V Alevra. “Bonner sphere spectrometers—a critical review”. en. In: *Nucl. Instrum. Methods Phys. Res. A* 476.1-2 (Jan. 2002), pp. 12–20 (cit. on p. 71).

[111] N. P. Baumann. *RESONANCE INTEGRALS AND SELF-SHIELDING FACTORS FOR DETECTOR FOILS*. Jan. 1963 (cit. on p. 74).

[112] Adam Konefał. *InTech-Undesirable radioisotopes induced by therapeutic beams from medical linear accelerators*. Dec. 2014 (cit. on p. 77).

[113] T B Ryves. “A New Thermal Neutron Flux Convention”. In: *Metrologia* 5.4 (Oct. 1969), pp. 119–124 (cit. on p. 87).

[114] F De Corte, A Simonits, A De Wispelaere, and J Hoste. “Accuracy and applicability of the k0-standardization method”. en. In: *J. Radioanal. Nucl. Chem.* 113.1 (June 1987), pp. 145–161 (cit. on p. 87).

[115] D J Thomas and P Kolkowski. *Thermal fluence and dose equivalent standards at NPL*. NPL Report. Mar. 2005 (cit. on pp. 89, 154).

[116] T. Goorley, M. James, Thomas Booth, et al. “Initial MCNP6 release overview”. In: *Nuclear Technology* 180 (Dec. 2011) (cit. on p. 90).

[117] V Vylet. “Response matrix of an extended Bonner sphere system”. en. In: *Nucl. Instrum. Methods Phys. Res. A* 476.1-2 (Jan. 2002), pp. 26–30 (cit. on p. 91).

[118] V Monti, M Costa, E Durisi, et al. “The e_LiBANS facility: A new compact thermal neutron source based on a medical electron LINAC”. en. In: *Nucl. Instrum. Methods Phys. Res. A* 953.163154 (Feb. 2020), p. 163154 (cit. on pp. 93, 153).

[119] “1. Fundamental principles and methods of particle detection”. In: *Methods in Experimental Physics*. Methods of experimental physics. Elsevier, 1961, pp. 1–288 (cit. on p. 123).

[120] Zhong He. “Review of the Shockley–Ramo theorem and its application in semiconductor gamma-ray detectors”. en. In: *Nucl. Instrum. Methods Phys. Res. A* 463.1-2 (May 2001), pp. 250–267 (cit. on p. 127).

[121] G F Knoll. *Radiation detection and measurement, 2nd ed*. United States: John Wiley and Sons Inc, 1989 (cit. on p. 127).

[122] *ORTEC data sheet*. `https://www.ortec-online.com/-/media/ametekortec/brochures/g/gem-a4.pdf?la=en&revision=127d8898-b91f-4052-b632-038e5247564d` (cit. on p. 128).

[123] R.I. Smith, G.J. Konzek, Pacific Northwest Laboratory, and Electric Power Research Institute. *Clean Critical Experiment Benchmarks for Plutonium Recycle in LWR's (foil Activation Studies)*. Clean Critical Experiment Benchmarks for Plutonium Recycle in LWR's. The Institute, 1978 (cit. on p. 130).

[124] K Debertin and R G Helmer. *Gamma- and X-ray spectrometry with semiconductor detectors*. Netherlands: North-Holland, 1988 (cit. on pp. 134, 141).

[125] C G Ryan, E Clayton, W L Griffin, S H Sie, and D R Cousens. “SNIP, a statistics-sensitive background treatment for the quantitative analysis of PIXE spectra in geoscience applications”. en. In: *Nucl. Instrum. Methods Phys. Res. B* 34.3 (Sept. 1988), pp. 396–402 (cit. on p. 134).

[126] Miroslav Morhác and Vladislav Matousek. “Peak clipping algorithms for background estimation in spectroscopic data”. en. In: *Appl. Spectrosc.* 62.1 (Jan. 2008), pp. 91–106 (cit. on pp. 134, 135).

[127] C V Hampton, B Lian, and Wm C McHarris. “Fast-Fourier-transform spectral enhancement techniques for γ-ray spectroscopy”. en. In: *Nucl. Instrum. Methods Phys. Res. A* 353.1-3 (Dec. 1994), pp. 280–284 (cit. on p. 135).

[128] M A Caccia, M Ebolese, and S Romualdo Maspero. “Background removal procedure based on the SNIP algorithm for gamma-ray spectroscopy with the CAEN Educational Kit.” en. In: *CAEN Educational Note* 3163.1-3 (Dec. 2013), pp. 1–4 (cit. on p. 135).

[129] Miroslav Morhav c. “An algorithm for determination of peak regions and baseline elimination in spectroscopic data”. en. In: *Nucl. Instrum. Methods Phys. Res. A* 600.2 (Mar. 2009), pp. 478–487 (cit. on p. 135).

[130] Rui Shi, Xianguo Tuo, Honglong Zheng, et al. “Step-approximation SNIP background-elimination algorithm for HPGe gamma spectra”. en. In: *Nucl. Instrum. Methods Phys. Res. A* 885 (Mar. 2018), pp. 60–66 (cit. on p. 135).

[131] R Bedogni, D Bortot, A Pola, et al. “A new active thermal neutron detector”. en. In: *Radiat. Prot. Dosimetry* 161.1-4 (Oct. 2014), pp. 241–244 (cit. on pp. 158, 279, 280).

[132] R Bedogni, D Bortot, A Pola, et al. “Experimental characterization of semiconductor-based thermal neutron detectors”. en. In: *Nucl. Instrum. Methods Phys. Res. A* 780 (Apr. 2015), pp. 51–54 (cit. on pp. 158, 279).

[133] R Bedogni, P Ferrari, G Gualdrini, and A Esposito. “Design and experimental validation of a Bonner Sphere Spectrometer based on Dysprosium activation foils”. en. In: *Radiat. Meas.* 45.10 (Dec. 2010), pp. 1201–1204 (cit. on pp. 165, 180).

[134] *The JRC Neutron Time-of-Flight Facility*. `https://joint-research-centre.ec.europa.eu/laboratories-and-facilities/jrc-neutron-time-flight-facility_en` (cit. on pp. 183, 187, 193, 219).

[135] Valeria Monti, M. Costa, Elisabetta Durisi, et al. “The e-LiBANS facility: A new compact thermal neutron source based on a medical electron LINAC”. In: *Nuclear Instruments and Methods in Physics Research Section A: Accelerators, Spectrometers, Detectors and Associated Equipment* 953 (Nov. 2019) (cit. on pp. 190, 216).

[136] William R Leo. *Techniques for nuclear and particle physics experiments*. en. 2nd ed. Berlin, Germany: Springer, Feb. 1994 (cit. on p. 197).

[137] *A CONSISTENT SET OF NUCLEAR PARAMETER: VALUES FOR ABSOLUTE INAA*. `https://www.gammadata.se/assets/Uploads/LaBr3-BrilLanCe-380-Data-Sheet.pdf` (cit. on p. 198).

[138] J J Doroshenko, S N Kraitor, T V Kuznetsova, K K Kushnereva, and E S Leonov. “New methods for measuring neutron spectra with energy from 0.4 eV to 10 MeV by track and activation detectors”. en. In: *Nucl. Technol.* 33.3 (May 1977), pp. 296–304 (cit. on p. 270).

[139] M Matzke. *Unfolding of pulse height spectra: the HEPRO program system*. Tech. rep. Braunschweig: Braunschweig Univ. Phys.-Tech. Bundesanst, 1994 (cit. on p. 271).

[140] M Tomás, F Fernández, M Bakali, and H Muller. “MITOM: a new unfolding code based on a spectra model method applied to neutron spectrometry”. en. In: *Radiat. Prot. Dosimetry* 110.1-4 (2004), pp. 545–548 (cit. on p. 272).

[141] M Reginatto and P Goldhagen. “MAXED, a computer code for maximum entropy deconvolution of multisphere neutron spectrometer data”. en. In: *Health Phys.* 77.5 (Nov. 1999), pp. 579–583 (cit. on p. 274).

[142] Warren S McCulloch and Walter Pitts. “A logical calculus of the ideas immanent in nervous activity”. en. In: *Bulletin of Mathematical Biophysics* 5.4 (Dec. 1943), pp. 115–133 (cit. on p. 278).

[143] Seyed Abolfazl Hosseini. “Neutron spectrum unfolding using artificial neural network and modified least square method”. In: *Radiat. Phys. Chem. Oxf. Engl. 1993* 126 (Sept. 2016), pp. 75–84 (cit. on p. 278).

[144] H A Bethe. “Nuclear physics B. nuclear dynamics, theoretical”. In: *Rev. Mod. Phys.* 9.2 (Apr. 1937), pp. 69–244 (cit. on p. 285).

[145] W Dilg. “Neutron total cross-sections at 18.8 eV”. en. In: *Z. Naturforsch. A* 29.12 (Dec. 1974), pp. 1750–1753 (cit. on pp. 286, 288).

[146] Leo Seren, Herbert N Friedlander, and Solomon H Turkel. “Thermal Neutron Activation Cross Sections”. In: *Phys. Rev.* 72.10 (Nov. 1947), pp. 888–901 (cit. on p. 288).

[147] T B Ryves and D R Perkins. “Thermal neutron capture cross-section measurements for 23Na, 27Al, 37Cl and 51V”. en. In: *J. Nucl. Energy* 24.8 (Nov. 1970), pp. 419–430 (cit. on p. 288).

[148] *A CONSISTENT SET OF NUCLEAR PARAMETER: VALUES FOR ABSOLUTE INAA*. `https://www.osti.gov/servlets/purl/5430238` (cit. on p. 288).

[149] L Venturini and B R S Pecequilo. “Thermal neutron capture cross-section of 48Ti, 51V, 50,52,53Cr and 58,60,62,64Ni”. en. In: *Appl. Radiat. Isot.* 48.4 (Apr. 1997), pp. 493–496 (cit. on p. 288).

[150] A M Hurst, R B Firestone, L Szentmiklósi, et al. “New measurement of the thermal-capture cross section for the minor isotope 180W”. en. In: *Nucl. Data Sheets* 119 (May 2014), pp. 91–93 (cit. on p. 288).

[151] P Schillebeeckx, B Becker, Y Danon, et al. “Determination of resonance parameters and their covariances from neutron induced reaction cross section data”. en. In: *Nucl. Data Sheets* 113.12 (Dec. 2012), pp. 3054–3100 (cit. on pp. 288, 289, 293–296).

[152] A Bensussan and J M Salome. “GELINA: A modern accelerator for high resolution neutron time of flight experiments”. en. In: *Nucl. Instrum. Meth.* 155.1-2 (Sept. 1978), pp. 11–23 (cit. on p. 288).

[153] H Postma and P Schillebeeckx. “Neutron Resonance Analysis”. In: *Neutron Methods for Archaeology and Cultural Heritage*. Cham: Springer International Publishing, 2017, pp. 235–283 (cit. on p. 288).

[154] D Tronc, J M Salomé, and K H Böckhoff. “A new pulse compression system for intense relativistic electron beams”. en. In: *Nucl. Instrum. Methods Phys. Res. A* 228.2-3 (Jan. 1985), pp. 217–227 (cit. on p. 288).

[155] J M Salome and R Cools. “Neutron producing targets at GELINA”. en. In: *Nucl. Instrum. Meth.* 179.1 (Jan. 1981), pp. 13–19 (cit. on p. 288).

[156] Klaus Guber, Carlos Paradela, Jan Heyse, et al. “Neutron nuclear data measurements for criticality safety”. In: *EPJ Web Conf.* 146 (2017), p. 11020 (cit. on p. 289).

[157] M.C. Moxon and J.B. Brisland. *Technical Report AEA-INTEC-0630*. Tech. rep. IAEA, 1991 (cit. on p. 290).

[158] F Gunsing, P Schillebeeckx, and V Semkova. *Summary Report of the Consultants’ Meeting on EXFOR Data in Resonance Region and Spectrometer Response Function*. Tech. rep. International Atomic Energy Agency (IAEA), 2013 (cit. on p. 290).

[159] corporate-body. JRCGEEL:Institute for Reference Materials and Measurements. *Results of time-of-flight transmission measurements for natCe samples at GELINA*. en. Publications Office of the European Union, Dec. 2016 (cit. on pp. 295, 297).

[160] S Kopecky, I Ivanov, M Moxon, et al. “The total cross section and resonance parameters for the 0.178eV resonance of 113Cd”. en. In: *Nucl. Instrum. Methods Phys. Res. B* 267.14 (July 2009), pp. 2345–2350 (cit. on p. 295).

[161] D C Larson, N M Larson, J A Harvey, N W Hill, and C H Johnson. “Application of new techniques to ORELA neutron-transmission measurements and their uncertainty analysis: the case of natural nickel from 2 keV to 20 MeV”. In: (1983) (cit. on p. 295).

[162] *Results of time-of-flight transmission measurements for ^{nat}V at a 50 m station of GELINA*. https://publications.jrc.ec.europa.eu/repository/bitstream/JRC108777/kjna28945enn.pdf (cit. on p. 303).

Appendices

A

Extended simulations results for NCT-ACS

A.1 Elements choice extended results

All the graphs presented in this appendix refer to the MC simulations described in section 3.2.2. These graphs show the response curves for all the studied elements after the initial selection.

As previously explained in the dedicated section, the pronounced peaks visible in some graphs correspond to the positions of the resonances of the studied element. The chosen binning does not allow for a detailed analysis of the structure but was selected to facilitate a comparative analysis with previous measurements conducted at the e-LiBaNS facility in Turin.

Furthermore, a detailed study of the shape of the capture cross-section was not within the scope of this work.

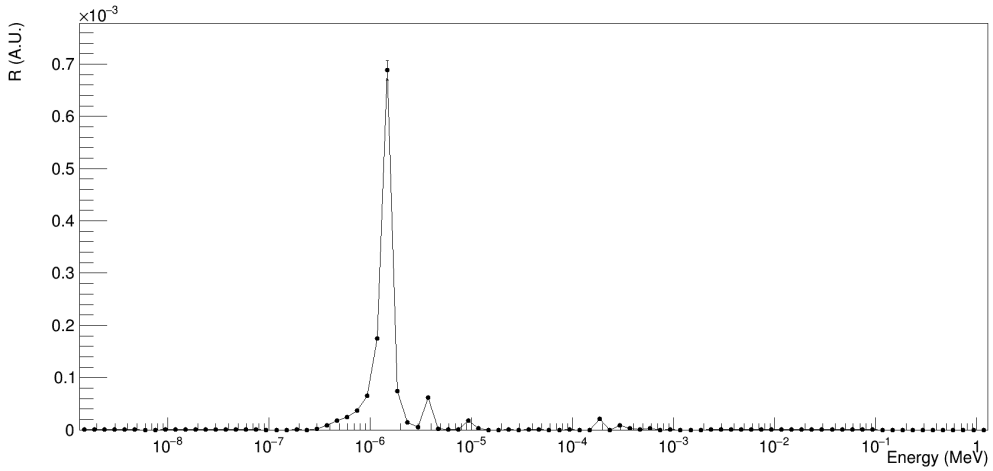

Fig. A.1.: MC results for element ^{115}In.

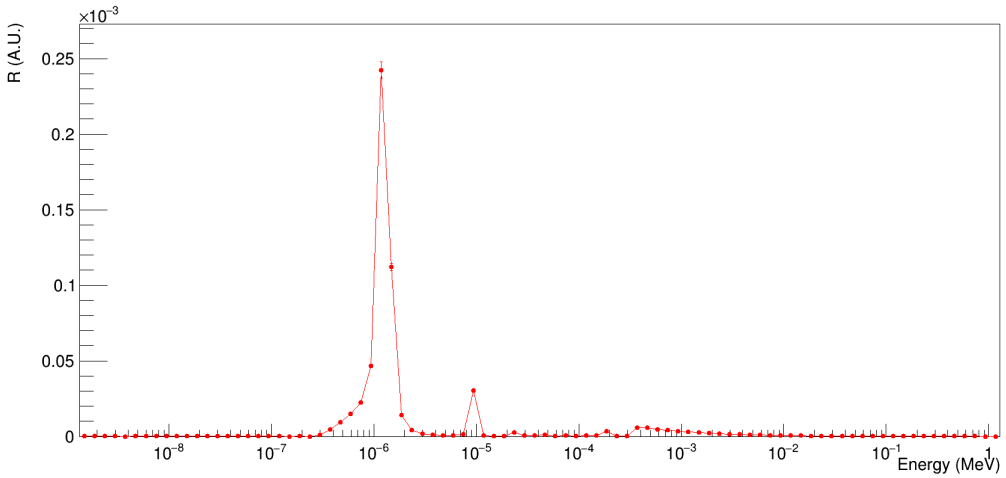

Fig. A.2.: MC results for element ^{193}Ir.

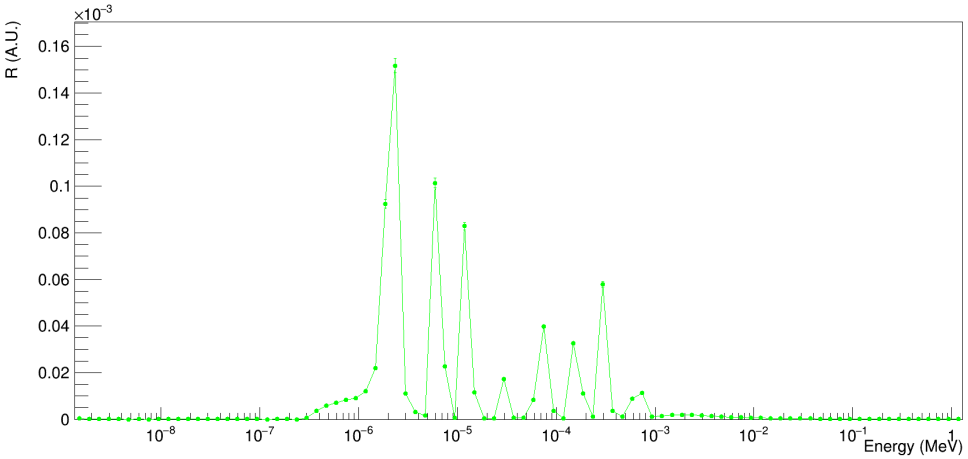

Fig. A.3.: MC results for element ^{185}Re.

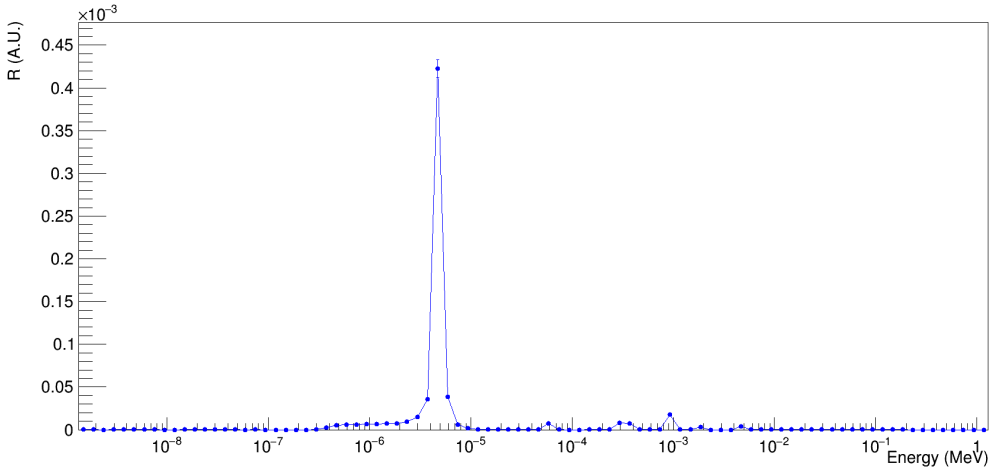

Fig. A.4.: MC results for element ^{197}Au.

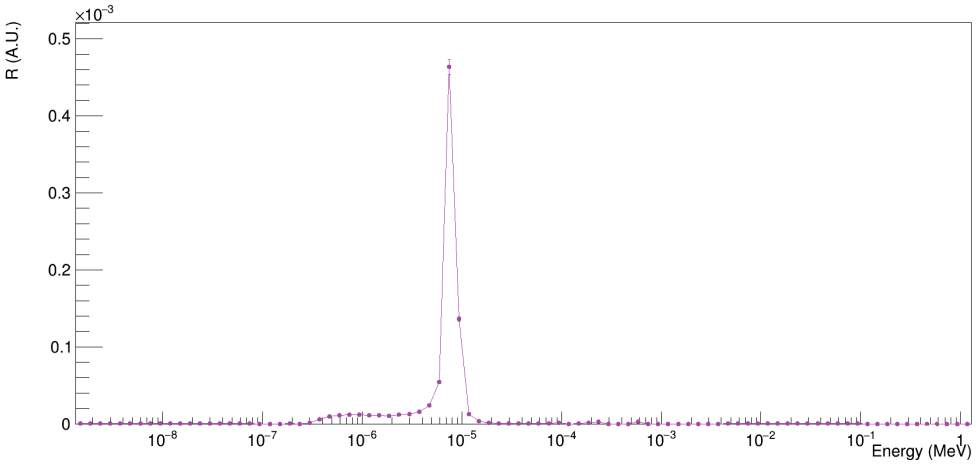

Fig. A.5.: MC results for element ^{152}Sm.

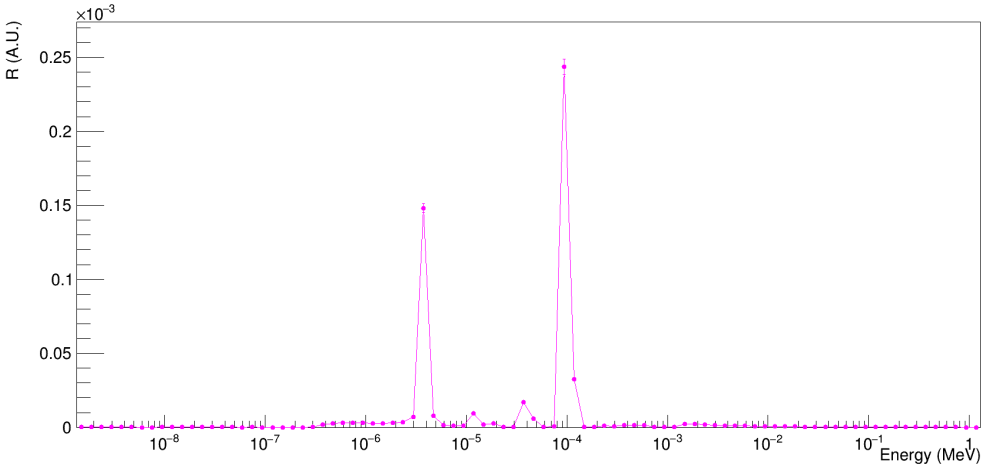

Fig. A.6.: MC results for element ^{165}Ho.

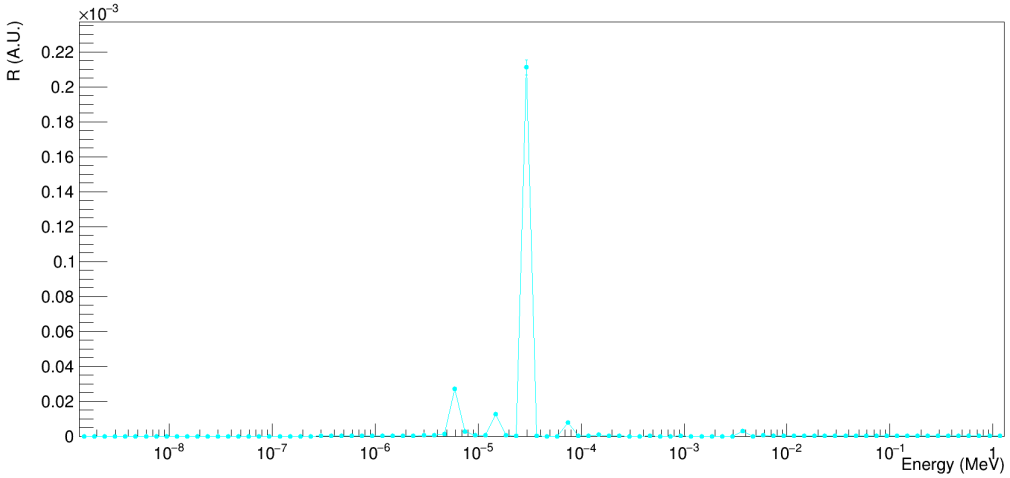

Fig. A.7.: MC results for element ^{121}Sb.

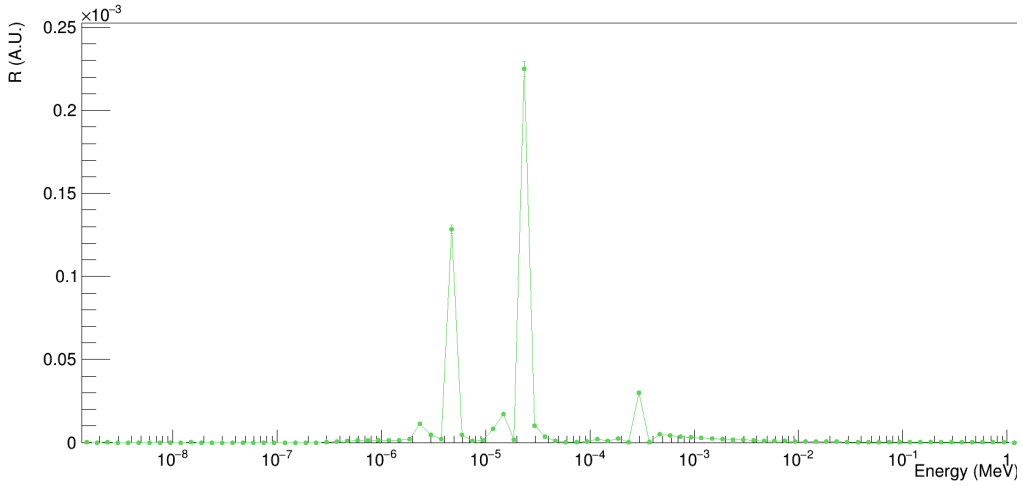

Fig. A.8.: MC results for element ^{175}LU.

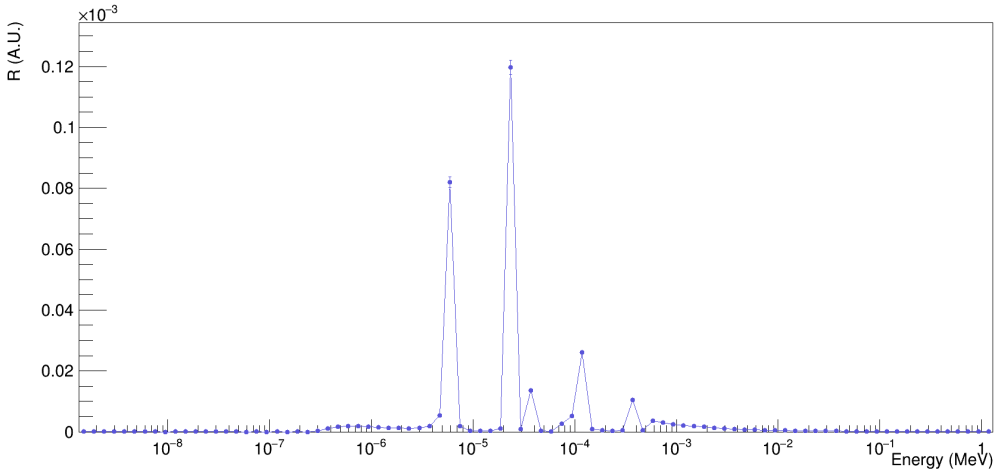

Fig. A.9.: MC results for element ^{179}Hf.

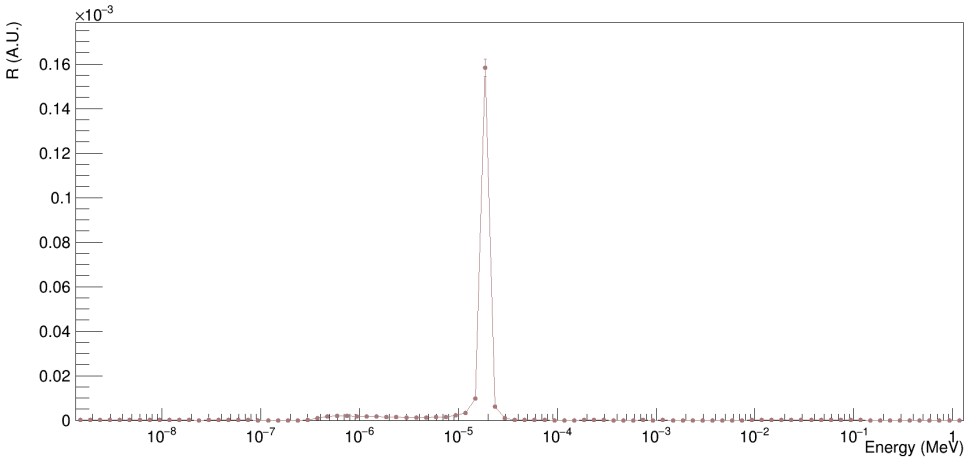

Fig. A.10.: MC results for element ^{186}W.

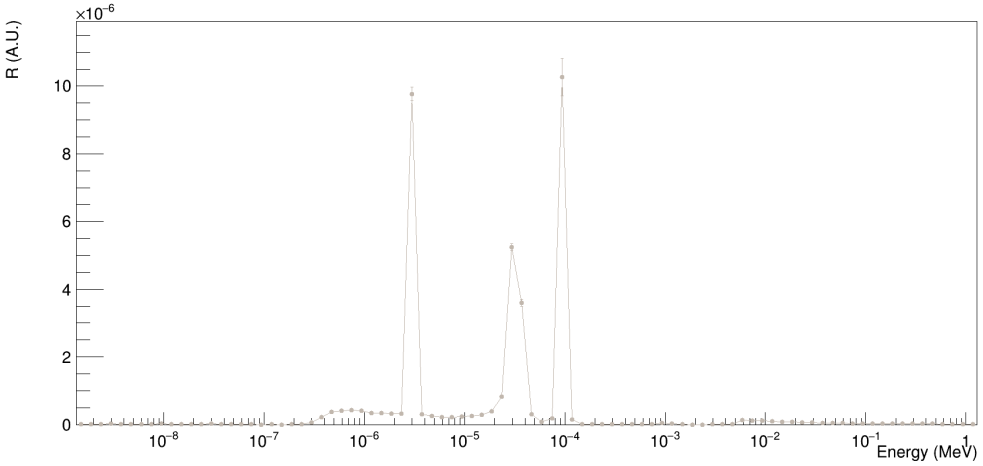

Fig. A.11.: MC results for element ^{108}Pd.

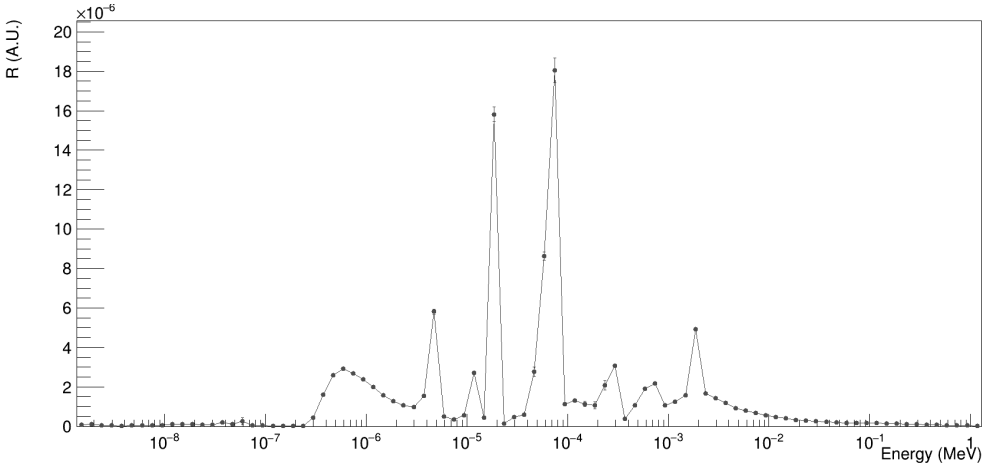

Fig. A.12.: MC results for element ^{187}Re.

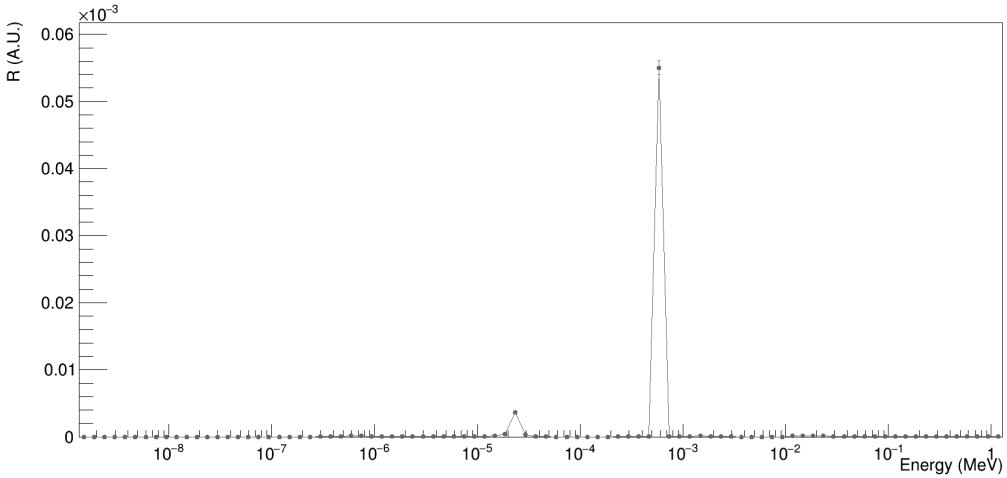

Fig. A.13.: MC results for element ^{158}Gd.

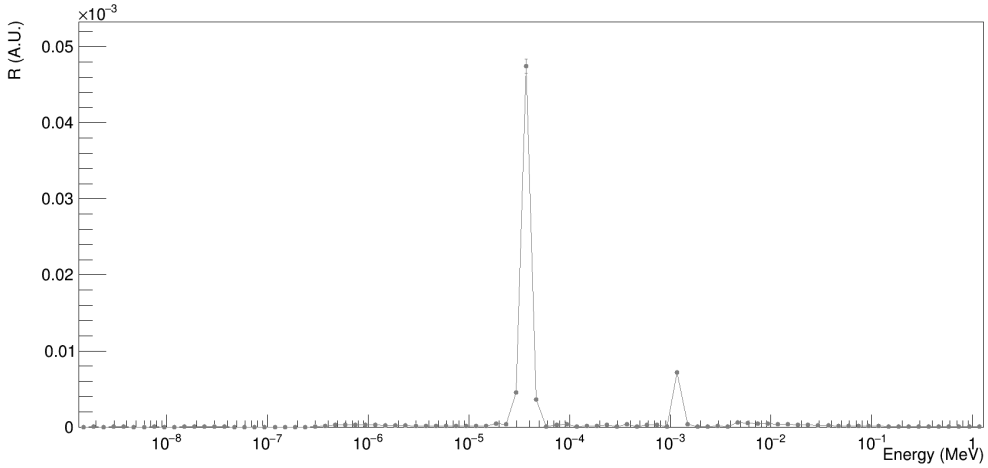

Fig. A.14.: MC results for element ^{127}I.

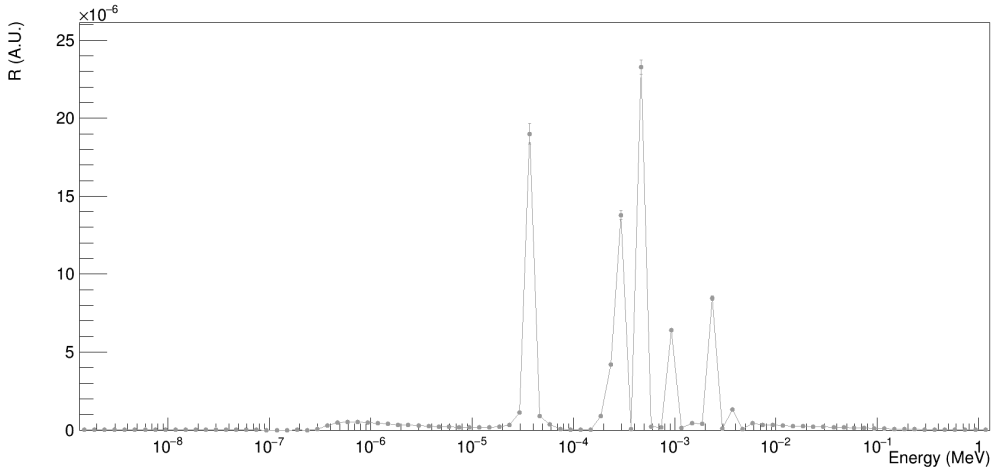

Fig. A.15.: MC results for element ^{79}Br.

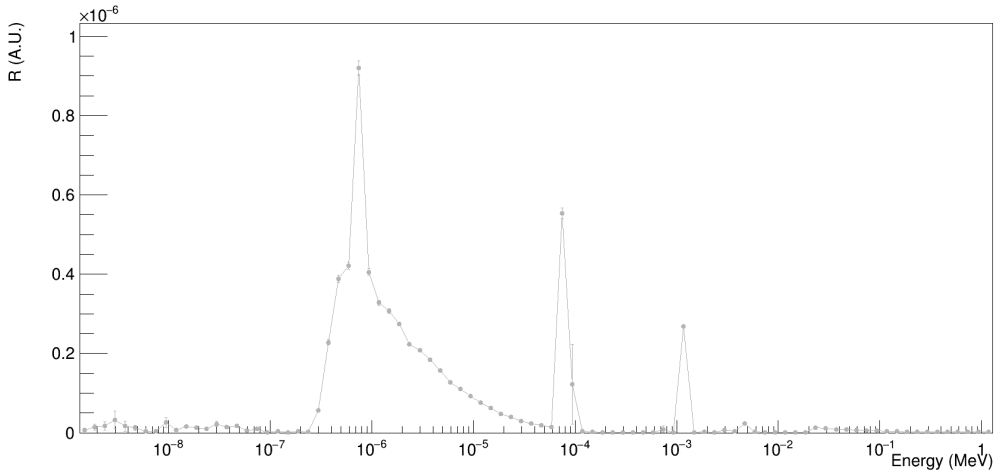

Fig. A.16.: MC results for element ^{139}La.

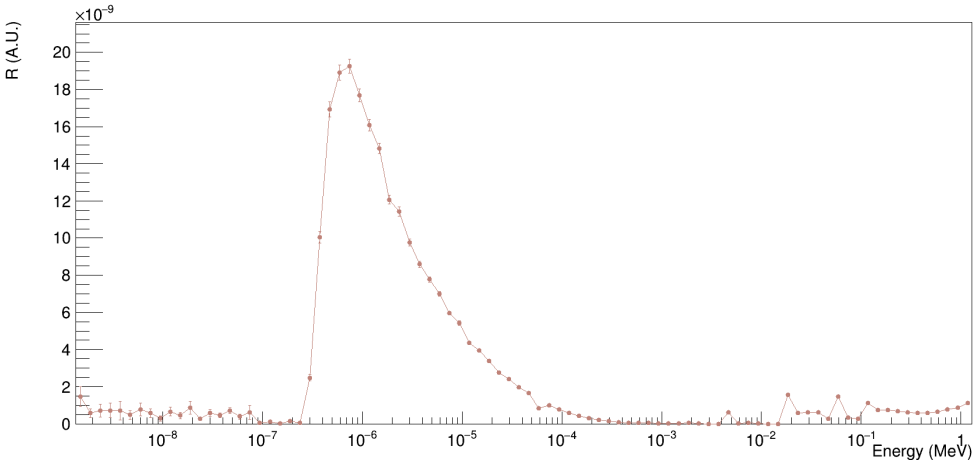

Fig. A.17.: MC results for element ^{138}Ba.

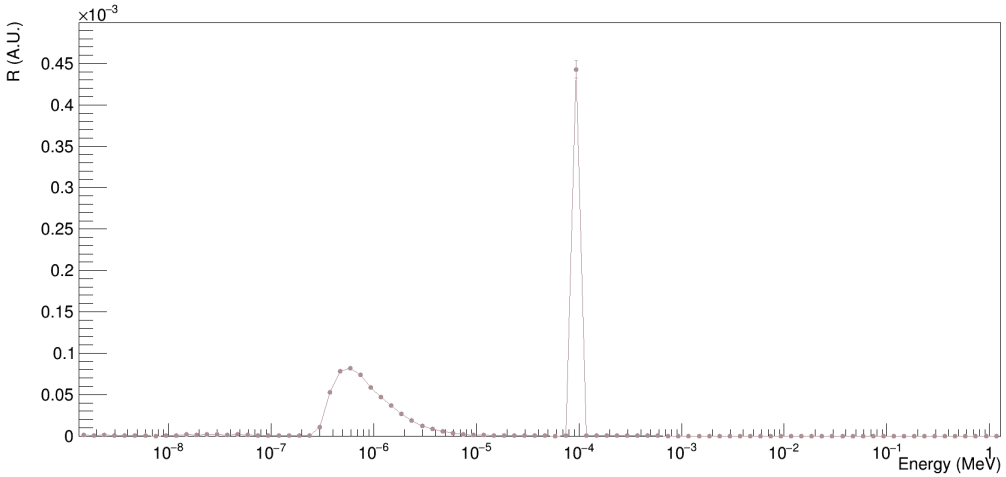

Fig. A.18.: MC results for element ^{196}Hg.

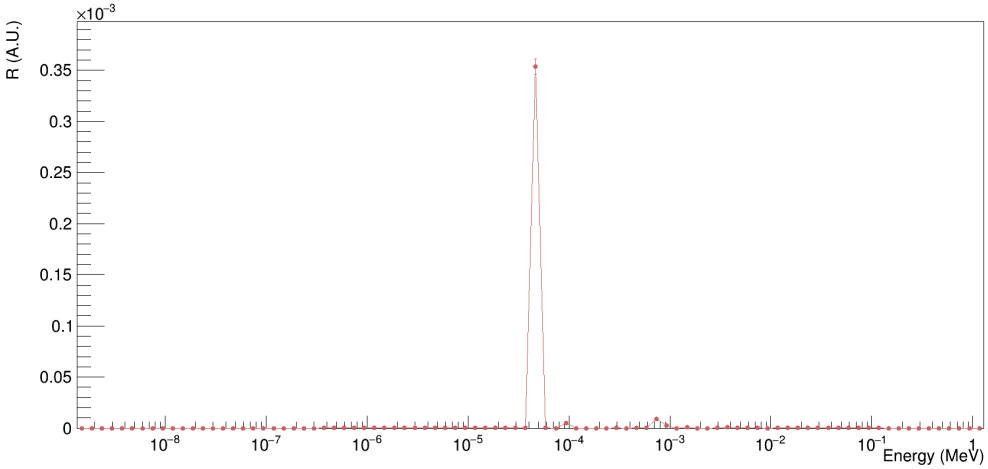

Fig. A.19.: MC results for element ^{75}As.

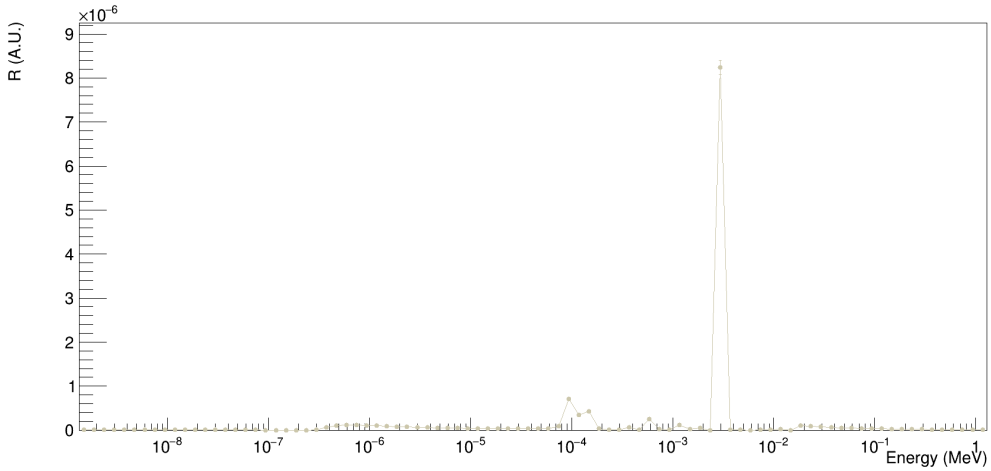

Fig. A.20.: MC results for element ^{81}Br.

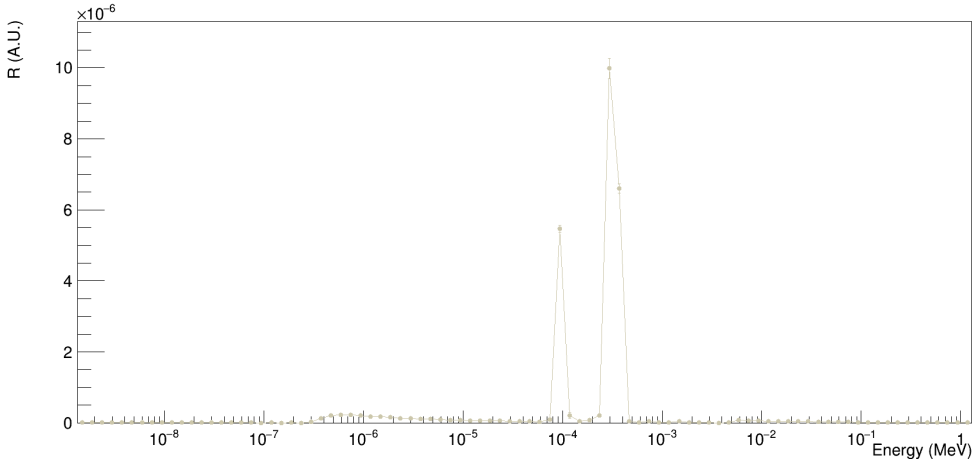

Fig. A.21.: MC results for element ^{71}Ga.

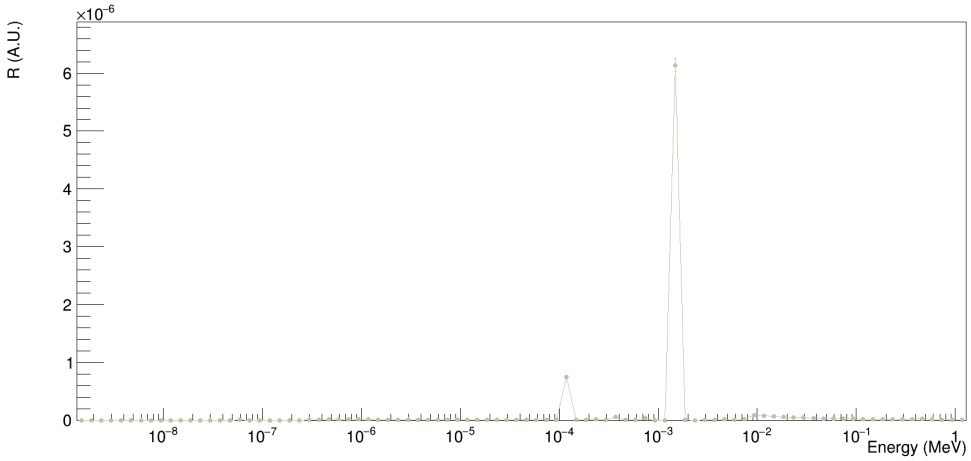

Fig. A.22.: MC results for element ^{114}Cd.

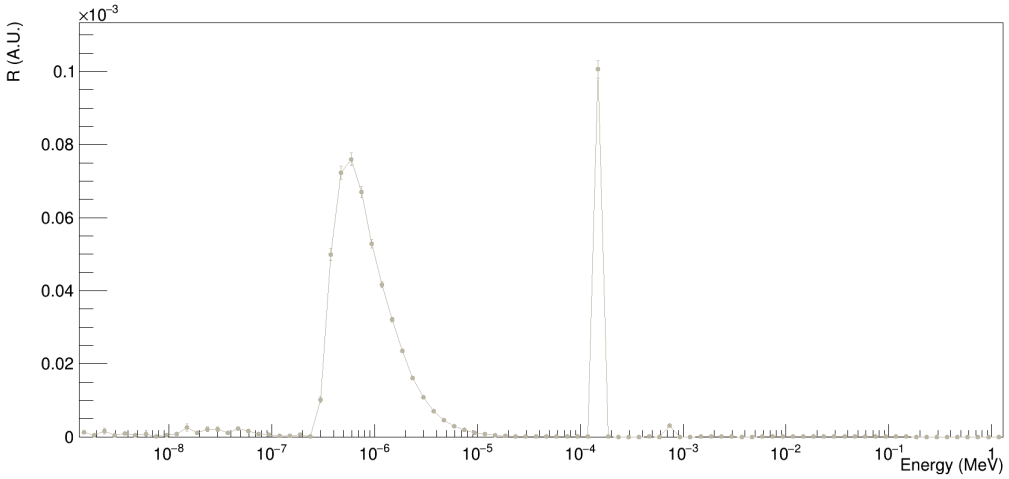

Fig. A.23.: MC results for element ^{164}Dy.

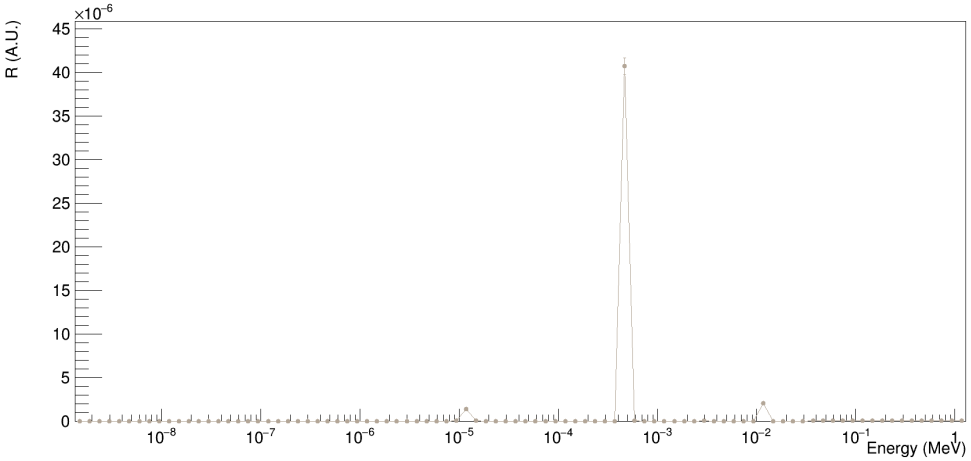

Fig. A.24.: MC results for element ^{98}Mo.

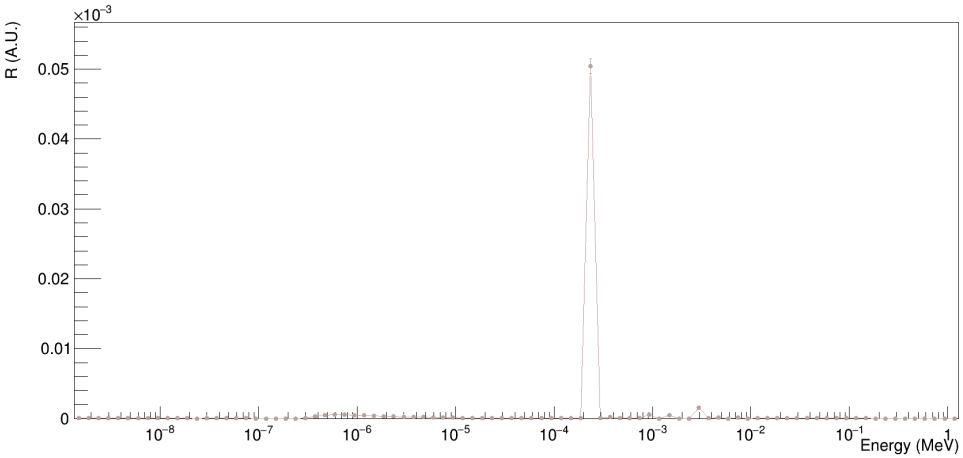

Fig. A.25.: MC results for element ^{141}Pr.

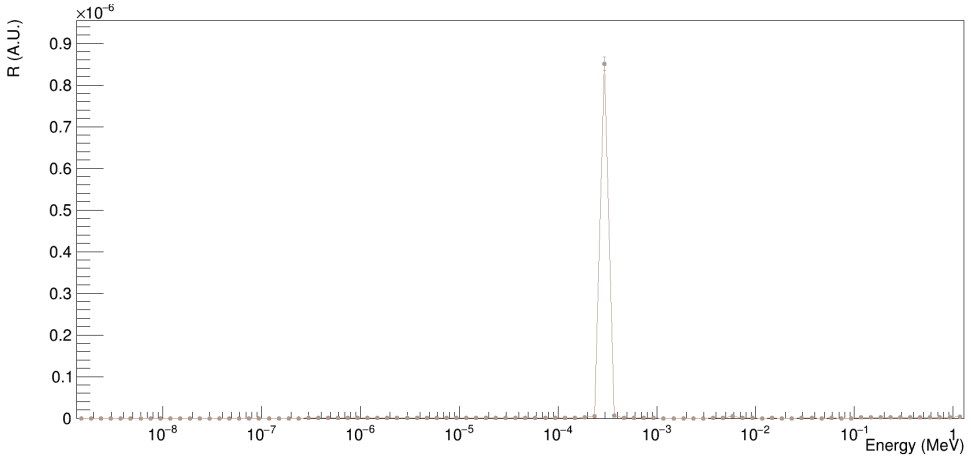

Fig. A.26.: MC results for element ^{96}Zr.

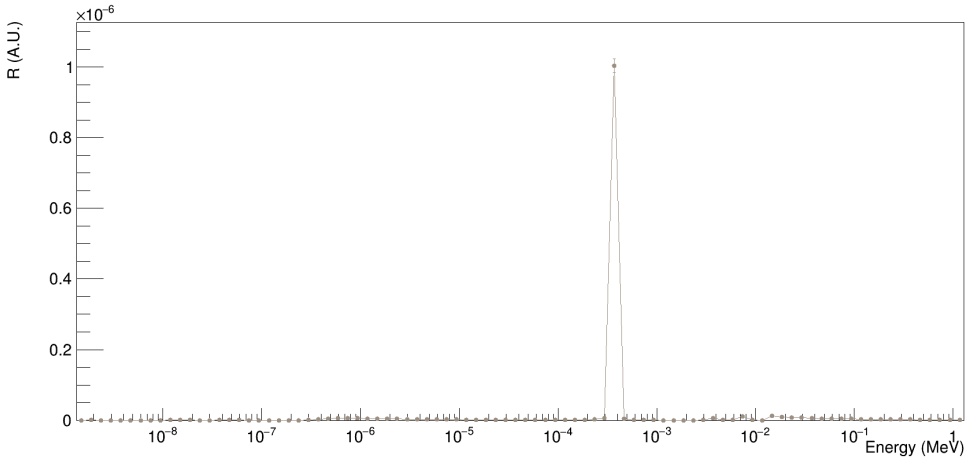

Fig. A.27.: MC results for element ^{87}Rb.

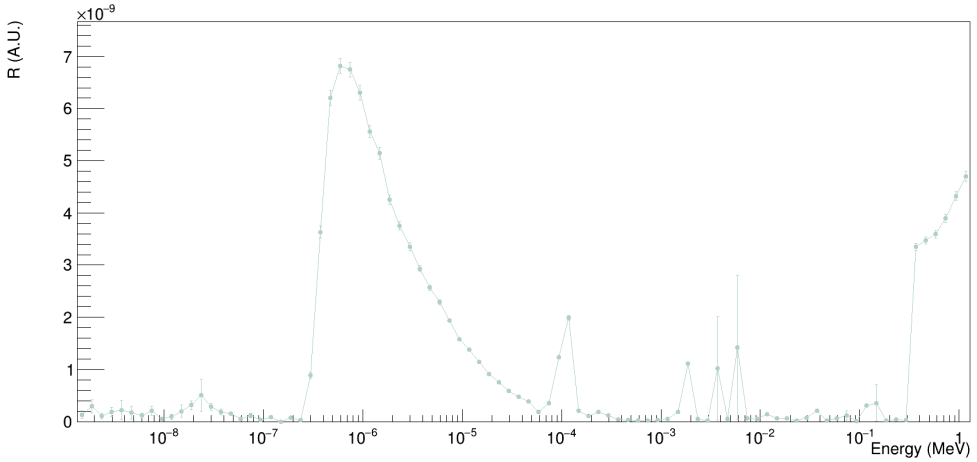

Fig. A.28.: MC results for element ^{122}Sn.

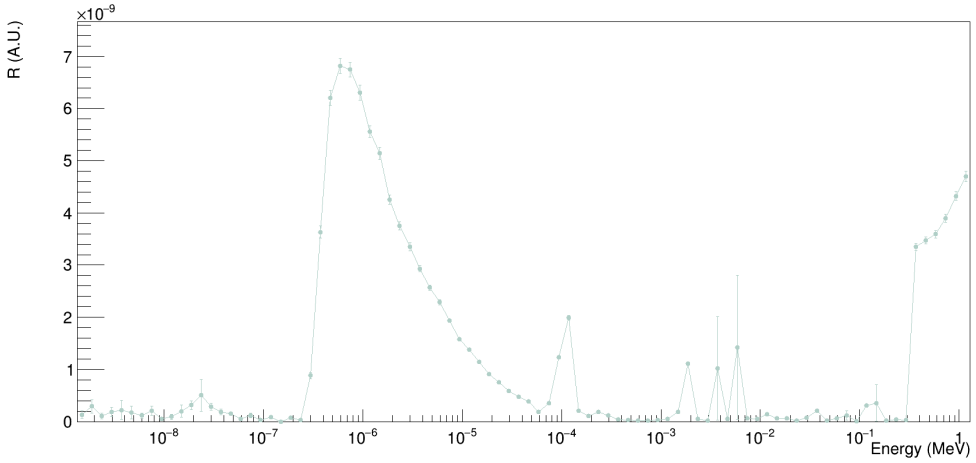

Fig. A.29.: MC results for element ^{55}Mn.

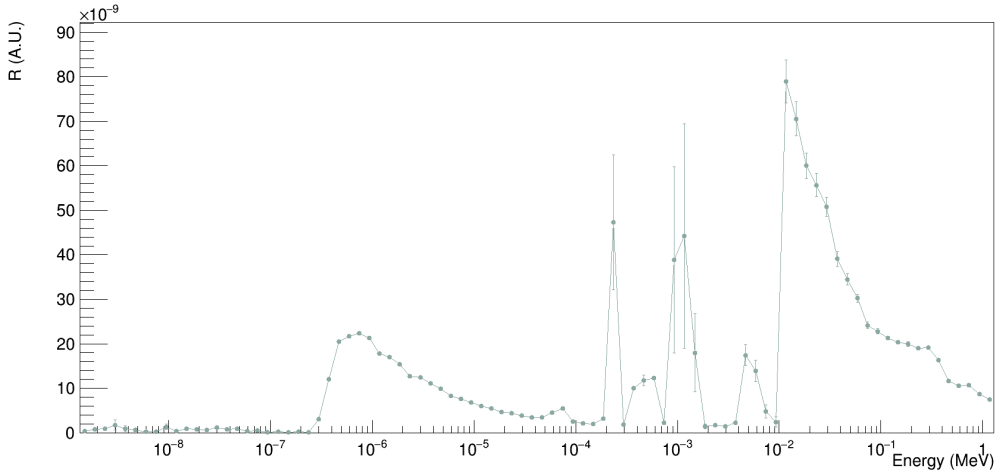

Fig. A.30.: MC results for element ^{104}Ru.

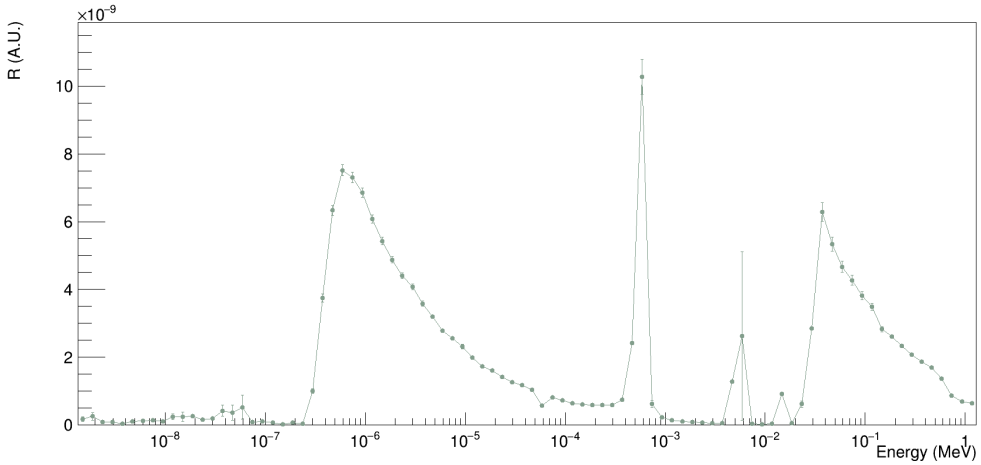

Fig. A.31.: MC results for element ^{76}Ge.

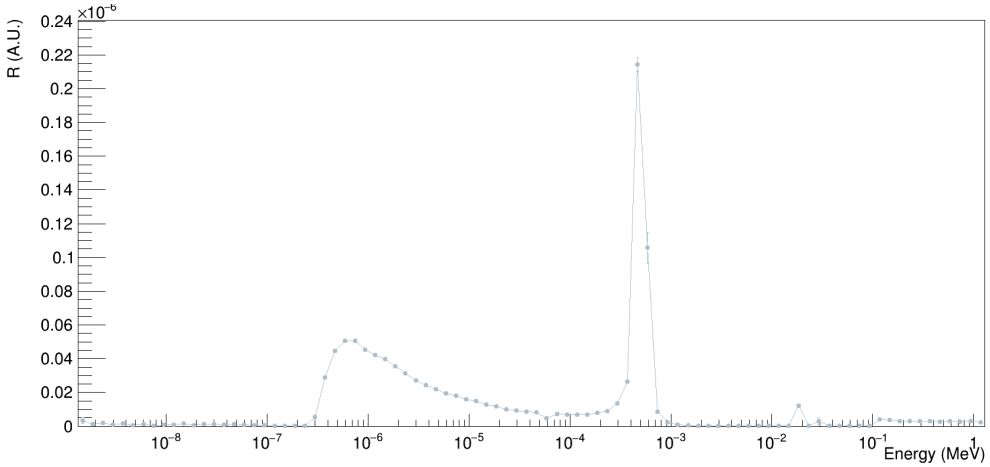

Fig. A.32.: MC results for element ^{68}Zn.

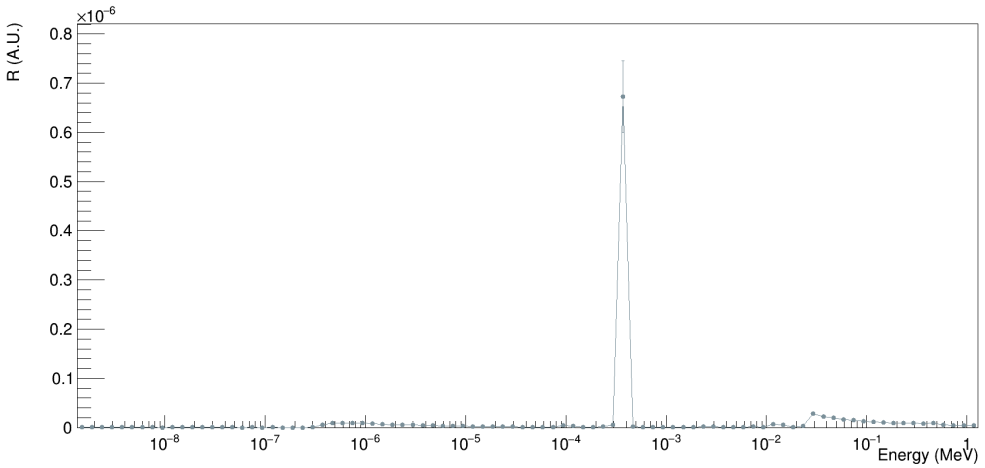

Fig. A.33.: MC results for element ^{100}Mo.

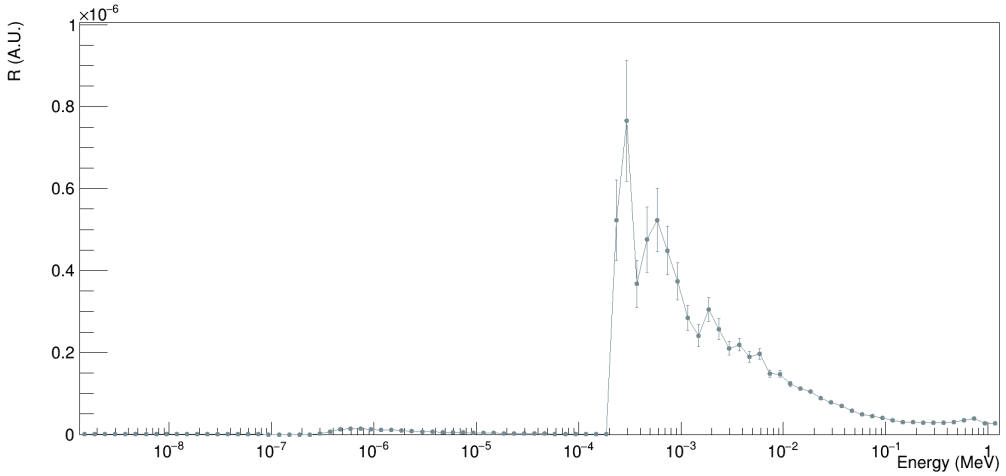

Fig. A.34.: MC results for element ^{96}Ru.

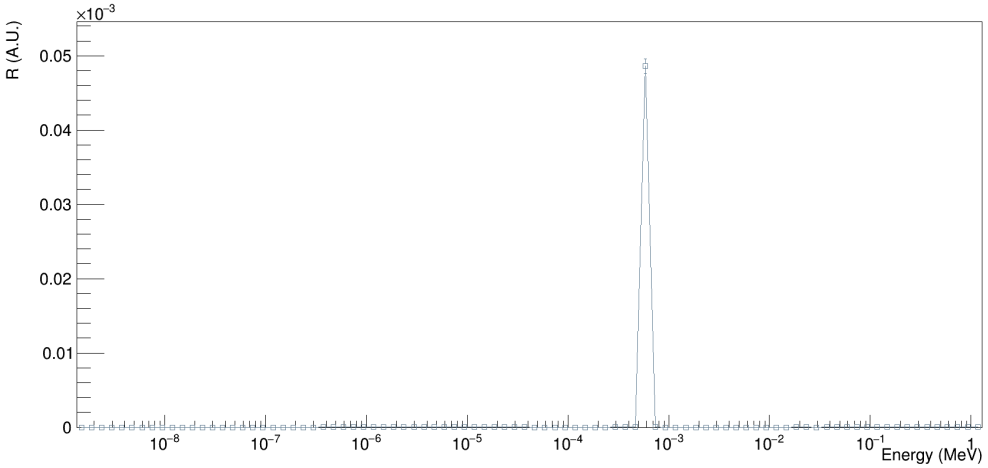

Fig. A.35.: MC results for element ^{86}Sr.

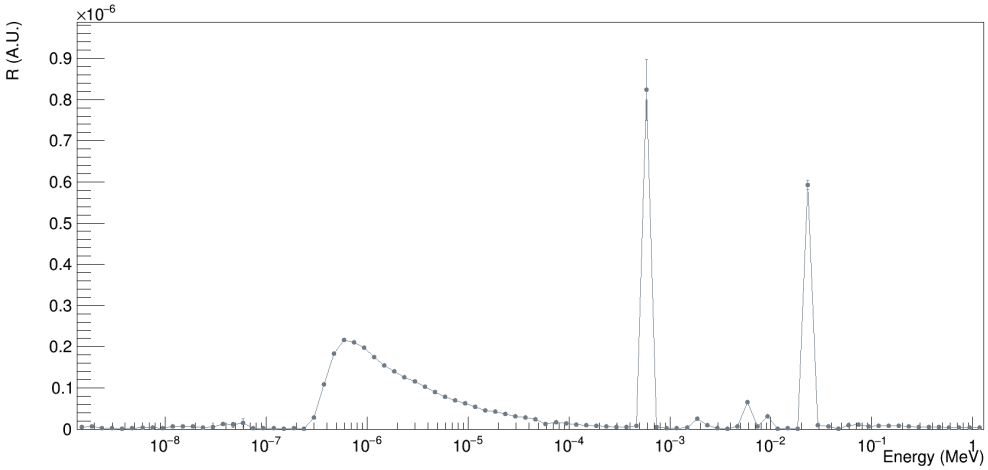

Fig. A.36.: MC results for element ^{63}Cu.

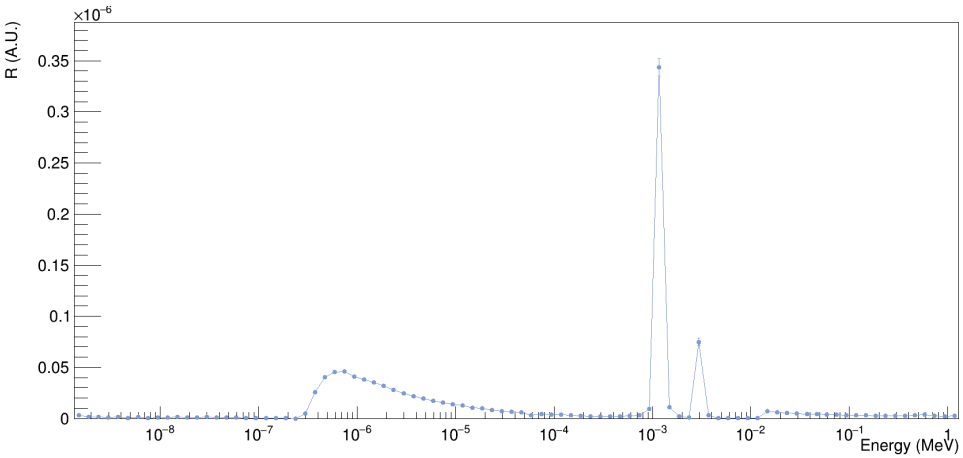

Fig. A.37.: MC results for element ^{142}Ce.

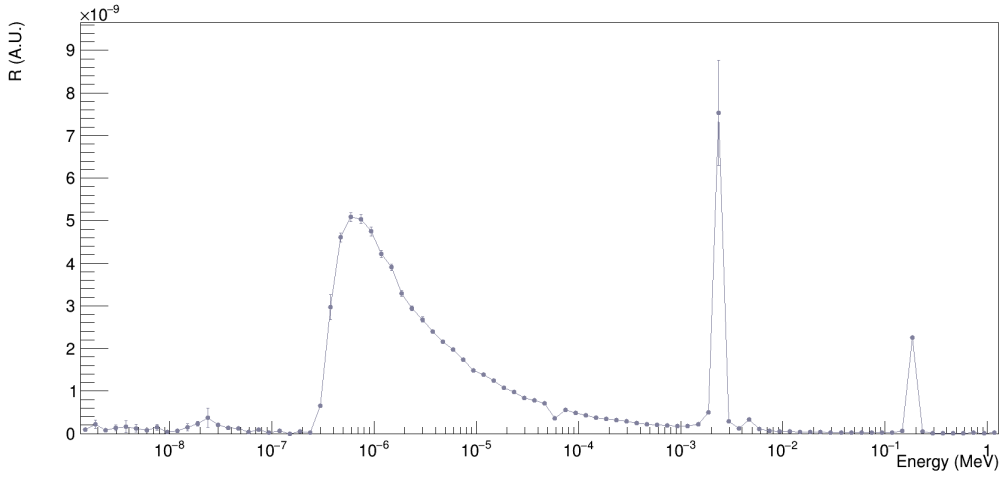

Fig. A.38.: MC results for element ^{30}Si.

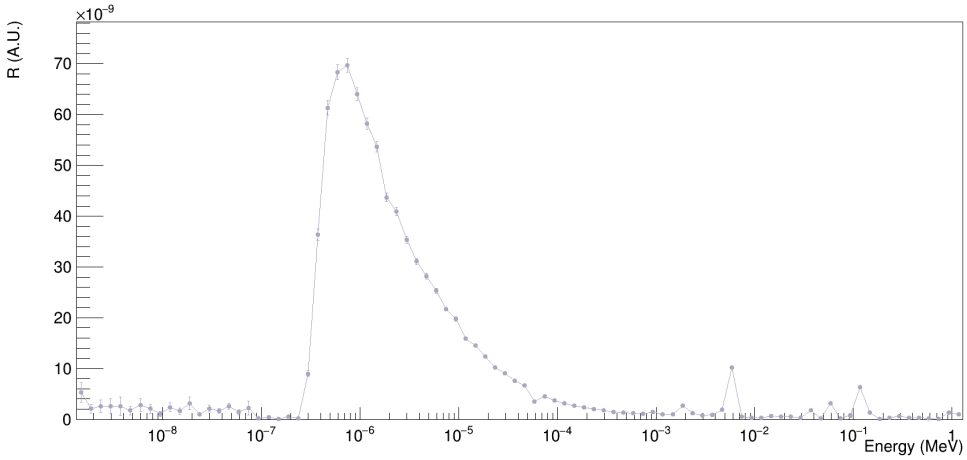

Fig. A.39.: MC results for element ^{41}K.

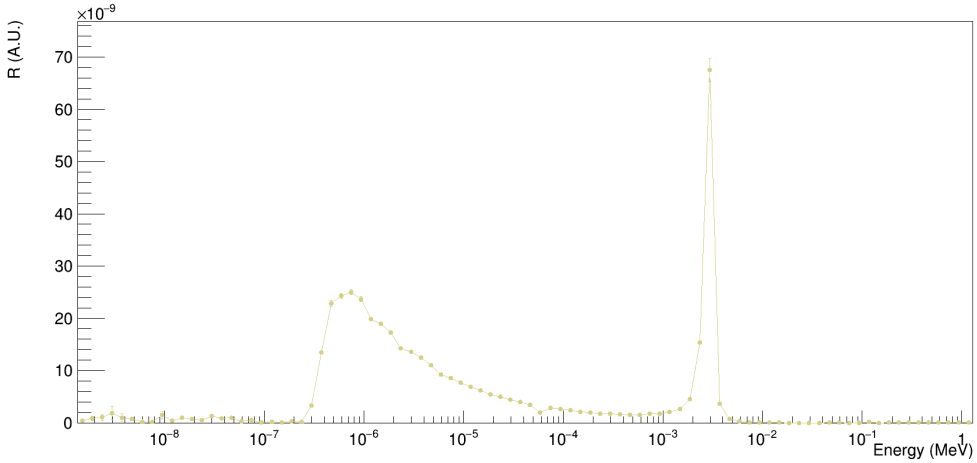

Fig. A.40.: MC results for element ^{23}Na.

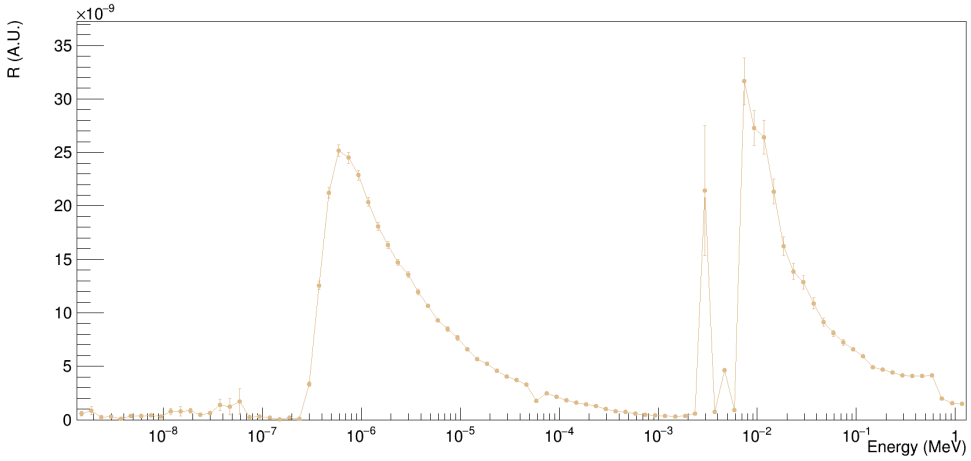

Fig. A.41.: MC results for element ^{74}Ge.

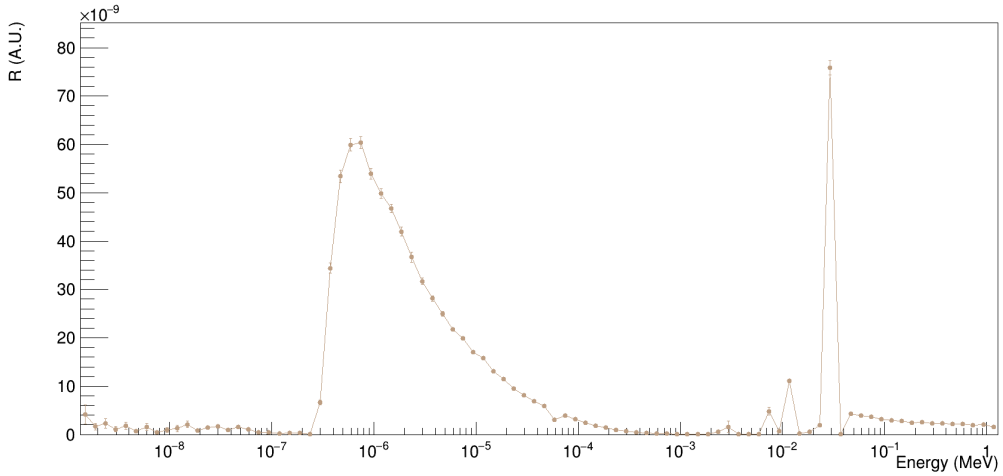

Fig. A.42.: MC results for element ^{89}Y.

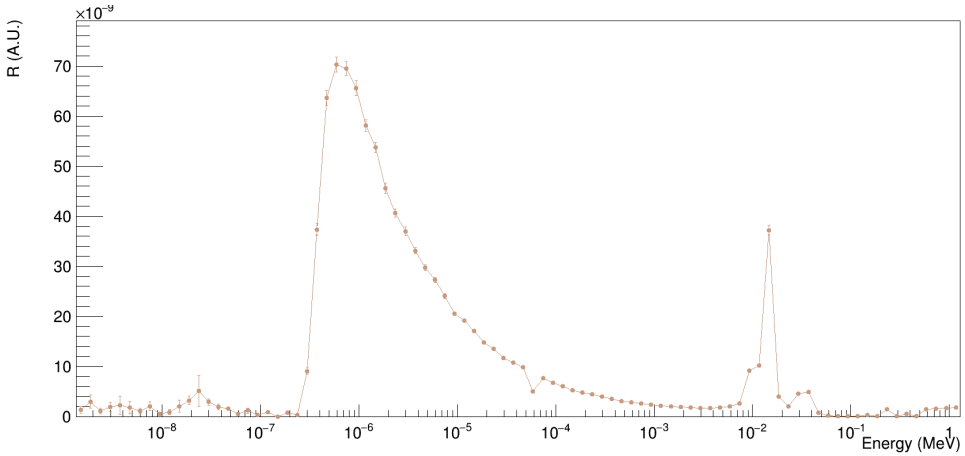

Fig. A.43.: MC results for element ^{64}Ni.

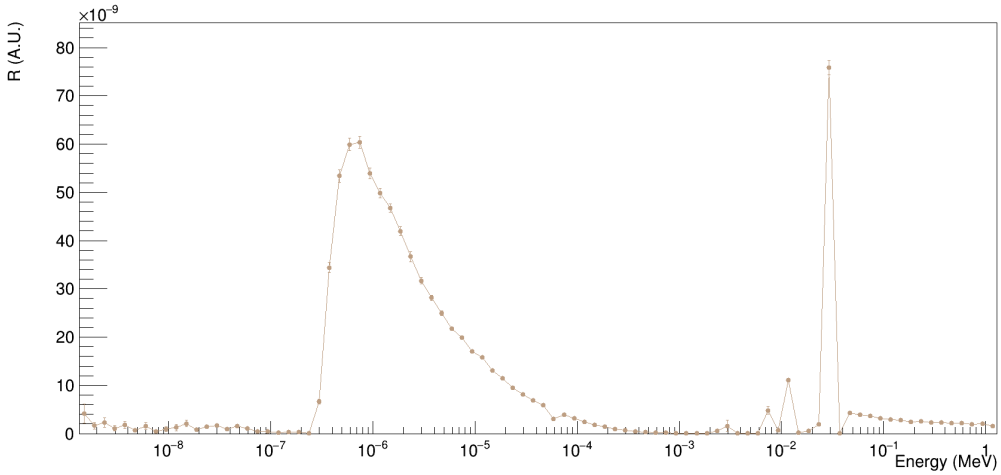

Fig. A.44.: MC results for element ^{89}Y.

A.2 First geometry extended results

In this section an extended version of the plots related tot he MC simulations on the first geometry simulated for NCT-ACS (section 3.3.1) are shown .

Graphics from A.45 to A.53 refer to simulations on the angular response.

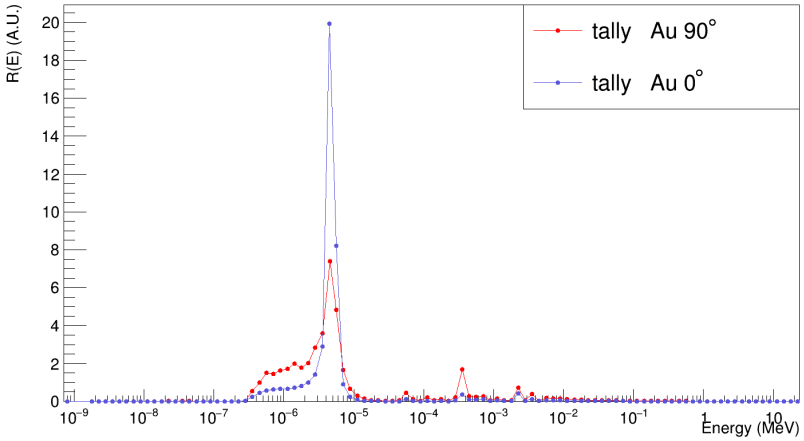

Fig. A.45.: Angular response curves for the Au foil for a neutron incoming angle of 0° and 90°. No normalization have been applied.

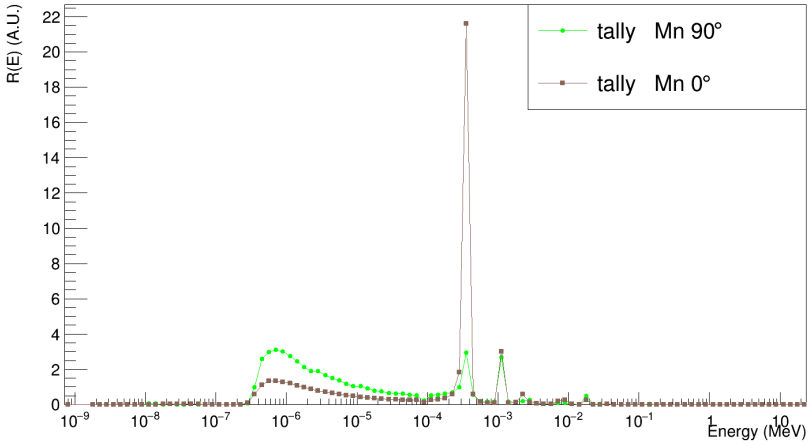

Fig. A.46.: Angular response curves for the Mn foil for a neutron incoming angle of 0° and 90°. No normalization have been applied.

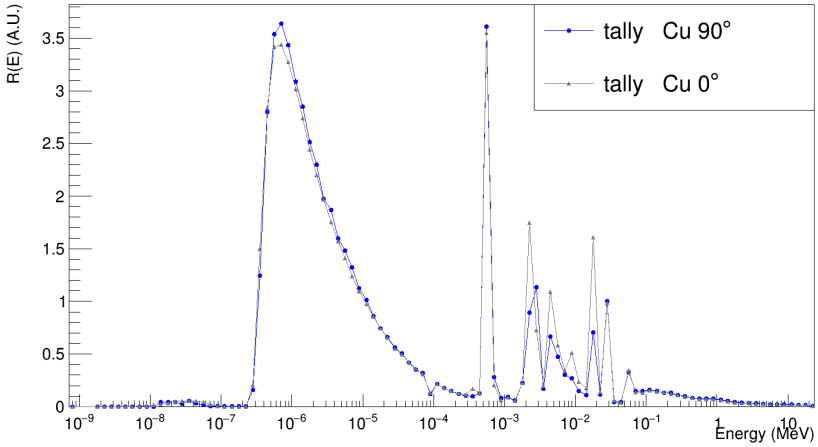

Fig. A.47.: Angular response curves for the Cu foil for a neutron incoming angle of 0° and 90°. No normalization have been applied.

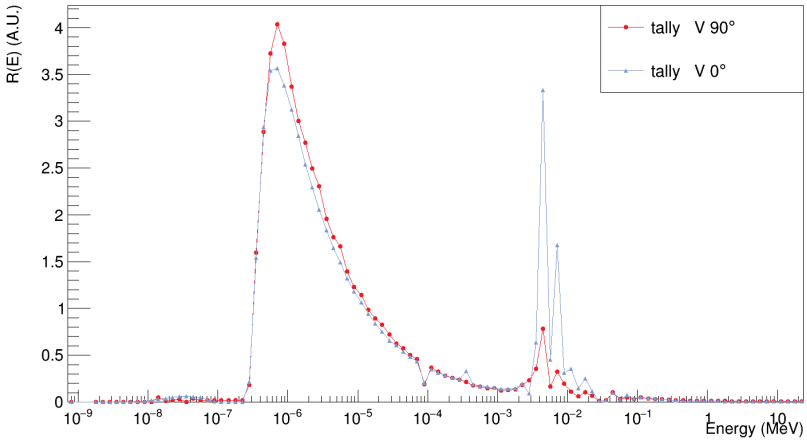

Fig. A.48.: Angular response curves for the V foil for a neutron incoming angle of 0° and 90°. No normalization have been applied.

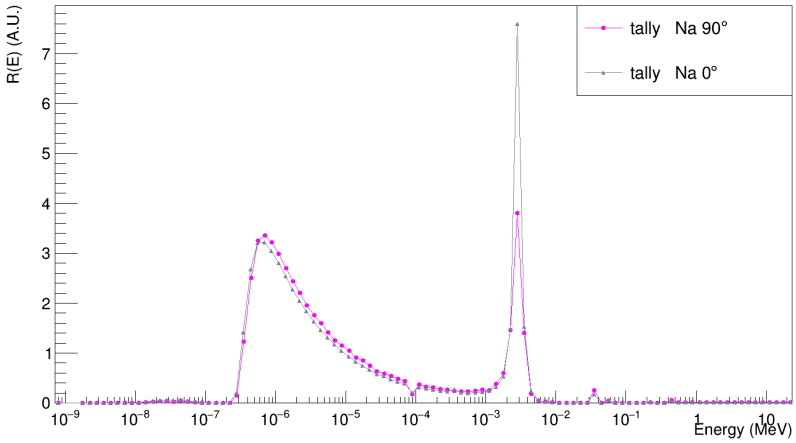

Fig. A.49.: Angular response curves for the Na foil for a neutron incoming angle of 0° and 90°. No normalization have been applied.

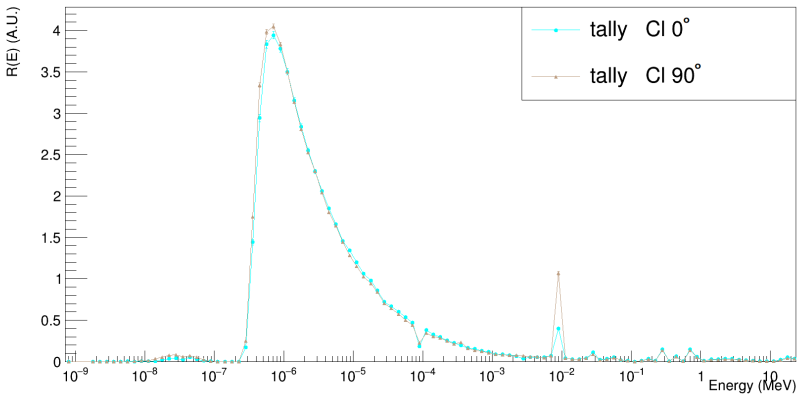

Fig. A.50.: Angular response curves for the Cl foil for a neutron incoming angle of 0° and 90°. No normalization have been applied.

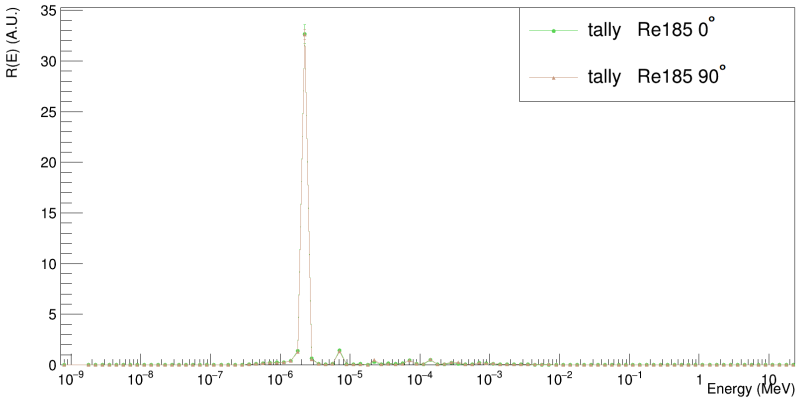

Fig. A.51.: Angular response curves for the ^{185}Re foil for a neutron incoming angle of 0° and 90°. No normalization have been applied.

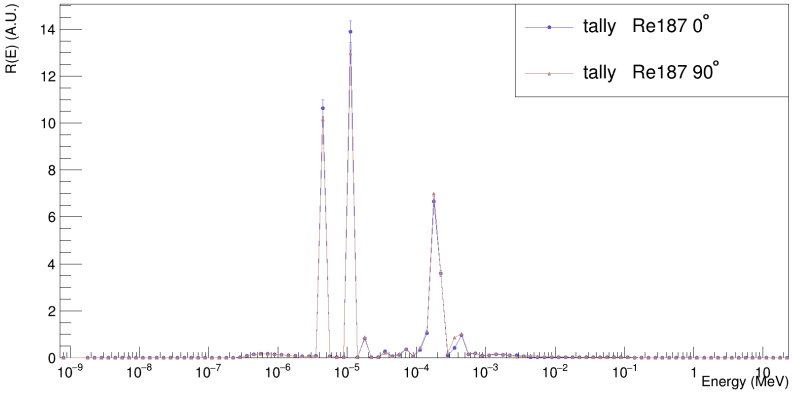

Fig. A.52.: Angular response curves for the ^{187}Re foil for a neutron incoming angle of 0° and 90°. No normalization have been applied.

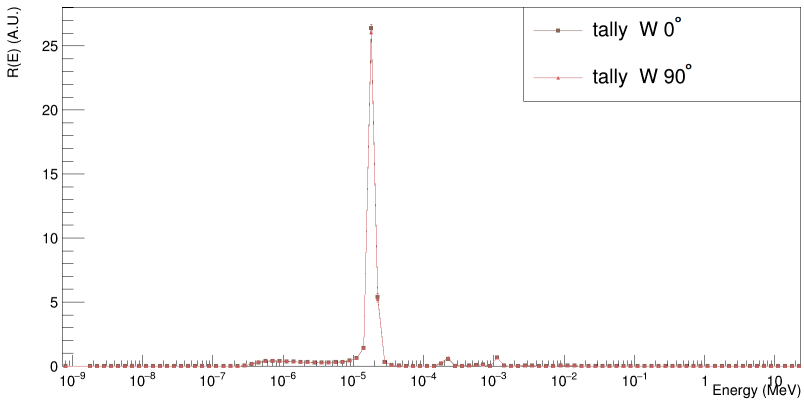

Fig. A.53.: Angular response curves for the W foil for a neutron incoming angle of 0° and 90°. No normalization have been applied.

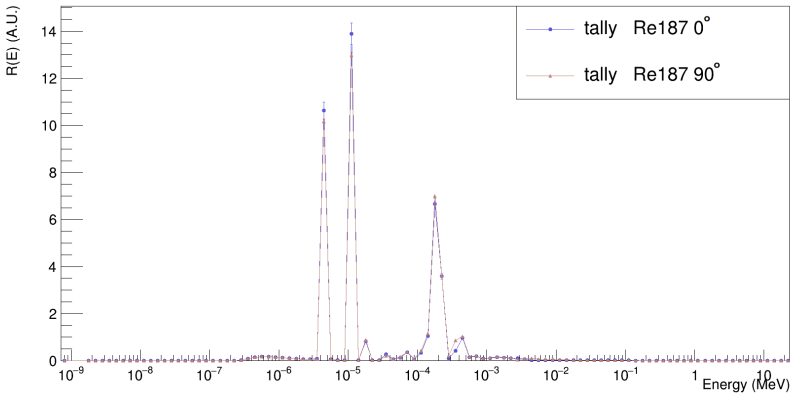

Fig. A.54.: Angular response curves for the ^{187}Re foil for a neutron incoming angle of 0° and 90°. No normalization have been applied.

A.3 Final geometry extended results

In this section an extended version of the plots related tot he MC simulations on the final geometry simulated for NCT-ACS (section 3.3.2) are shown.
The main plots are shown, it should be mentioned that these graphics represent only a fraction among all the possible combination of curves. These have been evaluated to be the most interesting and notable.

Graphics from A.55 to A.62 refer to simulations using a neutron fixed incoming angle of 30°. The results in function of the different thicknesses of the HDPE sphere are shown.

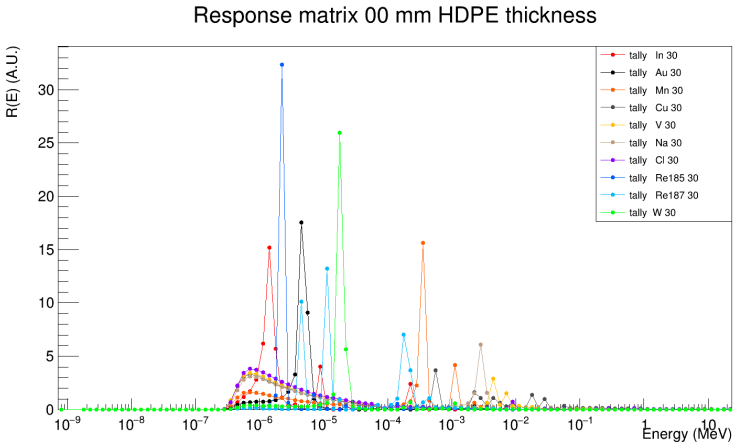

Fig. A.55.: Response curves for 00 mm HDPE thickness. An angle of 30° has been chosen for the incoming neutrons.

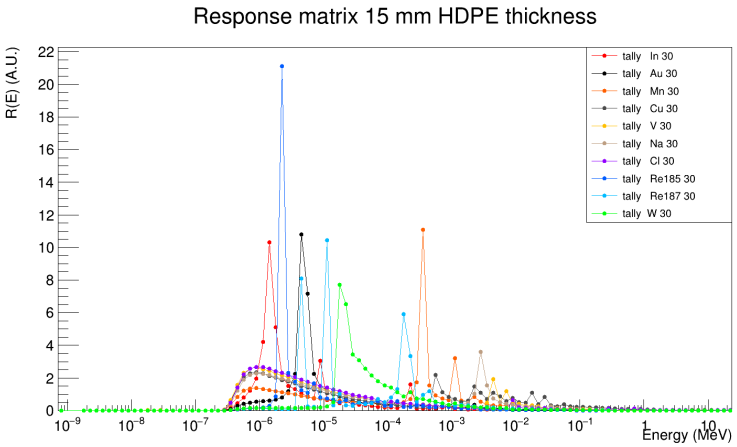

Fig. A.56.: Response curves for 15 mm HDPE thickness. An angle of 30° has been chosen for the incoming neutrons.

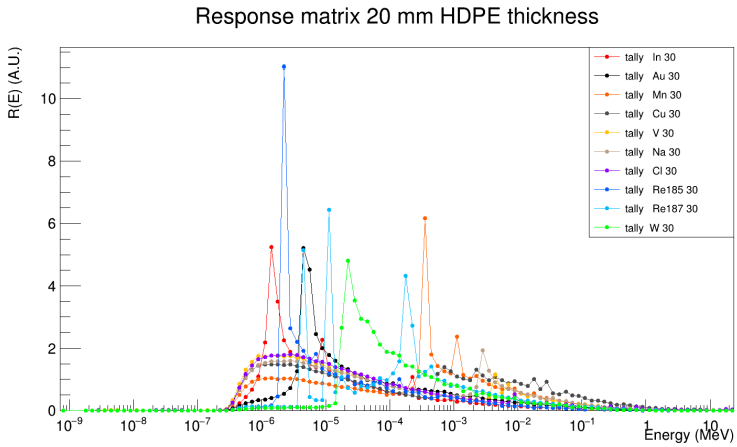

Fig. A.57.: Response curves for 20 mm HDPE thickness. An angle of 30° has been chosen for the incoming neutrons.

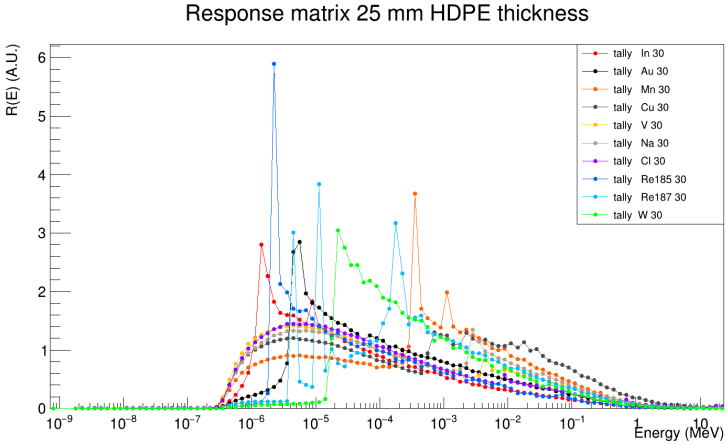

Fig. A.58.: Response curves for 25 mm HDPE thickness. An angle of 30° has been chosen for the incoming neutrons.

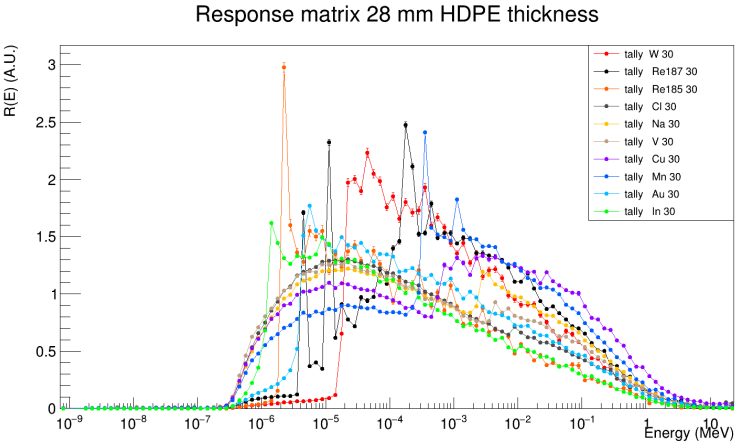

Fig. A.59.: Response curves for 28 mm HDPE thickness. An angle of 30° has been chosen for the incoming neutrons.

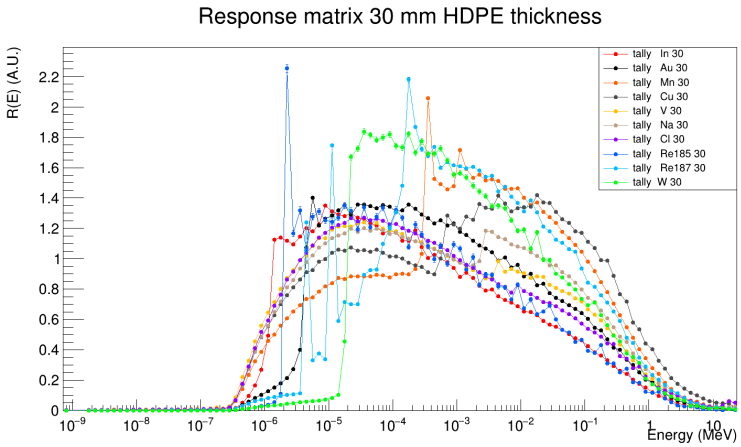

Fig. A.60.: Response curves for 30 mm HDPE thickness. An angle of 30° has been chosen for the incoming neutrons.

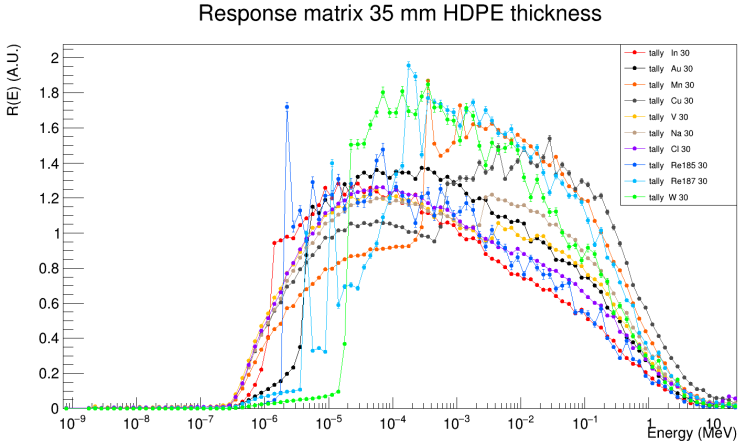

Fig. A.61.: Response curves for 35 mm HDPE thickness. An angle of 30° has been chosen for the incoming neutrons..

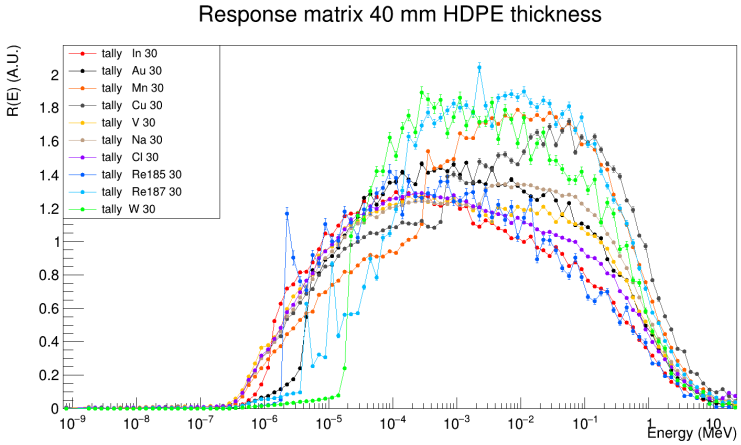

Fig. A.62.: Response curves for 40 mm HDPE thickness. An angle of 30° has been chosen for the incoming neutrons.

Graphics from A.63 to A.72 refer to angular response curves for all the elements in the 20 mm HDPE thickness.

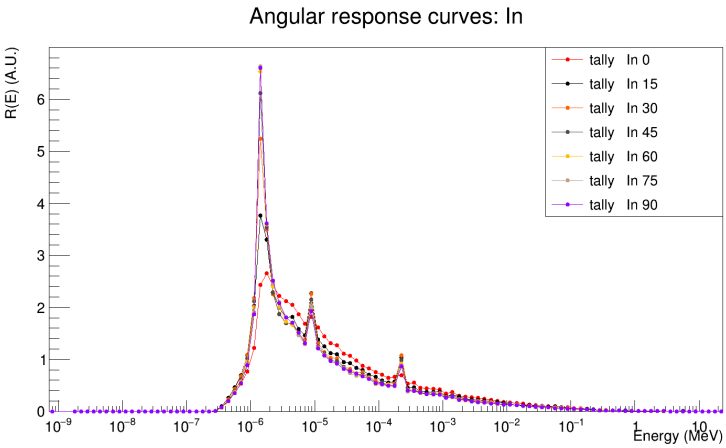

Fig. A.63.: Angular response curves for In foil, considering the 20 mm HDPE thickness.

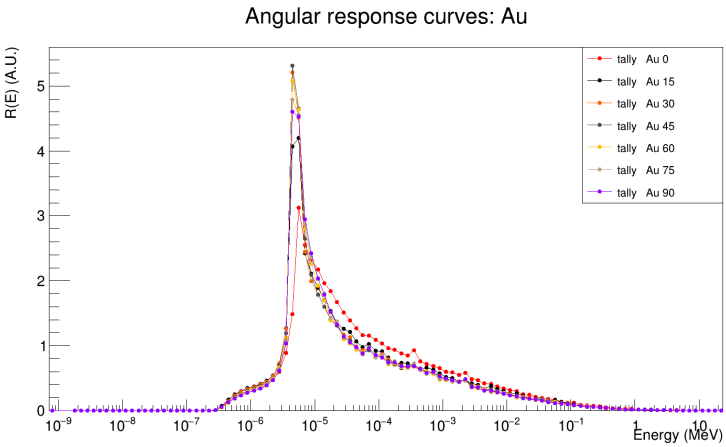

Fig. A.64.: Angular response curves for Au foil, considering the 20 mm HDPE thickness.

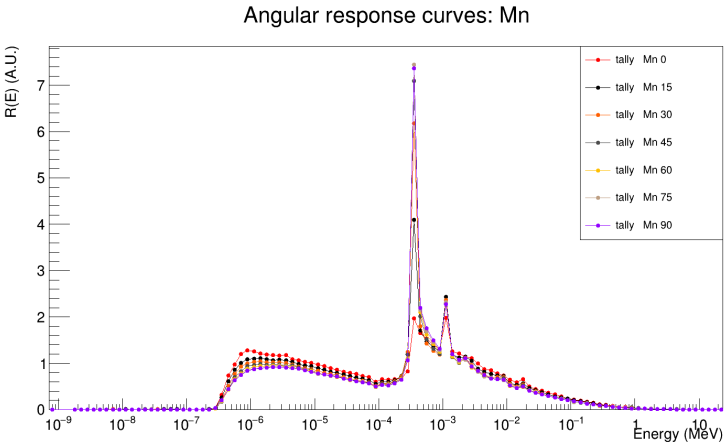

Fig. A.65.: Angular response curves for Mn foil, considering the 20 mm HDPE thickness.

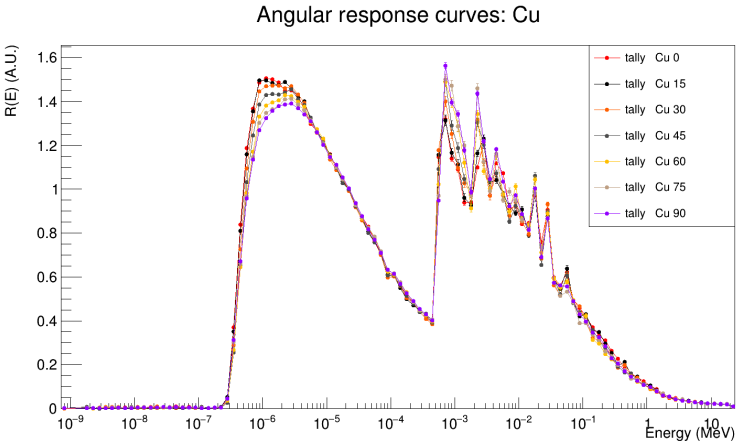

Fig. A.66.: Angular response curves for Cu foil, considering the 20 mm HDPE thickness.

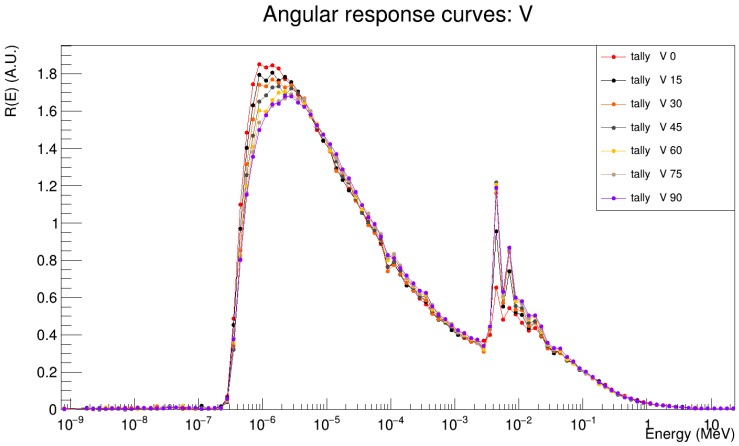

Fig. A.67.: Angular response curves for V foil, considering the 20 mm HDPE thickness.

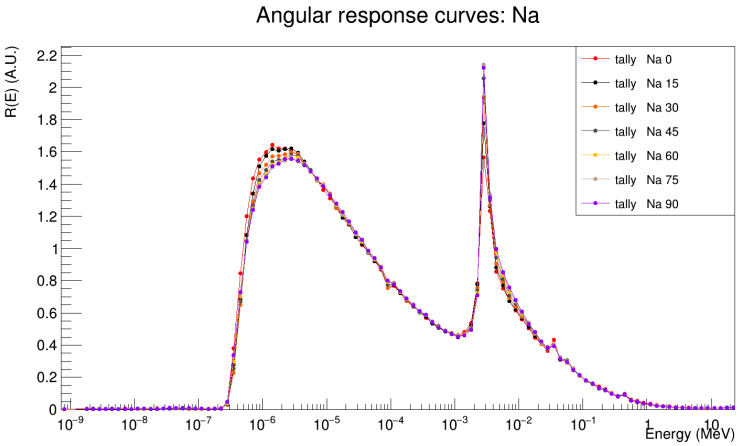

Fig. A.68.: Angular response curves for Na foil, considering the 20 mm HDPE thickness.

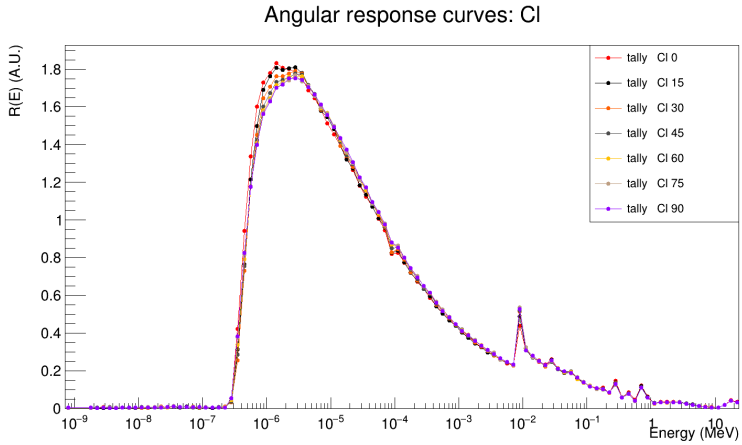

Fig. A.69.: Angular response curves for Cl foil, considering the 20 mm HDPE thickness.

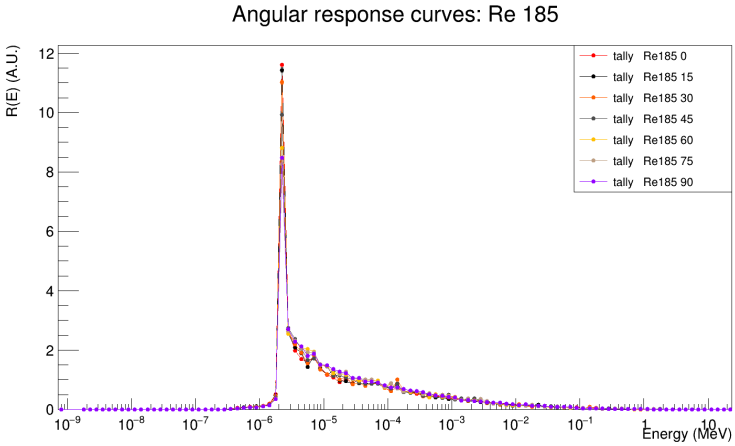

Fig. A.70.: Angular response curves for ^{185}Re foil, considering the 20 mm HDPE thickness.

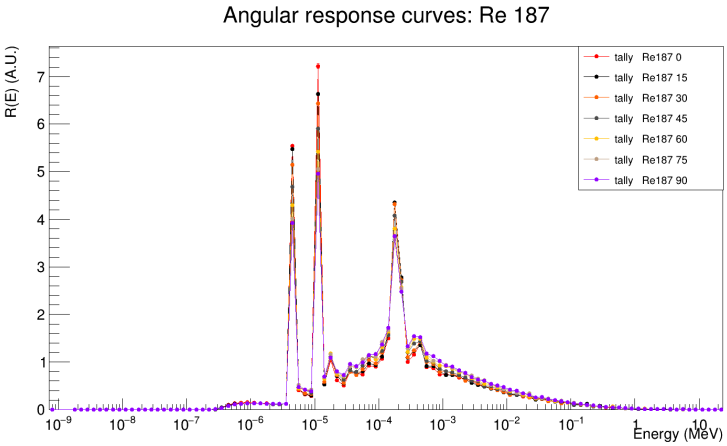

Fig. A.71.: Angular response curves for ^{187}Re foil, considering the 20 mm HDPE thickness.

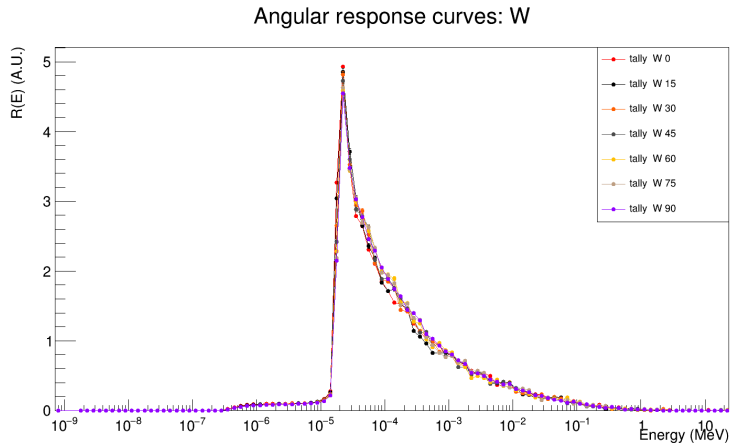

Fig. A.72.: Angular response curves for W foil, considering the 20 mm HDPE thickness.

Graphics from A.73 to A.82 refer to angular response curves for all the elements in the 28 mm HDPE thickness.

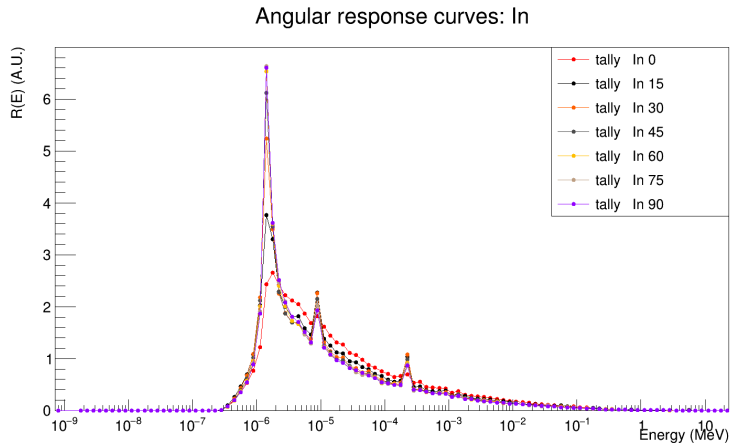

Fig. A.73.: Angular response curves for In foil, considering the 28 mm HDPE thickness.

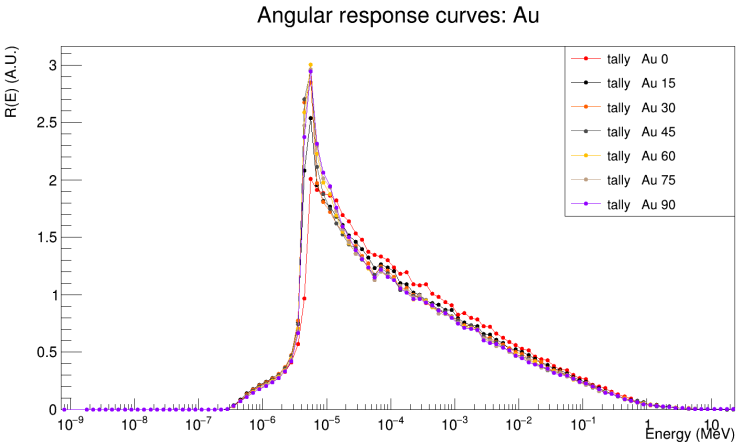

Fig. A.74.: Angular response curves for Au foil, considering the 28 mm HDPE thickness.

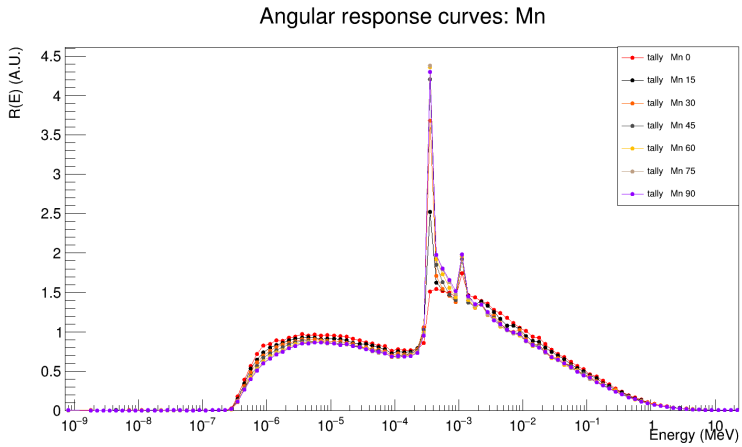

Fig. A.75.: Angular response curves for Mn foil, considering the 28 mm HDPE thickness.

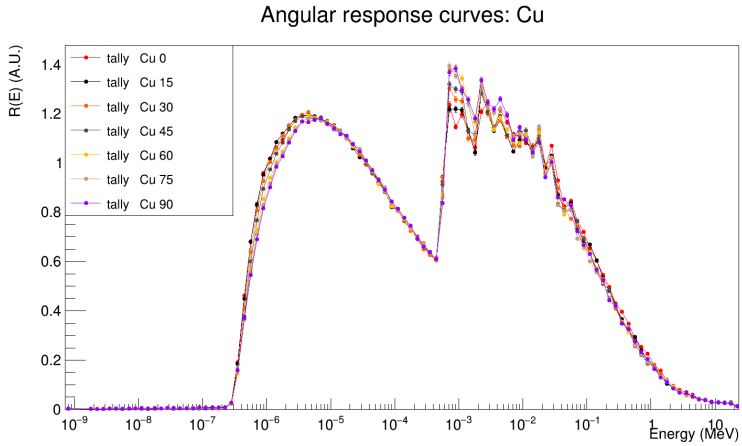

Fig. A.76.: Angular response curves for Cu foil, considering the 28 mm HDPE thickness.

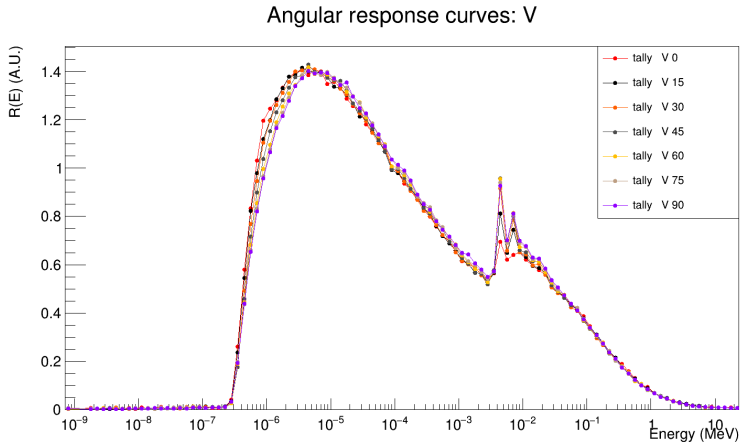

Fig. A.77.: Angular response curves for V foil, considering the 28 mm HDPE thickness.

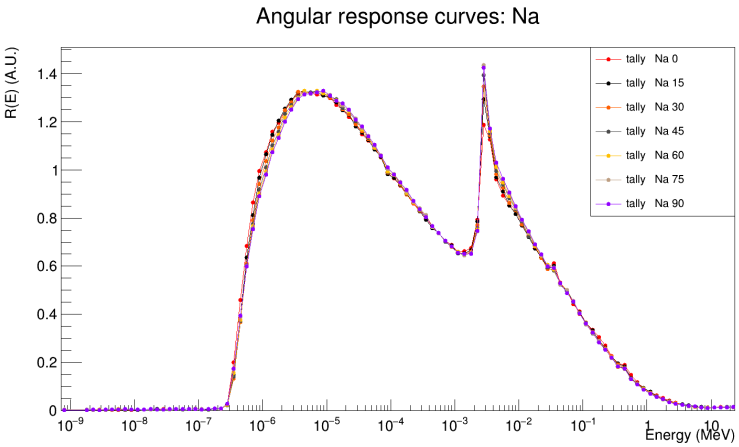

Fig. A.78.: Angular response curves for Na foil, considering the 28 mm HDPE thickness.

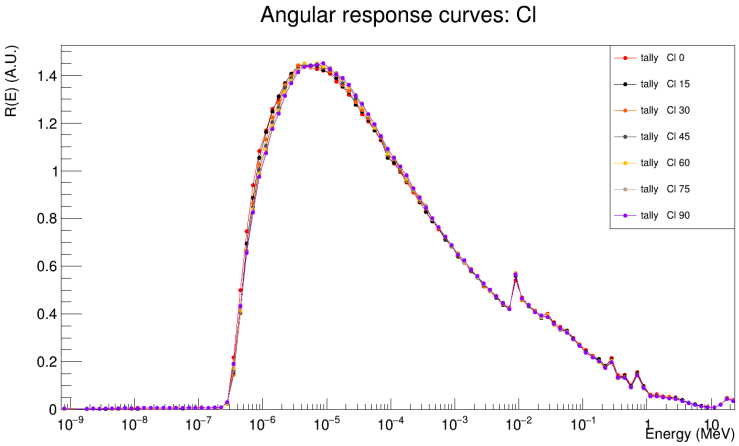

Fig. A.79.: Angular response curves for Cl foil, considering the 28 mm HDPE thickness.

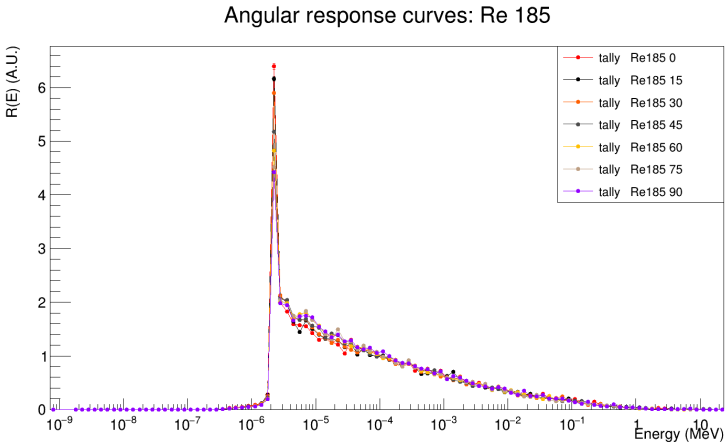

Fig. A.80.: Angular response curves for ^{185}Re foil, considering the 28 mm HDPE thickness.

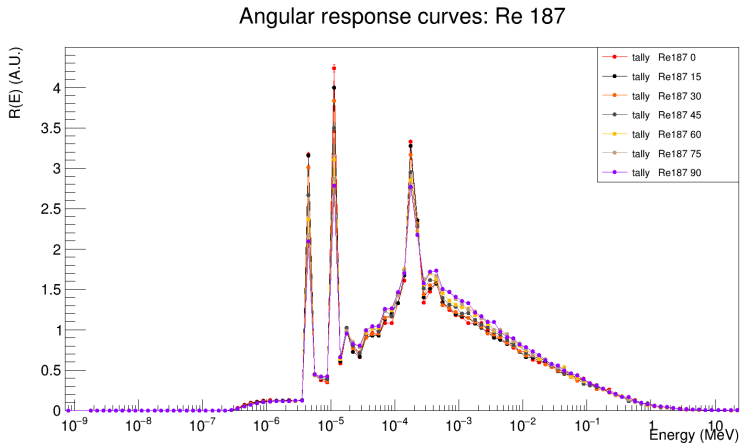

Fig. A.81.: Angular response curves for ^{187}Re foil, considering the 28 mm HDPE thickness.

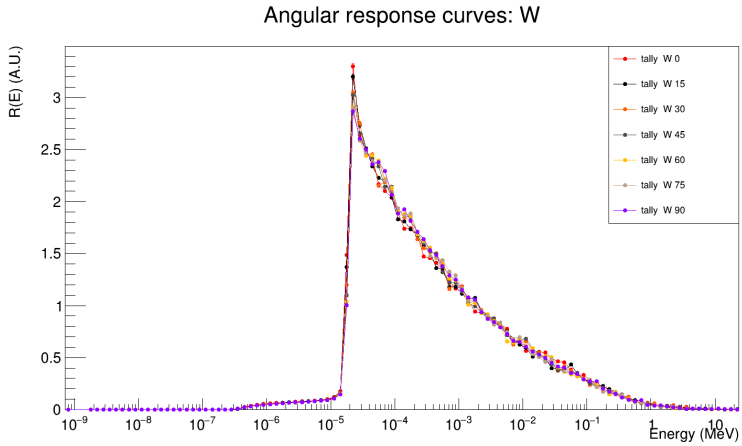

Fig. A.82.: Angular response curves for W foil, considering the 28 mm HDPE thickness.

B Hints about the unfolding methods

B.1 Introduction

While taking measurements there is always an alteration caused by the detector itself, which biases the experiment. This aspect is massively relevant for neutron application.
Such bias may lay in the fact that the instrument doesn't have a 100% efficiency, or it is due to the finite resolution of the electronics or even other sources. All these problems cause the experiment to drift from the ideal measurement expected.
In order to find the quantity that has been measured, the operator must correct such alterations. The deconvolution of the data is performed by creating a matrix that contains the information about the detector's smearing of the desired true quantity. This deconvolution is also known as "unfolding".
In neutron physics, while aiming at the determination of dosimetric quantities that are strongly dependent on the neutron energy, the neutron spectra must be measured. Measuring the neutron spectrum has the difficulty of being present at a wide range of energies (around 10 orders of magnitude spread) making it particularly hard to determine. Since there is no detector in existence capable of performing a single measure throughout the whole range of energies, the current metrological standard for the determination of the neutron spectra is the Bonner Spheres.

B.2 The Bonner spheres technique

As already mentioned in chapter 1, the Bonner Spheres is an instrument composed of several high density polyethylene spheres of different sizes, each containing inside a thermal neutron detector. The standard spheres can measure from cold neutrons up to 20MeV, with modified versions of the detectors including ranges up to 1GeV. The term "Bonner Sphere Spectrometer" (BSS) is born in 1960 at Rice University by Bramblett, Ewing and Bonner [42].
Since every Bonner Sphere is particularly sensible to a certain range of energy, but not exclusively sensible to said range, the eventual neutron spectra lies hidden in a sum of different measurements from each sphere at each energy. Such superposition

can be calculated using what is called the Fredholm Integral Equation of the First Kind:

$$C_i = \int R_i(E)\Phi(E)dE \tag{B.1}$$

Where C_i are the counts measured by the ith sphere, $R_i(E)$ is the response function of the ith sphere at a given energy E, and $\Phi(E)$ is the neutron spectra in place.

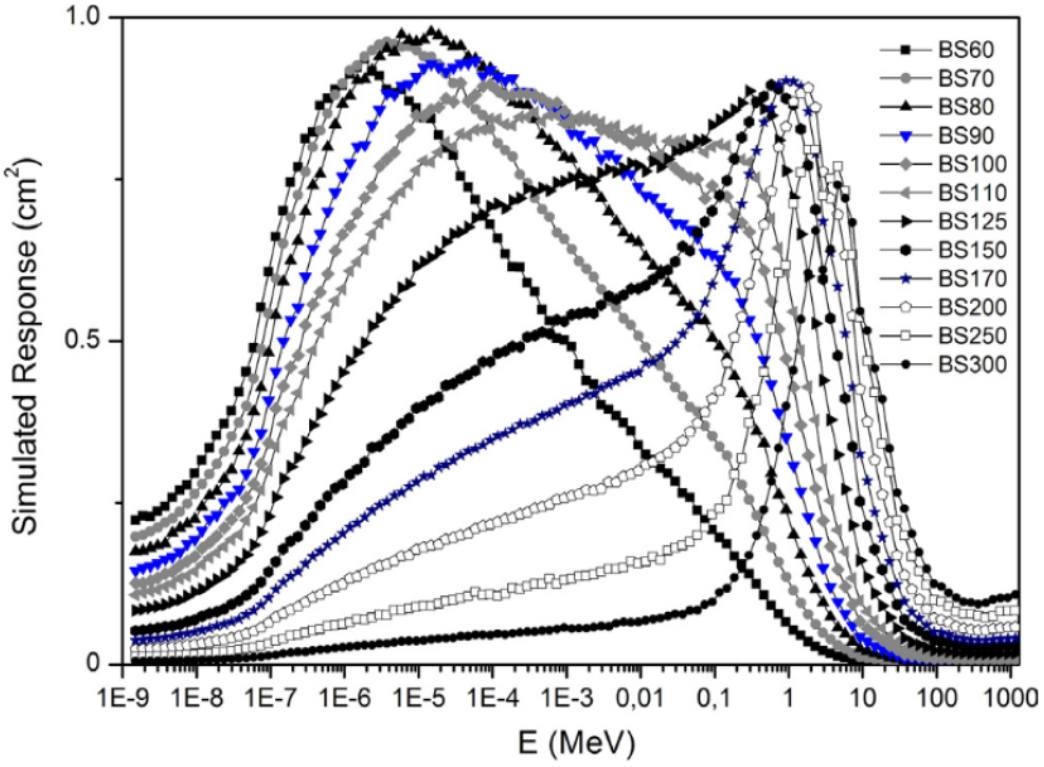

Fig. B.1.: Graphic representation of the response matrix of a system of Bonner Spheres.

Since the measure doesn't follow an analytic curve, in order to perform the measure and extract the neutron flux there is a need to discretize the function as is:

$$C_i = \sum_{k}^{M} R_{ik}\Phi_k \tag{B.2}$$

Where C_i are the counts measured by the ith sphere, R_{ik} is the response of the ith sphere at the kth interval, Phi_k is the neutron spectra value on the kth energy bin. i goes from 1 to N, being N the number of spheres, and k from 1 to M, where M is the number of energy bins, or channels, of the neutron spectra and the response matrix[1].

This discrete version of the Fredholm Integral Equation of the First Kind, when applied to the BSS measurement, it constitutes a system of N equations and M variables, with the most common case being M » N, implying that the system is

[1]Notation may vary on different algorithms presented further on as each one follows different formal approaches.

heavily underdetermined. Such condition makes it analytically impossible to solve, and thus forces the application of numerical methods to unfold the data.

B.3 Unfolding techniques throughout the years

Since the problem arose back in 1960, a myriad of solutions have been offered to solve the Fredholm equation in its discrete version. Despite such widespread variation of offered solutions, one common ground on each of them is the need of a "guess spectrum". Due to the fact that the phase space composing all the possible solutions is massive (consider a case of 100 bins on the spectra, with a precision of 10^{-4} on each bin, it would imply up to 10^{400} mathematically possible solutions) unless the numerical routine is given a hint on the region in which to find the solution, it would take a near-infinite amount of time to check every possible case, not to mention the fact that there may be more than one possible solution that meets the stopping requirements of the applied algorithm. In order to give the program a hint on where to find the solution, the typical approach is to offer a "Guess spectrum", which is essentially the result of a Monte Carlo simulation or a diffusion model calculation, which leads to an expected result on the measurement. Such spectra is given to the algorithm in order to have a starting point and a region around which to look for the optimal result.
The most relevant methods that will consequently be elaborated can be grouped in 4 families:

1. Iterative
2. Parametric
3. Heuristic
4. Artificial Intelligence

Each member of the four families has its pros and cons, and up to now no method has proven itself to be clearly superior, as there is none absent of flaws.

B.4 Iterative algorithms

Iterative algorithms are the oldest, yet proven to be extremely reliable. The main characteristic of this family of procedures is that the final result (the eventual unfolded spectrum) directly depends on the starting point. In principle, starting

from the same point, the algorithm will provide always the same result. They follow a formula which applies the same operation on the result of each iteration (thus the name). Two cases deserve to be on the highlight:

B.4.1 The SPUNIT algorithm

SPUNIT, unfolds the data using a deterministic iterative approach, meaning that, if the user were to execute twice the routine with the same input, the output won't change, and it's iterative in the sense that each iteration depends on the previous one. The formula to be used for the iteration is called the Doroshenko formula, or Doroshenko algorithm [138], created in 1977, which elaborates the spectra as follows:

$$\Phi^{i+1} = \frac{\Phi^i_j}{\alpha_j} \sum \frac{R_{kj}}{C^i_k} \tag{B.3}$$

Were Φ is the spectrum at the ith iteration, R_{kj} is the response matrix and C^i_k are the counts of the ith iteration. The factor α is the following array:

$$\alpha_k = \sum \frac{R_{kj}}{C^0_k} \tag{B.4}$$

Being C^0_k the counts measured with the Bonner Spheres.

As a test to value the good fit of the solution, the χ^2 test is applied, as follows:

$$\chi^2 = \frac{1}{N-1} \sum \frac{|C^0_k - C^i_k|^2}{u^2_i} \tag{B.5}$$

Being N the number of detectors and u^2_i the uncertainty propagation from the counts (C^0_i and C^i_k)

As said on the previous section, the method holds advantages and disadvantages:

1. Advantages:

    a) Relies on the counts from the spheres directly, holding a high physical meaning.

    b) Fast algorithm for modern computers, giving high precision results in seconds.

    c) As it is a simple algorithm it can be easily tested.

2. Disadvantages:

   a) Highly dependant on the initial guess spectrum.

   b) Given a completely wrong guess (or a flat one), the routine may not converge onto a physically relevant solution. This is due to the χ^2 test in which the stopping condition is based, which favours the gaussian shape.

Rellevant codes that implement SPUNIT are BUNTO (Turin, Fortran), NSDUAZ (Mexico, NI Labview) or AFITBUNKI (Texas, Fortran).

B.4.2 The GRAVEL algorithm

GRAVEL [139] is an iterative procedure that could be roughly considered a natural evolution from SPUNIT. The algorithm, also refered to as "Special Gradient Method", bases it's performance on a variation of the SAND-II algorithm developed in the US Air Force Weapons Laboratory back in 1967:

$$\Phi_j^{k+1} = \Phi_j^k \exp\left(\frac{\sum_i W_{ij}^k ln\left(\frac{C_i}{\sum_j R_{ij}\Phi_{ij}^k}\right)}{\sum_j W_{ij}^k}\right) \tag{B.6}$$

Where Φ_j^k is the resulting spectrum on the kth iteration on the jth energy bin, C_i are the counts measured, R_{ij} is the response matrix and W_{ij}^k is a weighting factor defined as:

$$W_{ij}^k = \frac{R_{ij}\Phi_j^k}{\sum_{j'} R_{ij'}\Phi_{j'}^k}\frac{C_i^2}{\sigma_i^2} \tag{B.7}$$

Where σ is defined as the error associated with the counts (typically it takes the value of the square root of said counts). Following the same procedure as in SPUNIT, the statistical check performed in order to create the stopping condition on the iterative procedure is done via the χ^2 test.
GRAVEL is an algorithm that relies in both the spectra and the counts, meaning it meets mid-way between the physical relevance of the result and the mathematical precision. The main pros and cons are listed below:

1. Advantages:

   a) Simple algorithm with a fast performance.

   b) Converges with a high precision.

c) Takes into account both the mathematical relevance and physical meaning of the solutions.

2. Disadvantages:

a) Highly dependable on the guess spectrum.

b) The χ^2 test prioritises the gaussian shapes.

Noteworthy algorithms that make use of the GRAVEL unfolding method are FRUIT-SGM (Frascati, NI Labview) or HEPROW (Braunschweig, Fortran).

B.4.3 Parametric algorithms

A completely different approach from that of the iterative procedures is that of the Parametric Algorithms, which rely on the superposition of different analytical functions in order to obtain an spectrum that leads to a similar results as those measured. The validation of the eventual result can be done from an evaluation of the hypothetical counts on the test spectrum, or with a straight up comparison of the test spectrum with the a priori (guess) information. The first method requires more computation power and implies a search on a full phase space, while the second method offers a much faster result and reliability of the output. The method that will be elaborated on this section is the MITOM algorithm [140], developed at the UAB, in Barcelona, in 2004.

B.4.4 The MITOM algorithm

The algorithm takes the assumption that the fluence energy distribution rate (spectrum) is constituted by the superposition of three mathematical functions, part of the thermal energy domain, the epithermal region and a fast peak. The final spectrum is the sum of each distribution normalised to the unit:

$$\Phi(E) = P_{Th}\Phi_{Th}(E) + (1 - P_{Th} - P_{Fast})\Phi_{Epi}(E) + P_{Fast}\Phi_{Fast}(E) \tag{B.8}$$

Being P_{Th} and P_{Fast} the probability for the thermal and fast components respectively. The sum of the three components must be 1.
The three functions that compose the MITOM algorithm are the following:

1.

$$\Phi_{Th}(E) = \frac{E}{T_c^2} exp\left(\frac{-E}{T_c}\right) \tag{B.9}$$

with T_c being 0.0025eV, which defines the most probable value of the Maxwellian thermal distribution. This equation is defined for energies below 0.1eV.

2.
$$\Phi_{Epi}(E) = E^{b-1}\left[\left(1 - exp\left(\frac{-E^2}{E_d^2}\right)\right)exp\left(\frac{-E}{\beta'}\right)\right] \tag{B.10}$$

where E_d is 0.0707eV and b and β' are parameters defined within the following limits: $-0.5 \leq b \leq 0.5$ and $0 \leq \beta' \leq 1$, with an energy range from 0.1eV up to 1keV.

3.
$$\Phi_{Fast}(E) = E^{\alpha}exp\left(\frac{-E}{\beta}\right) \tag{B.11}$$

having $0 \leq \alpha \leq 1$ and $1 \leq \beta \leq 2$, and defined for energies from 1keV up to 20MeV.

The superposition of those three curves, along with the associated probabilities allows the algorithm to recreate virtually any neutron spectrum generated by a source. Prior to the execution of the code there is the requirement of a a priori estimation of the total fluence number, $\Phi_{apriori}$, which drifts from the real one by a factor δ, estimated by the code.
The algorithm is in need, initially, of the count rates of the spheres in order to solve the uncertainties, plus an original starting point for all the active parameters $(\alpha, \beta, \beta', b, P_{Th}, P_{Fast}, \delta)$.
Once the original setup with all the information is ready, the program will execute a small random variation of individual parameters at each iteration, performing a χ^2 test on each energy bin in order to find the optimal solution. Such process is similar to the simulated annealing, which will be described further on.
On the matter of pros and cons of this procedure:

1. Advantages:

   a) Few parameters to tune, meaning the code is light and the performance high.

   b) Capability to expand the search by adding different functions.

   c) Every result is physically relevant.

2. Disadvantages:

a) Unless the neutron spectrum comes from a source, it won't converge to a solution.

b) Blind to small peaks or shapes that are not described by the functions.

c) Highly dependant on the guess spectrum to find a solution in reasonable computing time.

Codes that make use of parametric algorithms to perform the calculations: FRUIT-parametric mode (Frascati, NI Labview) and BONMA (London, R).

B.4.5 Heuristic methods

In computer science, artificial intelligence, and mathematical optimization, a heuristic is a technique designed for solving a problem more quickly when classic methods are too slow, or for finding an approximate solution when classic methods fail to find any exact solution. This is achieved by trading optimality, completeness, accuracy, or precision in benefit of speed. In a way, it can be considered a rough shortcut.
The purpose of a heuristic algorithm is to offer a near-optimal solution in a reasonable time frame. The solution may not be the global optimal, but it is close enough that the time benefit makes it worth it.
On a higher level from the heuristic algorithms stand the metaheuristics, which are essentially procedures that combine different heuristics to find the global optima on a problem. Compared to classical iterative methods or optimization algorithms (such as the Newton method), metaheuristics won't guarantee the global optimal solution, as they depend on stochastic procedures, and therefore are dependant on random variables generated, but they effectively search throughout complex spaces in a quick fashion, yielding a large set of feasible solutions to analyze. This feature proves them a useful approach for optimization problems. As can be seen in Figure B.2 , the variety of algorithms compressed under the scope of the metaheuristics is wide.

B.4.6 The MAXED algorithm

MAXED [141] is an algorithm developed back in 1998 by M. Reginatto and P. Goldhagen which applies the principle of maximum entropy (thus, information theory) to find the optimal spectrum making use of the simmulated annealing method to look for the solution.

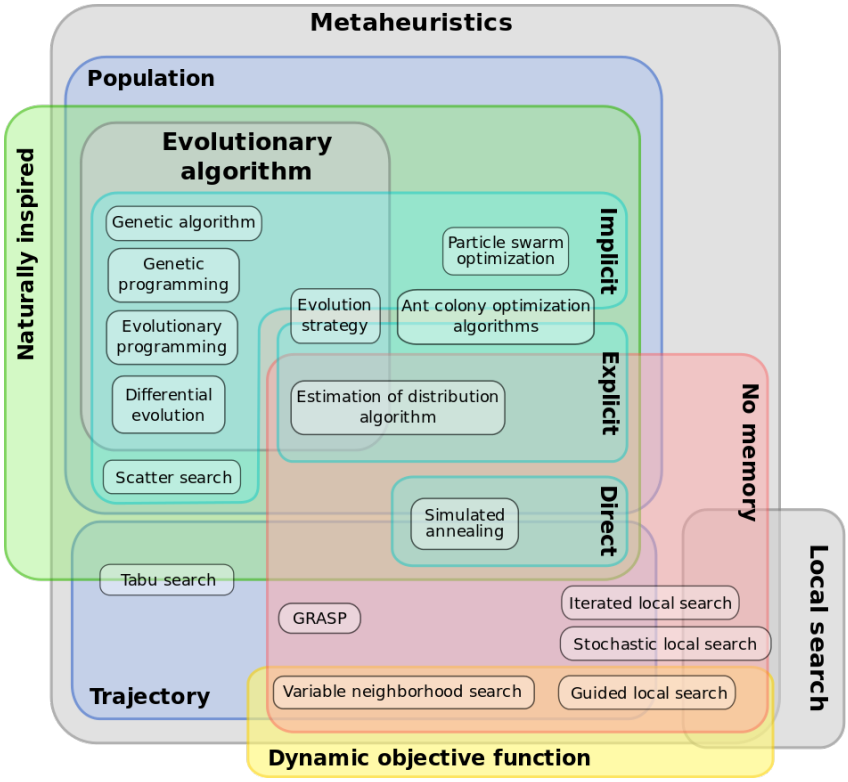

Fig. B.2.: Classification of different metaheuristic procedures.

Maximum Entropy Unfolding, the theory

The algorithm looks for what is known as Maxium Entropy, also named "Shannon's Entropy" in information theory. Such value is defined as:

$$S = -\sum_i P_i log Pi \tag{B.12}$$

Where P_i is a probability distribution (in the case at hand, a neutron spectrum normalized to the unit). This formula was originally introduced by Claude Shannon in 1948, and defines the amount of information carried by each event within the distribution.

In order to apply this theory to the neutron unfolding, first some restrictions must be applied to keep the "physical relevance":

$$N_k + \epsilon_k = \sum_i R_{ki}\Phi_i \tag{B.13}$$

$$\sum_k \frac{\epsilon_k^2}{\sigma_k^2} = \Omega \tag{B.14}$$

Where N_k are the counts from the kth detector, ϵ_k is the difference between the predicted value by the guess spectrum and the actual measured value for the kth detector, $R_k i$ is the response matrix, Φ_i is the solution spectrum and Ω is a value typically set equal to the number of detectors.

Considering all the spectra that meet the limitations described, the one holding the true spectrum measured will have the maximum information, thus maximizing the following value:

$$S = -\sum_i \left[\Phi_i ln\left(\frac{\Phi_i}{\Phi_i^{guess}} \right) + \Phi_i^{guess} - \Phi_i \right] \tag{B.15}$$

Where Φ_i^{guess} is the default guess spectrum on the measure.
The maximisation of equation B.15 with the constraints found in equations B.13 and B.14 is equivalent to the maximisation of a potential function $Z(\lambda)$ achievable through the Langrangian:

$$L(\Phi_i, \epsilon_k, \lambda_k, \mu) = -\sum_i \left[\Phi_i ln\left(\frac{\Phi_i}{\Phi_i^{guess}} \right) + \Phi_i^{guess} - \Phi_i \right] - \sum \lambda_k \left[\sum R_{ki}\Phi_i - N_k - \epsilon_k \right] - \mu \left[\sum N_k \lambda_k \right] \tag{B.16}$$

Where λ_k and μ are (m+1) Lagrange multipliers.
Following the mathematical elaboration by Reginatto and Goldhaggen in 1998, the variation of L is equivalent to a maximisation of the potential function Z:

$$Z = -\sum \Phi_i^{guess} exp\left(-\sum \lambda_k R_{ki} \right) - \left[\Omega \sum (\lambda_k \sigma_k^2) \right]^{\frac{1}{2}} - \sum (N_k \lambda_k) \tag{B.17}$$

In order to find the maximum of the function, the simulated annealing algorithm is used.

Simulated Annealing

The simulated annealing is a metaheuristic designed to approximate a global optima in a large space of an optimisation problem. The method derives from the Metropols-Hastings algorithm, created by Metropolis back in 1953 to generate sample states of a thermodynamic system. At each step of the algorithm, the heuristic considers some neighbouring state s* of the current state s, and with a certain probability decides whether to jump to the new state of remain at the current one. Those probabilities are conditioned in order to make the system tend to move to a lower energy state. The process is repeated either until the solution is sufficiently good or the computation time is exhausted.
By altering a state the algorithm creates its neighbours. One example can be found on the Travelling salesman problem, where the method must find the shortest route between a group of cities. From a certain route, a permutation between two cities creates a new state, which shall be avaluated by the algorithm as either better or worse.
Whether the new state is accepted or not deppends on some few conditions. Consider the energy E of a certain state s as E(s) and a probability distribution P that depends on the energy of both states and the temperature:

1. if $E(s') < E(s)$: The new state is accepted.

2. if $E(s') > E(s)$: The new state has a probability $P(E(s), E(s'), T)$ of being accepted.

Under these conditions, the algorithm is executed repeatedly, and after a certain number of iterations the temperature is reduced gradually, forcing the brownian motion to tend to the global point of minimum energy. The lower the temperature, the smaller the energy variations around a local will be, making the algorithm more precise on the right area.
This algorithm holds its own advantages and disadvantages when applied to the unfolding problem:

1. Advantages:

    a) As it is a method derived from information theory, is mathematically consistent.

    b) The application of the simulated annealing restores a fast solution with a high precision.

2. Disadvantages:

    a) Cannot operate without a guess spectrum.

    b) The mathematical and numerical precision is more important than the physical meaning of the result

B.4.7 The Artificial Intelligence approach

Artificial Intelligence (AI) is, in computer science, the intelligence demonstrated by machines, contrary to the natural intelligence from humans or animals. Colloquially the term is used to describe the pseudo-cognitive processes of certain algorithms, that mimic the human learning process for problem solving. AI became a field of research with own name in 1956, but it wasn't until the arrival of the XXI century that it gained popularity, partially thanks to the exponential improvement of computational capabilities, the technological improvements and the massive data analysis demands. To show how much the field has grown over the past 25 years, Figure B.3 show a rough diagram of the present most relevant subfields on AI:

The first uses of high-level AI applied to unfolding can be tracked as back as 2004, with the first application of Artificial Neural Networks (ANN) to find a solution to the Fredholm Integral Equation.

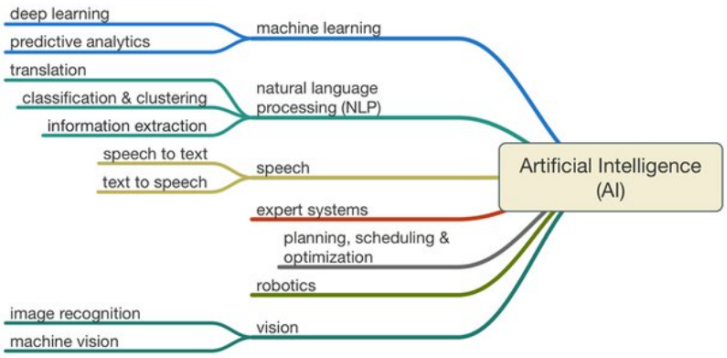

Fig. B.3.: Schematic diagram on the main application fields of artificial intelligence.

Artificial Neural Networks are computing systems inspired by the biological neural networks that constitute the animal's brains. They were first proposed by Warren McCulloch and Walter Pitts in 1943 [142]. Those complex algorithms are capable of leaning how to perform certain tasks and gradually improve their performance, generally without being specifically programmed to. One easy example is the image recognition, in which the program learns how to distinguish different elements of an image after being manually taught what elements constitute certain blocks, and create it's own parameters to distinguish in future situations said blocks.

Just like a brain, the neural network is able to pass the information from one neuron to another. In the most common application, the signal being passed through the computational synapse is essentially a real number, and the output of each neuron is the result of the non-linear function of the sum of the different inputs. The different connections between the different neurons are called "edges", and both the neurons and those edges have weights associated which vary throughout the training. ANNs are agregated into different layers, which perform specific operations and transformations to the data, and have one final output layer which combines all the results.

Naturally such technique can be applied to the unfolding of neutrons. Some groups have developed different methods to apply the ANN, an example can be seen on the work by S. Abolfazl in 2016 in Iran [143], which made use of the ANN combined with the least squares method.

Even though such algorithms are extremely performing, and the quality of their results is superior to other methods, they have their limitations: The algorithms are complicated and hard to manage, plus the computation time required to obtain the results is way too big to be applicable, for example, on a on-site measurement.

C

Thermal Neutron Rate Detector (TNRD)

C.1 Introduction

The Thermal Neutron Rate Detector TNRD [131] [132] has been developed within the NESCOFI@BTF project of INFN. It is a low cost, small size, easy-to-use, active neutron detector able to measure the thermal neutron fluence rate also in mixed neutron and gamma fields thanks to its minimal gamma sensitivity. It works over a wide range of thermal neutrons fluence rate values, from few neutrons cm^{-2} s^{-1} up to 10^7 cm^{-2} s^{-1}.

Fig. C.1.: TNRD detector.

TNRD is based on commercially available silicon detectors conveniently modified to make it sensitive to thermal neutrons. The sensitivity to thermal neutrons is obtained through the deposition of a thin ^{6}LiF layer by evaporation under controlled conditions. A special process allows to precisely deposit multiple detectors at the same time.
The ^{6}LiF acts as conversion layer, thermal neutrons are captured by the ^{6}Li and the emitted α particles and ^{3}H nuclei can reach the depletion region of the silicon detector and produce a readable signal. The thickness of the conversion layer is optimized to ensure a high conversion probability without stopping the charged products before they reach the silicon layer.
Photon rejection is obtained through an intrinsic compensation effect.
The active area of the sensor is 1 cm^2 and its overall dimensions are about 1.5 cm x 1 cm x 0.4 cm.

A commercial digitizer is used to transfer the signal to a PC and a software acquisition program allows visualizing the level and the duration of the voltage signal.

The net voltage level, which is proportional to the thermal flux, is obtained by subtracting the background signal extrapolated from the baseline before and after the voltage drop according to the following equation.

$$V_{net} = \overline{V} - \frac{1}{2}(\overline{V}_{letf} - \overline{V}_{right})$$

$\overline{V}$ is the time-averaged voltage output during the neutron shot and $\overline{V}_{left}$ and $\overline{V}_{right}$ are the time-averaged voltages before and after the neutron shot.

Due to the previous validation experiments, the TNRD is used as reference detector for the measurement of the thermal fluence rate inside the photoconverter. By giving an immediate indication on the flux density it can be easily used. On the contrary, the activation foils technique requires long exposition times and post-processing work to get a fluence rate value, resulting more complicate.
The response linearity of the TNRD in the range (10^2 - 10^6) cm^{-2} s^{-1} has been demonstrated in [131] as well as the isotropy of its response.

C.2 TNRD calibration

In order to use it to measure the thermal flux in the e-LiBANS cavity, the TNRD was calibrated in 2015 at the radial thermal column of the ENEA Casaccia TRIGA reactor where a stable thermal fluence rate form 10^2 cm^{-2} s^{-1} up to 1.5 10^6 cm^{-2} s^{-1} can be achieved.

The TNRD has been repeatedly exposed to the thermal beam and, according to the measured net voltage level, the calibration factor has been deduced. It was equal to:

$$C_{2015} = (0.249 \pm 0.010)\,\mu V\,cm^2\,s \tag{C.1}$$

Since many years was passed since the last calibration, a new measure was conducted at the HOTNES facilty in Frascaty.
As already mentioned, the thermal fluence rate is very well known and equal to

$$\dot{\Phi}_{th} = (763 \pm 22)\,cm^{-2}\,s^{-1}$$

Many irradiation were performed and the mean voltage value was considered. In figure C.2 an example of a TNRD signal is shown.

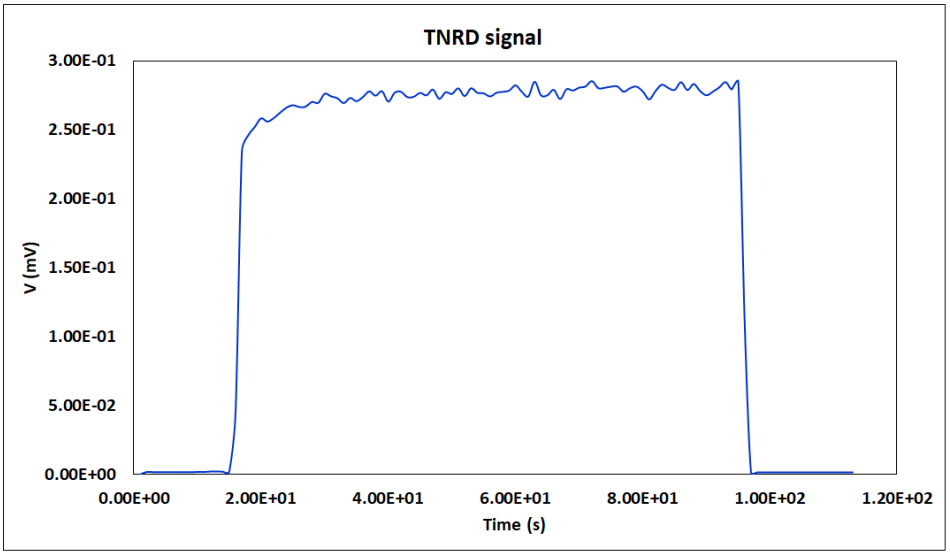

Fig. C.2.: TNRD detector signal at the HOTNES source in Frascati depending on the acquisition time.

Applying the same analysis method for the 2015 calibration, the obtained result is:

$$C_{2021} = (0.260 \pm 0.010)\,\mu\mathrm{V\,cm^2\,s} \tag{C.2}$$

The new calibration value was used for the thermal measurements in this work, in order to be more precise.
It should be noted that in over than 6 years, the calibration coefficient of the TNRD did not change sensibly, providing an interesting benchmark on the detector durability.

D

Nuclear Data for ^{nat}V

Transmission measurements on natural vanadium samples have been performed at the time-of-flight facility GELINA (EC-JRC-IRMM, Geel) to validate neutron resonance parameters for vanadium. In figure D.1, a top view of the facility is shwon:

Fig. D.1.: Top view of the GELINA facility.

This appendix will be useful to provide the experimental details required to deliver the data to the EXFOR data library which is maintained by the International Network of Nuclear Reaction Data Centres (NRDC). The experimental conditions and data reduction procedures are described.
In order to better understand the formalism and nomenclature used it could be useful to refer to section 1.3.

D.1 Status of nuclear data for ^{nat}V

Referring to [26] the bibliography presented on page 291 (23 - 6) has been studied in order to collect all the available data on vanadium.

D.1.1 Resonance Region

It should be noted that for the resonance parameters estimation, only few works presented complete or adequately referred data. In particular for the capture (kernel) measures, only Stieglitz and Winters report some results. The Atlas [26] shows only data from Winters, since the ones from Stieglitz are rough and characterized by a poor energy resolution.
Regarding the transmission measurements, there are more data by: Garg, Brusegan, Rohr, Stieglitz and Morgenstern.

In order to evaluate the agreement between the different measurements, the ratio between the available set of data respect to the Brusegan one was performed. The choice to use Brusegan work as a a reference is due to the fact that such measurement was produced at GELINA in 1997 with excellent experimental condition and data reduction analysis.
In figure D.2 the ratio plot is shown. It should be noted that, in general, there is a good agreement between the different measures, except for some out liars especially for high energy resonances.

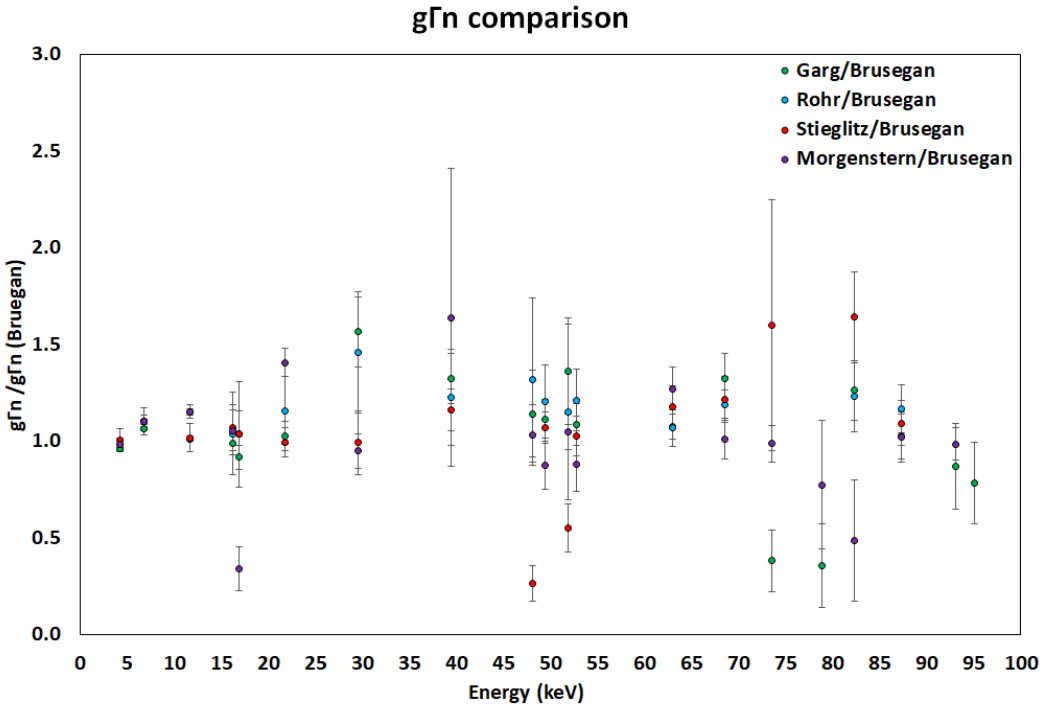

Fig. D.2.: $g\Gamma_n$ comparison for all the available transmission measurements on vanadium. Brusegan data were taken as reference values.

Thus can be concluded that the transmission data in literature are comparable and in good agreement.

Nevertheless, it should be also noted that few data were produced on Vanadium. Therefore new measurements could provide useful information and can reduce the uncertainties on precedent values, providing significant improvement to the actual nuclear data.

As already proposed by Bethe [144], the neutron strength function holds an important role in the resonance properties analysis. The definition of the strength functions for a certain angular momentum l can be calculated as:

$$S_l = \frac{< g\Gamma_n^l >}{(2l+1)D_l} = \frac{1}{(2l+1)\Delta E}\sum_j g_j \Gamma_{nj}^l \tag{D.1}$$

where the summation is carried over N resonances in an energy interval ΔE, g_j is the spin statistical weight factor for angular momentum $\vec{J} = \vec{I} + \vec{l} + \vec{\frac{1}{2}}$, and Γ_{nj}^l is the reduced neutron width and is related to the neutron width Γ_{nj} by

$$\Gamma_{nj}^l = \sqrt{\frac{1\,\text{eV}}{E_0}}\frac{\Gamma_{nj}}{V_l} \tag{D.2}$$

Being V_l is strictly related tot the penetrability factor and it is tabulated [26]. For the purpose of this work, the relationship between the p-wave reduced neutron width (Γ_n^1) and Γ_n is reported:

$$\Gamma_n^1 = \frac{\Gamma_n}{\sqrt{E_0}}\Big(1 + \frac{11369}{EA^{2/3}}\Big) \tag{D.3}$$

where the energy E is expressed in keV [26].
The resonances width coming from [26] have been therefore reduced using equation D.3 and the result is shown in figure D.3. This reduction aims to consider all the resonances like a p-wave resonance, allowing a direct comparison.

It should be noted that, in general, the distinction between s-waves ad p-waves is good, except for few values. Thus the parity assignment is verified and a value of 5 eV for the reduced resonance has been taken as discriminator between p-wave and s-wave.

As already mentioned, about the capture reaction, a lack in the literature data is present. In fact, only Stieglitz and Winters provided some data, a comparison between the two measurements was performed and the results has been divided into p-wave and s-wave behaviour.
The division was useful to better understand if there is a systematic difference due to the width of the resonance itself. The result is shown in figure D.4. It should be noted that for the Stieglitz measures, the maximum energy was 45.9 keV. Therefore, for higher energy values, only Winters data are available, and a comparison is no longer possible.

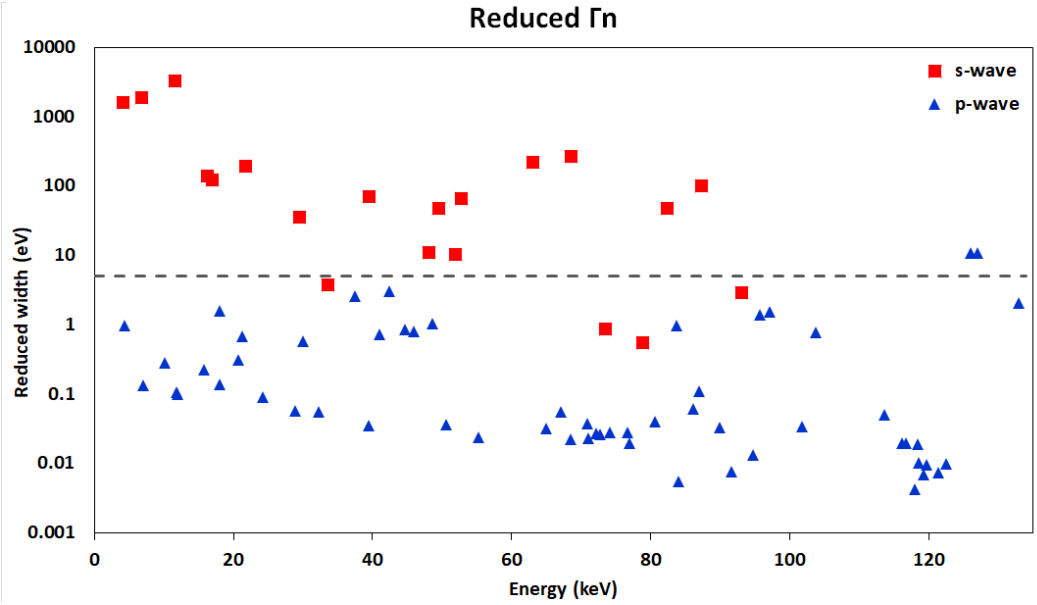

Fig. D.3.: Reduced neutron width of V resonances as a function of neutron energy assuming all resonances are p-wave. The dashed line represents a possible separation between s-wave and p-wave resonances.

It should be interesting to note that for the s-wave distribution, the differences can be substantial but they are energy-independent.
On the contrary, the p-wave data show massively differences, in fact, at low energies there is almost 1 order of magnitude of difference. Moreover, the p-wave ratio shows a dependence in energy with an increasing value from 0.15 up to 1.2.
Since the massive lack of data, it is not possible to determine if the energy dependence behaviour is due to the Winters or Stieglitz measures. Nevertheless, the former data should be considered more robust, since the excellent experimental conditions and better energy resolution.
Thus the necessity to produce new nuclear data on Vanadium is highly reinforced.

D.1.2 Thermal energy region

For the thermal capture cross section, references at page 290 of the atlas [26] (23 - 5) have been studied and corrected, where necessary.
A complete explanation over all the different techniques is not in the scope of this work, for more details please refer to the pertinent publications.

Among all the works presented in the Atlas reference table, only six authors presented the results explaining the experimental procedure. For those cases a complete and clear analysis was also provided, reinforcing the physical validity of the measure.
It should be noted that in the case of the Dilg measure [145] a correction has been made, since the isotopic abundance used at that time was calculated to be 99.7%

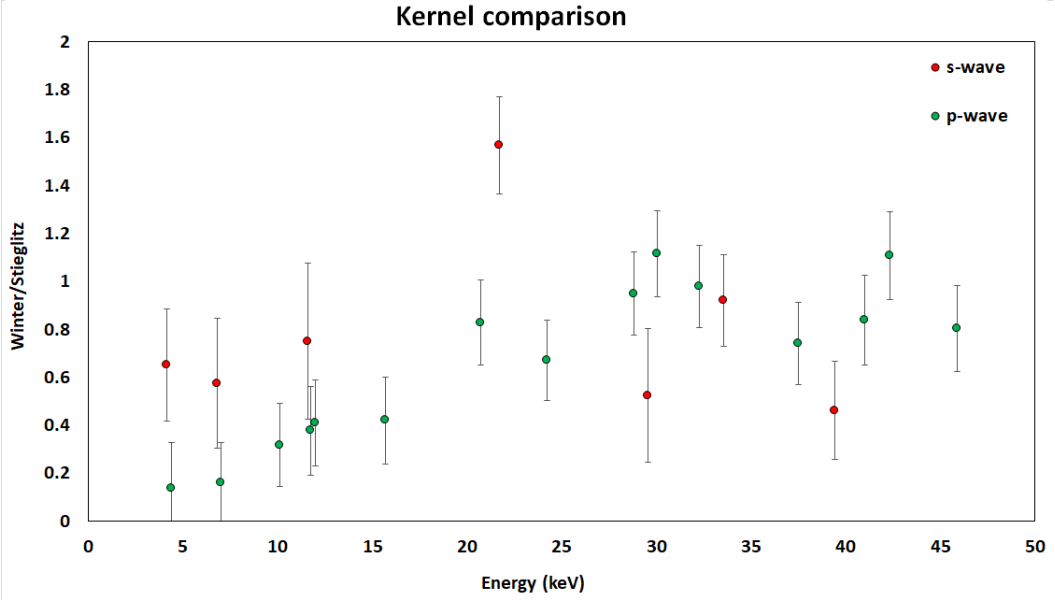

Fig. D.4.: Kernel comparison between Winters and Stieglitz data. A division between p-wave and s-wave has been used.

instead of 99.75%. This correction was considering that the ^{50}V presents a capture cross section of about 45 b [26], thus the need to correct the total capture cross section on $^{\text{nat}}$V subtracting the contribute of ^{50}V component.

$$\sigma_{\gamma,tot} = A_{50} \cdot \sigma_{\gamma,50} + A_{51} \cdot \sigma_{\gamma,51} \tag{D.4}$$

Being A_i and σ_i respectively the isotopic abundance and capture cross section for the different isotopes.

In figure D.5 the plot with the different measures is shown. Moreover, on the same plot are shown the values that can be found in some of the most used nuclear data library.

It should be noted that the weighted mean value is (uncertainty correspond to 1σ):

$$\sigma_\gamma = 4.96\,(0.02)\,\text{b}$$

providing a correction to the atlas [26] value of 4.94 (0.02) b. Thus probably it is due to a correction to the Dilg measure previously reported and to the exclusion of some of the presented measurements which were not reporting the whole experimental procedure.

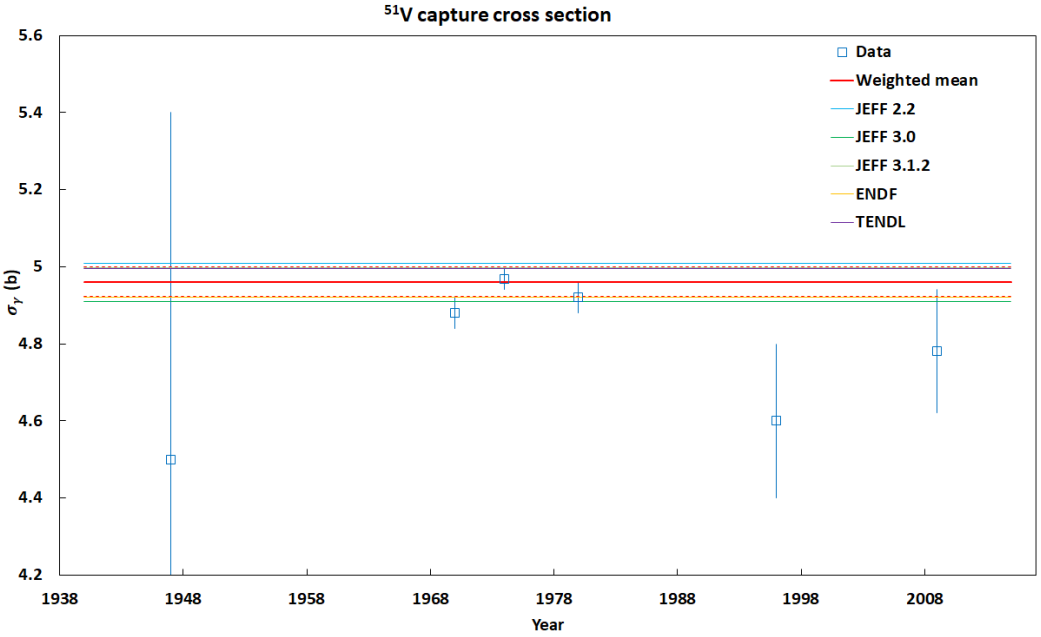

Fig. D.5.: Thermal capture cross section for ^{51}V. The red dotted lines represent the 2σ uncertainty region on the weighted mean. Some of the main libraries data are also reported. From left to right the data come from [146], [147],[145], [148], [149], [150].

D.2 Experimental Introduction

To study the resonance structure of neutron induced reaction cross sections, neutron spectroscopic measurements are required, which determine with a high accuracy the energy of the neutron that interacts with the material under investigation. To cover a broad energy-range such measurements are best carried out with a pulsed white neutron source, which is optimized for time-of-flight (TOF) measurements [151].
The TOF-facility GELINA [152] [153] has been designed and built for high-resolution cross section measurements in the resonance region. It is a multi-user facility, providing a white neutron source with a neutron energy range from 10 meV to 20 MeV. The GELINA facility can host up to 10 experiments at measurement stations located between 10 m and 400 m from the neutron production target.
The electron linear accelerator provides a pulsed electron beam with a maximum energy of around 150 MeV, a maximum peak current of 10 A and a repetition rate ranging from 50 Hz to 800 Hz. A compression magnet reduces the width of the electron pulses to about 1 ns [154] for compensating the widespread in energy of the electrons (figure D.6).

The electron beam hits a mercury-cooled uranium target producing Bremsstrahlung and subsequently neutrons via photonuclear reactions [155]. A representation of

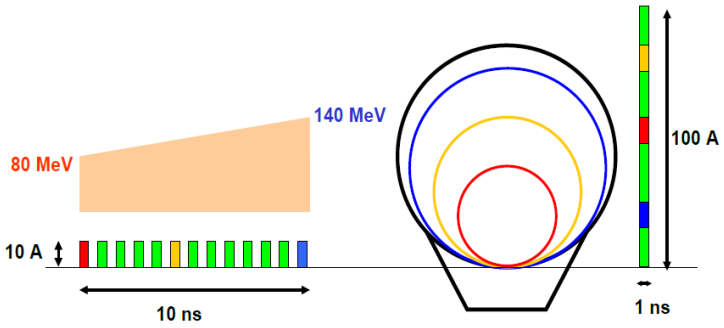

Fig. D.6.: Schematic view of the GELINA compression magnet.

the GELINA target is present near the control room of the accelerator, in figure D.7 a picture of the model is shown.

Two water-filled beryllium containers mounted above and below the neutron production target are used to moderate the neutrons. By applying different neutron beam collimation conditions, experiments can use either a fast or a moderated neutron spectrum. The neutron production rate is monitored by BF_3 proportional counters which are mounted in the ceiling of the target hall. The output of the monitors is used to normalize the time-of-flight spectra to the same neutron intensity. The measurement stations are equipped with air conditioning systems that maintain a constant temperature to reduce electronic drifts in the detection chains due to temperature changes.

In recent years, several experiments have been performed at the GELINA facility in support to criticality safety program. These new cross section measurements were motivated due to the concerns about data deficiencies in some existing cross-section evaluations from libraries such as ENDF/B, JEFF or JENDL for nuclear criticality calculations [156]. One of the investigated materials was vanadium (V), which is a key structural element. Recent data testing for ICSBEP critical benchmarks involving vanadium resulted in an overprediction of the experiment eigenvalue. The integral data testing is based on the JENDL-4.0 evaluation and does not have covariance data. Also, the ENDF/B-VII.1 and JENDL-4.0 resonance evaluations are based on the parameters (up to 100 keV) represented by the multi-level Breit-Wigner (MLBW) formalism. As a result, the MLBW resonance evaluation does not account for the resonance-resonance interference effects. New differential measurements and the corresponding resonance evaluation are needed to accurately predict the neutron resonances and to provide detailed resonance parameters and covariance data.

This appendix describes the transmission measurements carried out at GELINA with ^{nat}V metallic samples. To reduce bias effects due to e.g. dead time and background, the measurement and data reduction procedures recommended in [151]

Fig. D.7.: Realistic representation of the GELINA target system.

have been followed. The appendix provides the information required for extracting resonance parameters for ^{51}V (99.75% of the total isotopic abundance) by using the resonance shape analysis code REFIT [157]. In the description of the data the recommendations resulting from a consultant's meeting organized by the Nuclear Data Section of the IAEA (NDS/IAEA) have been followed [158].

D.3 Transmission technique

Measurements of cross sections are categorized into two types: transmission measurements, utilized to determine the total cross section, and reaction cross section measurements, which help deduce the partial cross section of a neutron-induced reaction (n, r).

In a transmission experiment, the measured quantity is the portion of the neu-

tron beam that passes through the sample without interaction. In the case of a parallel neutron beam perpendicular to a uniform material slab, this fraction or transmission T is derived by the Lambert-Beer law and can be written as:

$$T = e^{-\sum_k n_k \bar{\sigma}_{tot,k}} \tag{D.5}$$

Where $\sigma_{tot,k}$ is the Doppler broadened total cross section for the nuclide k and n_k is the number of atoms per unit area for the same nuclide.
From an experimental point of view, the transmission coefficient can be determined measuring the neutron flux while it passes through the sample (sample in C_{in}) and while the sample is out of the beam (C_{out})

$$T = \frac{C_{in}}{C_{out}} = \frac{\epsilon T \phi}{\epsilon \phi} \tag{D.6}$$

Figure D.8 represents a schematic example of how a transmission experimental setup is composed.

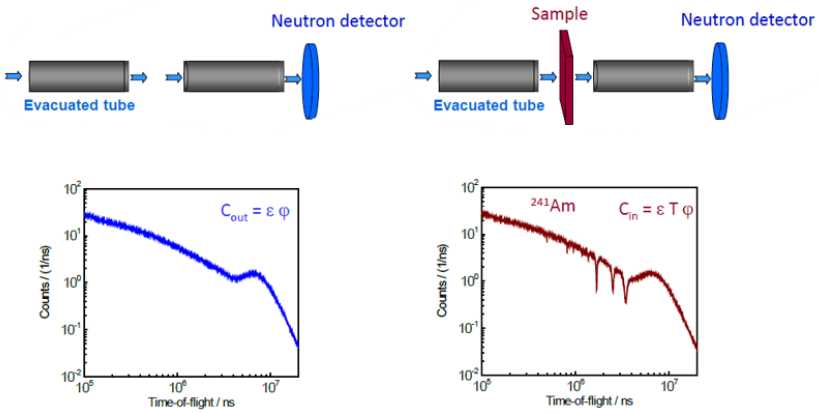

Fig. D.8.: Transmission measurement scheme. The ^{241}Am example is shown.On the left the sample out configuration is shown, while on the right the sample in situation is presented.

From equation D.6 is clear that the detector efficiency can be cancelled since it appears in both terms of the fraction. Therefore, the transmission calculation can be considered as an absolute measure.
The experimental value must be corrected taking into account the contribute of the background signal both in the sample-in and sample-out configurations:

$$T_{exp} = N \frac{C_{in} - B_{in}}{C_{out} - B_{out}} \tag{D.7}$$

Once the experimental value of the transmission coefficient is extracted, the total cross section can be evaluated fitting the transmission plot in function of TOF. In

order to correctly consider the experimental setup, equation D.5 can be transformed in:

$$T(t_m) = \int R(t_m, E) e^{-n\bar{\sigma}_{tot}(E_n) dE_n} \tag{D.8}$$

Where $R(t_m, E)$ is the response function of the TOF apparatus and of the detector, being t_m the measured TOF.

D.4 Experimental conditions

The transmission experiments were performed at the 50 m measurement station of flight path 4 with the accelerator operating at 800 Hz and an average beam current of about 60 μ A was deployed. The moderated neutron spectrum was used. A shadow bar made of Cu and Pb was placed close to the uranium target to reduce the intensity of the γ-ray flash and the fast neutron component. The flight path forms an angle of 9° with the direction normal to the face of the moderator viewing the flight path. The samples and detector were placed in an acclimatized room to keep them at a constant temperature of 20 °C. A schematic view of the experimental set-up is shown in figure D.9.

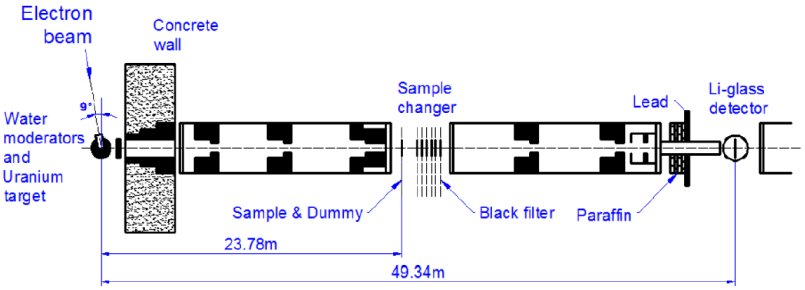

Fig. D.9.: Schematic representation of the transmission set-up at the 50 m transmission station of GELINA.

The partially thermalized neutrons scattered from the moderators were collimated into the flight path through an evacuated aluminum pipe of 50 cm diameter with annular collimators, consisting of borated wax, copper and lead. A set of Pb, Ni and Cu annular collimators was used to reduce the neutron beam to a diameter of 45 mm at the sample position. Additional lithium and B_4C collimators were installed to absorb neutrons that are scattered by the collimators. A ^{10}B overlap filter with an areal density of about 0.08 at/b was placed close to the neutron target to minimize the contribution of slow neutrons coming from previous accelerator bursts. The impact of the γ-ray flash in the neutron detector was reduced by a 16 mm thick Pb filter. The samples were placed in an automatic sample changer at a distance of approximately 25 m from the neutron source. Close to the sample position Na and Co black resonance filters were mounted in independent and automatic filter changers

to determine the background contribution at 2850 eV and 132 eV, respectively, and to obtain its time dependence.
In figure D.10 a picture of the Na and Co filters is shwon.

Fig. D.10.: Picture of the Na and Co filters used for the background estimation through the black resonance technique [151].

The neutron beam passing through the sample and filters was further collimated and detected by a 6.35 mm x 151.6 mm diameter NE912 Li-glass scintillator. The scintillator was connected through a boron-free quartz window to a 127 mm EMI 9823 KQB photomultiplier (PMT), which was placed outside the neutron beam perpendicular to its axis. The detector was placed at about 47.67 m from the neutron target and the diameter of the neutron beam at the detector position was about 90 mm.

The output signals of the detector were connected to conventional analog electronics. The anode pulse of the PMT was fed into a constant fraction discriminator to create a fast logic signal which defines the time the neutron has been detected. The signal of the 9^{th} dynode was shaped by a spectroscopic amplifier to determine the energy deposited by the ^{6}Li(n,t)α reaction in the detector. A module was included to produce a fixed dead time in the whole electronics chain directly after the detection of an event. This dead time t_d = 3305 (10) ns was continuously monitored by recording the time interval between successive pulses.
The time-of-flight (TOF) of the detected neutron was derived from the time difference between the stop signal T_s, obtained from the anode pulse of the PMT, and the start signal T_0, given at each electron burst. This time difference was processed with a multi-hit fast time coder with a 1 ns time resolution. The TOF and the pulse height

of each detected event were recorded in list mode using a multi-parameter data acquisition system developed at the JRC Geel. Each measurement was subdivided in different cycles. Only cycles for which the ratio between the total counts in the transmission detector and in the BF_3 neutron monitor deviated by less than 1 % were selected.

All the measurements were performed with two natural vanadium metallic discs of 0.35 and 2 mm thicknesses, separately or combined, providing data for three different areal densities. The main characteristics of the samples are reported in table D.1. The areal density of the natural samples was derived from a measurement of the weight and the area with an uncertainty better than 0.1 %.

Thick (mm)	Mass (g)	Area (mm^2)	Areal Density (at/b)
0.35	10.503 (0.010)	5031.37 (0.09)	(2.468 (0.002)) x 10^{-3}
2.00	68.812 (0.010)	5074.64 (0.09)	(16.030 (0.002)) x 10^{-3}

Tab. D.1.: Characteristics of the vanadium samples used for the transmission measurements. Each areal density was calculated by using the experimentally determined mass and area.

D.4.1 Experimental transmission

In order to correctly account for systematic effects due to the background model, equation D.7 can be modify introducing a factor K:

$$T_{exp} = N \frac{C_{in} - KB_{in}}{C_{out} - KB_{out}} \tag{D.9}$$

For most of the cases K = 1.00 (0.03). All spectra were normalized to the same TOF-bin width structure and neutron beam intensity. The latter was derived from the response of the BF_3 beam monitors. To avoid systematic effects due to slow variations of both the beam intensity and detector efficiency as a function of time, data were taken by alternating sample-in and sample-out measurements in cycles of about 600 seconds. Such a procedure reduces the uncertainty on the normalization to the beam intensity to less than 0.25 % [151]. This uncertainty was evaluated from the ratios of counts in the ^{6}Li transmission detector and in the flux monitors. To account for this uncertainty the factor N= 1.0000 (25) was introduced in equation D.9. The background as a function of TOF was approximated by an analytic expression

applying the black resonance technique.
The measured time-of-flight (t_m) of a neutron creating a signal in the neutron detector was determined by the time difference between the start signal (T_0) and the stop signal (T_s):

$$t_m = (T_s - T_0) + t_0 \tag{D.10}$$

Where t_0 is a time-offset which was determined by a measurement of the γ-ray flash. The flight path distance L = 47.670 (4) m, i.e. the distance between the centre of the moderator viewing the flight path and the front face of the detector, was derived previously from results of transmission measurements using uranium standard references [159].

D.5 Background correction

In a time-of-flight transmission measurement, the background can be described as a combination of both time-independent and time-dependent components [151].

$$B(t) = B_0 + B_\gamma(t) + B_{no}(t) + B_{ns}(t) + B_{ne}(t) \tag{D.11}$$

In measurements utilizing a moderated neutron beam, the contribution $B_\gamma(t)$ primarily arises from the detection of 2.2 MeV γ-rays generated by neutron capture in hydrogen within the moderator. This component poses a challenge for suppression via pulse-height discrimination since the energy deposition of a 2.2 MeV γ-ray in a Li-based scintillator is similar to that of the charged particles produced in the ^{6}Li(n,t)α reaction. The temporal distribution of these 2.2 MeV γ-rays corresponds directly to the deceleration process of neutrons within the moderator. Monte Carlo simulations conducted for the GELINA facility suggest that this component can be characterized by an exponential decay with a decay time of approximately 25.4 µs [160]. The decay constant identified in a comparable investigation using a Li-glass scintillator at ORELA was found to be 25.4 µs [161].
Extra γ-ray background emerges from high-energy γ-rays and Bremsstrahlung scattered within the target-moderator assembly. Their energy spectrum primarily consists of Compton-scattered γ-rays around 250 keV, allowing substantial reduction through an appropriate pulse height threshold. Furthermore, their arrival time aligns with that of fast neutrons.

The second time-dependent component, $B_{no}(t)$, arises from overlapping neutrons, detected, but originating from a prior cycle. This contribution can be mitigated by introducing a ^{10}B (used for this work) or Cd overlap filter into the beam. Evaluating the $B_{no}(t)$ component, highly dependant on the operational frequency and type of overlap filter used, can be approximated through measurements conducted under

similar experimental conditions. This assessment might occur at a lower frequency of the accelerator or by extrapolating the time response towards the end of a cycle. The second approach has been used within this work.

The third time-dependent component, $B_{ns}(t)$, primarily arises from beam neutrons that undergo scattering within the detector station. Assessing their temporal behavior involves conducting measurements under controlled experimental conditions that effectively eliminate the influence of overlap neutrons and 2.2 MeV γ-rays. Achieving such conditions necessitates a strategic combination of operating frequencies and filters. A minor component, $B_{ne}(t)$, contributes to the background due to neutrons scattered in the surroundings or alternate flight paths, notably in multi-user facilities. This component typically exhibits minimal temporal dependence, making its distinction from the time-independent background, B_0, challenging. Thus, determining the combined contribution, $B_0 + B_{ne}(t)$, requires measurements with the beam deactivated.
Finally, the time independent background component, here denominate as B_0, includes all the phenomena which are not related to the machine operations. For instance, such categories comprehend: radioactivity, cosmic ray induced signal, electronic noise among other relevant factors.
In summary, the background relative to Time of Flight (TOF) can be delineated using an analytical approach employing the black resonance method. This method involves defining free parameters within the analytical expression through a fitting process that aligns with observed resonance dips in the TOF spectra. Measurements incorporating black resonance filters determine these free parameters. Ensuring the filter's thickness guarantees a transmission through the filter at the resonance energy of less than 10^{-4}. Ideally, these black resonances exhibit a significant ratio between capture and scattering cross sections. To optimize accuracy, these filters should be positioned far from the detector's location.
As already mentioned, during the measurements here discussed, Na and Co filters have been used. Expanding the background function presented in D.11:

$$B(t) = b_0 + b_1 e^{-\lambda_1 t} + b_2 e^{-\lambda_2 t} + b_3 e^{-\lambda_3 (t+\tau_0)} \tag{D.12}$$

Being τ_0 the time difference between two cycles (1.25 ms).

D.5.1 Background analysis approaches

For this measurement, two different approaches were considered. In the first one, the Na and Co filters were kept fixed in the beam in order to account for the dependence of the background level on the presence of the sample [151]. This is the more accurate way of estimating the background contribution during the experiment but

with the drawback of losing information in the energy region around the filters black resonances. A model uncertainty of 3% was already derived in [159] from a statistical analysis between the estimated background and the observed background in the black resonance dips. Therefore equation D.9 can be used for this configuration.

In the second approach, no permanent black resonance filter was included in the experiment in order to access the whole energy range. For the thickest vanadium sample, the resonance at 4.1 keV could be used as black resonance. Therefore, this resonance was used to determine the background level for the sample-in measurements in a way similar to the measurement with the fixed Na filter. Moreover, it was also used to estimate the effect of the presence of the Na and Co black resonance filters in the background level. An increment of the background level of around 13% was observed when removing the filters, which was used for the determination of B_{out}. In the case of the thin vanadium sample, the same increment in the background level has been considered to determine B_{in} and B_{out} from the background obtained from the corresponding cycles with Na and Co filters in the beam. An uncertainty of 5% was derived for this procedure in previous experiments. In this specific case, the factor K is extimated differently in the two measurement conditions, therefore the equation D.9 must be changed in:

$$T_{exp} = N \frac{C_{in} - K_{in} B_{in}}{C_{out} - K_{out} B_{out}} \tag{D.13}$$

D.6 Data Analysis

As already mentioned three different configuration have been analyzed: 0.35 mm, 2 mm and 2.35 mm V thickness. In particular for all these configurations two set of data have been considered: with Na and Co filters and without any filters. The adequate considerations were reported in the previous sections.
Therefore, a total of 6 configurations have been analyzed. The following analysis have been reproduced for all the available data set, showing very similar trend. Therefore, all the plots and comments that will be presented can be extended to all the analyzed cases.

D.6.1 Background analysis

As already discussed, the constant and overlapping term can be determined evaluating the shape of the TOF spectra at the end of the cycle. Thus the first fitting model was:

$$B_{03}(t_m) = b_0 + b_3 e^{-\lambda_3 t_m} \tag{D.14}$$

It should be noted that the term τ_0 is not present, this was due to the necessity to fit the end of the cycle, therefore the time translation was considered equal to zero. In the successive analysis this time shift will be fixed to $\tau_0 = 1.25$ ms.

In figure D.11 and D.12 two different examples for this procedure can be shown. The TOF neutron spectra are represented in black, while the fitting function in red.

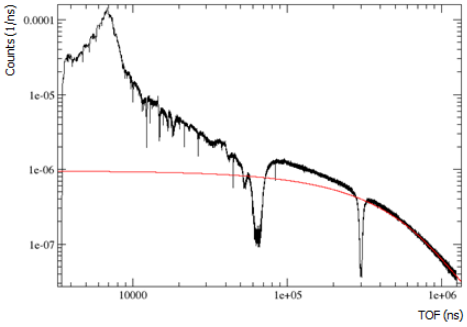

Fig. D.11.: End cycle fitting procedure for 0.35 mm vanadium sample considering the sample-in condition.

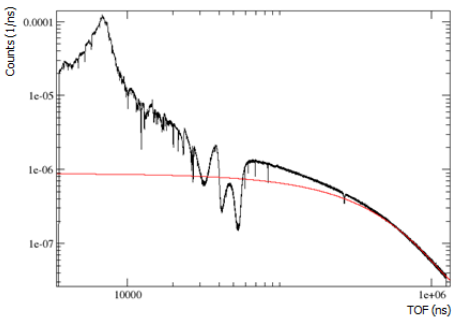

Fig. D.12.: End cycle fitting procedure for 2.00 mm vanadium sample considering the sample-in condition.

It should be noted that the fitting intervals have been intensely studied in order to reduce the χ^2 value. In all the conditions the obtained values were under the critical value considering a significance level α=0.05

Once the b_0, b_3 and λ_3 parameters have been calculated, the total background can be extracted. The only free parameters to be defined are b_1 and b_2, corresponding to the γ component and to the scattered neutorns component.
It should be useful to explain how the two different set of data have been analyzed:

1. **Data with Na and Co filters:**
   In this case, the parameters estimation derives directly from the fitting procedure. The two black resonances allow to find out the values of b_1 and b_2. In this case the fit was conducted, while the degrees of freedom are represented by the background parameters themselves.

2. **Data without any filters (thickes samples):**
   In this case, the background can be estimated referring to other set of data. In particular, the ratio b_1/b_2 has been evaluated from previous measurement (with Na and Co filters). Then, the ratio was used to calculate the value of b_2 knowing the value of b_1. In fact, the V resonance can be used as a black resonance in the thickest configurations. In these cases the fit was conducted, having only 1 degree of freedom: b_1.

Data without any filters (thin samples):
In the thin sample configuration, the b_1 parameter was not directly calculable. Therefore the ratio b_1/b_2 from the filters measures was not sufficient. In order to calculate b_1, its diminution between the sample-in and sample-out configuration due to the presence of the filters, has been calculated in the thick case. The percentage decrease has been then applied to the thin configuration with the same filters, being able to extract b_1. Then b_2 was calculated, knowing the b_1/b_2 ratio. While a fit was not possible due to the absence of degrees of freedom, an analytical function has been employed for the background estimation.

The results of the background analysis considering all the different configurations are shown in figures from D.13 to D.18:

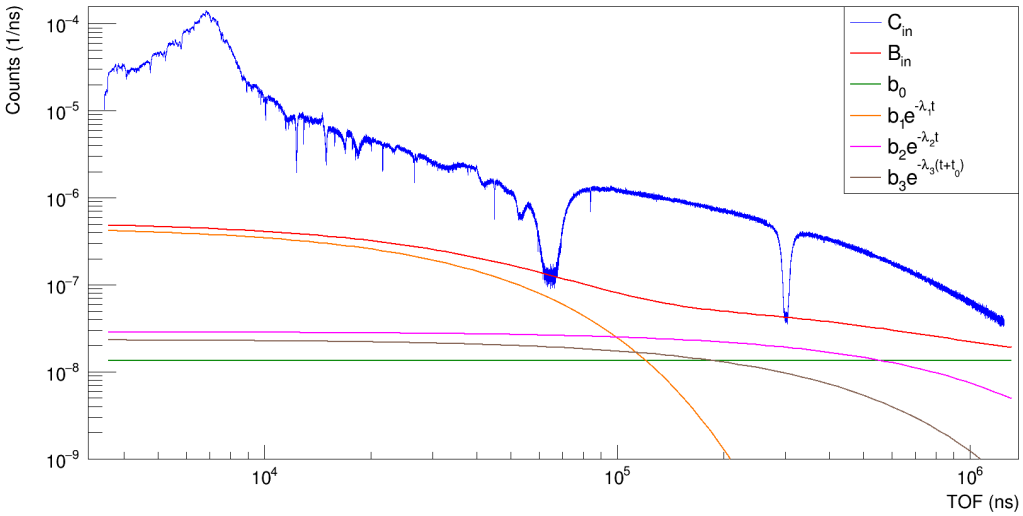

Fig. D.13.: TOF spectrum obtained with Na and Co fixed filters and the 0.35 mm vanadium sample (C_{in}) in the beam together with the total background (B_{in}) and its different components.

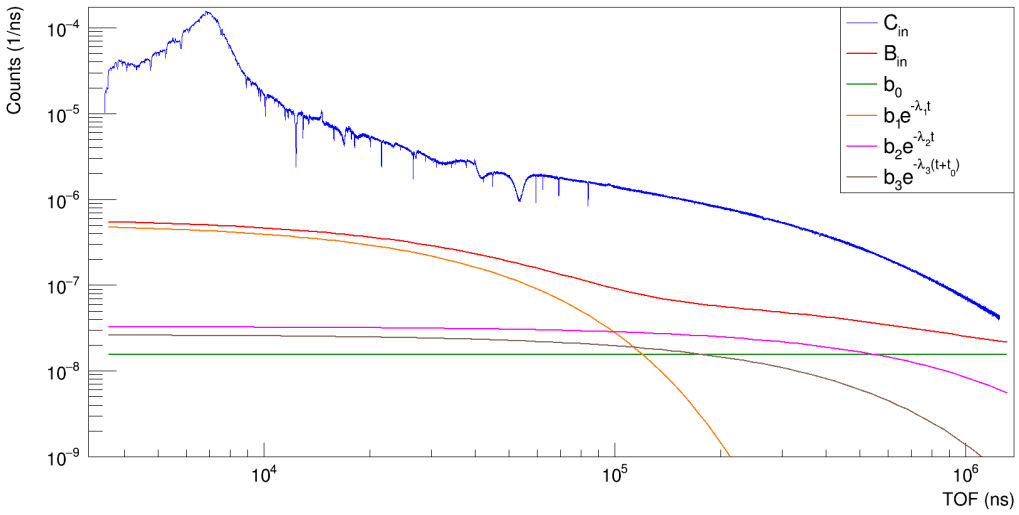

Fig. D.14.: TOF spectrum obtained with the 0.35 mm vanadium sample (C_{in}) in the beam together with the total background (B_{in}) and its different components. No fixed black resonance filters were present.

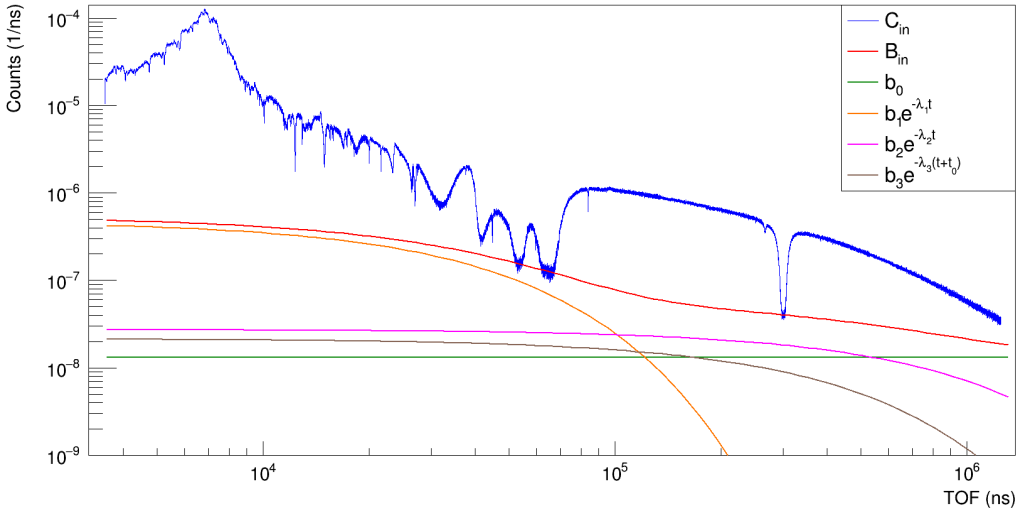

Fig. D.15.: TOF spectrum obtained with Na and Co fixed filters and the 2.00 mm vanadium sample (C_{in}) in the beam together with the total background (B_{in}) and its different components.

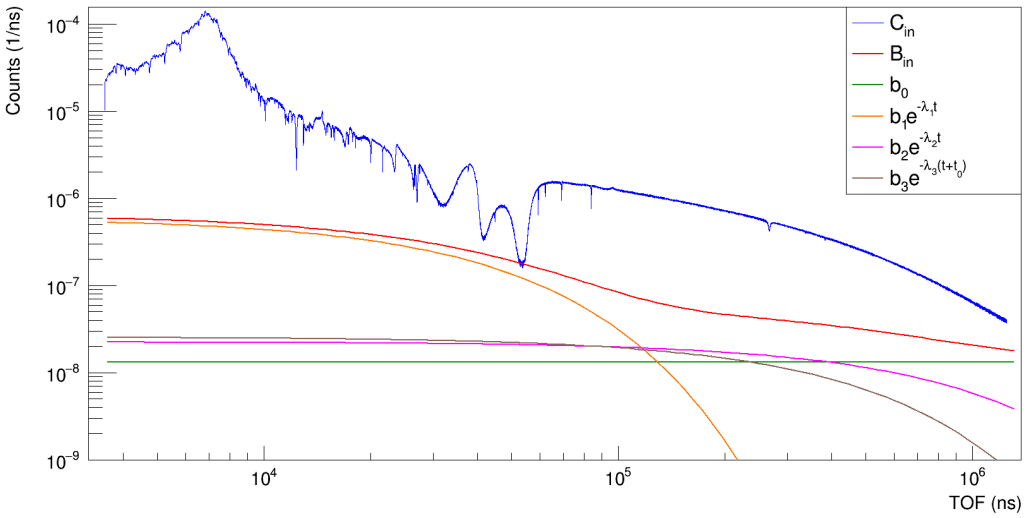

Fig. D.16.: TOF spectrum obtained with the 2.00 mm vanadium sample (C_{in}) in the beam together with the total background (B_{in}) and its different components. No fixed black resonance filters were present.

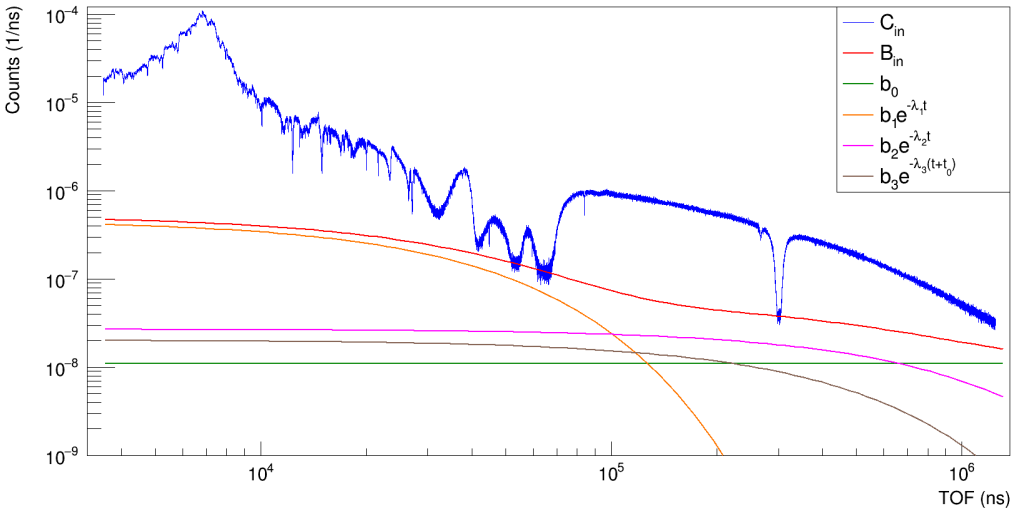

Fig. D.17.: TOF spectrum obtained with Na and Co fixed filters and the 2.35 mm vanadium sample (C_{in}) in the beam together with the total background (B_{in}) and its different components.

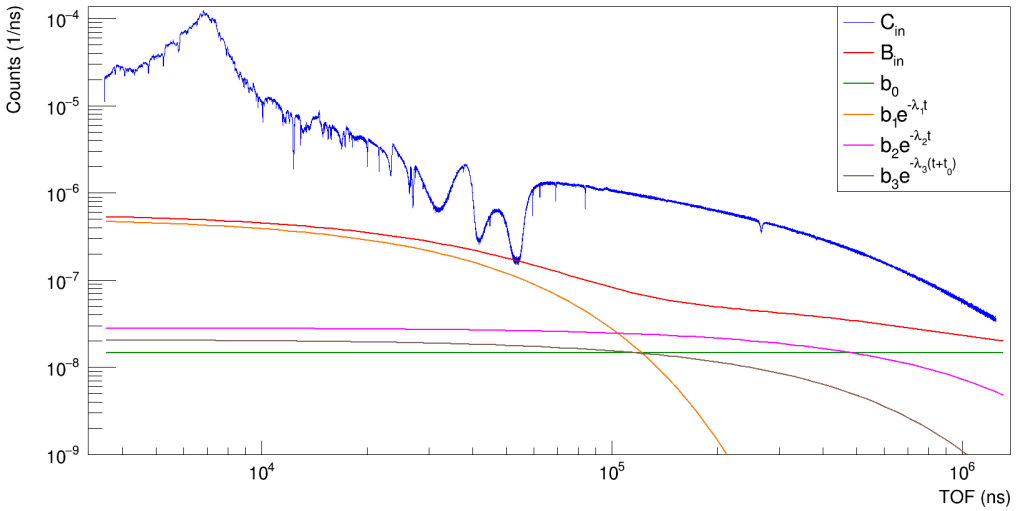

Fig. D.18.: TOF spectrum obtained with the 2.35 mm vanadium sample (C_{in}) in the beam together with the total background (B_{in}) and its different components. No fixed black resonance filters were present.

It should be noted that in the 2.00 mm and 2.35 mm samples the V strong resonance could be used as an extra black resonance to estimate the background, while in the thin sample it was not longer possible.
Very similar results can be obtained for the sample-out conditions, for brevity they are not reported here.
All the conducted fits produced χ^2 values under the critical value, therefore the background calculations can be considered statistically valid.

The background parameters can be shown in tables D.19, D.20 and D.21 respectively dedicated to the 0.35 mm, 2 mm and 2.35 mm configuration. The Φ symbol means "No Filters".

Filt.	ID	b_0 (10^{-8}) ns	b_1 (10^{-7}) ns	λ_1 (10^{-5}) ns^{-1}	b_2 (10^{-7}) ns	λ_2 (10^{-6}) ns^{-1}	b_3 (10^{-7}) ns	λ_3 (10^{-6}) ns^{-1}
Φ	C_{in}	1.56	5.28	2.94	0.327	1.35	29.4	2.95
Φ	C_{out}	1.57	5.56	2.94	0.333	1.35	29.3	2.95
Na+Co	C_{in}	1.36	4.67	2.94	0.289	1.35	9.39	2.95
Na+Co	C_{out}	1.35	4.92	2.94	0.295	1.35	9.57	2.95

Fig. D.19.: Parameters for the analytical expressions of the background correction for the sample-in and sample-out measurements for the vanadium sample of 0.35 mm thickness.

Filt.	ID	b_0 (10^{-8}) ns	b_1 (10^{-7}) ns	λ_1 (10^{-5}) ns^{-1}	b_2 (10^{-7}) ns	λ_2 (10^{-6}) ns^{-1}	b_3 (10^{-7}) ns	λ_3 (10^{-6}) ns^{-1}
Φ	C_{in}	1.33	5.92	2.94	0.226	1.35	8.28	2.95
Φ	C_{out}	1.50	6.86	2.94	0.391	1.35	7.35	2.95
Na+Co	C_{in}	1.32	4.70	2.94	0.274	1.35	7.94	2.95
Na+Co	C_{out}	1.56	5.40	2.94	0.311	1.35	9.32	2.95

Fig. D.20.: Parameters for the analytical expressions of the background correction for the sample-in and sample-out measurements for the vanadium sample of 2 mm thickness.

Filt.	ID	b_0 (10^{-8}) ns	b_1 (10^{-7}) ns	λ_1 (10^{-5}) ns^{-1}	b_2 (10^{-7}) ns	λ_2 (10^{-6}) ns^{-1}	b_3 (10^{-7}) ns	λ_3 (10^{-6}) ns^{-1}
Φ	C_{in}	1.48	5.23	2.94	0.283	1.35	8.07	2.95
Φ	C_{out}	1.81	6.28	2.94	0.354	1.35	9.76	2.95
Na+Co	C_{in}	1.10	4.61	2.94	0.278	1.35	6.23	2.95
Na+Co	C_{out}	1.47	5.35	2.94	0.291	1.35	8.25	2.95

Fig. D.21.: Parameters for the analytical expressions of the background correction for the sample-in and sample-out measurements with both vanadium samples.

It should be noted that the set of background parameters for configuration without filters is consistent with the previous GELINA report [162].
Thus the background analysis should be considered to be consistent with the previous work.

D.6.2 Transmission coefficient

Using equations D.9 and D.6 for the different configurations, the transmission spectra have been calculated. The spectra have been transformed from TOF to Energy using the AGS code.
Figures D.22 and D.23 show the 2.35 mm sample results for both the Na and Co filters and without any filters configurations:

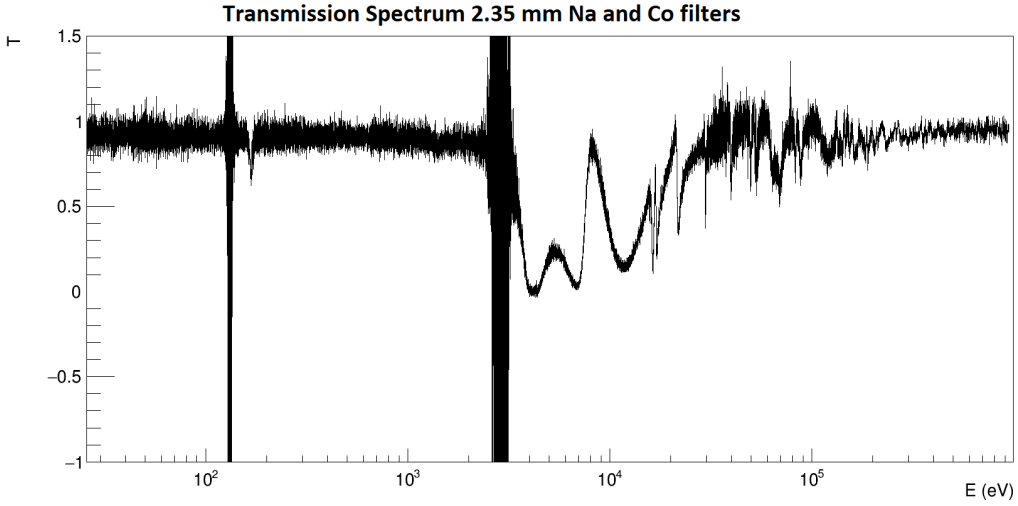

Fig. D.22.: Transmission spectrum for the 2.35 mm configuration with Na and Co filters. The first vanadium resonance analysis is disturbed by the presence of the Na filter.

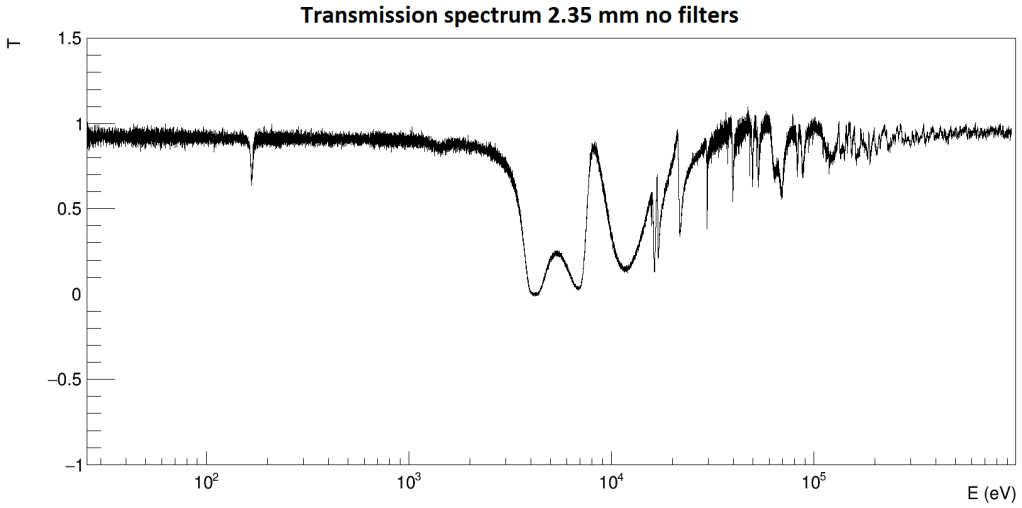

Fig. D.23.: Transmission spectrum for the 2.35 mm configuration without any filters. The first vanadium resonance analysis is not longer disturbed by the presence of the Na filter.

As can be clearly visible, the presence of the filters introduces some very peaked structure in the transmission spectrum. This is due to the low statistics in the filter region which can produce some massive oscillations while performing the ratio in

equation D.9. Moreover, the Na black resonance is very close to the first vanadium resonance, thus the difficulty to correctly evaluate the experimental data in this region.
The Co filters, on the contrary, is not disturbing the measure since its resonance energy is far below the keV energy region.

While studying the data acquired without any filters (for brevity: no-filters or NF), it should be noted that the absence of the black resonances allow to evaluate the whole energy range, without losing any information. Moreover, the transmission spectrum is cleaner and presents less oscillations and a better statistics.

With the aim to validate the background analysis, a comparison between the transmission spectra obtained with the Na and Co filters and the spectra obtained in the no-filters configuration has been performed. It should be noted that the configuration with the Na and Co filters has been considered as the reference distribution, since the background estimation was validated by the fitting procedure and by the χ^2 test. The comparisons have been performed considering the same sample thickness, figures D.24, D.25 and D.26 show the results with the residuals distribution in blue. The energy range that is shown in the graphics is a zoom in the region from 2 keV up to 1 MeV, where all the vanadium resonances are present.

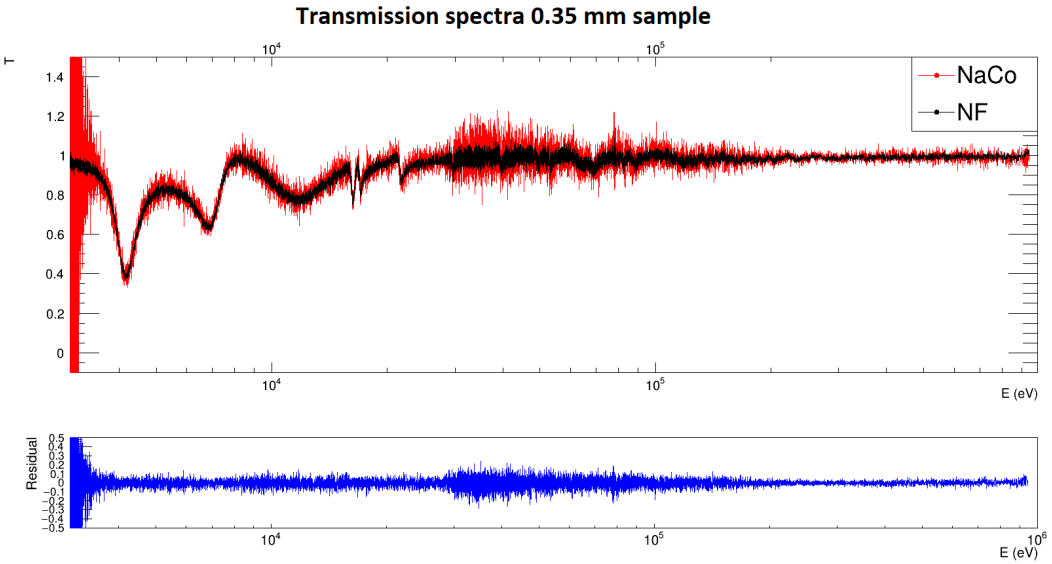

Fig. D.24.: Comparison between Na and Co filters (red) and no filters (black) configurations for the 0.35 mm sample. In blue the residuals distribution is shown.

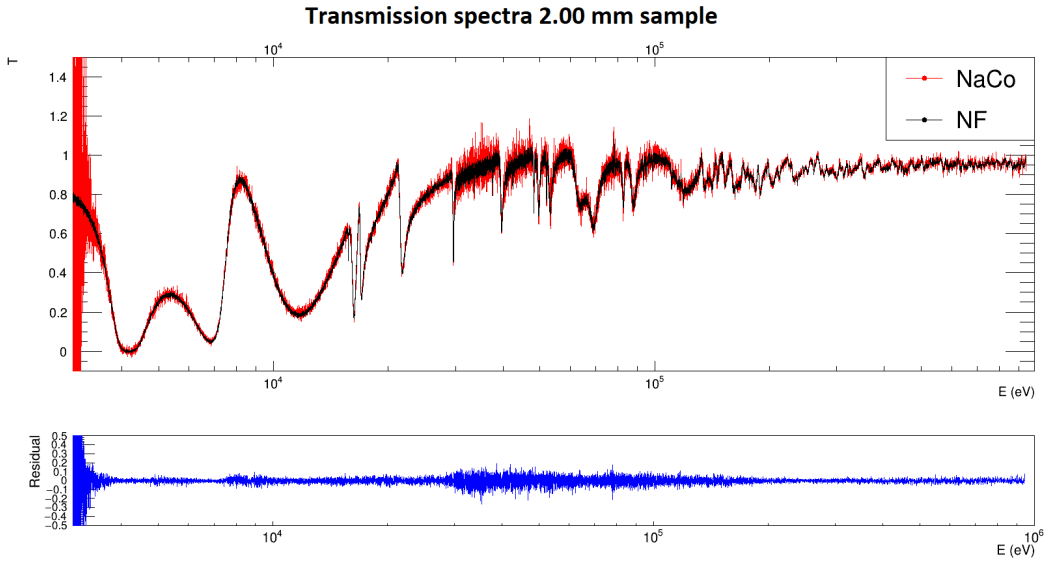

Fig. D.25.: Comparison between Na and Co filters (red) and no filters (black) configurations for the 2.00 mm sample. In blue the residuals distribution is shown.

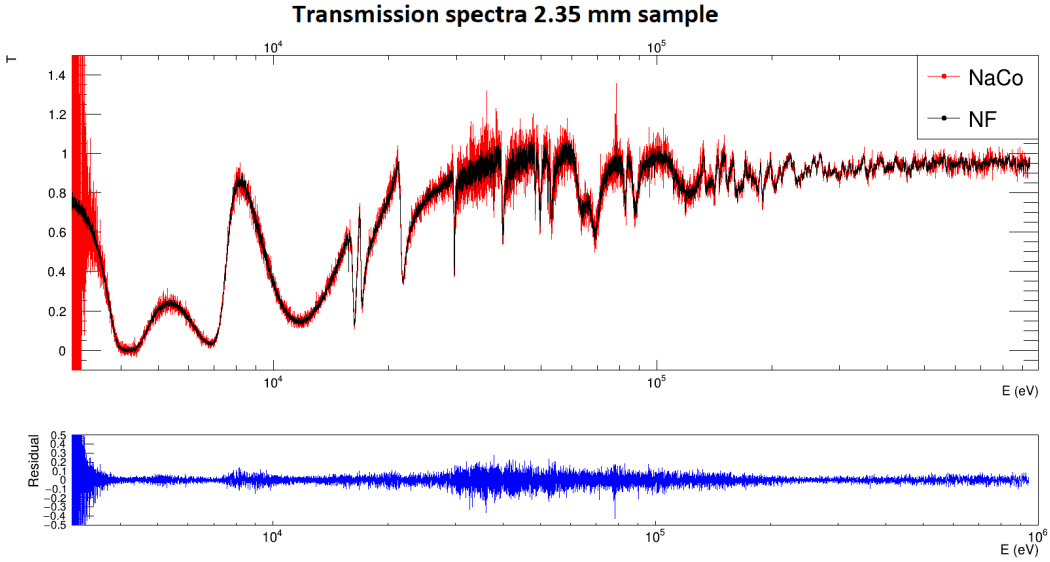

Fig. D.26.: Comparison between Na and Co filters (red) and no filters (black) configurations for the 2.35 mm sample. In blue the residuals distribution is shown.

It should be noted that there is an excellent agreement between the transmission spectra in the two different configurations. Moreover it should be considered that the residual distribution does not present any structure, meaning that the differences are due only to stochastic phenomena and not to some systematic smearing.
To better evaluate this aspect, a z variable was calculated for all the different energy bin i:

$$z^i = \frac{T^i_{NF} - T^i_{Na,Co}}{\sqrt{(\sigma^i_{NF})^2 + (\sigma^i_{Na,Co})^2}} \tag{D.15}$$

The histogram containing z was then evaluated. Figures D.27, D.28 and D.29 show the different distributions for all the sample thicknesses.

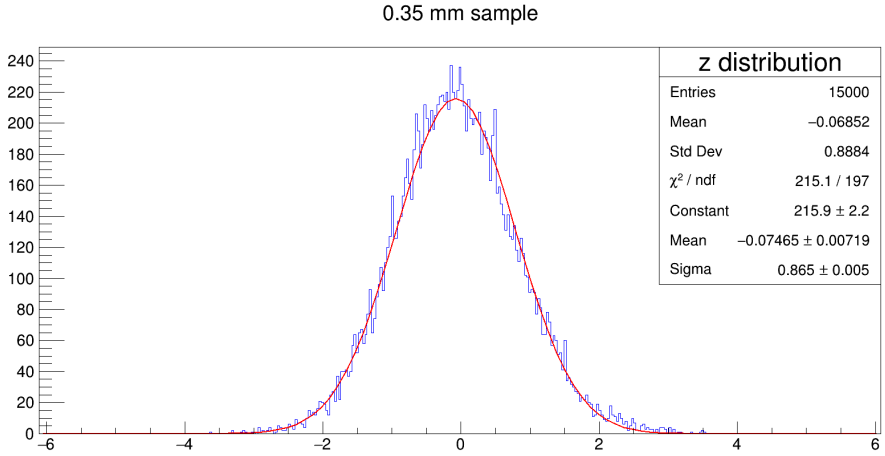

Fig. D.27.: z distribution for the 0.35 mm sample. A gaussian fit has been performed (red line), the χ^2 value was below the critical value ($\chi^2 = 231$).

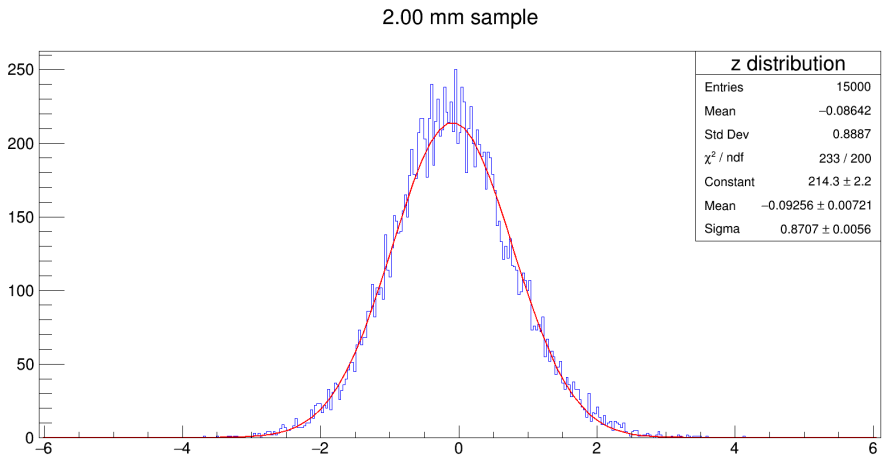

Fig. D.28.: z distribution for the 2.00 mm sample. A gaussian fit has been performed (red line), the χ^2 value was below the critical value ($\chi^2 = 234$).

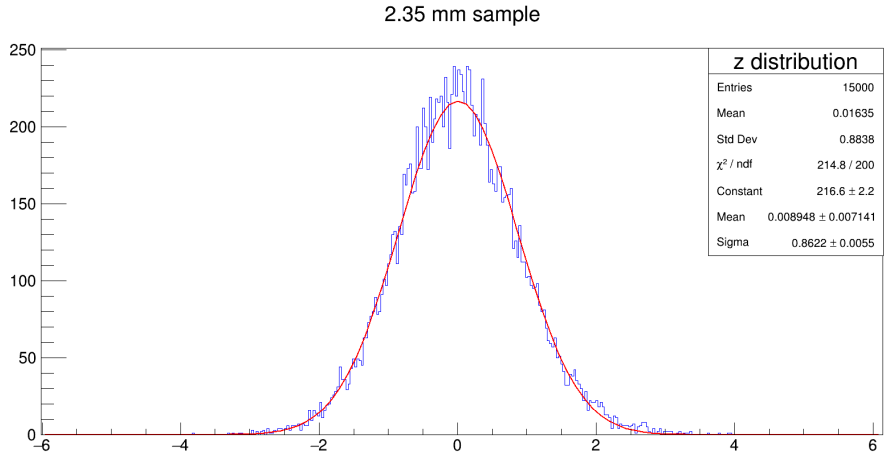

Fig. D.29.: z distribution for the 2.35 mm sample. A gaussian fit has been performed (red line), the χ^2 value was below the critical value ($\chi^2 = 234$).

Some considerations should be made in order to better understand the results:

- The chi square values are below the critical value for all the sample configurations. That means that the Gaussian function is statistically valid for approximating the data. Thus the distribution can be considered symmetric since the asymmetry index for a Gaussian distribution is 0.

- The mean values are close to zero. In particular, they derive from the definition of the z variable, so the positive or negative sign are not directly related to any statistical quantities.

- The standard deviations of the distribution are way higher than the mean values. Thus the data distributions can be considered to be centered in zero without committing a strong assumption.

- No accumulation points are present in the distributions (no undesired peaks), meaning that the transmission calculation is consistent over all the energy range and that there are no zones were the set of data are significantly different between each other.

Therefore, it can be concluded that the different set of data are statistically equivalent, providing perfectly compatible results. In addition,it should be noted that all the previous considerations lead to conclude that no systematic errors in the transmission factor calculations have been committed.
Furthermore, considering the nature of the z variable, it can be affirmed that all z values lesser than the critical value 1.96 ensure compatibility between the data

from the two distributions T_{NF} and $T_{Na,Co}$. Since the analyzed distributions show standard deviations of 0.86 - 0.87, it can be calculated that the critical z value corresponds to approximately 2.25 standard deviations. Therefore, 97.5% of the data within the energy range of 2 keV to 1 MeV are found compatible in both configurations, with and without filters, assuming a significance level of $\alpha = 5\%$. This observation further reinforces the analysis procedure utilized, validating the robustness of the background analysis previously presented.

List of Figures

List of Tables

Ringraziamenti

Dopo un percorso lungo più di tre anni, è difficile trovare le parole adatte per ringraziare tutte le persone che mi sono state vicine e che mi hanno aiutato.

Un grande ringraziamento va a tutto il gruppo di Torino, con una dedica particolare a Marco e Valeria per il loro aiuto e costante appoggio, anche nei momenti di difficoltà.
Voglio ringraziare anche il gruppo del Lemrap di frascati, venire da voi è sempre stato piacevole e molto istruttivo. Ho trovato amici e stimoli nuovi.
Voglio ringraziare di cuore anche i membri del JRC di Geel, in particolare Peter, Carlos e Stefan per avermi accolto e avermi aiutato durante il periodo trascorso da loro.

Ringrazio i miei ex compagni di università Giulio, Luca, Francesco e Gloria per tutti i pranzi insieme, per tutte le chiaccherate più o meno serie e per molto altro ancora.
Penso che la gratitudine sia qualcosa che non sia giusto misurare in base al tempo trascorso insieme. Per questo motivo voglio ringraziare immensamente tutte le persone del dormitorio 202 e 203 di Boeretang. Quei pochi mesi trascorsi insieme sono stati tra i più intensi e belli mai vissuti. Conoscere nuove persone è sempre prezioso, incontrare nuovi amici è un dono. Grazie a voi e a tutte le serate trascorse insieme.
Voglio ringraziare anche il gruppo di amici "Bevoni". Nonostante le vite di tutti noi ci abbiano portato a sentirci di meno, il vostro affetto e la vostra vicinanza sono stati per me importanti e di questo ve ne sono grato.
Dedico un pensiero e un ringrazimaneto anche a tutti gli altri amici di gruppi differenti che mi sono stati vicini in questi anni. Che il coronamento di questi tre anni possa essere anche vostro.

Voglio ringraziare immensamente la mia famiglia: siete delle persone straordinarie e ho sempre potuto contare sul vostro aiuto quando ne avevo bisogno. Auguro a tutti voi di poter avere un futuro felice e sereno, poichè nulla al mondo è più prezioso. Ci saranno giorni tristi e difficili, ma come voi avete aiutato me a superarli, io farò lo stesso con voi.

Infine voglio ringraziare una persona speciale che ha significato talmente tanto per me che non riesco nemmeno a trovare le parole per spiegarlo. Il tempo trascorso insieme è stato il dono più grande che potessi desiderare. Anche se le nostre strade si sono separate io non posso e non voglio dimenticare ciò che abbiamo condiviso. Il suo supporto e il suo amore mi hanno permesso di raggiungere questo traguardo e a lei dedico l'intero lavoro. Grazie Chiara.